Université d'Ottawa · University of Ottawa

FACULTÉ DE ÉTUDES SUPÉRIEURES ET POSTDOCTORALES

FACULTY OF GRADUATE AND POSTDOCTORAL STUDIES

Cory ZURELL

AUTEUR DE LA THÈSE - AUTHOR OF THESIS

Ph.D. (Civil Engineering)

GRADE - DEGREE

Department of Civil Engineering

FACULTÉ, ÉCOLE, DÉPARTEMENT - FACULTY, SCHOOL, DEPARTMENT

TITRE DE LA THÈSE - TITLE OF THE THESIS

Aerodynamics of Circular Cylinder Inclined to Airflow and Wind-Induced Vibrations of Dry, Inclined Cables at High Wind Speeds

H. Tanaka

DIRECTEUR DE LA THÈSE - THESIS SUPERVISOR

CO-DIRECTEUR DE LA THÈSE - THESIS CO-SUPERVISOR

EXAMINATEURS DE LA THÈSE - THESIS EXAMINERS

D. Lau

M. Mohareb

M. Saatcioglu

T. Stathopoulos

J.-M. De Koninck, Ph.D.

LE DOYEN DE LA FACULTÉ DES ÉTUDES SUPÉRIEURES ET POSTDOCTORALES

DEAN OF THE FACULTY OF GRADUATE AND POSTDOCTORAL STUDIES

AERODYNAMICS OF A CIRCULAR CYLINDER INCLINED TO AIRFLOW AND WIND-INDUCED VIBRATIONS OF DRY, INCLINED CABLES AT HIGH WIND SPEEDS

by
Cory Zurell

A thesis
presented to the University of Ottawa in partial fulfillment of the requirements for
Doctor of Philosophy in Civil Engineering

Department of Civil Engineering
University of Ottawa
Ottawa, Canada
K1N 6N5

January 2004

The Ph.D. in Civil Engineering is a joint programme
with Carleton University administered by the
Ottawa-Carleton Institute for Civil Engineering

Your file Votre référence
ISBN: 0-494-01780-5
Our file Notre référence
ISBN: 0-494-01780-5

Dedication

This thesis is dedicated to the memory of my dad. Of the many lessons I took from him, he taught me one of the most important lessons in engineering and in life:

Measure twice and cut once.

Acknowledgements

This thesis is the result of a research project conducted in conjunction with the Institute for Aerospace Research of the National Research Council of Canada (NRC). Funding was provided by a Natural Science and Engineering Research Council (NSERC) CRD grant jointly applied for by the University of Ottawa (Dr. H. Tanaka) and RWDI Inc. (Dr. P. A. Irwin) of Guelph, Ontario.

The important contributions of Dr. S. Cheng of the University of Ottawa, Dr. G. L. Larose, Mr. M. G. Savage and the many technicians at the NRC, and Dr. J. Bogunović Jakobsen of Stavanger University College, Norway, are gratefully acknowledged.

Many thanks go to my brother, Kirk, for willingly proof-reading my thesis.

Greatest thanks are due my supervisor, Dr. Hiroshi Tanaka, for his tremendous support, guidance, and advice throughout my studies at the University of Ottawa. It was a wonderful learning experience and a great pleasure working with him.

I would like to thank my wife, Rebecca, for her continued love and support, and for keeping me focussed when I required it.

Financial assistance for my studies was provided by the Ontario Graduate Scholarship programme and the Natural Sciences and Engineering Research Council (NSERC) Postgraduate Scholarship programme.

Abstract

Cable-stayed bridges are an efficient and elegant solution to bridging long spans. Though a widely used structural system, several significant issues are still unresolved regarding a cable-stayed bridge's performance, particularly with respect to the response of the cables to wind.

As tension members, stay cables have a very low diameter-to-span ratio such that the effect of bending stiffness on a cable's vibration characteristics is inconsequential. Coupled with this, stay cables have very little internal mechanical damping, thus they are quite susceptible to dynamic excitation. Several vibration mechanisms have been identified, however for some, including the potentially more damaging mechanisms, the required conditions and generating mechanisms are not completely understood.

Aerodynamically, a stay cable is simply a circular cylinder exposed to wind. A circular cylinder positioned normal to airflow is a touchstone topic in the fields of aerodynamics and fluid mechanics. A circular cylinder inclined to airflow, from a fundamental viewpoint, has been given very little attention considering the body of work concerning the former case.

The objective of this study was to determine the characteristics of the airflow about an inclined circular cylinder, and to determine and clarify necessary conditions for the generation of galloping vibrations and high-speed vortex vibrations in dry, inclined stay cables. A wind tunnel study was conducted in which a static circular cylinder was exposed, at varying relative wind-cylinder angles, to wind speeds corresponding to a Reynolds number range of 1×10^5 to 6×10^5. Surface pressure data was recorded to determine both the instantaneous and time-averaged pressures and forces on the section. Using the matrix computation software Matlab, programs were written to evaluate and analyse lift and drag forces, and pressure, lift, and drag coefficients. From the extensive data compiled, several significant conclusions concerning flow about an inclined or yawed cylinder and about the galloping and high-speed vortex vibration phenomena result.

Concerning flow about an inclined circular cylinder, the drag force coefficient is generally lower for lower relative inclination angles. This trend reverses over a small range of speeds within the critical Reynolds number range. Note that this and the following findings are based on the minimum inclination angle tested of 54.7°.

The rate of reduction in the drag force coefficient through the critical Reynolds number range is larger for larger relative inclination angles. The drag coefficient values converge during the drag crisis, regardless of the relative inclination angle.

The net lift force that appears during the drag crisis initiates at a lower wind speed for lower relative wind-cylinder angles. The upper bound at which this net lift force disappears does not seem to be affected by inclination angle. The magnitude of this net lift force is smaller for cylinders inclined at smaller inclination angles.

As with a circular cylinder positioned normal to the flow, a Strouhal number of about 0.2 can be used to predict the Karman vortex shedding frequency for a cylinder inclined to the flow, however the inclination angle must also be considered in addition to the wind speed and cylinder diameter.

The results of this study indicate that the Glauert-Den Hartog criterion—long established as a necessary condition for galloping of bluff bodies—is applicable in predicting the conditions for the galloping of dry, inclined cables. Conditions necessary for this galloping mechanism include, but are not limited to, a relative wind-cable angle of 60°, with the airflow in the critical Reynolds number range. This form of galloping appears to be velocity-restricted and is potentially related to the flow regime characterized by the formation of a single-laminar separation bubble. A significant span-wise correlation in the dynamic lift coefficient is evident under the above conditions.

An estimate of mechanical damping required to prevent galloping vibrations was evaluated. The resulting required damping is significantly higher than levels present in typical existing stay cables, indicating susceptibility of existing prototype cables to galloping vibrations.

No indication of a relatively low frequency mechanism was found in this test to assist in further explaining the limited-amplitude, high-speed vortex excitation witnessed in a previous dynamic model wind tunnel test. As evidence of this mechanism is restricted to wind tunnel tests of dynamic models, perhaps the formation of axial vortices—thought to be the cause of this phenomenon—is dependent upon motion of the cable or model. Future wind tunnel testing concerning this phenomenon using dynamic models should include particular attention paid to scaling parameters, including Reynolds number and Strouhal number.

Table of Contents

List of Tables

List of Figures

Nomenclature

Symbols

a	A vibration amplitude
B	A linear dimension
c	A constant
C_D	Aerodynamic Drag Coefficient
C_L	Aerodynamic Lift Coefficient
C_N	The coefficient of aerodynamic drag based on the force normal to the axis of an inclined cable, in the along wind direction.
C_p	Mean pressure coefficient
D	Cable diameter
F	A force
F_D	A drag force
F_L	A lift force
F_N	A drag force normal to the axis of an inclined cylindrical section
f	Frequency
f_0	Natural frequency
f_v	Frequency of vortex shedding
Iu	Turbulence intensity
L	Length
m	Mass per unit length
p	Pressure
p_0	Static offset pressure
R_e	Reynolds Number
r	Model radius
S_c	Scruton Number
S_t	Strouhal Number
U	Mean wind speed
U_{CRIT}	Critical wind speed
V	Velocity
V_r	Reduced Velocity
y	A general displacement
$\dot{y}$	A general velocity
$\ddot{y}$	A general acceleration
α	Angle of attack, model spring rotation angle, an angle
β	Prototype cable yaw angle
δ	Logarithmic Damping Decrement
ϕ	Relative angle between cable axis and mean wind direction
γ	Angle of attack
θ	Prototype cable inclination angle
ν	Kinematic Viscosity of Air, 0.150 cm^2/s at 20°C
ρ	Air Density – 1.225 kg/m^3
ω	Radial frequency
ζ	Damping ratio

Abbreviations

CFRP	Carbon Fibre-reinforced Polyester
FFT	Fast Fourier Transform
HDPE	High-density Polyethylene
NRC	National Research Council of Canada
PSD	Power Spectral Density

Subscripts

i	Pressure tap index
L	Lift component
m	Model
N	Drag component
p	Prototype

Chapter 1: Introduction

In recent decades, cable-stayed bridges have been used with increased frequency due to their ability to efficiently bridge long spans at a lower cost than the more traditional suspension bridge. Longer spans, resulting from advances in construction materials and technologies, as well as accepted analysis methods, have produced new challenges for designers.

From a wind design aspect, stay cables have traditionally been examined largely for wind drag forces transferred to the deck and pylons. Beginning with the Tacoma Narrows Bridge failure in 1940, dynamic effects due to service and climatic loading have been closely scrutinized with respect to the bridge deck and pylons. The cables, themselves, have only more recently been regarded as dynamic elements. Significant stay cable vibrations were first observed in the 1970's: on the Koehlbrand Bridge in Germany in 1974 (Ruscheweyh, 1999), and in 1976 on the Brotonne Bridge in France (Wianecki, 1979).

Because of their very nature, combined with their uses, cables are very sensitive to dynamic effects. In structural applications cables are used as long-span tension members. A small cross-section can be used to effectively support a substantial load. In cable-stayed bridge construction, 200 mm diameter cable may span 400 m—a depth-to-span ratio of 1:2000—and therefore the contribution of the cable's bending stiffness against lateral displacement is inconsequential, relative to other factors. Combined with this, a cable's structural self-damping is extremely low, and as a result vibrations may be excited relatively easily by mechanisms caused by normal climatic and service loads.

The behaviour of fluid flow around a circular cylinder positioned normal to the flow direction is a touchstone concept in the fields of aerodynamics and fluid mechanics. Myriad studies have investigated this topic, and the resulting dynamic mechanisms and behaviour are well documented and generally accepted. Though closely associated, a relative unknown is the behaviour of a circular cylinder inclined or yawed to a flow. Such a configuration is, however, widespread, including stay cables, marine risers, guy wires, power transmission lines, and so forth. Research has tended to focus on such specific applications rather than the fundamental concept, and as a result comprehensive information is quite limited.

Several vibration phenomena have been identified in bridge stay cables over the last thirty years, and in some cases remedial measures to suppress the vibrations have had to be implemented after the bridge was complete—always a costly endeavour. Many variables affect a cable's dynamic behaviour including the type of cable used, the length, the magnitude of tensile force, the cable surface, the

meteorological conditions at the site, and the architecture of the bridge. More recently designers have attempted to account for potential cable vibrations, however accurate prediction and adequate suppression of all forms of vibration has not yet been achieved.

Of the known vibration phenomena, the excitation mechanisms of several are well explained. Two forms of vibration—dry, inclined cable galloping, and high-speed vortex vibration—are not yet well defined. There have been few observed incidents of these two phenomena on prototype bridges. They have, however, been reliably produced in wind tunnel tests. As bridge spans—and costs—increase, consideration during the design phase of damaging vibrations in the finished bridge becomes more essential. Results of several research studies have included limited information about galloping and high-speed vortex excitation of inclined cables. These phenomena were usually not the focus of the studies but rather an unexpected result. Usually these phenomena arose during testing focussing on another particular type of cable vibration: rain-wind vibration. Consequently, published information concerning galloping and high-speed vortex excitation is not altogether complete. Previous studies have begun to define the conditions required for galloping or high-speed vortex vibration to arise. There is not yet, however, a definitive set of aerodynamic requirements and thus no definitive set of design criteria for cable-stayed bridges yet exists. Some researchers have proposed criteria for galloping instability. Subsequent findings have provided enough evidence to bring these criteria into question, though not enough evidence to render them invalid, and so further study is necessary. Further, and more critical, could these forms of cable vibration occur to a damaging degree on prototype bridges, existing cable-stayed bridges around the world could suddenly be rendered inadequate.

The study presented in the following document involves measurement of surface pressure variations about a static model of an inclined cable caused by airflow in a wind tunnel. These extensive pressure measurements allow determination of both the mean and time-dependent flow characteristics about the cable model. Unlike many other previous studies in which high-speed vortex vibration and dry, inclined cable galloping have been observed, the focus of this study is to investigate these two phenomena specifically. The objective of this study is to further examine and clarify flow properties about a circular cylinder inclined to airflow, and particularly to examine the required conditions and excitation mechanisms behind dry, inclined cable galloping and high-speed vortex excitation. As well, this study will further clarify the relationship between the two phenomena. Specifically, through the use of pressure time history data, the applicability to dry, inclined cable galloping of the Glauert-Den Hartog criterion—long accepted as a necessary condition for galloping instability of a bluff body—may be determined. As well, the influence of Reynolds number, signifying the relationship between

the flow's inertial and viscous forces, and conspicuously absent from previous studies, will be examined.

A general overview concerning stay cables and the associated vibration phenomena is presented in the following chapter. This summary includes descriptions of the various types of cable typically used for cable-stayed bridges, the various known vibration phenomena that affect stay cables, and the existing and some proposed methods of suppressing and controlling stay cable vibrations. Chapter 3 presents a review of the existing knowledge regarding the characteristics of flow about a circular cylinder, as well as a thorough review of the two specific aerodynamic mechanisms forming the basis of this study: galloping and high-speed vortex vibration of a dry, inclined cable. Chapter 4 provides an overview of the experimental approach, including a description of the model and the wind tunnel facilities, and an outline of the extensive testing regime. The analysis and discussion of the study results are presented in Chapter 5, with the conclusions and recommendations for future study summarized in Chapter 6.

Chapter 2: Stay Cables and Vibrations

2.1 Typical Composition of Bridge Stay Cables

Cable used for bridge stay cables has evolved over the years as better systems have been developed. The first modern cable-stayed bridges were built using wire rope comprised of helical coils of steel wires (Virlogeux, 1995). As with all bridges, longevity is extremely important, and so the cables must be protected from weather and fatigue. Corrosion protection of these first cables consisted of using an inert substance to fill gaps and voids between the strands, and subsequently coating the cable with a thick, protective paint. Later wire rope cables were composed of galvanized wire.

Lock-coil cables soon became the preferred choice over wire rope for stay cables. Lock-coil cables are comprised of an inner core of the traditional round steel wires, galvanized against corrosion, and surrounded by two or three layers of galvanized, interlocking, Z-shaped strands. Sometimes a few additional intermediate layers of wedge-shaped strands are used between the core and the outer Z-shaped strands. The outer strands provide a smoother, tighter surface, and due to the tight fit of the specially-shaped strands, the density of lock-coil cables is significantly higher (up to 30%) than wire rope (Gimsing, 1983). As a result, a smaller diameter is required to provide the same material area. These cables can be additionally protected through filling any voids with a protective paint, oil wax, or polyethylene.

Parallel wire strands of significant size have also been used on various bridges. Whereas wire rope has strands wound around a central wire, parallel wire strands are simply a group of parallel wires. Such strands require wrapping to confine the wires together, but have the advantage over wire rope and lock-coil cables in that no strength or stiffness is lost due to the helical winding of strands.

Though wire rope and lock-coil cables are still used, longer cables prompted a progression to cables comprised of a bundle of parallel strands contained in a steel, and later high-density polyethylene (HDPE), duct. The strands are usually 7 mm or 15 mm diameter. The duct would normally be injected with grout or oil wax for protection against moisture; the wires could also be galvanized for added protection. This system provides the beneficial characteristic of limiting bending stresses in the cable due to the independence of the strands, however this also reduces what little bending stiffness the cable would otherwise possess.

Parallel strand cables have led to cables comprised of individually protected, parallel strands. Each strand is made of galvanized wires, its voids filled with oil wax, and the strand covered with HDPE.

The cable comprised of these strands is covered with a polyethylene duct for protection and better aerodynamic characteristics. Each strand in a parallel strand configuration can be installed and tensioned separately.

Stay cables have also been made of pre-stressing bars. This option receives limited attention on large bridges as pre-stressing bars have a low fatigue resistance, and their installation requires heavy equipment (Virlogeux, 1995).

Future stay cables could include the use of composite materials employing carbon fibre. Compared to a steel cable, a carbon fibre reinforced polyester (CFRP) cable, equivalent in load capacity, would be of significantly lighter weight and smaller diameter.

Several issues must be addressed with respect to the choice of cable for any given bridge. Cost, of course, is a concern for any project. Installation of the cables can be a significant factor. Lock-coil cables of the scale used in long-span cable-stayed bridges are extremely costly, and due to their size (say 200 mm diameter and 300 m long) can be extremely difficult and costly to install. With the option to install each strand individually, protected parallel strand cables do not require such large equipment for their installation.

Given the desired design life of a bridge, maintenance is another significant issue in the choice of the cable system. Little maintenance is desired since replacing cables can be extremely difficult and costly, and so cables must be adequately protected from fatigue and corrosion. High internal damping is effective in preventing fatigue. Parallel strand cables were originally grouted with cement to prevent corrosion. Frequently fatigue issues arose, and when the cement was substituted with oil wax, the behaviour of the cable seemed to improve; the oil wax provided an increased level of damping. CFRP cables have significant durability potential in that corrosion is not a concern as it is with steel cables.

Lastly, aerodynamic considerations play a part in the cable selection. The surface texture of lock-coil cables and wire rope can affect the drag and aerodynamic behaviour of the cable. Conversely, a parallel strand cable is larger in diameter than a lock-coil cable, and so a larger drag force results than with lock-coil cables. For the Normandy Bridge in France, better than half of the horizontal bending moment created in the bridge deck is due to wind drag on the cables (Virlogeux, 1995), and so a change in the cable diameter can have significant consequences on the overall design.

Using CFRP cables would significantly lessen the wind drag seen by bridges of lock-coil or parallel strand cable construction—a reduction of 15-20% in wind loading for a large cable-stayed bridge is conceivable (Ostenfeld and Larsen , 1992). CFRP cables, being significantly lighter than steel cables,

are significantly more susceptible to vibrations. Furthermore, needing a smaller cross-sectional area than a steel cable in order to carry the same load, the resulting overall bridge structure could be more flexible, further complicating the aerodynamic behaviour. At present, cost of CFRP tends to prohibit its consideration.

2.2 Vibration Characteristics of Stay Cables

Considering their length—in some cases far exceeding 400 m—and composition, stay cables have virtually no effective bending stiffness. This coupled with extremely low/virtually no internal, structural self-damping, relatively small forces may excite cables to relatively large amplitudes.

The vibration characteristics of a stay cable are quite complicated. Stay cables, of a scale of interest to the present study, have a fundamental frequency in the range of 0.3 Hz. to 3 Hz. A cable's self-weight induces sag which is also dependent upon the tension in the cable. When the sag becomes large enough it affects the vertical vibration frequency by raising it, whereas the horizontal, or sway, frequency is initially unaffected by the sag. Frequencies and vibration characteristics can be further complicated by the flexibility of the supports; the pylons and especially the deck are far from being fixed supports in the classical, analytical sense of the term.

Structural self-damping values of bridge stay cables typically range from 0.01% to 0.2% of critical damping. The type of cable used, as described in Section 2.1, affects very much the level of self-damping. Normal engineering practice would assume up to 3% – 5% of critical damping for traditional structural building systems of steel or concrete: fully an order of magnitude greater than that of the best case for cables. Further, vibrations in normal structures can usually be controlled with an economical increase in the stiffness or adjustment in the mass of the structural system. Unfortunately little can be done to economically raise the effective damping of stay cables.

The consequences of uncontrolled cable vibrations are obviously serious. Damage from fatigue or full rupture of the cable or the cable anchorage would require expensive repairs, at best, or even catastrophic failure of the bridge structure, at worst. Even if the structure is perfectly able to withstand such vibrations, serviceability requirements limit movement of the deck for safe passage of traffic. As well, public perception needs to be considered; at the worst extreme, a bridge perceived to be unsafe is as useless as a bridge that is unsafe.

2.3 Stay Cable Vibration Phenomena

Bridge stay cables have been witnessed to vibrate in various manners, depending upon the specific cable characteristics and the environmental conditions in which the vibration occurs. The various phenomena include:

- Vortex shedding vibration
- Buffeting
- Wake effects/resonant buffeting
- Parametric excitation
- Aerodynamic instability, including:
  - Reynolds number-related instability
  - Rain-wind induced vibration
  - Dry inclined cable galloping
  - High-speed vortex excitation of dry, inclined cables

2.3.1 Vortex Shedding (Aeolian) Vibration

The behaviour of flow around a circular cross-section is principally influenced by viscous and inertial forces and may be characterized by ranges of Reynolds number. Reynolds number is the ratio of inertial forces to viscous forces and is given by:

$$R_e = \frac{U\,D}{\nu} \tag{2.1}$$

where U is the flow velocity, D, the diameter of the section, and ν, the airflow's kinematic viscosity. Flow around a circular cylinder at very low velocity ($R_e \approx 1$) follows the surface and detaches at the most leeward point; it is dominated by viscous forces. As the velocity of the flow is increased, corresponding to $R_e \approx 20$, the pressure around the cylinder will not be sufficient to keep the flow forced against the body's surface on the leeward side and inertial effects begin to dominate. The flow detaches prematurely (this location is referred to as the separation point) and a region of eddies forms at the leeward side of the cylinder. This slow moving region of eddies—the wake—is bounded by a shear layer extending from the separation point on each side of the body. Outside of this shear layer is the faster moving free airflow. As a result of the difference in flow velocity on either side of the shear layers, the shear layers tend to roll up on themselves, forming vortices. Increasing the flow velocity further ($30 < R_e < 5000$) sees the flow separation point organize into a line along the cylinder where the

shear layers roll into line-like vortices extending along the cylinder. Such vortices are formed and shed from alternating sides of the cylinder, and move downstream slightly slower than the adjacent flow. This phenomenon is also known as Kármán vortex formation. The frequency, f_v (Hz), of the vortex shedding is given by the well-known Strouhal relation:

$$f_v = \frac{US_t}{D} \tag{2.2}$$

where U is the mean wind speed, D, the diameter of the cylinder, and S_t, the Strouhal number; circular cross-sections typically have a Strouhal number of approximately 0.2 (Simiu and Scanlan, 1996). Increasing the flow velocity still further causes the flow across the surface to become turbulent. The separation point will no longer be an organized line, and thus organized vortices will not form; the flow in the cylinder's wake becomes turbulent. Further information on this subject is presented in Section 3.1.1.

This alternating vortex formation results in alternating pressure variations, and thus forces, acting on the cylinder, normal to the flow direction. Complications arise in a system where the cylinder is allowed to move. When the frequency of the vortex formation matches the natural frequency of the cylinder, the pressure variations drive the motion at that particular frequency and resonance results. Additionally, the movement of the cylinder, itself, alters the flow and controls the formation of the vortices. At this point, were the flow to increase slightly, the frequency of vortex formation would still be governed by the cylinder's motion and resonance would continue; the motion would not be suppressed. This phenomenon is called lock-in; refer to Figure 2-1.

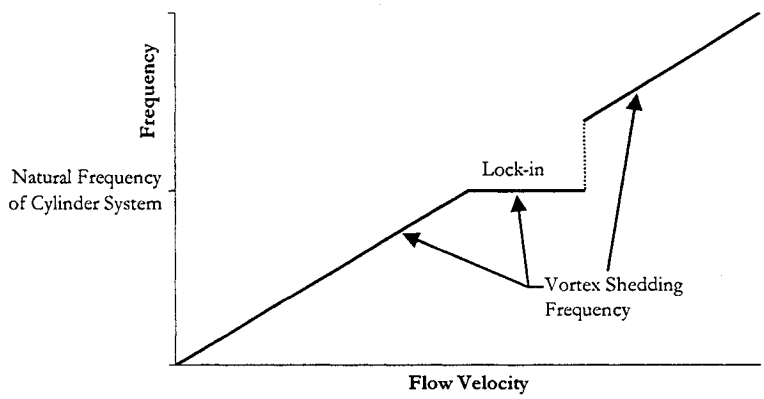

Figure 2-1: Vortex shedding frequency with wind velocity over elastic structure (from Simiu and Scanlan (1996))

The lock-in phenomenon is, thankfully, self-limiting. With increasing amplitude, the shedding pattern loses its uniformity and breaks up; thus the maximum sustained vibration double amplitude tends to be limited to approximately one diameter (Blevins, 1977).

As stated in Section 2.2, stay cables have a fundamental frequency in the range of 0.3 – 3.0 Hz. As the diameters of cables used for cable-stayed bridges are relatively small (150 – 250 mm diameter), the critical wind speeds that cause resonance in the lower modes are very low. Consequently the energy acting on the cable is very low, at worst producing very small amplitude vibrations. At higher wind speeds, higher modes of vibration may be excited, but as the frequency of vibration increases, mechanical self-damping also increases. Vibration amplitudes due to vortex shedding are usually in the order of a few millimetres, and, though fatigue has to be considered, these vibrations are not usually a great concern. A logarithmic damping decrement of δ>3% is recommended to avoid fatigue problems (Stubler *et al*, 1999). This value usually has to be higher anyway to suppress other forms of vibration.

2.3.2 Buffeting

Buffeting is unsteady, random loading resulting from fluctuations in the oncoming airflow. Generally this is not a harmful phenomenon for stay cables, though as with vortex shedding, fatigue may be a cause for concern. Vibration amplitudes tend to be limited due to the high tension in the cable supporting the dead load of the deck and the relatively small projected area exposed to wind. (With high-voltage transmission lines however, the tension is a function of the cable's self-weight alone, and so buffeting effects are more serious.) Buffeting can pose problems if sudden shocks are induced into cross tie cables (to be discussed in Section 2.4.2) with insufficient pre-tensioning. As well, some researchers propose aerodynamic instability may occur in bridges composed of two planes of stay cables as a result of buffeting. In theory, if the wind speed is such that the travel time of the flow from one stay plane to the next corresponds to half of a cycle of the deck's torsional vibration mode, the buffeting may excite motion in the deck (Virlogeux, 1998). In randomly fluctuating airflow, this phenomenon is not likely to result in prolonged excitement.

2.3.3 Wake Effects/Resonant Buffeting

There are different manifestations of this phenomenon however they all result from the same mechanism. Fundamentally, a stay cable's dynamic behaviour can be significantly altered by the airflow resulting from the close presence of another element or obstruction upwind.

A wake effect mechanism with the potential for serious consequences is the response of stay cables located leeward of bridge pylons. As mentioned in Section 2.3.1, because of the relatively small diameter of a stay cable, critical wind speeds that cause lower mode resonance in cables through vortex shedding are quite low. Bridge pylons have a width in the order of several metres, and thus high winds may cause vortex shedding at a frequency in the range of the cables' fundamental frequencies. Consequently, the cables may experience high energy buffeting of a harmonic nature (resonant buffeting), and large amplitude vibrations may occur. Limited possibilities exist for this phenomenon due to the inclination of the cables relative to the pylons.

Occasionally, to limit cable size, twin cables are used in lieu of a single stay. The two cables are spaced relatively close together and if the wind is incident along a line joining the two cables, the second cable may be influenced by the wake of the first. Again the critical wind speed producing vortices at a resonant frequency is rather low, therefore possessing low energy, and so the result would not be very significant. However, if the cables are close enough—in the order of a couple of diameters—the wake of the first will excite the second. This resulting movement will then have an effect on the flow around the first, upstream cable, thus increasing the effects on the second, and so on; a vicious circle develops. This phenomenon appeared in the cables of the Yobuko Bridge in Japan, where the downwind, 76 mm to 84 mm diameter cables, spaced two diameters from their upstream twins, vibrated to approximately two diameters (Yoshimura *et al*, 1995). This phenomenon disappears as the distance separating the two cables increases.

A similar effect occurs among the individual, parallel strands of a stay not yet enclosed by a duct. This usually only occurs during construction. The external strands may be excited by the wind and vibrate, contacting the inner strands. The result is a significant level of unsettling and undesirable rattling called 'breathing of strands' (Virlogeux, 1998). This action is suppressed once the duct is installed over the strands.

2.3.4 Parametric Excitation

Vibrations of stay cables can be excited by motion in the anchorage points. A cable's self-damping is very low, and so even small movements of the deck or pylons due to wind or traffic loads may cause large amplitude motions in a stay cable. This mechanism can be especially serious if the fundamental frequencies of the stay cables and those of the overall structure coincide. This was shown to be the case of the Normandy Bridge during design were it not for the presence of cross tie cables to raise the fundamental frequencies of the stays to higher modes (Virlogeux, 1995). However, rectifying such a problem is not necessarily as simple as modifying the frequencies of the cables. In 1995, cables of the

Second Severn Crossing in England experienced extremely large amplitude vibrations. Engineers determined that occasionally the deck motion corresponded to the frequency range of the cables. Cross tie cables were installed to restrict the cable oscillations, which they did, however with the ties in place the vibrations of the deck increased substantially (Stubler *et al*, 1999). This behaviour seemed to indicate that the deck was indeed exciting the cables; the cables were accepting energy from the deck movement, and acting like dampers. Unfortunately, once restricted, the cables could no longer accept the same level of energy, thus the amplitude of deck vibrations increased.

Stubler *et al* (1999) suggest two criteria to consider with regard to parametric excitation:

Appearance and comfort (at U=15 m/s):

$\frac{a}{L} < 0.0006$, where a is the amplitude of vibration, L the cable length

Admissible deviation angle:

$\frac{a}{L} < \frac{\alpha}{\pi}$, where α is the admissible deviation angle at the cable anchor point.

2.3.5 Aerodynamic Instability

Several phenomena that could, and do, result in aerodynamic instability in stay cables have been identified in the last few decades. Reynolds number effects on stability are relatively minor compared with the other three phenomena described in this section. Rain-wind induced vibration has been seen to be a very serious phenomenon, while dry, inclined cable galloping and high-speed vortex excitation, though potentially serious, are relative unknowns.

The latter three phenomena are specific to inclined cables. A section in airflow, symmetric about the flow vector, does not experience sustained lift; no resultant force transverse to the flow exists. As soon as a section loses the property of symmetry, it will experience a resultant lift force. When rain is present, various factors cause the rainwater to vary the shape of the section, causing instability. Called rain-wind vibration, this is discussed in Section 2.3.5.2.

Round cables present a circular section to winds normal to the cable axis, and a symmetric elliptical section (of varying aspect ratio dependant upon the relative angle between wind and cable) to winds from any other direction. And so, an outright resultant lift force, independent of wind speed and due to the cross-section geometry, will not occur. However, winds acting on a stay cable from angles

other than normal to the cable axis may cause vibrations and instability due to a more complicated flow regime initiated by the relative angle between wind and cable axis. This is discussed in Sections 2.3.5.3 and 2.3.5.4.

2.3.5.1 Reynolds Number-related Instability

At a certain critical range of Reynolds number (given by Equation (2.1)), there is a significant and abrupt reduction in drag (40 – 60%). This critical range is also affected by the roughness of the section's surface; a rougher surface will have a lower critical R_e value. A cable vibrating parallel to the wind direction experiences a fluctuating relative wind velocity. If this range of fluctuation corresponds to the critical R_e range, a *drag crisis* may occur; as the cable sways into the wind, the relative velocity is higher corresponding to a lower drag force—swaying with the wind, the relative velocity is lower, corresponding to a higher drag. These two mechanisms combine to continuously augment the vibration amplitude. This has been a significant source of problems for power transmission lines, made worse by the contribution of helical stranding on the effective roughness, however, though stay cables are not immune to such excitation, no problematic instances have been reported attributed to this phenomenon.

2.3.5.2 Rain-wind Induced Vibrations

Rain-wind induced vibrations of inclined cables emerged during the mid-1980's as one of the greatest concerns of bridge engineers. Under certain wind conditions, large, limited amplitude vibrations seemed to occur when it rained, but did not occur under the same wind conditions without rain. This phenomenon is quite significant as large amplitudes may be experienced under relatively low wind speeds. Beginning with Hikami and Shiraishi (1988), field observations and wind tunnel testing by several researchers have clarified quite specific conditions conducive to this vibration mechanism. These conditions are:

- moderate rain. Neither light drizzle nor a downpour is conducive to such vibrations.
- wind speed of 6 – 18 m/s, with the majority of the cases documented in the range of 8 – 12 m/s. The resulting reduced velocity (Equation (3.6)) range has been observed to be 20 – 90.
- fundamental frequency of cable vibration in the range of 0.6 – 3.0 Hz
- cable diameters ranging from 140 mm – 225 mm
- Reynolds number in the transition range from sub-critical to critical: $6\times10^4 – 2\times10^5$
- cables on the leeward side of the pylons; the wind is tending to lift the cables

- cable inclination of 20° – 45° from horizontal (though rain-wind vibrations have also been observed for nearly vertical hangers on arch bridges)
- angle of azimuth of the stay plane relative to the wind direction of 20°–60° (Some give this range as 30° – 80°)
- a certain small-scale roughness on the duct (usually polyethylene), akin to a build-up of dirt and grit under normal service conditions
- the bridge location usually in close proximity to a large body of water, or with relatively flat surroundings, indicating that a low level of turbulence and fairly uniform flow over the cable length are required

These conditions cause the formation of two streams of water on the cable. One stream forms on the lower face of the cable duct, drawn by gravity. The other stream forms on the upper face of the cable duct, produced by the combined effects of gravity, wind, and capillary action. The presence of these two streams effectively alters the cross-section of the cable resulting in a change in the aerodynamic forces acting on the cable, thus oscillations result. This phenomenon has been found by Japanese researchers to be directly linked to the existence of the upper stream, however others (Ruscheweyh, 1999b; Verwiebe, 1998) have shown vibrations can occur with just the lower rivulet. In fact, Verwiebe (1998) found there to be three distinct types of rain-wind vibrations: a predominantly across-wind or a predominantly along-wind vibration involve both upper and lower rivulets; the third involves only the lower rivulet, with the resulting motion predominantly across-wind, though including a significant along-wind component.

As vibrations arise, the inertia of the water streams, combined with the motion, cause the water streams to move circumferentially on the cable surface at the same frequency as the cable vibration. This motion, in turn, produces cyclical changes in the aerodynamic response by varying the separation point of the flow, thus cyclically changing the lift and drag forces and increasing the oscillation intensity (Ruscheweyh, 1999b). It is a sort of self-sustained oscillation.

Observed rain-wind vibrations have tended to be in the plane of the cables, though with some transverse motion. The peak-to-peak responses of vibrating cables have reached up to two metres (Matsumoto *et al*, 1992)—obviously a serious concern for designers.

In cases where no specific measures are taken to break up the formation of the upper stream, Irwin (1997) suggests the following Scruton number limit to avoid rain-wind vibration problems:

$$S_C = \frac{m\delta}{2\pi\rho D^2} > 10 \qquad (2.3)$$

where m is the mass/length, δ, the logarithmic damping decrement, ρ, the air density, and D, the cable diameter. For typical stay cables, the logarithmic decrement should therefore be greater than 3 – 6% (Stubler *et al*, 1999).

This phenomenon has been well studied, and the mechanism is well described, qualitatively. As well, various methods have been developed to suppress such vibrations. However, no definitive answer exists as to whether or not this phenomenon will occur on a given bridge, or exactly how much damping is enough to suppress these oscillations. And so, though the mechanism is well established, studies are required to determine effective, reliable and practical prevention and control.

2.3.5.3 Dry, Inclined Cable Galloping

The unstable, aerodynamic phenomenon of galloping has long been associated with power transmission cables, particularly when the cables have been partially coated with ice by freezing rain. The ice, driven by wind and gravity usually forms on one side, towards the bottom; the resultant cross-section is somewhat egg-shaped. The aerodynamic forces caused by this alteration may cause extremely large-amplitude vibrations resulting in clashing with adjacent cables or, ultimately, failure of the cable or its connections to the transmission tower. Referred to as *negative aerodynamic damping*, the aerodynamic forces augment the vibrations rather than suppress them. The galloping mechanism is further explained in Section 3.2.1.1.

So-called dry, inclined cable galloping was first reported in wind tunnel studies conducted in Japan. It differs from the traditional form of galloping in that it occurs for cables of circular cross-section[1]. This type of vibration has not, however, been expressly observed in actual bridge cables; Irwin *et al* (1999) claim, *"some field observations appear more consistent with galloping than rain/wind oscillations"*, though no specifics are given. A potentially critical finding of some study results is that additional damping does not seem to have a significant effect in controlling these vibrations. The onset velocity for galloping motion increases only a small amount with an increase in damping, and therefore could still lie within the foreseeable design wind speed range. The ramification of this result is that a potential exists of many existing cable-stayed bridges being susceptible, theoretically, to this vibration mechanism, and an attempt to prevent the problem though an increase in damping may not be

---

[1] Limited instances of conventional galloping of stay cables have been observed in the past. Matsumoto *et al* (1989b) reported galloping of cables which were sheathed in a tube of hexagonal cross-section. Wind tunnel tests confirmed a negative slope of the lift force coefficient, thus indicating galloping.

effective. Subsequent study results have somewhat contradicted these initial findings, making them appear relatively conservative.

The actual aerodynamic mechanism producing this reaction has yet to be clearly defined, and there is sufficient reason for discussion as to whether this is a practical problem, or even a legitimate one. That it has not been expressly observed in prototype cables and seems to be very sensitive to support conditions in wind tunnel studies, the phenomenon may be more a function of the supports in the wind tunnel model than the behaviour of an actual cable. As well, perhaps motion witnessed in some wind tunnel tests, heretofore described as galloping, was in fact limited-amplitude vibration in which the maximum amplitude was not yet achieved and simply the limits of the test equipment were reached. Further study is therefore needed to determine what problems, if any, are posed by this mechanism.

This phenomenon is thoroughly reviewed in Section 3.2.1.

2.3.5.4 High Speed Vortex Excitation of Dry, Inclined Cables

Many of the most serious cable vibrations observed in the field have involved the rain-wind vibration mechanism. Some observed vibrations, however, have been reported to occur without rain, and at a much higher wind speed range than for rain-wind vibrations. This phenomenon has been attributed to high-speed vortex excitation. These vibrations, which are of limited amplitude, occur at higher velocities than those at which normal Kármán vortex excitation (described in Section 2.3.1) would excite the lower vibration modes. Though limited study has been performed concerning this phenomenon, it is thought that the mechanism producing vibrations under these conditions involves a suggested axial airflow along the back of the inclined cable. Matsumoto (1998) observed that vortices shed from this axial flow would interact with vortices produced by Kármán vortex shedding, intermittently enhancing the Kármán vortex. For their test, they found the Kármán vortex to be enhanced at every third shedding by an axial vortex at a certain discrete wind velocity. The amplified vortices would be produced on alternating sides of the cable, and consequently the cable would be excited similar to, but to a much greater amplitude than, normal vortex vibration.

As with all vibrations, damping devices have been used to suppress these vibrations, however, as with most vibration phenomena, the optimum amount of damping is not known. On the Meiko West Bridge I in Japan, for example, cross ties between stay cables were originally installed on the bridge to control cable vibrations, but the tie-to-stay connections were damaged anyway due to severe

vibrations (Matsumoto *et al*, 1997). Much more needs to be known about this phenomenon in order to predict it, and efficiently prevent or control it.

This phenomenon is thoroughly reviewed in Section 3.2.2.

2.4 Methods of Vibration Suppression

Suppression of cable vibrations is critical to the longevity of a bridge. Besides simple comfort and peace of mind for those using a bridge, unwanted vibrations in the cables lead to fatigue of the anchor points for which repairs are extremely costly. If a cable vibrates at 2 Hz for only, say, 2% of the time, over the course of only one year this translates into over one million cycles. For bridges built with a service life of 75 to 100 years, fatigue becomes a serious concern.

Several methods have been developed to suppress cable vibrations. These methods can be split into two categories: mechanical and aerodynamic. Mechanical measures suppress vibrations through damping or restriction of motion; aerodynamic solutions prevent vibrations by altering the airflow such that the generating mechanisms do not occur. The choice of method depends on several factors:

- *Efficiency* – how effective a particular method is in suppressing all expected, or certain specific, vibration phenomena. A certain method may adequately suppress certain vibrations, but not others. It may even produce vibration mechanisms that would not otherwise occur.

- *Maintenance* – what is required to maintain a suppression method over the design life. Some methods may not require any ongoing maintenance, while others may require regular review and maintenance to be effective.

- *Aesthetics* – how the suppression method affects the overall visual statement of the bridge. Some methods may be concealed and will not alter the appearance of the bridge, while others will be visually predominant and may detract from the appearance.

- *Cost* – as with all things, cost can prohibit certain methods in some cases. Cost factors can arise in capital cost and/or maintenance costs over the design life.

2.4.1 Duct Shape

The idea of altering the cable shape arose as a means of preventing rain-wind vibrations. Rather than a smooth duct, the surface is modified to prevent the formation of the upper stream of water, thus eliminating the precipitating factor for the rain-wind mechanism. Several different shapes have been

tried. The first involved forming longitudinal channels along the length of the duct to prevent transverse movement of water on the duct surface, preventing the upper stream from forming. This modification was implemented on the Higashi-Kobe Bridge. The drawback to this solution is twofold: the overall diameter of the cable is increased slightly, thus increasing the projected area subjected to drag, and more importantly the irregular shape increases the drag coefficient significantly—from 0.5 for a smooth cylinder to 1.35 for the new shape, in the supercritical Reynolds number range (Virlogeux, 1998). As well, in an attempt to mitigate certain vibration mechanisms, other mechanisms may appear. For this same surface modification, though rain-wind vibrations did not arise, vibrations at higher wind speeds, and without rain, materialized (Matsumoto, 1998).

Other shapes investigated include the addition of helical fillets to the duct, and dimpling of the duct surface—akin to a golf ball. The former, as tried on the Normandy Bridge, involved forming two helical fillets in the duct surface, 1.3 mm deep with a pitch length of 600 mm. This alteration resulted in an acceptable increase in drag coefficient from 0.5 to 0.63 in the supercritical Reynolds number range (Virlogeux, 1995), while impairing the formation of a continuous upper water stream. The latter modification was investigated by Miyata *et al* (1994). Extensive wind tunnel tests were performed on cable models with varying degrees and patterns of roughness in an attempt to prevent rain-wind vibrations. They found that the model with only discrete patches of dimples had a comparable drag coefficient at sub-critical flow velocities to that of a smooth cable. The critical Reynolds number was significantly lower than that of a smooth cable, and the drag coefficient dropped significantly at the critical R_e range, remaining approximately constant thereafter with increasing velocity. Thus turbulent flow occurs at a lower velocity for the dimpled surface and the drag force at higher wind speeds is less that that of a smooth cable. Testing under conditions that would produce rain-wind vibrations with smooth cables, the dimpled cable remained steady; due to the lower critical Reynolds number, turbulent flow began prior to the velocity range necessary for rain-wind vibrations. As stated in Section 2.3.5.2, turbulent flow impairs rain-wind vibrations. Tests were also done without rain, and unstable vibrations that occurred for the smooth cable did not occur for the discretely roughened cable, indicating similar suppression of non-rain induced vibrations. This type of duct alteration was implemented on the cables of the Tatara Bridge in Japan.

Matsumoto (1999) suggested yet another aerodynamic alteration involving the installation of elliptical rings on the cable surface. At an appropriate pitch length, the rings control the flow field around the cable such that vibration mechanisms would be suppressed. Wind tunnel tests support this modification, though it has not been implemented on an actual bridge. One could foresee the potential for problems arising as a result of ice accumulation, in certain climates, because of the rings.

Shaping the duct provides an effective means of inhibiting vibrations, while minimally affecting the aesthetics of the bridge, though one must realize the potential exists for unexpected vibrations to arise when others are suppressed. In the case of the discrete roughness impressed on the cable surface, there is a significant benefit of lower drag force at high wind speeds. Though there is an additional initial cost associated, maintenance over the design life is minimal.

2.4.2 Damping Ropes (Tie Cables)

Tie cables are much smaller than stay cables, and simply tie the stays together—see Figure 2-2. They have been used as both a permanent and a temporary solution to suppress stay cable vibrations. The cable array of a cable-stayed bridge is composed of numerous cables of varying lengths, and possibly of varying angles of inclination. As a result, each cable has its own unique fundamental frequency. As such, under a given set of circumstances, some cables will vibrate while other cables will not be excited. In tying the stays to one another those cables not excited will act essentially as dampers for those trying to vibrate. The ties stiffen the structure and restrict movement in the lower modes of vibration and since higher modes require significantly more energy to occur, they are less likely to appear under expected wind speeds.

Tie cables are frequently used to suppress vibrations during construction or as a temporary measure when unexpected cable vibrations arise after a bridge is complete. Frequently ropes made of hemp (due to its high internal damping) are attached to each cable and anchored to the bridge deck.

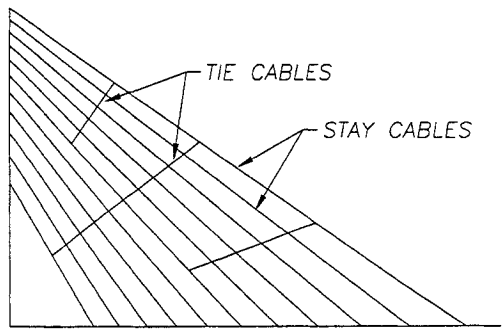

Figure 2-2: Tie cables

On the Normandy Bridge, tie cables were used as a permanent solution to alter the vibration frequencies of the stay cables as their fundamental frequencies were predicted to be in the same range as the structural frequency of the bridge as a whole (Virlogeux, 1998). Had no action been taken, the cables would have been quite susceptible to excitation caused by deck movement, and likewise the deck could have been susceptible to excitation caused by cable vibration.

Tie cables may tie together some or all of the stays, or even extend to the bridge deck. Tie cables suppress all types of vibration, though in some cases, such as rain-wind vibration, it may not be the optimal solution. Raising the natural frequency of a cable above 3 Hz is thought to be sufficient to

eliminate rain-wind effects, unless otherwise assured by damping (Virlogeux, 1998). As a result the number of ties required may be high, and so combining tie cables with other suppression methods may be warranted.

There are several drawbacks with the use of tie cables to suppress vibration. Most obviously they tend to detract from the clean, elegant statement of a cable-stayed bridge. As well, unless the ties are pre-tensioned adequately, their connections are liable to fatigue failure, or even rupture if they are fully unloaded and then suddenly pulled taut by stay cable motion. A serious drawback arises if cross ties are used as a remedial measure to mitigate vibration concerns after a bridge has been built. If ties are not considered during design, their addition and subsequent tensioning alters the geometry of the stay cables. The angles between the stay and the deck, and the stay and the pylon, are reduced, resulting in an increased stay tension that directly affects the moments in the deck and pylon. As well, the change in the angles may impose unwanted bending at the stay cable anchorage points. Finally, tie cables directly restrict movement vertically but only indirectly restrict horizontal motion, though this has not been found to be critically detrimental to their effectiveness.

2.4.3 Hydraulic Dampers

A common remedy to controlling unwanted vibrations is the installation of dampers. The most common and effective system involves two hydraulic dampers (essentially oversized shock absorbers as on an automobile) positioned at opposing angles, normal to the cable axis, attached to the cable a short distance from the lower anchor point, and extending down to the bridge deck. Hydraulic dampers of this sort are quite effective, however as cable length increases, they become less so. They incur greater capital cost on the bridge project, require monitoring and maintenance, and, since they cannot usually be hidden from view, may detract from the aesthetics of the bridge. Also, as this system damps the cable motion against the deck, parametric excitation cannot be effectively controlled.

2.4.4 Other Methods of Suppressing Cable Vibrations

Recently, alternative methods of suppressing unwanted vibrations have been proposed. The first described below has significant merit, while the second, though theoretically valid, is not likely to be an acceptable option. The third and fourth are among several variations on the principle behind hydraulic dampers.

2.4.4.1 Injection of Elastomeric Compound

Recently developed in France, and still in the testing stage, this process was originally intended as a simpler means of protecting cable strands from corrosion rather than using the traditional, and somewhat problematic, oil wax. The process involves injecting a visco-elastic resin to fill the cable duct and coat the strands to prevent corrosion. The resin coating was found, unexpectedly, to possess impressive damping characteristics. With the coating, the cable's ability to internally dissipate vibration energy is increased. In testing performed on a test cable, the resin improved the damping coefficient by a factor of two, and into the range considered adequate to suppress most cable vibrations (Fargier and Stubler, 2001). This process seems to be a very effective method for suppressing stay cable vibrations—aesthetics would not be affected, maintenance would seem to be unnecessary, and there appears to be great efficiency potential.

2.4.4.2 Damper Cables

Cables under a tensile load have extremely low internal damping, thus the inherent problems with stay cables. Slack cables (wire rope or lock-coil), however, possess a relatively high level of internal damping due to inter-strand friction when the cable is bent. Such is the premise behind Stockbridge dampers used to suppress vibrations in high voltage transmission cables.

Recently Sauter *et al* (2001) proposed using the same mechanism to suppress vortex-induced vibrations in stay cables. Curved damper cables mounted between adjacent stay cables would dissipate energy through inter-strand friction caused by bending deformations induced in the curved cable by the relative movements of the stays. These curved cables could be mounted near the upper end of the stay cables, near the pylon; see Figure 2-3. Sauter's study into such damper cables show potential exists with regards to the effectiveness of this system.

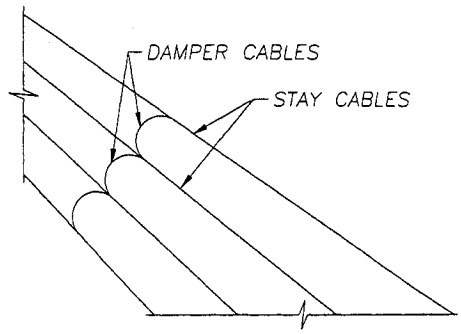

Figure 2-3: Damper cables

Though this is a novel, and potentially effective mechanism for controlling vibrations in stay cables, maintenance issues aside, an engineer would likely be hard-pressed to convince those controlling the architectural design of the bridge of the benefits of this system.

2.4.4.3 Magnetic Damper

This system involves the use of a magnet to alter the behaviour of the cable vibrations. A magnet apparatus is attached to the bridge deck near the lower cable anchor point, similar to the placement of hydraulic dampers. The magnet is close enough for the cable to make contact when vibrating above a pre-determined amplitude limit. This system assumes that aerodynamic damping corresponding to higher modes of vibration is positive for the wind velocity range that produces instability in the lower modes (Fujino *et al*, 2001). With large amplitude vibrations, the cable contacts and is held by the magnet until the cable tension exceeds the magnetic force. At this point the cable detaches from the magnet, and in so doing, higher modes of vibration are generated. Essentially energy is 'transferred' from lower modes to higher modes, and through positive aerodynamic damping at higher modes, the energy is dissipated, thus the oscillation amplitude is reduced.

This system is a passive mechanism, and has been installed on Japan's Ikara Bridge. It is thought a semi-active device would significantly improve the effectiveness of this premise. Using an electromagnet, the attraction and release points could be adjusted to maximize the energy transfer.

As with hydraulic dampers, this system involves greater capital cost, as well as monitoring and maintenance, and may detract from the bridge aesthetics.

2.4.4.4 Friction and Viscous-friction Dampers

Another type of damper installed at the lower end of cables involves a viscous-friction system. A rigid sleeve extends for a short distance up the cable from the deck. The end of this sleeve supports a ring of viscous material attached to the cable. Cable motion is suppressed through the absorption of energy by the visco-elastic material due to the relative movements of the cable and the sleeve.

A similar sleeve apparatus has been used in conjunction with materials to absorb the cable vibration energy through friction alone. The Uddevalla Bridge (formerly the Sunningesund Bridge) in Sweden employs this system to limit cable vibration amplitudes greater than L/3000 (the longest cable is about 210 m) (Kovacs *et al*, 1999). In this system, mounted to the sleeves on sprung ring plates are the *soft friction partners*, grey cast iron, which are pressed against the cable-mounted *hard friction partners*, stainless steel. Thus, cable vibration energy is dissipated through sliding friction between the two. Eight months after installation, no gross cable oscillations had been reported (Hjorth-Hansen *et al*, 2001).

The same deficiencies exist for these devices as for hydraulic dampers, save that their presence may be less noticeable.

Chapter 3: Literature Review

3.1 Characteristics of Flow About a Circular Cylinder

Characteristics of fluid flow about circular cylinders placed normal to the flow direction is an evergreen research topic in the fields of fluid mechanics and aerodynamics. Though not entirely two-dimensional, the flow behaviour can be adequately approximated as two-dimensional if the cylinder is normal to the flow. For such a fundamental concept—fluid flow past a cylinder—surprisingly little has been done to determine the behaviour of a flow past a circular cylinder inclined or yawed to the flow direction.

3.1.1 Flow About a Circular Cylinder Placed Normal to the Flow Direction

Significant study of the characteristics and effects of flow about a circular cylinder placed normal to the flow direction extends back throughout the 20th century and into the 19th century, and the phenomenon still attracts much attention. The flow regime can be broken into several sections spanning the flow velocity spectrum from fully laminar flow to fully turbulent flow. Each section can further be broken into sub-sections based on the changing characteristics of the flow. Neither the fully laminar state, nor the fully turbulent state is of particular interest for most applications; the transition between the two states is the most practically relevant part of the full regime. Among the extensive literature devoted to this topic, a thorough review and comprehensive compilation of previous research is presented in two volumes by Zdravkovich (1997a, 1997b). As well, ESDU 80025 (1980) provides comprehensive information concerning flow perpendicular to a circular cylinder, including empirical data with which to predict the circumferential pressure distribution based on user-specific parameters.

Flow around a circular cylinder is typically regarded as a two-dimensional phenomenon. Though there are span-wise variations, simplifying the issue to nominally two-dimensional flow about a circular section is sufficient for most applications. The behaviour of the flow and the resulting forces on the cylinder are principally governed by Reynolds number (given by Equation (2.1)). Summarized from Zdravkovich (1997a), flow about a circular cylinder can be broken into fifteen regimes within five states (illustrated in Figure 3-1):

The first state is laminar flow which can be divided into three regimes:

- L1: no-separation (R_e= 0 to 4 – 5), characterized by the flow being continuously attached to the surface all around the circumference of the section

- L2: closed wake (R_e=4 – 5 to 30 – 48), characterized by the formation of a steady, symmetric closed near-wake

- L3: periodic wake (R_e=30 – 48 to 180 – 200), characterized by the oscillation of the shear layers (wake boundaries) at the confluence point of the wake—eddy formation

The second state is defined by transition in the wake and is divided into two regimes:

- TrW1: far-wake (R_e=180 – 200 to 220 – 250), characterized by the transition of the laminar eddies in the wake to turbulence

- TrW2: near-wake (R_e=220 – 250 to 350 – 400), characterized by the transition to turbulence of the eddies during formation

The third state is the sub-critical state of transition-in-shear-layers and is divided into three regimes:

- TrSL1: development of transition waves (R_e=350 – 400 to 1×10^3 – 2×10^3), characterized by undulations of the free shear layers

- TrSL2: formation of transition eddies (R_e=1×10^3 – 2×10^3 to 2×10^4 – 4×10^4), characterized by the formation of the transition waves into discrete eddies which then roll into alternate eddies behind the cylinder

- TrSL3: burst to turbulence (R_e=2×10^4 – 4×10^4 to 1×10^5 – 2×10^5), characterized by a burst to turbulence in the free shear layers; the formation of eddies occurs close to the rear of the cylinder. Eddy (vortex) shedding is strongest in this regime.

The fourth, and usually most significant, state is the critical state of transition-in-boundary-layers. This is the state in which the *drag crisis* occurs. It is comprised of five regimes:

- TrBL0: pre-critical regime (R_e=1×10^5 – 2×10^5 to 3×10^5 – 3.4×10^5), characterized by the transition to turbulence in the free shear layers along separation lines on the surface of the section

- TrBL1: one-bubble regime (R_e=3×10^5 – 3.4×10^5 to 3.8×10^5 – 4×10^5), begins with a discontinuous fall in the drag coefficient and the formation of a laminar separation bubble on one side of the cylinder resulting in an asymmetrical pressure distribution—a net lift. The separation bubble is formed by the laminar separation of the flow from the surface of the

cylinder, subsequent reattachment to the surface a small distance later before turbulent separation.

- TrBL2: two-bubble regime (R_e=3.8×10^5 – 4×10^5 to 5×10^5 – 10×10^5), begins with another discontinuous fall in the drag coefficient and the formation of a second laminar separation bubble on the other side of the cylinder. The net lift force disappears.

- TrBL3: supercritical regime (R_e=5×10^5 – 10×10^5 to 3.5×10^6 – 6×10^6), characterized by the irregular disruption of the laminar separation bubbles span-wise and corresponding suppression of periodic eddy formation

- TrBL4: post-critical regime (R_e=3.5×10^6 – 6×10^6 to unknown), characterized by transition to turbulence of the boundary layer prior to separation

Finally, the fully turbulent state is divided into two regimes: T1, invariable, and T2, ultimate. The onset R_e value for the turbulent state is unknown and the flow characteristics can realistically only be hypothesized due to the complications arising from compressibility in air and cavitation in water at such high R_e values.

Discussion of the results of the present study presented later will reference the above regime classification.

The characteristics of the flow are also influenced by other parameters including surface roughness, flow turbulence, blockage, and oscillation of the cylinder. Surface roughness effects, for example, can greatly alter the onset of the Transition-in-boundary-layers (TrBL) state, as illustrated in Figure 3-2.

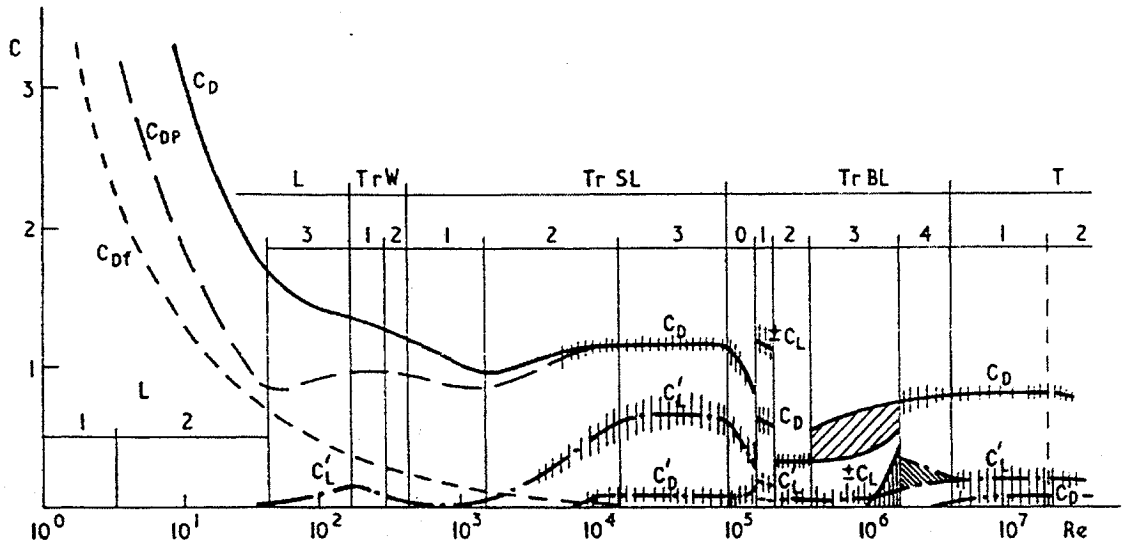

Figure 3-1: Variation of aerodynamic force coefficients for disturbance-free flow (reproduced from Zdravkovich (1997a))

In the above figure:

C_D – mean drag coefficient; $C_D = C_{Dp} + C_{Df}$

C_{Dp} – portion of mean drag coefficient due to asymmetric pressure distribution on the upstream and downstream side

C_{Df} – portion of mean drag coefficient due to viscous friction on the surface of the cylinder

C_D' – fluctuating fluid-dynamic drag coefficient

C_L – mean lift coefficient

C_L' – fluctuating fluid-dynamic lift coefficient

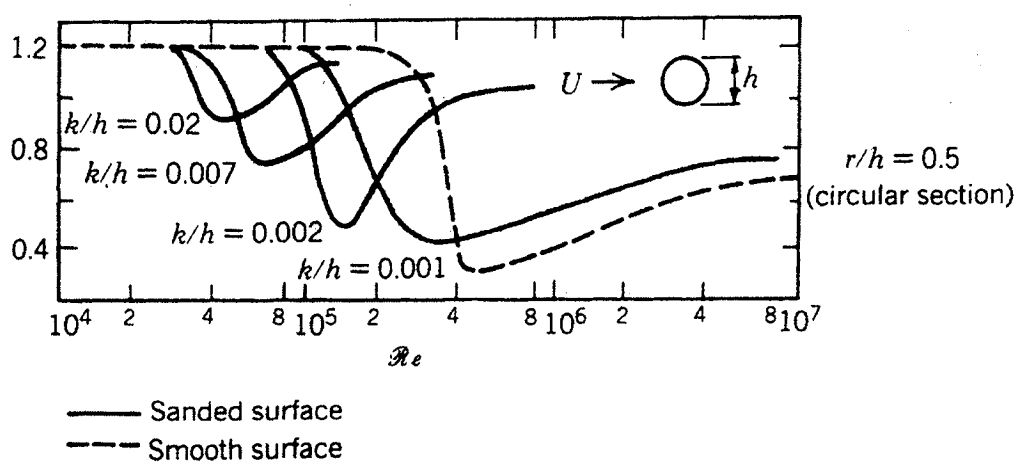

Figure 3-2: Influence of Reynolds number and surface roughness on drag coefficient (reproduced from Simiu and Scanlan (1996))

3.1.2 Flow About a Circular Cylinder Inclined to the Flow Direction

Most research related to examining flow characteristics about an inclined circular cylinder has always had a specific goal or application at its root. Studies have involved numerous applications—from inclined stay cables exposed to wind to marine risers exposed to wave action and so on—under very specific circumstances. Consequently little information is available concerning flow about an inclined or yawed circular cylinder from a fundamental viewpoint, and particularly when the flow is in the critical Reynolds number range.

An early study was completed by Bursnall and Loftin (1951). Their study involved the determination of the pressure distribution about a 2" (51mm) diameter, polished brass, circular cylinder at yaw angles of 0° (normal to flow), 15°, 30°, 45°, and 60°, under smooth flow conditions throughout the critical Reynolds number range, up to $R_e=5\times10^5$. Among their conclusions they reported that the decrease in drag in the critical Reynolds number range became more gradual with an increase in yaw angle. As well, at greater yaw angles the onset of the drag crisis was found to occur at lower wind speeds. Concerning the pressure distribution about the cylinder, they found the laminar separation bubble to be less well-defined with the cylinder yawed to 15° and 30° than it was with the cylinder normal to the flow. The separation bubble did not appear for yaw angles of 45° and 60°. They concluded generally that the flow and force characteristics could not be determined based solely on the component of flow normal to a yawed cylinder.

Another potentially relevant study is presented in Aero Tech. Memo. 291 by T. H. Trimble and P. T. Malone (July 1975) from the Aeronautical Research Laboratories, Australia, entitled *The normal, tangential, lift and drag forces measured near* $R=10^5$ *on some circular cylinders inclined to large angles in an airstream.* Unfortunately this report is unavailable for release outside the Australian Department of Defence.

Mahar *et al* (1985) performed testing on a rigid glass bar of finite length, varying the angle of attack while maintaining a constant flow speed corresponding to $R_e=7.1\times10^3$ (sub-critical; no variation in aerodynamic forces was found over the range of $1.4\times10^3 - 7.1\times10^3$). They found the mean drag force to vary in a somewhat sinusoid relationship with the relative wind-cylinder angle from a maximum of about 1.2 when placed normal to the flow down to virtually zero when aligned with the flow. They also found the mean lift to vary with the relative angle. Positioned normal to the flow, virtually no net lift was observed as one would expect. Aligned with the flow, similarly no net lift was observed. At angles between these two extremes, a net lift occurred. Being sub-critical flow, this is somewhat curious, however this net lift could have been due to the model being of finite length, and thus flow around the ends may have contributed to this result.

ESDU 80025 (1980) provides comprehensive information concerning flow perpendicular to a circular cylinder and includes a section on the effects of inclination on the flow regime. This section provides recommendations for the derivation of the drag force and the force normal to the cylinder, however it concludes with a caution that the recommendations are tentative and unverified by test data, and that more research is clearly warranted.

More recent studies of inclined cable aerodynamics—presented in the following section—have made some headway into discovering the characteristics of the flow about a circular cylinder, however thorough (or even brief) consideration of Reynolds number effects has been conspicuously absent. As mentioned in the previous section, the behaviour of the flow and the resulting forces on a circular cylinder are principally governed by Reynolds number. An exception to this tendency of neglecting Reynolds number effects is a paper by Larose and Zan (2001). In it, they point out that rain-wind vibrations occur in the critical Reynolds number range and argued that unsteady aerodynamic forces could arise due to Reynolds number effects causing wind-speed limited galloping. They also advise that adequate modelling of rain-wind vibration must consider Reynolds number effects.

3.2 Inclined Cable Aerodynamics

Studies of high-speed vortex excitation and galloping of stay cables originally developed out of tests conducted to examine rain-wind vibrations. As mentioned in Section 2.3.5.3, galloping behaviour has not been expressly observed in prototype cables, and arose unexpectedly in wind tunnel tests. Presently, therefore, it is largely a theoretical phenomenon however it holds potentially serious consequences were it to appear in prototype stay cables. So-called limited amplitude, high-speed vortex vibrations, however, have been witnessed on prototype bridges, as well as reliably reproduced in wind tunnel tests.

These two aerodynamic phenomena seem related in that axial flow along the leeward side of an inclined cable is thought to be the key motivator for both mechanisms. This axial flow develops as a result of the relative angle between the airflow and the cable axis. As air flows around the cable section, a portion of the flow follows the surface circumferentially and then flows axially along the leeward side of the cable in the along-wind direction. This axial flow complicates the flow regime about the cable which would not otherwise occur were the cable normal to the flow.

The effect of this axial flow on the cable behaviour, with respect to the two vibration mechanisms discussed here, can be summarized in quite simple terms. For the high-speed vortex vibration mechanism, the axial flow is thought to shed vortices that intermittently combine with Kármán

vortices (see Section 2.3.1) to produce enhanced vortices at a lower frequency than the normal Kármán frequency for a given wind speed (Matsumoto, 1998). For the dry, inclined galloping mechanism, this same axial flow is believed to act in a similar fashion as a splitter plate inserted in the wake of a cylinder. A splitter plate prevents the interaction of the flow behind a cylindrical section, causing unsteady pressure variations, and thus galloping (Matsumoto *et al*, 1990). As simply as these phenomena can be described, the actual mechanisms and required conditions are not yet well defined and the division between the two—that is, what aspect of the axial flow effect differentiates between galloping and vortex excitation—is unclear.

3.2.1 Dry, Inclined Cable Galloping

3.2.1.1 Galloping of Slender Structures

The mechanism causing galloping of a slender structure has been extensively developed beginning in the first half of the 20th century. Condensed from Simiu and Scanlan's *Wind Effects on Structures* (1996), the equation of motion for a given cross-section of mass per unit length, m, mechanical damping ratio, ζ, and radial frequency, ω, is:

$$m(\ddot{y} + 2\zeta\omega\dot{y} + \omega^2 y) = F \tag{3.1}$$

F is the aerodynamic force acting on the section, given by:

$$F = -\tfrac{1}{2}\rho U B(\frac{dC_L}{d\alpha} + C_D)_0 \dot{y} \tag{3.2}$$

where ρ is the air density, U, the airflow velocity, B, the nominal dimension of the section normal to the velocity vector, $dC_L/d\alpha$, the slope of the lift coefficient taken with respect to angle of attack, α, and C_D, the drag coefficient. The angle of attack is dependent upon the velocity of the section normal to the airflow.

Rearranging, where F can be referred to as the aerodynamic damping of the system, the total damping coefficient is:

$$2m\zeta\omega + \tfrac{1}{2}\rho UB(\frac{dC_L}{d\alpha} + C_D)_0 = c \tag{3.3}$$

The system will be stable when $c > 0$, and may be unstable when $c < 0$. Since the mechanical damping term can be expected to be positive—and, in the case of cables, very low—sufficient negative aerodynamic damping causes the system to self-excite. Thus instability can be predicted by satisfying the following relationship—the Glauert-Den Hartog criterion:

$$\frac{dC_L}{d\alpha} + C_D < 0 \tag{3.4}$$

Since the drag coefficient will always be positive, this relationship will be satisfied when a sufficient negative change in the lift coefficient, with respect to the angle of attack, is achieved. Quasi-steady theory has been found to be an acceptable means of analysing the Glauert-Den Hartog criterion; mean lift and drag coefficients of a static cross-section may be used to produce a satisfactory dynamic analysis (Simiu and Scanlan, 1996).

A further troubling issue with galloping is the effect of turbulence. With many types of vibration, turbulence has a calming effect. With galloping, turbulence may reduce or, more importantly, may enhance the propensity toward galloping.

Theoretically, galloping is a divergent vibration. Once the onset velocity is reached, negative aerodynamic damping results in self-excited oscillations, thus the vibration amplitude will continue to increase. There is no upper velocity limit above which galloping will cease. In reality this is not strictly the case. Galloping is non-linear in nature (Simiu and Scanlan, 1996) and as a result, a real structure in real wind will have a finite vibration amplitude, however the vibrations will be large, and will grow quickly with increasing wind velocity. Figure 3-3 illustrates the difference between the theoretical and real cases.

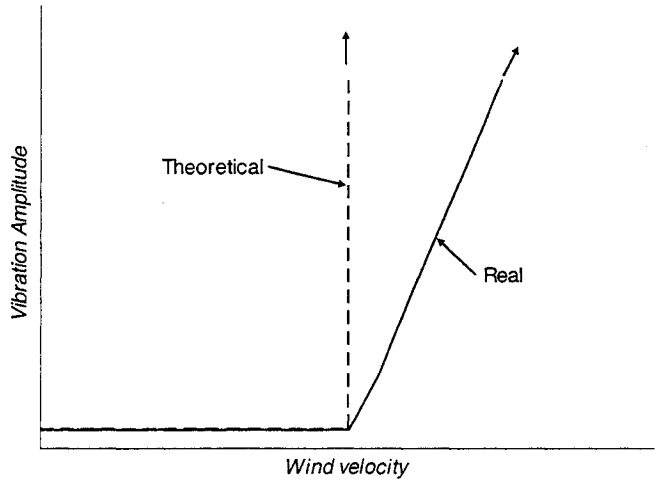

Figure 3-3: Galloping response, theoretical versus real

3.2.1.2 Galloping of Dry, Inclined Cables

In the 1980's, many researchers were pursuing studies on rain-wind induced vibrations of inclined stay cables (refer to Section 2.3.5.2). Of course in doing so, they usually compared the rain-wind case to that of wind alone. Hikami and Shiraishi (1988) performed wind tunnel tests to examine the mechanism seemingly producing vibrations in the cables of the Meikonishi Bridge in Japan. The prototype cables vibrated to a maximum double amplitude of 55 cm at a wind speed of only 14 m/s, only when it was raining, and only for cables on the more leeward side of the bridge pylon. In wind tunnel tests, the researchers found their model to be stable without rain, but when rain was simulated with a water spray, a definite limited-amplitude, velocity-restricted vibration occurred. Further study found these vibrations to be dependent upon the existence of the so-called "upper water rivulet" (Section 2.3.5.2 describes this phenomenon in more detail).

Conversely, Matsumoto *et al* (1990) proposed that these vibrations were more a function of a fundamental instability of inclined cables, wherein the addition of rain simply amplified the effect. This proposal was based on observations of prototype cable vibrations that occurred without rain but differed from normal vortex-induced vibration, and occurred for cables windward of the pylons as well. Wind tunnel experiments to investigate this premise yielded results further supporting this theory. Tests on cable models inclined and/or yawed to the airflow displayed instability without rain, while with rain the instability seemed to be amplified. Unlike the findings of Hikami and Shiraishi (1988), besides occurring without rain, this instability was not restricted by an upper bound of the velocity range nor did it exhibit a limit in amplitude—at least as far as the model support equipment

could display. Though not fully realized at that point, essentially each group of researchers was observing a different mechanism for cable vibration.

Through flow visualization tests, Matsumoto *et al* (1990) confirmed that a secondary axial flow forms in the leeward wake of an inclined cable, and proposed that it acted as a splitter plate placed in the wake of a cylinder. They noted previous research showing that a splitter plate prevents the interaction of the airflow in the cylinder's wake after diverting around the cylinder section and they reasoned this axial flow could have a similar effect. Subsequently, Matsumoto *et al* (1989a) performed a test in which a cylinder was placed normal to the airflow and an artificial axial flow was induced along the leeward surface. They indeed found that vibrations resulted from the addition of the axial flow.

Through further testing, Matsumoto *et al* (1992) clarified that the upper water rivulet and the axial flow could both, separately, cause instability in inclined cables. They determined the water rivulet to cause velocity-restricted, limited-amplitude vibrations at lower wind speeds, while the axial flow produced divergent oscillations at higher wind speeds.

In the research conducted to account for rain-wind vibrations for the design of the Higashi-Kobe cable-stayed bridge in Japan, Saito *et al* (1994) found they could produce divergent vibrations of an inclined cable at high wind speeds, without rain conditions. They reported that no upper velocity limit seemed to exist above which the vibrations would cease. The divergent nature of the vibrations seemed to be extremely sensitive to alterations in the supporting system; this observation has been noted by several other studies. More importantly, increased damping showed little effect on increasing the onset velocity of galloping; therefore simply increasing damping by installing dampers at the bridge deck anchorage point of a prototype stay cable would not necessarily be an effective method of vibration suppression. Matsumoto *et al* (1997) also found galloping to be less impacted by damping increases than other vibration phenomena.

Saito *et al* (1994) also observed rain-wind vibrations in their study, which occurred over a limited velocity range and were of lower amplitude. Turbulence seemed to stabilize both dry and rain-induced vibrations.

In the early 1990's, Honda *et al* (1995) performed wind tunnel tests to investigate potential vibrations for the Tatara Bridge in Japan. This bridge is presently the world's longest cable-stayed bridge, with a span of 890 m—the longest cables are about 460 m, with a fundamental frequency of approximately 0.26 Hz. Their tests on a prototype-size, dynamic cable model revealed divergent vibrations occurring at the onset reduced-velocity given by:

$$\left[\frac{V}{fD}\right]_{onset} = 10\,S_c^{\frac{2}{3}} \tag{3.5}$$

where V is the wind velocity, f, the natural frequency of the cable, D, the cable diameter, and S_c, the Scruton number given in Equation (2.3). This equation applies directly for a relative angle between the wind and cable axis of 45°; for a relative angle of 60°, they found that the onset reduced velocity reached a limit of 100 for a frequency of 1.07 Hz and Scruton number above 100. This upper limit corresponded to the critical Reynolds number for the model. Reduced velocity, V_r, is a non-dimensional value given by:

$$V_r = \frac{V}{fD} \tag{3.6}$$

where V is the wind speed, f, the frequency of vibration, and D, the diameter of the cable.

The suggested criterion, proposed by Irwin (1997) based the results of Saito *et al* (1994), defining the wind speed at which dry, inclined galloping begins is given by:

$$U_{CRIT} = 35fD\sqrt{S_c} \tag{3.7}$$

By this equation, damping values have to be relatively high to prevent galloping—significantly higher (e.g. nearly three times higher for the Cochrane Bridge, Mobile, Alabama, U.S.A. (Irwin *et al*, 1999)) than the value required for the suppression of rain-wind vibration. Though resulting in a higher onset velocity than Equation (3.5), Equation (3.7) still predicts values well within the design range of many existing bridges. To illustrate, consider a bridge cable 150 mm in diameter, with a fundamental frequency of vibration of 1 Hz, and assume a Scruton number of 10 (Irwin's suggestion for preventing rain-wind vibrations (Irwin, 1997). Based on Equation (3.5), the onset wind speed for galloping would be approximately 7 m/s (25 km/h); based on Equation (3.7), the onset wind speed would be only 16.6 m/s (60 km/h).

During the latter half of the 1990's, research tended to focus on rain-wind vibrations and high-speed vortex vibration of dry, inclined cables rather than galloping. Presumably this trend was due to the elusiveness of galloping while the other two types of vibrations were actually observed for prototype cables. Galloping was usually noted as a somehow-related mechanism.

A previous phase (Phase 1) of the current research project was conducted in the spring of 2001 in the Institute of Aerospace Research (IAR) Propulsion Wind Tunnel at the National Research Council's

(NRC) Montreal Road Campus, Ottawa, by Cheng and Tanaka, of the University of Ottawa, along with NRC personnel. The findings of this study were detailed in the report, *Inclined Cable Aerodynamics* (Cheng and Tanaka, 2001), prepared for RWDI Inc. of Guelph, Ontario. The purpose of Phase 1 was to explore the divergent galloping phenomenon and evaluate the criteria that arose from the studies conducted by Saito *et al* (1994) given by Equation (3.7). The study examined the behaviour of a 160 mm diameter cable section model mounted on spring supports at each end. Phase 1 was successful in producing both high-speed limited-amplitude vibrations (high-speed vortex excitation) and what was believed to be divergent vibrations (galloping).

The model set-up for which galloping was believed to have occurred had the cable inclined into the wind at an angle of 60°, with the spring rigs rotated by 54.7°. This orientation translates into a prototype inclination of 45° with a yaw of 45°. The wind speed at which the significant vibrations occurred was 32 m/s ($V_r \approx 140$, $Re = 3.4 \times 10^5$). The motion was primarily along the vertical spring direction (rotated 54.7° from the along wind direction), with a small orthogonal motion component.

That the observed vibration was indeed galloping is something of a hypothesis. The vibration amplitude increased steadily over the course of three minutes to a maximum of about 80 mm at which point the model had to be stopped due to restrictions on the spring supports vibration clearance. No firm conclusion about galloping can be established by this observation as perhaps this case was merely building up to a limited-amplitude vibration larger than that permitted by the model. Compared to the limited-amplitude vibration responses though, the rate of vibration amplitude growth was much greater in this configuration. The vibrations increased steadily to the point at which the model was manually suppressed over only two and a half minutes; the largest limited-amplitude vibrations reached their maximum amplitude after about five minutes.

The results of Phase 1 indicate the criterion proposed by Irwin (1997) based on the results of Saito *et al* (1994) to be conservative. However one should note that some of the wind tunnel test conditions reported by Saito *et al* (1994) and Honda *et al* (1995) in which divergent motion was observed differ from those of Phase 1. Saito *et al* (1994) used a steel pipe, 160 mm in diameter (same as for Phase 1) and conditions for divergent vibrations included an onset wind speed of about 8 m/s ($V_r = 80$, $Re \approx 8.5 \times 10^4$) with a relative angle between the wind and cable of 45°. Honda *et al* (1995) used a model 155 mm in diameter and found divergent vibrations beginning at approximately 4 m/s ($V_r = 100$, $Re \approx 4.1 \times 10^4$) for a relative angle of 45° and damping corresponding to $S_c = 21$, and also at a speed of approximately 8 m/s ($V_r = 200$, $R_c \approx 8.3 \times 10^4$) for a relative angle of 60° and similar damping. Again the conditions for galloping observed in Phase 1 were a wind speed of about 32 m/s ($V_r \approx 140$,

R_e=3.4×10^5) and a relative wind-cable angle of 60°. This onset wind speed is much higher than the results from the other researchers. The surface roughness of each of the other studies' models is not known, but all tests used a steel pipe covered with a polyethylene sleeve for prototype stay cables. The turbulence intensity for the other studies was not explicitly detailed, though Saito *et al* (1994) examined turbulence effects on rain-wind vibration through the addition of different lattice arrangements. They produced Iu=0.5, 2, 5, and 10%, so the cases without lattice are assumed to have very low turbulence levels. Thus it is likely that the critical Reynolds number range of each test is reasonably similar. Assuming this, the onset of vibrations in the other studies occurred within the sub-critical Reynolds number regime.

3.2.2 High Speed Vortex Excitation of Dry, Inclined Cables

During the 1980's, much focus was given to vibrations due to rain-wind vibrations of stay cables. As this mechanism was a serious threat to the longevity of stay cables and the safety of cable-stayed bridges, increased attention to any sort of vibration developed. As a result, vibrations were reported occurring under conditions different than those required for rain-wind vibration—particularly when rain was not falling. In the late 1980's, Matsumoto *et al* (1989a) reported, without specifics, observations of cable vibrations occurring without rain, but with characteristics similar to rain-wind vibrations.

In the mid-1990's, Matsumoto *et al* (1994) reported field observations of cables vibrating not only due to rain-wind vibration, but also in conditions without rain, at low frequencies, and at wind speeds of approximately 40 m/s, during a typhoon. The maximum amplitude of these vibrations was about 230 mm—much smaller than for rain-wind vibrations, but significant, especially under such high-energy wind conditions. Unfortunately, the researchers were unable to conclude as to whether or not the vibrations were limited by an upper velocity boundary, as the wind speed did not rise above 40 m/s, but they proposed a heretofore unknown, high-speed vibration mechanism had been observed in naturally turbulent wind. They theorized the vibrations were excited by a type of vortex shedding with a longer period than Kármán vortex shedding, given the wind speed at which the vibrations occurred.

Matsumoto *et al* (1995a) further explained that these high-speed vibrations occurred for the cables of the Higashi-Kobe Bridge. The cables had been fitted with ducts designed with axial protuberances to prevent rain-wind vibrations (as mentioned in Section 2.4.1). An analysis of the cable vibrations revealed peaks in the power spectral density of the cable's acceleration corresponding to reduced velocities of approximately 40, 80, 120, 200, and 400.

Additional bridges exhibited similar cable vibrations later in the 1990's. Matsumoto *et al* (1997) reported observed cable vibrations occurring on the Meiko West Bridge I and the then-under-construction, Meiko West Bridge II. Bridge I had originally been built with inter-stay tie cables. These tie cables had suffered damage at their connections due to severe vibrations, and so observations were made to determine a better means of suppression. Many of the vibrations occurred during rainstorms and so were thought to be rain-wind vibrations. Some however occurred without rain and at higher reduced velocities than one would expect Kármán vortex vibrations for a given frequency; in one case the wind speed was approximately 40 m/s. The reduced velocities at which vibrations occurred, like previous observations, tended to be multiples of 20. As well, the cables occasionally displayed a beating motion, indicating a combination of vibration modes.

Matsumoto *et al* (1997) conducted further wind tunnel tests of both rigid and dynamic models to explore cable vibrations. Though expecting to observe galloping as in previous studies, they in fact saw a limited amplitude response with characteristics resembling the prototype vibrations, including vibrations occurring at reduced velocities of multiples of 20. Again, the researchers proposed that a form of vortex-induced vibration was occurring, one that possessed a longer period than Kármán vortex excitation.

Matsumoto *et al* (1995a) had previously attempted to explain this high-speed vibration phenomenon as the complication of normal, two dimensional "sheet-like" vortex shedding by the addition of a third dimension in the form of the axial flow in the cable's wake, resulting in occasionally enhanced vortices. Matsumoto (1998) was able to clarify the suspected mechanism through flow-visualization during wind tunnel tests. Through the use of liquid paraffin in the airflow Matsumoto observed vortices shed from the axial flow, which then combined with, and enhanced, Kármán vortices. The axial vortices shed at a lower frequency than the Kármán vortices. At a reduced velocity of 20 he found an axial vortex was shed once for every three Kármán vortices, thus every third Kármán vortex was enhanced, and thus a form of vortex shedding with a lower frequency was essentially produced. Matsumoto *et al* (1999) further noted that, for a reduced velocity of 40, an axial vortex combines with every fifth or sixth Kármán vortex, and so forth for reduced velocities of higher multiples of 20.

The axial flow seems to be the key factor in both high-speed vortex shedding and galloping behaviour. As galloping has only truly been observed in wind tunnel tests, this may suggest that the magnitude of the axial flow (a function of both velocity and volume) is the key aspect dictating which of the two phenomena will arise. Perhaps in real conditions the axial flow does not reach a great enough rate to result in the onset of galloping, and thus only high-speed vortex shedding appears. Matsumoto *et al* (2001a) observed galloping behaviour in wind tunnel tests, but in subsequent tests,

only high-speed vortex shedding occurred. In the latter tests, the artificially applied axial flow was weaker than in the former tests, supporting the theory of dependency on axial flow rate.

Matsumoto *et al* (2001c) performed a study on a large-scale cable model, 110 mm in diameter and 30 m long, f_0=1.37 Hz, in natural wind. They reported on two vibration events—one occurring with rain, the other without. For the case without rain, the power spectral density (PSD) of the acceleration showed peaks corresponding to Kármán vortex excitation of the 7th and 8th modes; the wind speed was 12.28 m/s. However, PSD analysis of the tensile force in the cable model showed peaks at 1.07 Hz (the first out-of-plane mode) and 1.37 Hz (the first in-plane mode). They found the first in-plane mode corresponded to a reduced velocity of 80, and was a good possible indication of high-speed vortex excitation.

The previous phase (Phase 1) to the present study, briefly outlined in Section 3.2.1.2, found cases of limited amplitude, velocity-restricted vibrations (Cheng and Tanaka, 2001). These vibrations occurred for the model/spring configurations given in Table 3-1.

Table 3-1: Limited Amplitude Motion (Cheng and Tanaka, 2001)

	Prototype Angles		Model Angles		Motion Observed		
Set-up No.	Inclination Angle, θ	Yaw Angle, β	Inclination Angle, Φ	Spring Rig Rotation, α	U (m/s)	Reduced Velocity	Amplitude (mm)
2A	60	0	60	0	18-19	79-84	67
1B	45	0	45	0	24-26	106-114	31
1C	30	35.3	45	54.7	34-38	150-167	25
3A	35	0	35	0	22	96	20

All of the vibration cases listed above occurred at wind speeds corresponding to the critical Reynolds number range. Two responses were witnessed: one was a regular, harmonic motion, while the other included a regular beating motion, similar to that described by Matsumoto (1998). The amplitude seemed to depend on the orientation, with smaller amplitudes corresponding to smaller angles of inclination. The vibration motion for set-up 1C, which simulated a yawed, inclined cable, followed an elliptical trajectory with the major axis of the ellipse lying along the "vertical" axis (actually rotated 54.7° about the cable axis). Matsumoto *et al* (1989a) reported similar elliptical orbits of prototype cable vibrations.

3.3 Remarks Regarding Existing Published Information

For all the wealth of information concerning flow about a circular cylinder, very little addresses the possibility of the cylinder being positioned in any way other than normal to the flow. There are

however many practical applications of such a configuration, not the least of which being a stay cable. Many vibration mechanisms potentially damaging to stay cables have been identified, but several are not yet fully understood and thus they are a cause for concern to bridge designers. Were there the volume of information detailing the flow about an inclined or yawed cylinder that exists for a cylinder normal to flow, perhaps such mechanisms would be better understood.

Results of several research studies, specific to stay cables under certain conditions, have included limited information about galloping or high-speed vortex excitation of dry, inclined cables, but in many cases these phenomena were not the focus of the studies but rather an unexpected result. Usually the phenomena arose during testing for rain-wind vibration. Consequently, published information specific to galloping and high-speed vortex excitation is not altogether complete and definitive design criteria for cable-stayed bridges do not exist. As noted above, Honda *et al* (1995) proposed a relationship for aerodynamic instability, which, compared to that proposed by Irwin (1997) based on the work of Saito *et al* (1994), seems conservative. Likewise, Irwin's criterion seems conservative based on the results of the study by Cheng and Tanaka (2001). There is insufficient evidence in each case to rule the previous findings invalid and so further study is necessary.

The division between high-speed vortex excitation and dry, inclined cable galloping is quite ambiguous, and this too needs clarity. Again as noted above, many times while the researchers assumed they would observe one mechanism in a wind tunnel test, the other appeared. To develop effective means to prevent such vibrations, a better understanding of the mechanisms causing these phenomena is needed first.

Coupled to this, the effect of Reynolds number has been conspicuously absent from previous studies. The relationship between inertial and viscous forces is an important one with respect to circular cylinders in airflow. In the case of stay cables, natural wind generally spans the critical Reynolds number range for typical stay cable diameters. One must therefore assume that Reynolds number effects play a significant role in the aerodynamic behaviour of stay cables.

Chapter 4: Experimental Approach

4.1 Overview

This research project investigating the aerodynamic behaviour of inclined circular cylinders and the related application to dry, inclined stay cables was conducted in conjunction with the Institute for Aerospace Research (IAR) of the National Research Council of Canada (NRC). A previous phase (Phase 1) to the present study occurred in the spring of 2001. Phase 1 involved wind tunnel testing of a dynamic model for which the dynamic displacements of each end were recorded and analysed to determine conditions necessary for high-speed vortex excitation and for galloping.

Wind tunnel testing for Phase 2—the present study—encompasses the measurement of the dynamic surface pressure about a rigid, stationary cable model over various wind speeds and with the model mounted at various angles to the airflow. Analysis of the dynamic pressure data obtained from this study is anticipated to reveal significant information concerning the characteristics of airflow around an inclined circular cylinder, and conditions necessary to produce high-speed vortex excitation and dry, inclined cable galloping. Regarding the galloping mechanism in particular, as noted in Section 3.2.1.1 galloping of a bluff body is regarded as a quasi-steady mechanism. Thus, through the measurement of surface pressures on a stationary model, a specific aim of this study is to determine the applicability of quasi-steady theory in the prediction of galloping of a dry, inclined cable.

Phase 2 testing took place from March 21 to April 15, 2002.

4.2 Wind Tunnel Facilities

Testing took place in the Institute for Aerospace Research 2m×3m wind tunnel located at the National Research Council's Montreal Road Campus in Ottawa. The facility is a continuous, horizontal, single closed-circuit wind tunnel. The tunnel has a working section 1.9 m high, 2.7 m wide, and 5.2 m long; the cross-sectional area of the test section is 5.07 m^2.

The maximum tunnel wind speed is 140 m/s with a speed uniformity of ±0.7% and a turbulence level of 0.13%. All testing took place under smooth flow conditions. The blockage ratio varied depending upon the orientation of the model and ranged from a minimum of approximately 3.3% to a maximum of approximately 4.1%. No correction was made for blockage effects.

4.3 Cable Model

The cable model consists of an 89 mm diameter, 7.9 mm wall, steel pipe, approximately 3 m long. This diameter was chosen partly to achieve a length-to-diameter ratio of at least 20 to minimize the effects of boundary conditions on the span-wise pressure distribution along the model. The surface of the pipe was finished to achieve a certain roughness (surface roughness-to-diameter ratio of approximately 6.5×10^{-6}) to maintain a reasonable similarity in Reynolds number effects between Phase 1 and Phase 2. The pipe was fitted with 192, 1 mm pressure taps arranged in five circumferential rings of 32 taps each, and two longitudinal lines on the leeward side (when model is at 0° yaw) of 16 taps each, excluding taps common to the rings. Refer to Figure 4-1 for an elevation sketch of the model, and to Figure 4-2 for sections. A record of the tap numbering is presented in Appendix F. A photo of the model installed in the wind tunnel is presented in Figure 4-3.

The pressure taps were connected to electronic scanning units. To minimize the length of tubing required to connect the taps to the units, the scanning units were required to be placed inside the model, thus the size of the units also partly controlled the model diameter. The model was composed of four sections of pipe with threads machined at each end to permit assembly and access to the scanning units. Refer to Figure 4-4.

The model mounted in the wind tunnel was found to be quite rigid, relatively speaking, in that lateral deflections of any note could not be caused by pushing hard against the model. To determine and exclude any frequency effects due to the model and supporting system, its natural frequencies were logged using an accelerometer. This was completed for the vertical and 60° degree incline orientations. A tare record was taken as well as the forced response achieved through hitting the pipe a single strike with a rubber mallet. These frequency response records are included in Appendix L.

The pressure taps of the five rings were spaced with a greater concentration on the leeward (0° yaw) side (see Figure 4-2) with an initial intention to better depict the region of flow separation and unsteady pressures. Due to constraints in the mounting of the model in the wind tunnel, this intention could not be fully realized; as the model was yawed, the mounting supports could not be fashioned to simultaneously rotate the cable about its own longitudinal axis. Maintaining the initially windward taps always on the windward-most side of the model was not possible. Similarly, the two lines of pressure taps intended to be on the leeward side of the model rotated to the side and then windward face as the model was yawed. Consequently, in the interest in examining axial flow effects, data from these taps is only relevant for yaw angles close to zero.

The cable model was mounted vertically in the test section, securely attached to the wind tunnel's upper and lower turntables. The model was initially mounted normal to the flow as a benchmark case, and subsequently inclined into the airflow to achieve a relative wind-cable angle of 60° with no yaw, and then inclined to 54.7°. For the inclined cable configurations, end plates (see Figure 4-5) were mounted on the cable model to reasonably prevent the boundary layer flow, and particularly the horseshoe-swirl system, from affecting the flow regime about the pressure taps. The diameter of the end plates was approximately 250 mm. The end plates were mounted approximately 100 mm from the floor and roof; the boundary layer for the wind tunnel is approximately 83 mm.

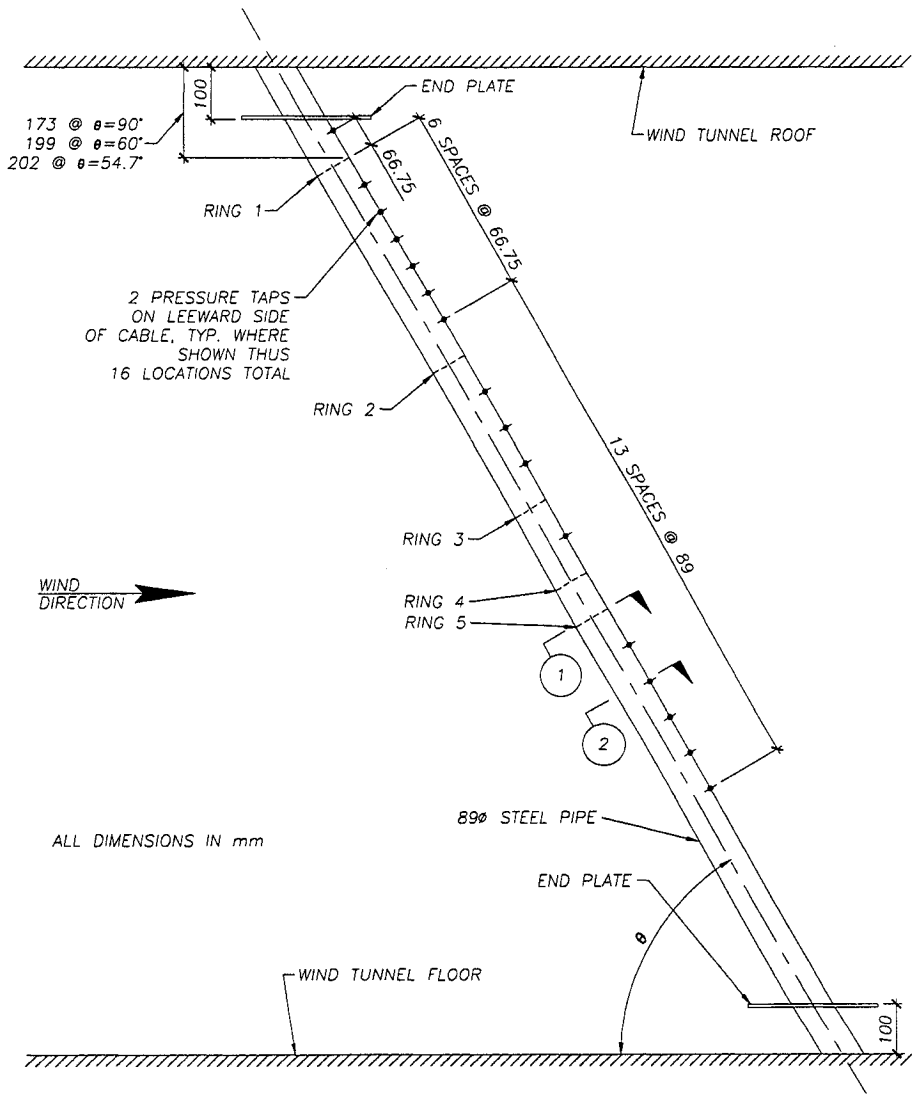

Figure 4-1: Cable model elevation

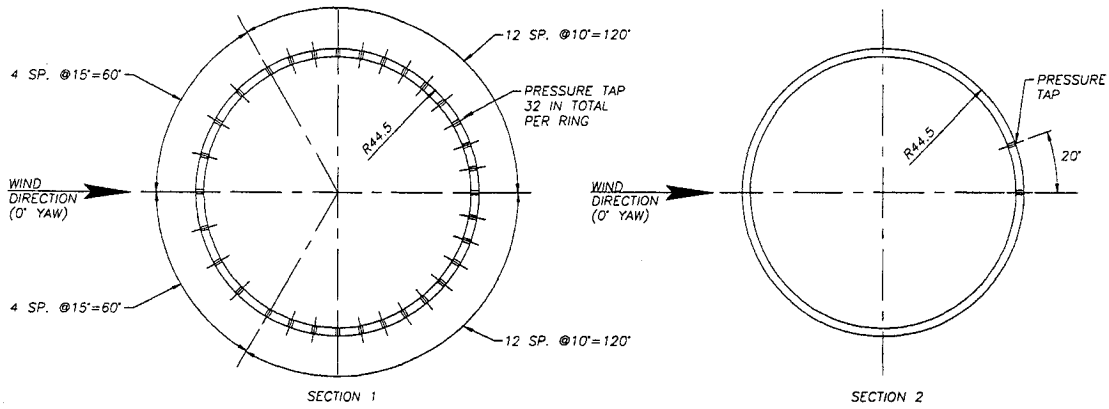

Figure 4-2: Cable model sections showing pressure tap locations

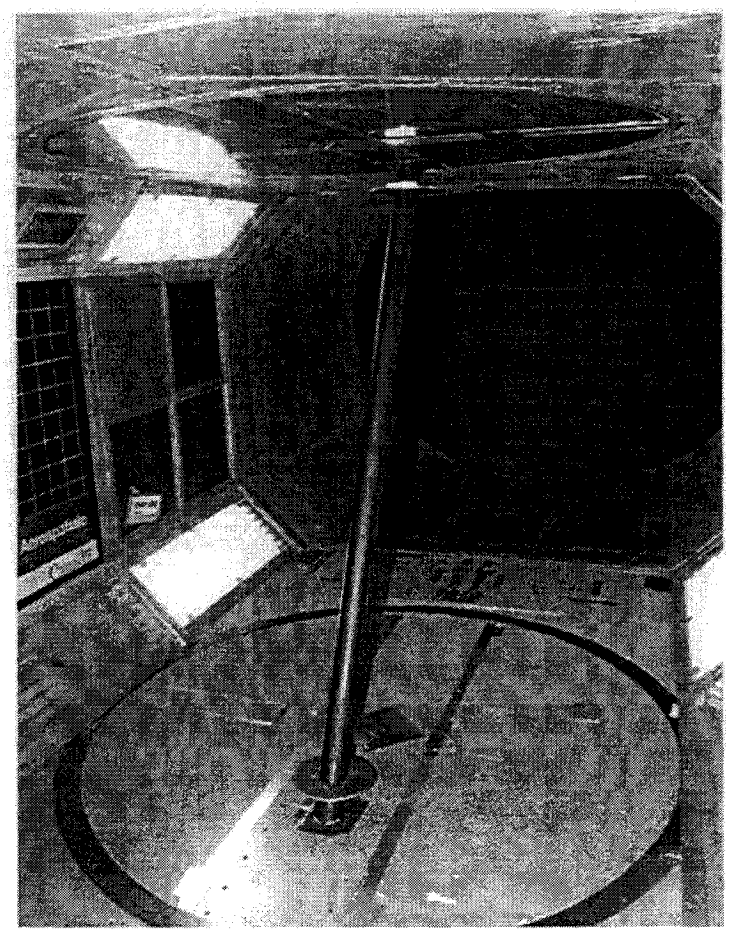

Figure 4-3: Cable model in NRC 2x3 wind tunnel

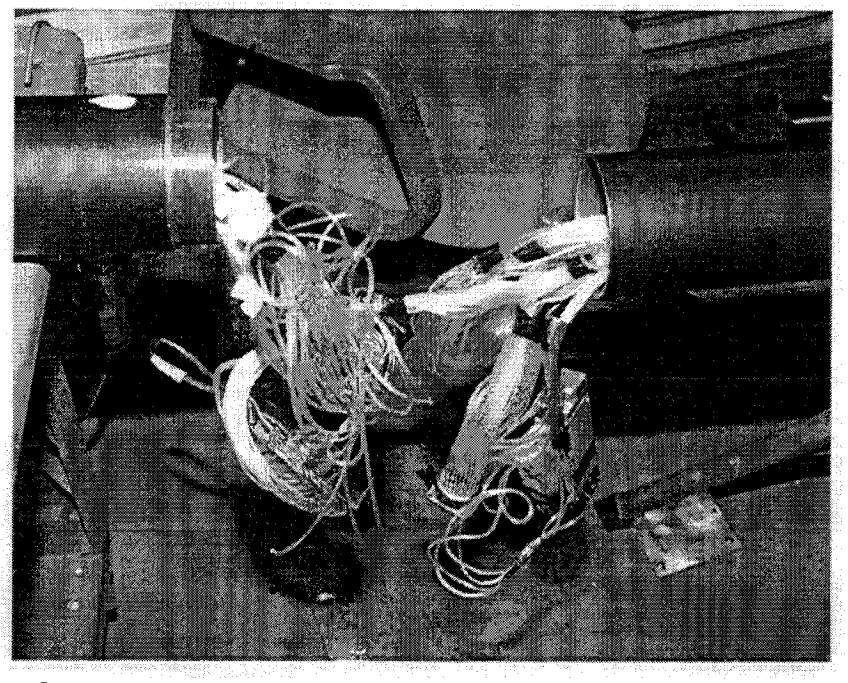

Figure 4-4: Cable model threaded connection showing pressure tap tubes and scanning units

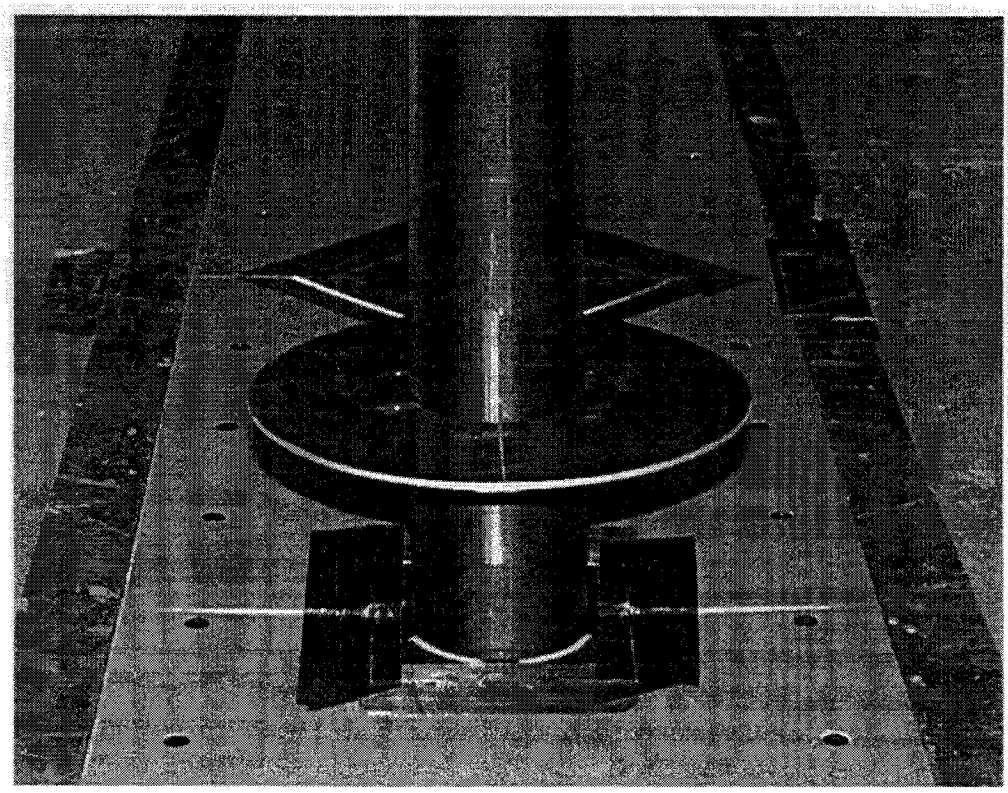

Figure 4-5: End plate (bottom)

4.4 Data Collection and Analysis

The pressure scanning units were connected to the wind tunnel facility's data acquisition system which recorded the relevant data, including tap pressures, wind speed, Reynolds number (based on stream velocity and model diameter), inclination angle, θ , yaw angle, β , scan sampling rate, sampling time, static offset pressure of the wind tunnel, and static pressure of the airflow, q. The data was corrected to account for the size and length of tubes used to connect the pressure taps to the scanning units. All analysis presented herein was completed using the corrected data.

Pressure values were recorded at two scan rates: 400 Hz and 1200 Hz. The lower scan rate of 400 Hz was the maximum possible sampling rate for all 192 taps. Frequencies of potential aerodynamic response mechanisms were not known beforehand, thus the maximum sampling rate was used. The higher scan rate of 1200 Hz was possible by reducing the number of taps sampled at one time to 64, corresponding to the taps of rings 2 and 4. At this scan rate, potential higher frequency mechanisms missed by the lower scan rate could be recorded. The scan times were generally one minute for the 1200 Hz scan rate and two minutes for the 400 Hz scan rate.

The pressure taps were connected to electronic pressure scanning units (ZOC 33 and ZOC 22 modules, Scanivalve Corp.). The taps were connected to these units using 1.5 mm diameter urethane tubing. Dynamic pressure readings were desired from the pressure taps, therefore to minimize the degree of correction the data would require, the tubing length was kept to a practical minimum of 1 m.

The pressure occurring at the tap location is measured at the scanning unit. The tube in between contains a column of air which possesses dynamic characteristics of its own. The recorded instantaneous pressure reading contains the actual pressure value at the tap which has been distorted by the dynamic characteristics of this air together with a phase shift representing the time between when a certain pressure occurs at the tap and when that same pressure value is recorded at the unit. This distortion must be eliminated from the recorded instantaneous pressure readings leaving only a record of the dynamic pressure occurring at the tap. To accomplish this, the frequency response of each tube was measured prior to the actual tests. After testing, the raw test data of each tap was corrected for magnitude and phase shift distortion. Examples of the frequency response curves used for correction of the data are included in Larose *et al* (2003).

Due to some difficulties in assembling the model, some pressure taps were damaged or were otherwise impaired. The affected taps are tap 64 on ring 2 and tap 142 on ring 5, taps 169, 170 and 173 on line 1, and taps 184, 185 and 186 on line 2. For analysis purposes, pressure values for taps 64

and 142 were estimated as the average of the pressure values from the adjacent taps on the respective rings.

The corrected data files resulting from the wind tunnel tests were analysed using programs written for MATLAB v6.5 r13—a matrix computation software. Copies of these programs are included in Appendix M.

In addition to the pressure data, flow visualization using oil film was performed in an attempt to physically see indications of vibration mechanisms—particularly high-speed vortex excitation.

4.5 Test Cases

The model was initially mounted vertically in the wind tunnel in order to obtain a benchmark case. Airflow around cylinders placed normal to the flow has been widely studied and, therefore, comparing this case to established experimental results provides a good check to ensure the pressure data collected for the inclined cases can be considered reliable.

In Phase 1 the largest limited amplitude vibrations, as well as the vibrations believed to be galloping, occurred with the model inclined into the wind at an angle of 60° (the differences in the two vibration cases were the rotation of the spring support system and the flow speed). For the static model, the vertical inclination and horizontal yaw angles are not individually important as much as is the relative angle between the cable and airflow produced by the two. This wind-cable relative angle is given by:

$$\phi = \arccos(\cos\theta\cos\beta) \tag{4.1}$$

where θ is the vertical angle of inclination of the cable taken with respect to the horizontal, and β is the horizontal yaw angle taken with respect to the airflow direction. Derivation of this relationship is presented in Appendix A. The focus of Phase 2 was therefore a wind-cable relative angle of 60°. This relative angle was achieved in two ways. Initially the model was inclined into the wind to an angle of 60°. Subsequently it was inclined to an angle of 54.7°, which, when combined with a yaw angle of 30°, produces an effective relative angle of 60°.

At each of these two inclination angles the model was rotated through a range of yaw angles from 0° to 120° for each wind speed. The wind speeds were varied from 15 m/s to 99 m/s. In addition, some test runs were completed with various intensities of axial flow induced with compressed air along the

leeward side of the model to determine what effect such varying intensities have on the pressure distribution about the model.

The first phase of the present study (detailed in Cheng and Tanaka, 2001) resulted in the production of limited amplitude vibrations for four different model configurations as summarized in Table 3-1. The largest vibration response occurred under the following conditions:

- $\theta=\phi=60°$, $\beta=0°$
- $\alpha=0°$
- U=18-19 m/s; $R_e \approx 1.86 - 1.96 \times 10^5$

This configuration was reproduced using the static model of the present study. Theoretically, instability should be expected to occur under the following conditions:

- $\phi=60°$, therefore $\theta=60°$, $\beta\approx0°$ (Setup 1) or $\theta=54.7°$, $\beta\approx30°$ (Setup 2)
- $R_e = R_e$, therefore $(UD)_{\text{dynamic test}}=(UD)_{\text{static test}}$ produces U=32.3-34.2 m/s

Some variability in the expected onset velocity may result due to small variations in surface roughness effects between the two models and differences in turbulence levels between the two wind tunnels.

The first phase of the present study also produced what was believed to be divergent galloping vibrations under the following conditions:

- $\theta=\phi=60°$, $\beta=0°$
- $\alpha=54.7°$
- U=32 m/s; $R_e \approx 3.41 \times 10^5$

For the static model of the present study, theoretical instability should therefore be expected to occur under the following conditions:

- $\phi=60°$, therefore $\theta=60°$, $\beta\approx0°$ (Setup 1) or $\theta=54.7°$, $\beta\approx30°$ (Setup 2)
- $R_e = R_e$, therefore $(UD)_{\text{dynamic}}=(UD)_{\text{static}}$ produces U=57.5 m/s

The majority of the test cases were completed at both sampling frequencies.

A full summary of the testing regime is presented in Appendix B.

Chapter 5: Analysis of Results and Discussion

5.1 Analysis of Pressure Data

Local pressure readings about and along the model were recorded over one (1200 Hz) and two minute (400 Hz) timeframes. The pressure value (either instantaneous or mean) at each tap can be expressed as a non-dimensional pressure coefficient given by:

$$C_p = \frac{p - p_o}{\frac{1}{2}\rho U^2} \tag{5.1}$$

where the numerator is the difference between the tap pressure, p, and the free stream pressure, p_o, and the denominator term is the free stream dynamic pressure.

The mean lift and drag forces acting on the model at each ring are the integration of the mean pressure value of each pressure tap around the circumference of the cylinder. The mean drag force has been evaluated in this analysis as being perpendicular to the cable axis, in the along-wind direction. The mean lift force has been evaluated as being perpendicular to the cable axis, normal to the airflow. With reference to Figure 5-1, the mean aerodynamic forces per unit of span are given by:

$$F_N = \oint p_{iN}\, r d\alpha = \oint p_i r \cos\alpha \, d\alpha \tag{5.2}$$

$$F_L = \oint p_{iL}\, r d\alpha = \oint p_i r \sin\alpha \, d\alpha \tag{5.3}$$

F_N and F_L are the mean drag force (normal to the cylinder) and mean lift force, respectively, p_i is the mean pressure value at tap i, r is the model radius, and α is the angle location of the tap taken with respect to the along-wind direction.

The three-dimensional angle relationships and the orientation of the lift and drag forces are illustrated in Figure 5-2. Complete development of the angle relationships is presented in Appendix A.

As with pressure values at each tap, the mean lift and drag effects can be expressed as non-dimensional coefficients. The drag coefficient based on the force normal to the cylinder is obtained from:

$$C_N = \frac{F_N}{\frac{1}{2}\rho U^2 B} \tag{5.4}$$

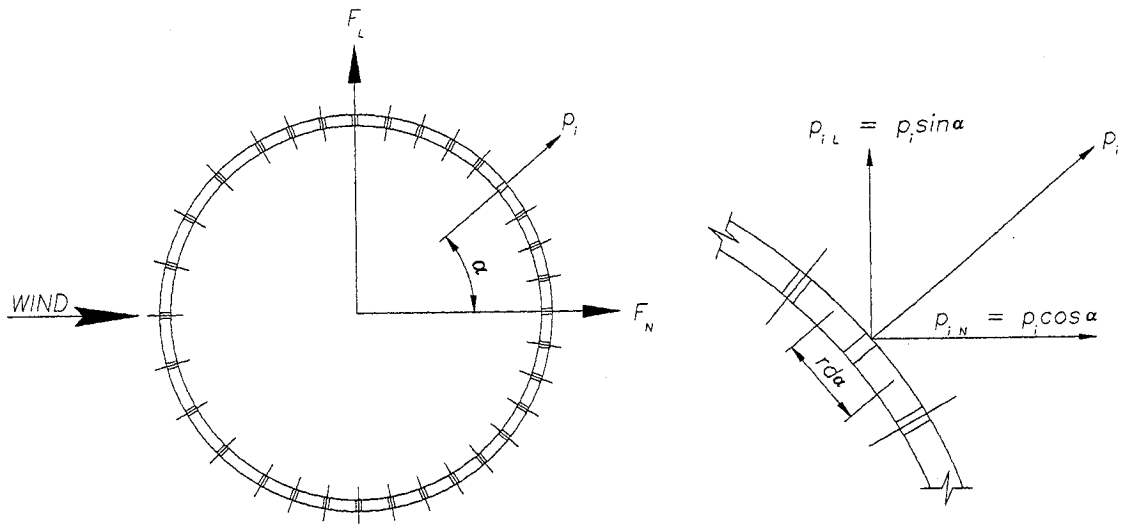

Figure 5-1: Lift and drag forces based on ring pressure taps

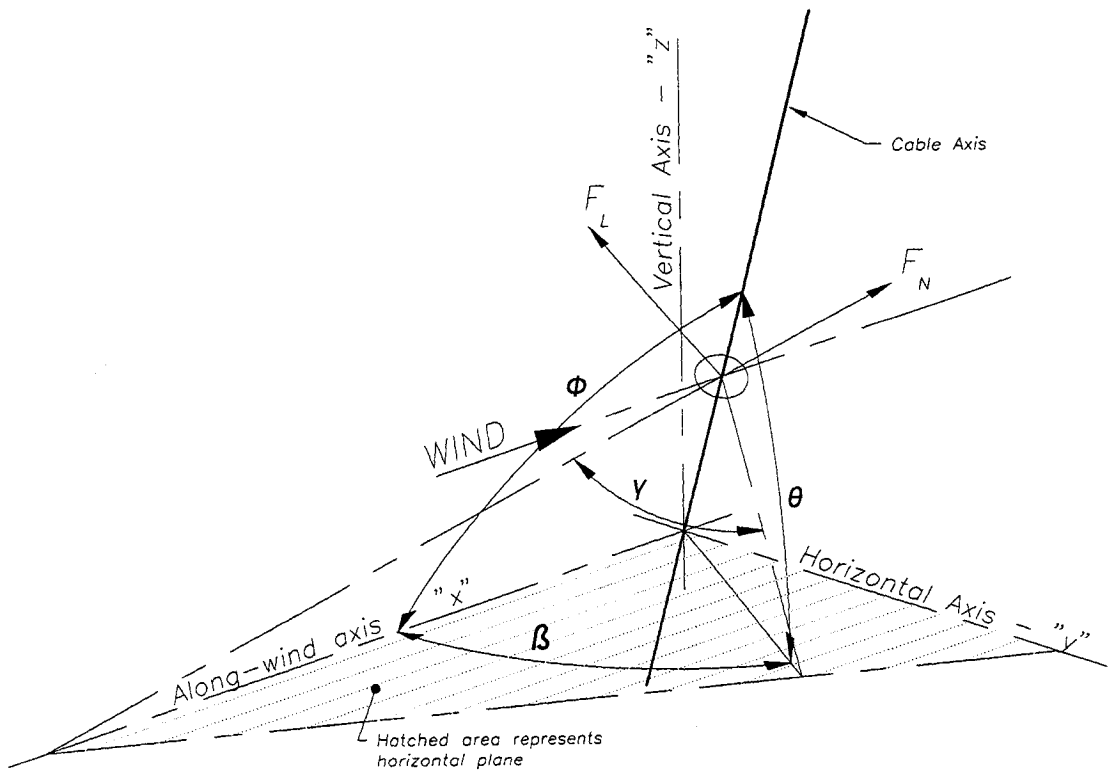

Figure 5-2: Cable model reference angles

The lift coefficient for the section is obtained from:

$$C_L = \frac{F_L}{\frac{1}{2}\rho U^2 B} \tag{5.5}$$

where F_N and F_L are the aerodynamic forces per unit length given above, ρ is the air density, U, the free stream wind speed, and B, the diameter of the cable model.

5.2 Wind Tunnel Blockage

Wind tunnel tests are used to simulate natural phenomena under controlled conditions, however in attempting to do so one must accept some concessions. Any measured results are affected by constraints imposed by the boundaries or limitations of the wind tunnel on the airflow, and so any measured results may require correction to obtain the corresponding open air, prototype results. Placing a body in a wind tunnel essentially reduces the cross-sectional area of the tunnel, thus causing the flow to accelerate to compensate for the constriction. Corrections may be required to produce corresponding prototypical values. Corrections for blockage depend upon the blockage ratio, the shape of the body, and the flow characteristics, as well as upon the value of interest, be it drag, lift, pressure, and so forth.

As previously mentioned in Section 4.2, the blockage ratio varied depending upon the orientation of the model. For this study no correction was made to the data to account for blockage effects. Blockage ranged from a minimum of approximately 3.3% (model vertical) to a maximum of approximately 4.1% (model inclined 54.7° and yawed 90°).

For a circular cylinder normal to the flow in the Reynolds number range of 10^4 to 10^5, blockage ratios of less than 6% have been found to result in only slight variations in the pressure distribution and drag coefficient, and the Strouhal number is unaffected (West and Apelt, 1981). Zdravkovich (1997b) suggests that for circular cylinders, when the diameter is less than 0.1 of the breadth of the test section, blockage effects may be ignored in the TrSL, TrBL and T states.

No particular information is available for yawed or inclined cylinders, however for this case of an inclined cylinder, the evaluation of the Glauert-Den Hartog criterion is affected only to the extent that the drag and lift coefficients are affected. For instance, the corrected drag coefficient, expecting it to be lower than the measured value, would push the sum of drag plus slope of lift coefficient lower, therefore correction needs only really be considered if the resulting sum does not break the critical threshold of zero. Further, the magnitude of percent difference between the measured and corrected

drag coefficients would be only slightly higher than the blockage ratio itself; based on suggested correction methods the corrected drag coefficient would be, at worst, about 5% lower than the measured value (West and Apelt, 1981; Melbourne, 1982). In general, the results of this study are being used for qualitative evaluation rather than direct quantitative comparisons with previous results, and so variation of even 5% has little bearing on the resulting conclusions.

5.3 Validation of Model Pressure Readings

5.3.1 Pressure Data Stationarity

The stationarity of the collected data is reasonably assumed as the physical parameters of each test record are time invariant and the wind tunnel equipment maintained by the NRC is regarded as reliable.

A few suspect data were apparent and so a brief analysis was performed on the test data to confirm that the pressure readings are stationary over the duration of the recording times. Resulting mean lift and drag coefficients were used as indicators of aberrant data. Due to the volume of data, the full results of this analysis have not been included however anomalous cases are outlined in Appendix J. These irregularities have been taken into consideration in all further analysis.

5.3.2 Flow Past a Circular Cylinder Placed Normal to the Flow Direction

Initially the cable model was installed in the wind tunnel normal to the flow direction to provide a simple but effective means of verifying the pressure readings, and to provide a reference for the subsequent inclined orientations. A circular cylinder positioned normal to airflow is a long-studied and well-established case, and therefore acquiring data for this orientation allowed comparison with standard accepted results, thus validating the pressure readings. Empirical predictions of the pressure distribution and drag coefficient have been derived from ESDU Item Number 80025 (1980). Comparisons of the experimental and predicted mean pressure distributions are presented in Figure 5-3 for two wind speeds that approximately bound the critical Reynolds number range. At both speeds the resulting pressure distribution is approximately symmetrical—a characteristic also indicated by the lift coefficient of approximately zero—and closely resemble the predicted distribution.

The resulting mean drag and lift coefficients based on the pressure readings of the five rings are presented in Figure 5-4; the plot of the drag coefficient also includes a prediction based on the ESDU data (A similar empirical prediction for the lift coefficient through the critical Reynolds number range does not exist). As expected, the mean drag coefficient in the sub-critical Reynolds number range is

approximately 1.2. The lowest value of the mean drag coefficient is approximately 0.3, as expected. The drag crisis for this model occurs over the range of wind speeds approximately bounded by $30 \leq U_{Crit} \leq 65$ m/s ($1.8\times10^5 \leq R_e \leq 3.8\times10^5$).

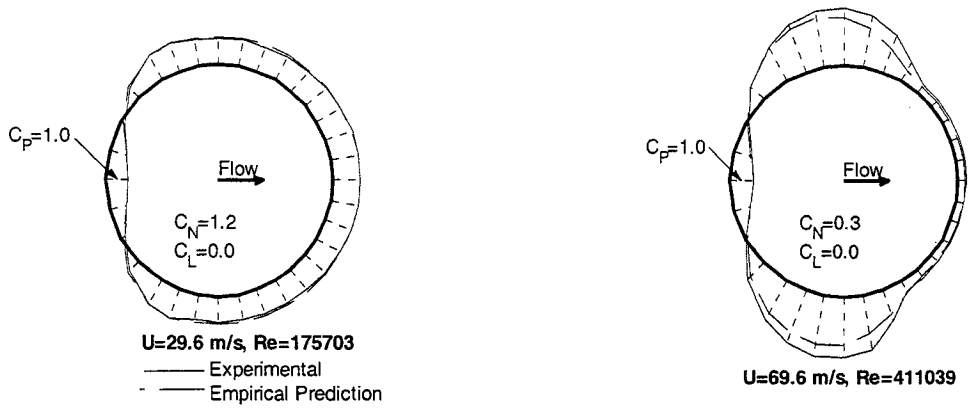

Figure 5-3: Mean pressure distribution about a circular cylinder placed normal to airflow; experimental result (Ring 4) and empirical prediction at a) beginning of critical Reynolds number range, and b) end of critical Reynolds number range.

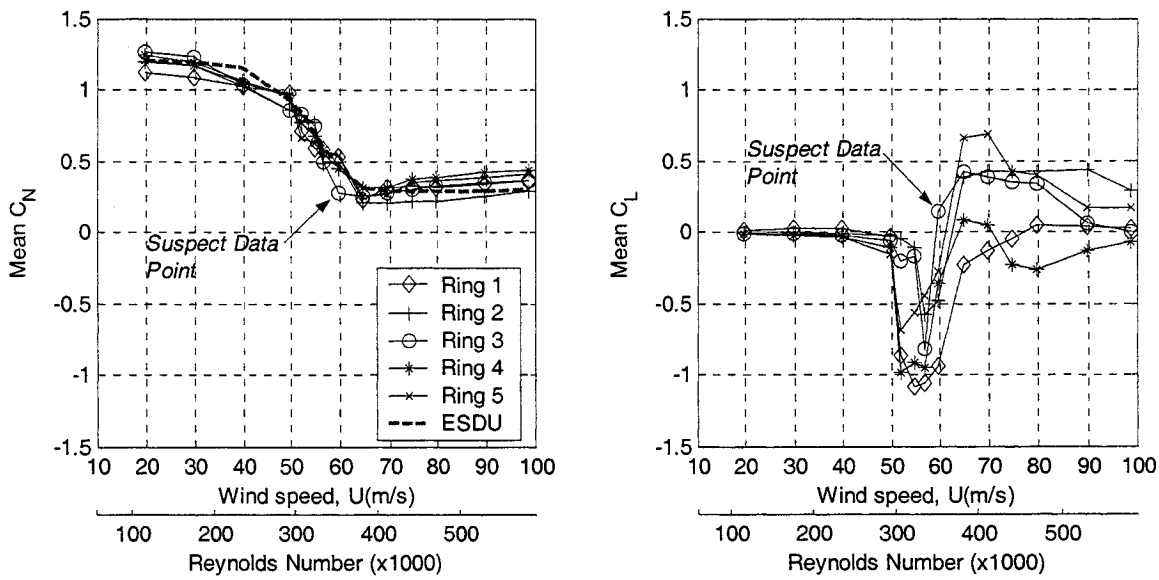

Figure 5-4: Variation of mean drag and lift coefficients with wind speed for a circular cylinder positioned normal to airflow

The test results agree well with the classification of the flow by Zdravkovich (1997a). Flow past a circular cylinder in the pre-critical range (R_e=1×10^5 – 2×10^5 to 3×10^5 – 3.4×10^5) should yield no net lift due to the cylinder's symmetry about the direction of flow. Once the lower bound of the critical range is reached (R_e=3×10^5 – 3.4×10^5), a stable mean pressure distribution asymmetric about the direction of flow occurs—a laminar separation bubble forms initially on one side of the cylinder—and so a net lift force will occur. Further increase in the wind speed (to approximately R_e=3.8×10^5 – 4×10^5) will cause the formation of a separation bubble on the other side of the section and the pressure distribution will begin to even out, becoming more symmetric; the net lift force will lessen. This point should correspond to the minimum mean drag force on the section. The mean lift coefficient presented in Figure 5-4 follows this expected behaviour. The progression from the pre-critical symmetrical pressure distribution to the formation of the asymmetric single-bubble distribution to the symmetric two-bubble distribution over the critical Reynolds number range is quite evident in pressure distributions of Ring 4 presented in Figure 5-5.

The results of the pressure data compiled from the test cases of the model positioned normal to the flow are in good agreement with published data.

Figure 5-5: Mean pressure distribution about a circular cylinder placed normal to airflow; experimental results (Ring 4) over a range of wind speeds covering the critical range.

5.3.3 Inclined Cylinder – Effect of End Plates

The model was inclined into the airflow to angles of 60° and 54.7°. To minimise end effects on the airflow about the model, endplates were installed positioned approximately 100 mm from the wind tunnel floor and ceiling; the wind tunnel boundary layer was known to be 83 mm. The endplates were 250 mm diameter and parallel to the floor and ceiling (refer to Figure 4-1).

The presence or absence of endplates does not appear to have a noticeable direct effect on the drag and lift forces at rings 2 and 4, and one can reasonably assume too at rings 3 and 5. Test runs with and without endplates were not completed at the low scan rate, thus the effect of the endplates on the pressure distributions around ring 1 and along the leeward lines of pressure taps is not known. One can assume the end plates would significantly affect the pressure distribution around this location owing to its close proximity to the tunnel ceiling.

Comparing the mean drag and lift coefficients presented in Figure 5-6 (without endplates) and Figure 5-7 (with endplates), the mean drag differs from one case to the other by 0% to ±5%. The mean lift in each case is largely similar, remaining approximately zero except during the critical range. Here the mean lift trend is similar with the only significant difference being a noticeably larger lift occurring on Ring 2 at 55 m/s with endplates installed.

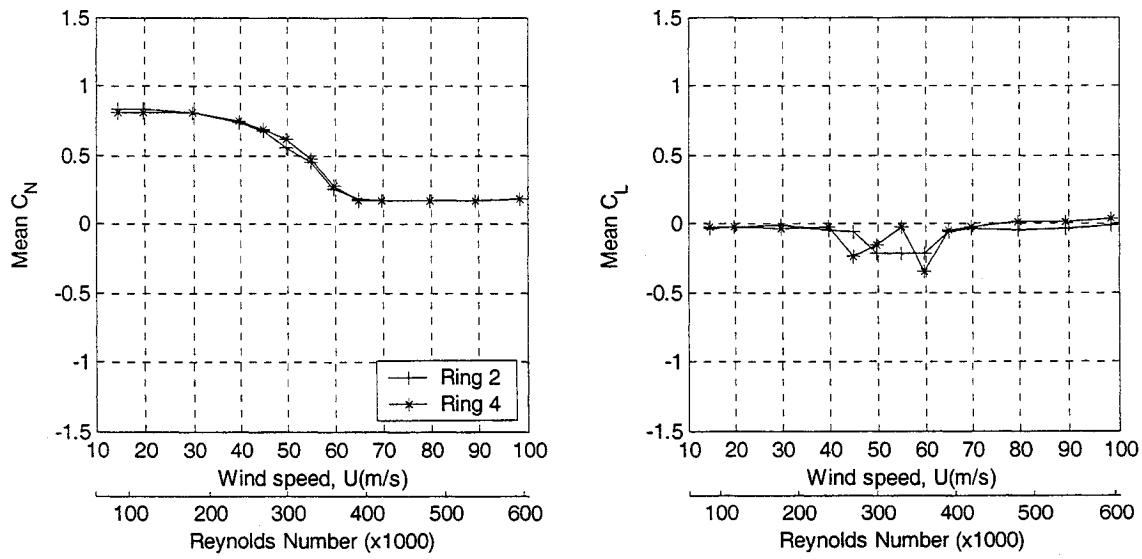

Figure 5-6: Variation of mean drag and lift coefficients with wind speed for a circular cylinder, without endplates, inclined into the airflow, θ = 60°

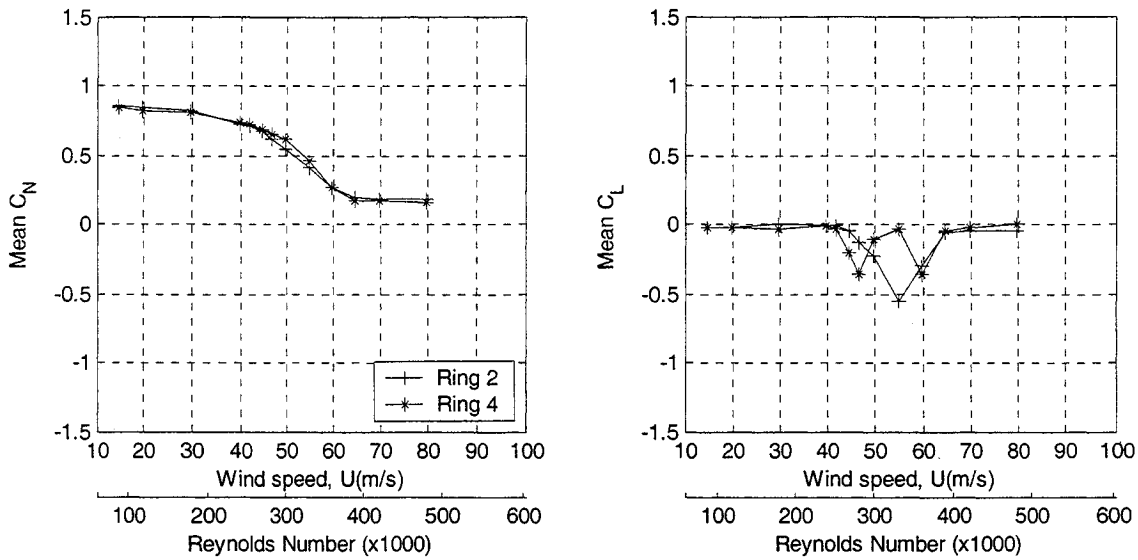

Figure 5-7: Variation of mean drag and lift coefficients with wind speed for a circular cylinder, with endplates, inclined into the airflow, θ = 60°

5.3.4 Inclined Cylinder – Ring 1 Results

The pressure readings of the top ring (ring 1) of pressure taps have quite obviously been impacted by the proximity of the roof of the wind tunnel. Figure 5-8 and Figure 5-9 present mean lift and drag coefficients versus wind speed for the two inclined configurations without yaw rotation. Without adverse boundary effects, the line representing ring 1 would be expected to generally follow the trend shown by rings 2 to 5. As it appears, ring 1 is obviously affected by boundary effects of either the tunnel ceiling, or the end plate, or both. This was an anticipated result. Consequently, ring 1 data is unreliable in reasonably representing a typical section of a prototype stay cable and will therefore be largely ignored in the analysis to follow.

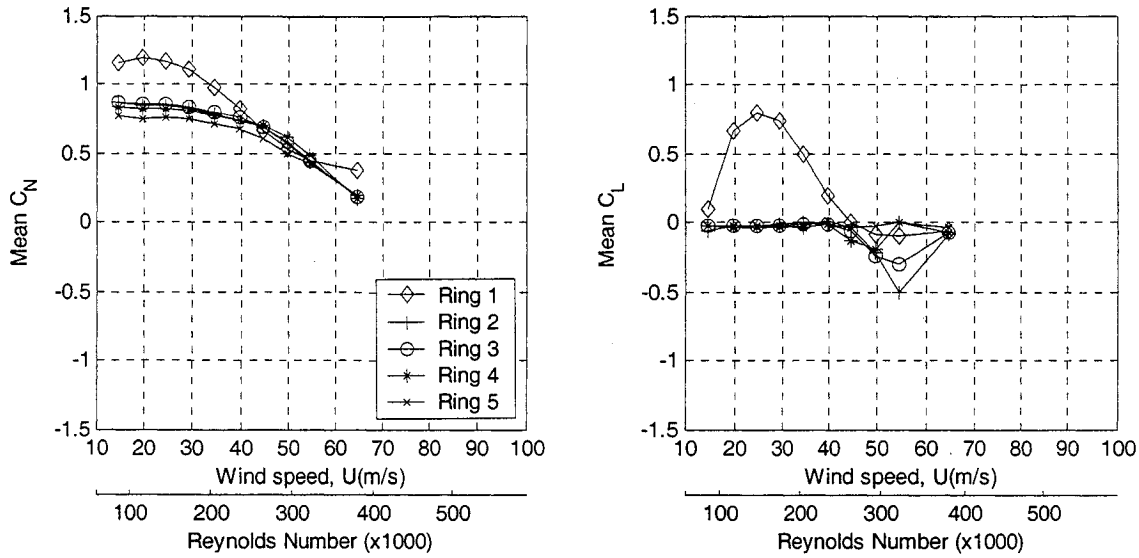

Figure 5-8: Variation of mean drag and lift coefficients with wind speed for a circular cylinder inclined into the airflow; $\theta = 60°$, $\beta = 0°$

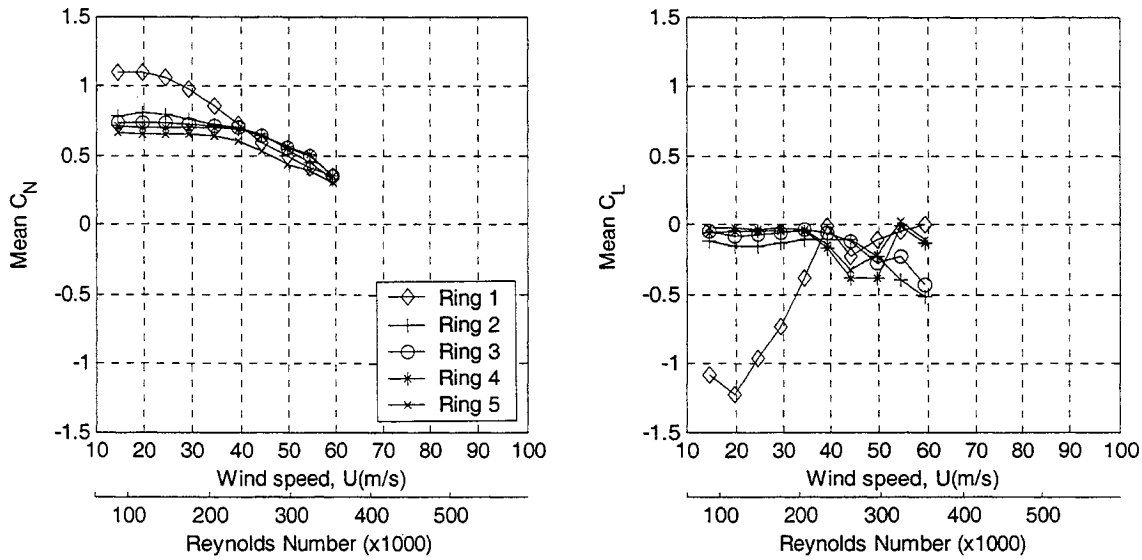

Figure 5-9: Variation of mean drag and lift coefficients with wind speed for a circular cylinder inclined into the airflow; $\theta = 54.7°$, $\beta = 0°$

5.4 Flow About an Inclined Circular Cylinder

A tremendous body of work exists concerning the characteristics of flow across a circular cylinder positioned normal to the flow. Frequently this configuration has been reasonably reduced to a two-dimensional concept, and for most applications it has been adequately detailed.

A circular cylinder positioned at a non-right angle results in notable changes in the aerodynamic behaviour of the flow. An acute relative angle changes the effective section the airflow encounters from a circle to an ellipse, but this in itself is of secondary importance as the elliptical section is symmetric about the direction of flow regardless of the relative angle. More importantly, this relative angle also means two-dimensional flow is no longer a realistic simplification; the flow must be considered in three-dimensions as the cylinder's span has not only an across-wind component, but an along-wind component as well.

5.4.1 Effects of Varying Relative Angle, ϕ, on Lift and Drag

Restricting the focus for the time-being to the effects of a varying relative angle on the drag and lift forces exerted on the cylinder, several notable variations occur with a changing relative angle. The drag coefficient (again, based on the drag force perpendicular to the cable axis in the along-wind direction) is generally lower for a non-right angle between the wind direction and cable axis. Figure 5-10 through Figure 5-13 depict the relationship between the mean drag and lift coefficients and the wind-cable relative angle over a range of Reynolds numbers. Derived from the data of these figures, Figure 5-14 through Figure 5-17 depict the relationship between the mean drag and lift coefficients and the wind speed over a range of wind-cable relative angles.

For wind speeds immediately below the critical range, the mean drag coefficient ranges from approximately 0.75 for ϕ=55° up to about 1.2 for ϕ=90°. This result is reasonably intuitive considering the coefficient is based on the drag force normal to the cylinder's axis, however this difference changes as the wind speed is increased through the critical Reynolds number range. As the drag begins to fall, the rate of decline is greater for relative angles closer to 90° than for those angles closer to 55° and 60°. The drag coefficient values converge at wind speeds in the vicinity of $R_e=3.2\times10^5$ as shown in Figure 5-14 through Figure 5-17. In fact the trend of larger drag coefficients for larger relative angles appears to reverse—that is, the drag appears to decrease for increasing relative angles—at approximately this same Reynolds number, as shown by Figure 5-10 through Figure 5-13. At a higher Reynolds number of about $R_e=3.8\times10^5$, the original trend has reappeared.

Testing at higher wind speeds did not include the full yaw sweep but rather only a select yaw range for the analysis presented in Section 5.5 to follow, thus the characteristics of the drag coefficient variation based on the relative angle cannot be determined for these higher speeds. Future testing in this field of study should include full angle variation throughout the entire critical Reynolds number range.

Trends in the variation in the lift coefficient over the range of relative angles are not overly apparent from Figure 5-10 through Figure 5-13. However, comparing the variation of lift with increasing wind speed in Figure 5-14 through Figure 5-17, as well as Figure 5-4 (ϕ=90°) and Figure 5-7 (ϕ=60°), reveals a notable difference. The onset wind speed at which a net lift appears, corresponding to the formation of a laminar separation bubble, is lower for lower relative wind-cylinder angles. Figure 5-4 clearly indicates that the stable asymmetric pressure distribution appears at approximately $R_e=3.0\times10^5$ for a cylinder normal to the flow, while this so-called one-bubble regime begins at approximately $R_e=2.6\times10^5$ for a cable inclined to ϕ=60° as shown in Figure 5-7. The compiled data of Figure 5-14 through Figure 5-17 confirm these approximate values. Thus the transition from the TrBL0 regime to the TrBL1 regime occurs at lower Reynolds number values for lower angles of inclination

Though not fully confirmed by Figure 5-14 through Figure 5-17 due to the limited wind speeds, Figure 5-4 and Figure 5-7 indicate that upper bound for this net lift regime—that is, the speed at which a second laminar bubble forms—appears not to be affected by the cylinder inclination. Related to this transition between TrBL1 and TrBL2, Figure 5-4 indicates the lift does not return promptly to zero for the cylinder normal to the flow; Zdravkovich (1997a) reports a similar scenario described by some researchers. In the case of an inclined cylinder (Figure 5-7), the return of the lift to zero appears to be quick and stable.

The magnitude of the lift is quite obviously greater when the cable is at right angles to the flow. In fact, the maximum mean lift coefficient for the section positioned normal to the flow is fully double that for the section inclined to 60° and 54.7°. Bursnall and Loftin (1951) found the separation bubble to be less well defined for an inclination of 60° relative to the flow direction. This could in part explain the difference in magnitude of the lift coefficients.

These general characteristics stated above are only applicable for inclination angles higher than 54.7°.

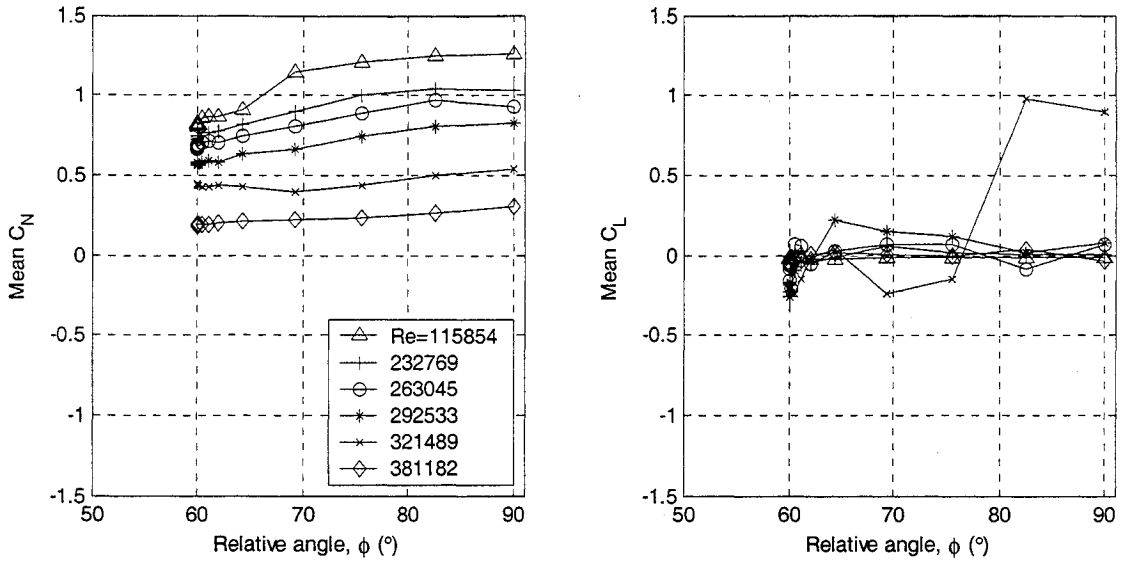

Figure 5-10: Variation of mean drag and lift coefficients with relative angle between wind and cylinder (60° model inclination angle, low scan rate, average of rings 2 – 5)

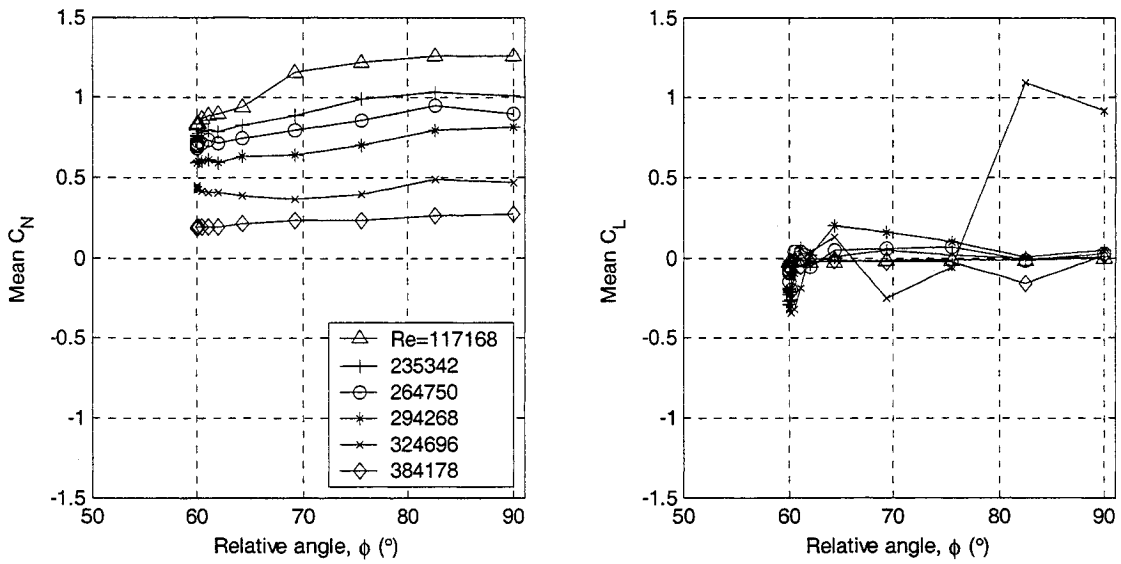

Figure 5-11: Variation of mean drag and lift coefficients with relative angle between wind and cylinder (60° model inclination, high scan rate, average of rings 2 and 4)

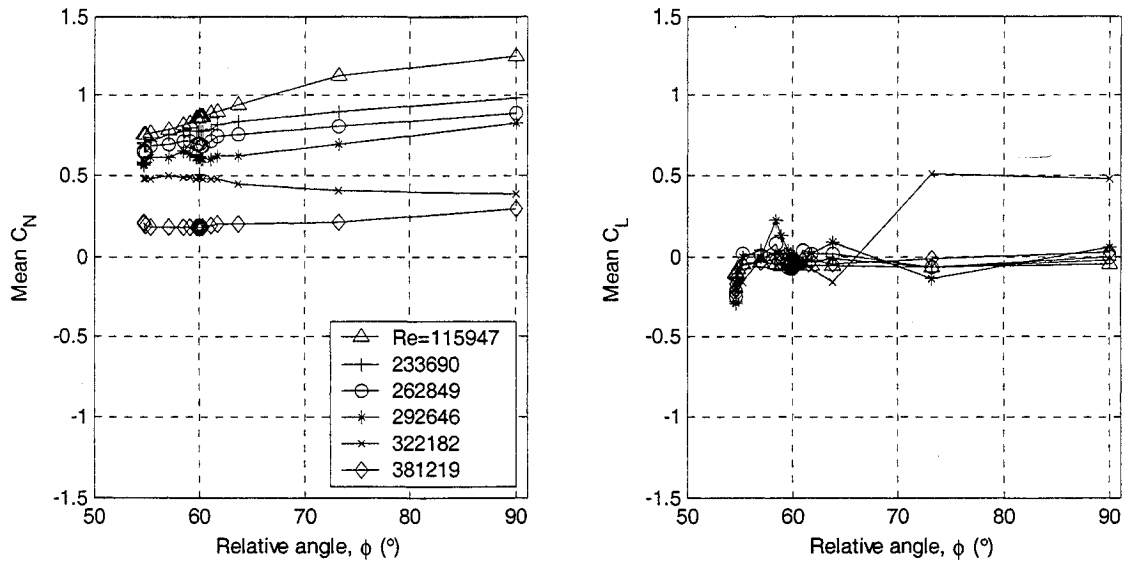

Figure 5-12: Variation of mean drag and lift coefficients with relative angle between wind and cylinder (54.7° model inclination, low scan rate, average of rings 2 – 5)

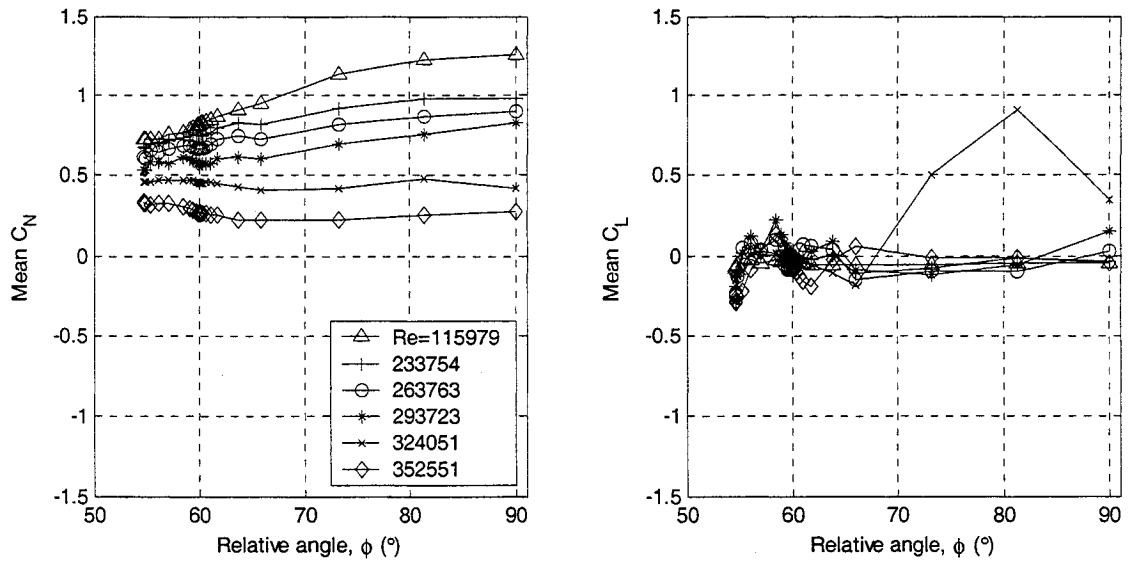

Figure 5-13: Variation of mean drag and lift coefficients with relative angle between wind and cylinder (54.7° model inclination, high scan rate, average of rings 2 and 4)

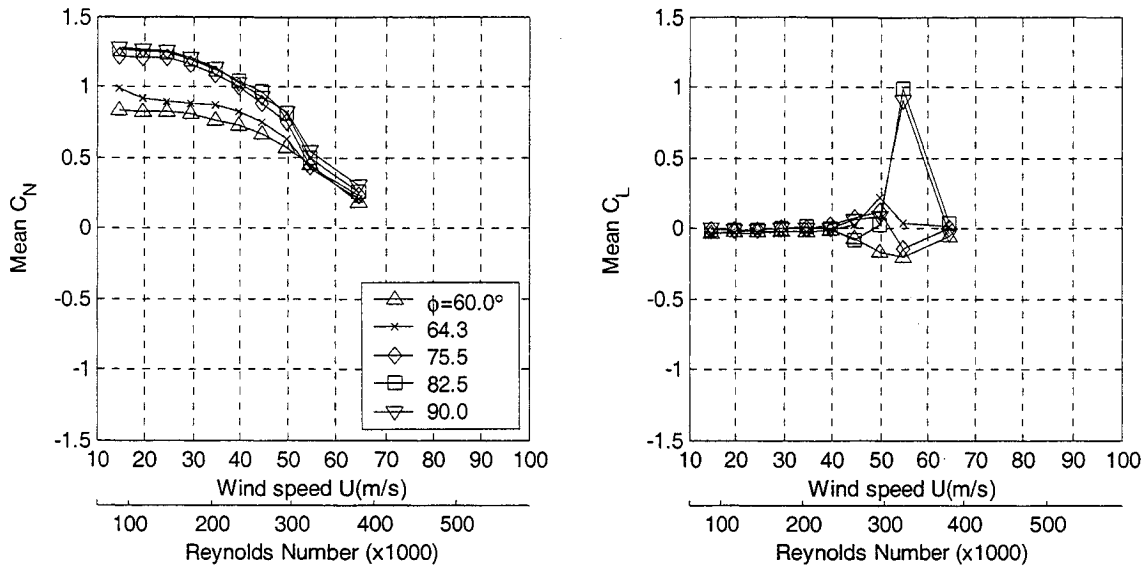

Figure 5-14: Variation of mean drag and lift coefficients with wind speed for a circular cylinder inclined to varying relative angles (60° model inclination angle, low scan rate, average of rings 2 – 5)

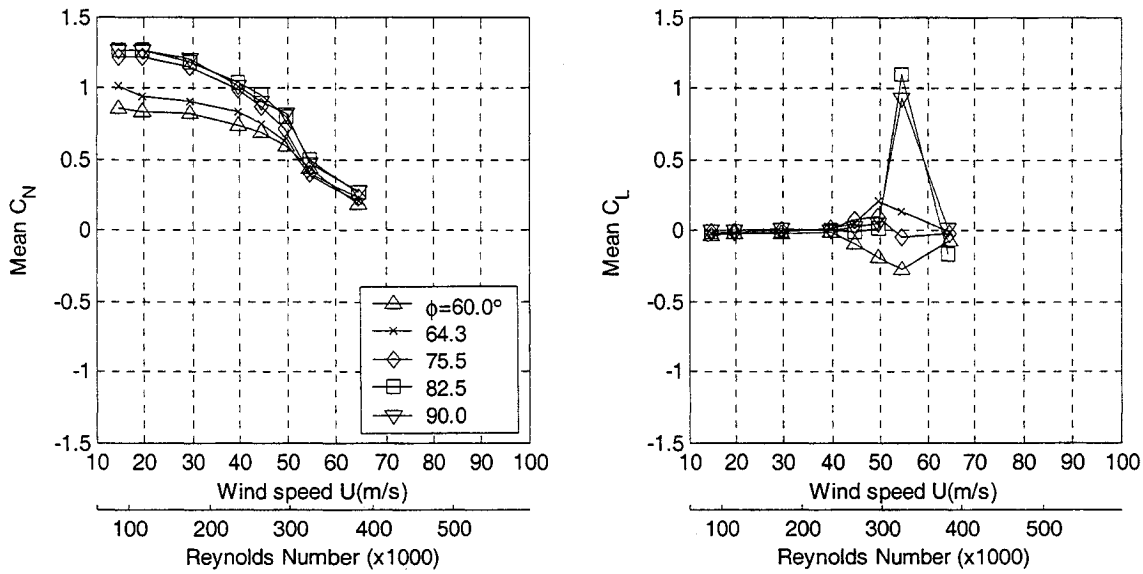

Figure 5-15: Variation of mean drag and lift coefficients with wind speed for a circular cylinder inclined to varying relative angles (60° model inclination angle, high scan rate, average of rings 2 and 4)

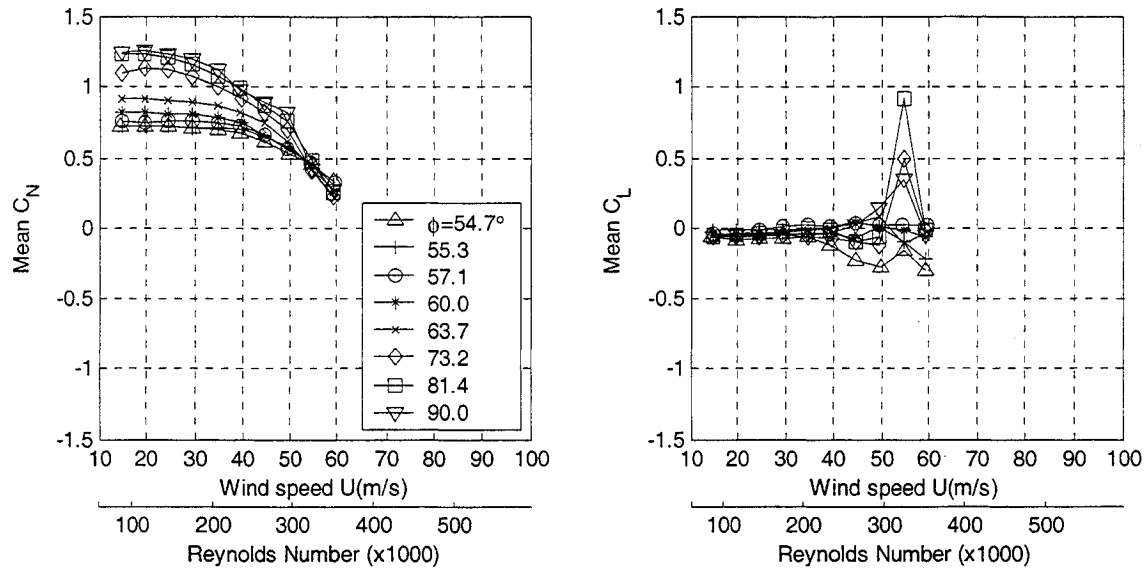

Figure 5-16: Variation of mean drag and lift coefficients with wind speed for a circular cylinder inclined to varying relative angles (54.7° model inclination, low scan rate, average of rings 2 – 5)

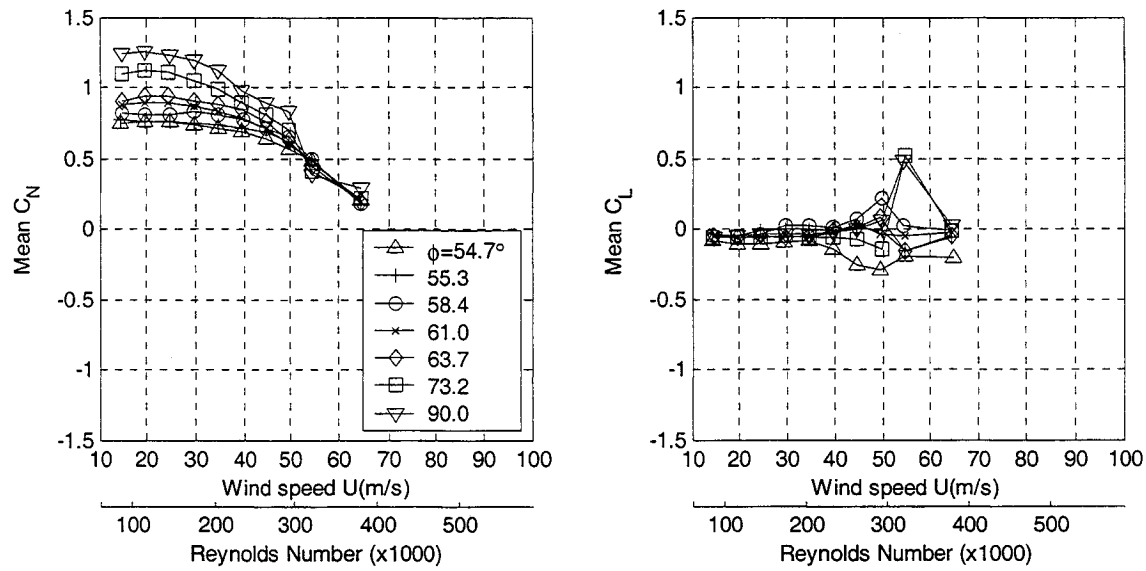

Figure 5-17: Variation of mean drag and lift coefficients with wind speed for a circular cylinder inclined to varying relative angles (54.7° model inclination, high scan rate, average of rings 2 and 4)

The frequency distribution of the instantaneous lift coefficient also presents a dependence on cylinder inclination. Strong cyclic variations in the dynamic lift on a cylinder are characteristic of the TrBL0 regime. This is known as vortex shedding, the frequency of which can be predicted by the well-known Strouhal number introduced in Section 2.3.1 and given by Equation (2.2). For a circular cylinder the Strouhal number is given in the range of 0.18 to 0.2, depending upon the reference one consults.

Figure 5-18 and Figure 5-19 present the power spectral densities (PSD) of the lift coefficients for rings 2 and 4, at inclination angles of 90° and 60°, respectively. The PSD was determined using a Fast Fourier Transform (FFT) length of 2048. For the inclined cylinder, the dominant frequency of vortex shedding ($f_v \approx 36$ Hz) is noticeably lower than that of the same cylinder positioned normal to the flow ($f_v \approx 42$ Hz). Further, the spectral distribution is rather more dispersed about the principal shedding frequency for the case of the inclined cylinder indicating less power potential for excitation at the dominant frequency. (Note the different vertical scales.)

Plotting the PSD against a dimensionless frequency (represented by the Strouhal number) the cylinder positioned normal to the flow produces the expected result—the dominant dimensionless frequency is approximately 0.2 (see Figure 5-20). This same result is achieved if the dimensionless frequency for the inclined case also includes the term $(\sin\phi)^{-1}$. The Strouhal number is approximately 0.2 for an inclined cylinder only if either:

- the component of the flow velocity normal to the cylinder axis is considered instead of the free stream velocity, or;
- if one takes the representative dimension, D, to be the dimension of the cylinder parallel to the flow. That is, the diameter of the cylinder divided by the sine of the inclination angle.

This result is shown in Figure 5-21. Therefore, the vortex shedding frequency of an inclined cylinder is dependent upon the inclination angle, in addition to the wind speed and cylinder diameter.

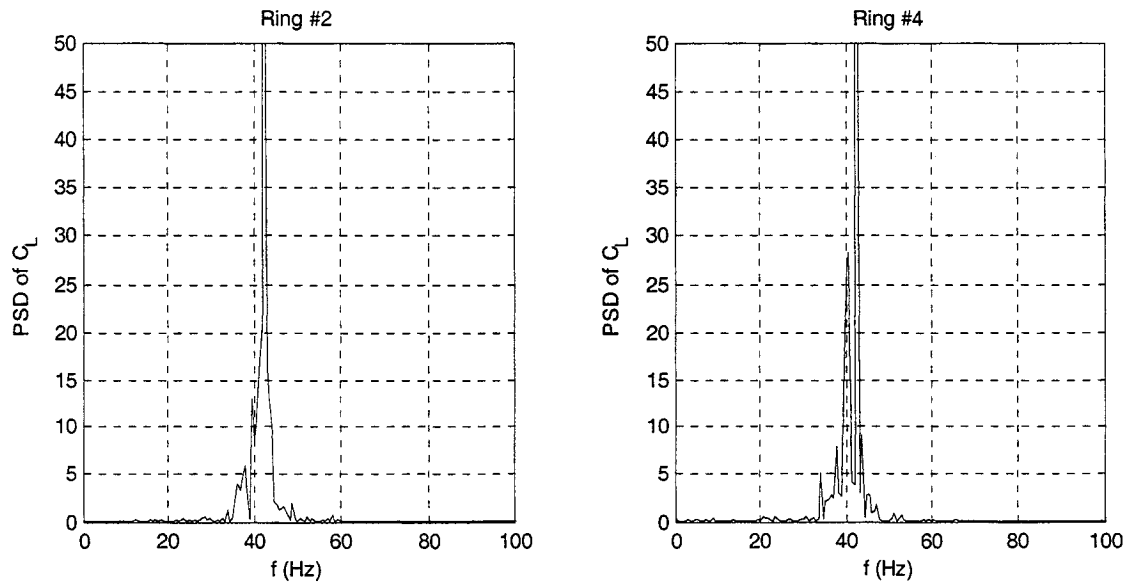

Figure 5-18: Power spectral density of C_L (rings 2 and 4, high scan rate); $R_e = 1.14 \times 10^5$, $\phi = 90°$

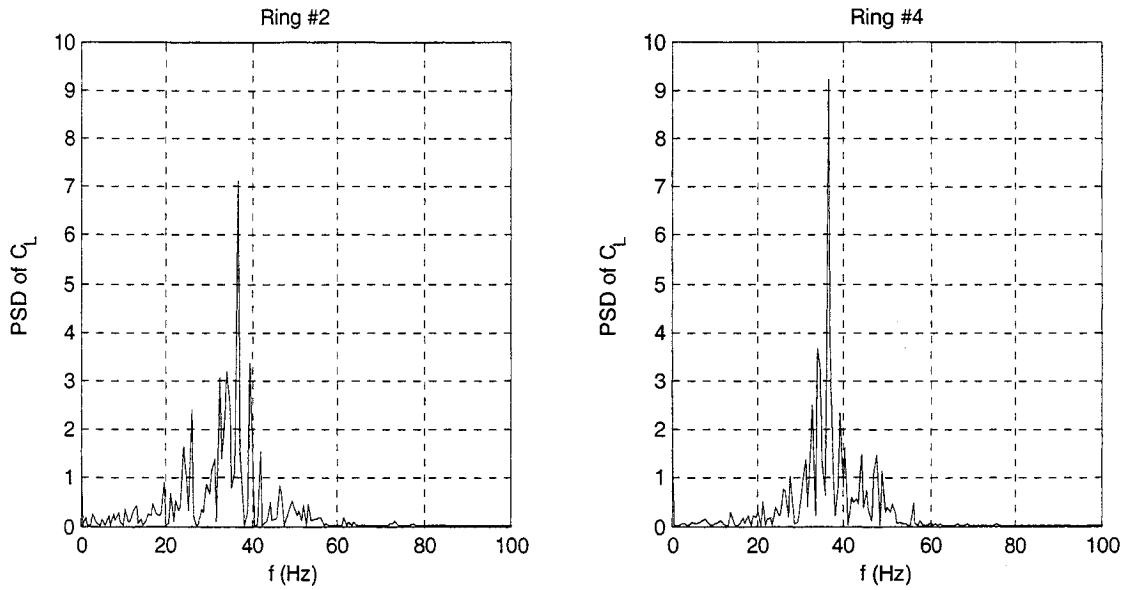

Figure 5-19: Power spectral density of C_L (rings 2 and 4, high scan rate); R_e= 1.20×10^5, ϕ=60°

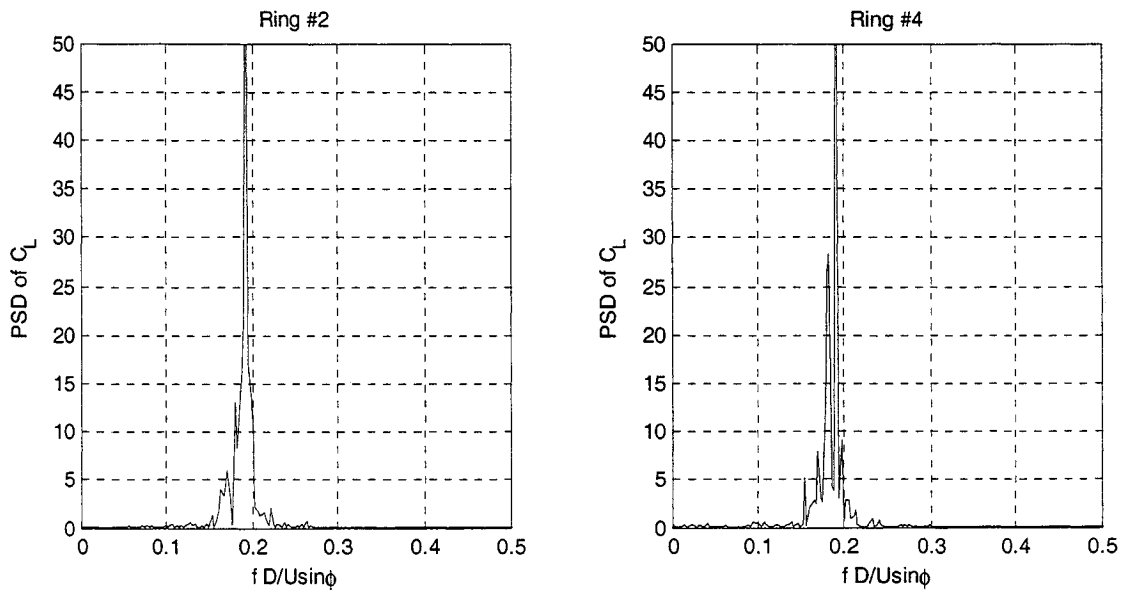

Figure 5-20: Power spectral density of C_L (rings 2 and 4, high scan rate) plotted against dimensionless frequency (Strouhal number); R_e= 1.14×10^5, ϕ=90°

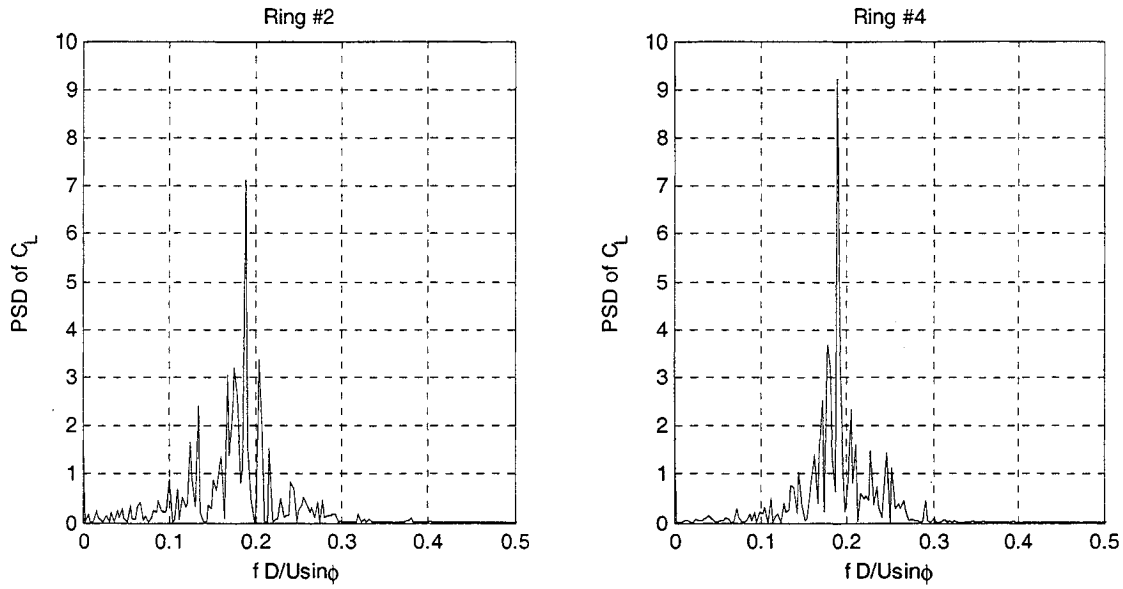

Figure 5-21: Power spectral density of C_L (rings 2 and 4, high scan rate) plotted against dimensionless frequency (Strouhal number); $R_e = 1.20\times10^5$, $\phi=60°$

5.4.2 Circumferential Pressure Distribution About a Cylinder Inclined to the Flow

Results presented in the previous section indicate that mean drag and lift coefficients are generally lower in magnitude for an inclined cylinder as opposed to a cylinder positioned normal to the flow direction. To this end, pressure values around the circumference of the cylinder can be expected to differ in magnitude also.

Figure 5-22 presents the circumferential pressure distribution of ring 2 for both 90° (run 750_012) and 60° (run 750_031) inclinations, and at various wind speeds throughout the critical Reynolds number range. (No plot is included for U=30 m/s as 750_012 contained aberrant data as detailed in Section 5.3.1.) The pressure coefficients at each tap are generally lower for the inclined cylinder, and this was reflected in the difference in the mean drag and lift coefficients. The onset of the asymmetrical pressure distribution—formation of a separation bubble—occurs at a lower wind speed for the inclined cylinder, and this too was reflected by the mean lift coefficients, but more specifically the asymmetric pressure distribution can be described as a more gradual for the inclined cylinder. That is, for the speed of U=59.7 m/s, the pressure distribution gradually reduces over the top of the cylinder section shown in Figure 5-22 for the inclined case, while for the case of no inclination the reduction in the pressure distribution over the top of the section is significantly more abrupt. As well, the change in the pressure distributions over the progression of wind speeds appears to be more gradual for the inclined case. These points agree with the findings of Bursnall and Loftin (1951) that the separation bubble is less well-defined when the cylinder is inclined to 60°.

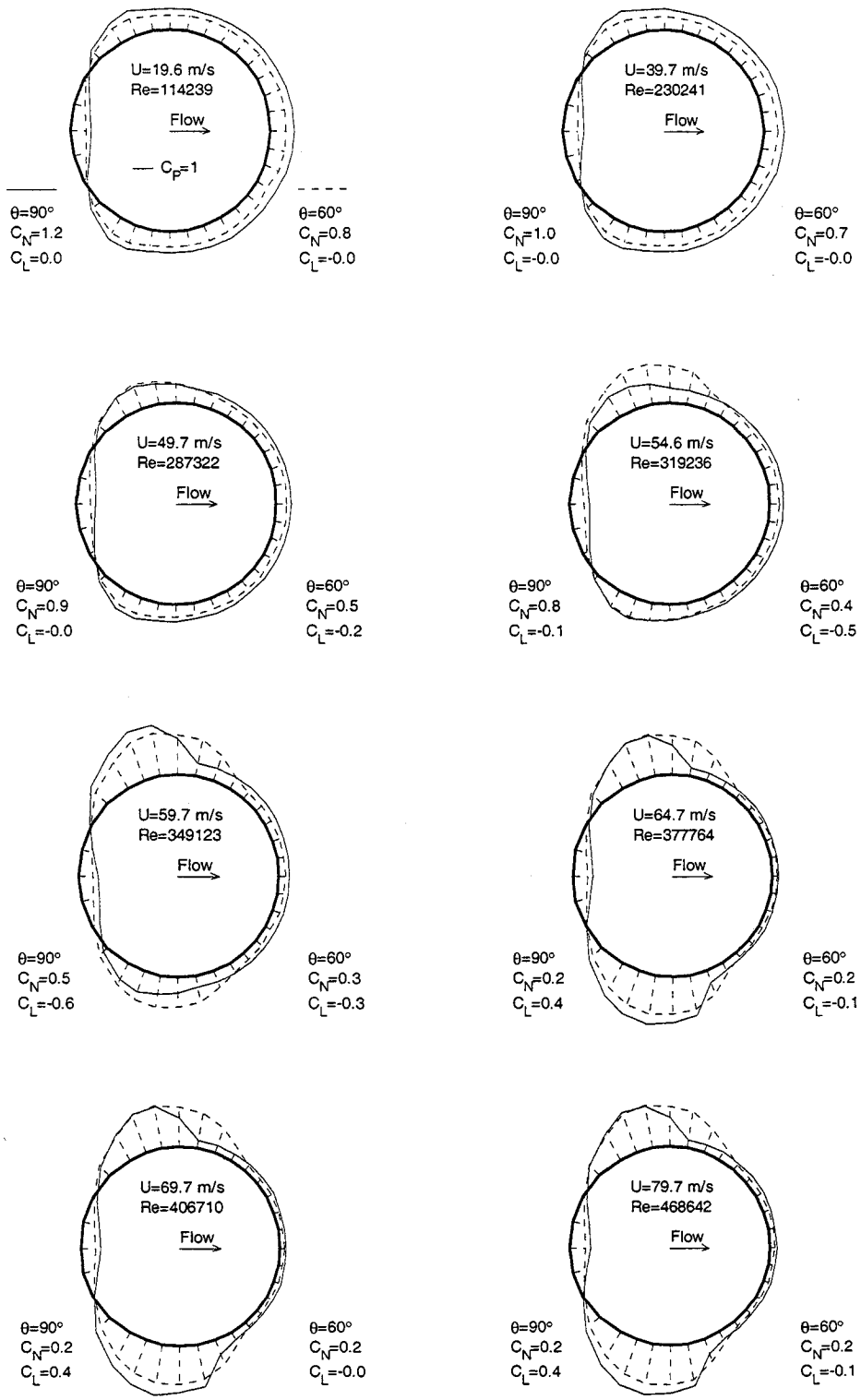

Figure 5-22: Mean pressure distribution about a circular cylinder (ring 2, high scan rate); dashed line represents θ=60°, solid line represents θ=90°

5.4.3 Span-wise Variations Due to Cylinder Inclination

In a wind tunnel setting, boundary conditions are an ever-present variable, more so with an inclined cylinder than with a cylinder positioned normal to the flow. The effects of boundary conditions on a cylinder placed normal to the flow are generally limited to unrepresentative pressure distributions about the ends of the cylinder within the boundary layer at the tunnel walls (assuming an appropriate cylinder diameter/tunnel width aspect ratio). Inclining the cylinder adds an along-wind component to the span, and therefore adds the potential for up-wind effects to affect down-wind regions along the span.

At pre-critical wind speeds and lower inclination angles, there is generally a distinct spread between the drag coefficients of rings 2 to 5 (though some inconsistencies occur). In particular, the drag coefficients are slightly greater the further upstream (and closer to the tunnel ceiling) the ring is positioned. This spread closes as the relative angle approaches 90° as can be seen in Figure 5-23. Also this spread closes as the wind speed is increased as illustrated by the progression of Figure 5-23 through Figure 5-29.

This variation is doubtless the result of the discontinuity imposed by the wind tunnel roof. Consider the so-called axial flow introduced in the literature to explain, in part, dry inclined cable galloping and high-speed vortex vibration of stay cables. Intuitively, this axial flow along the leeward side of the cylinder may not be as fully developed at ring 2 as it is at ring 5 simply because there is not as much of the cylinder above and upstream of ring 2. Further as the wind speed increases, the spread in the drag coefficient values decreases, potentially indicating that the significance of the axial flow to the drag coefficient is less with increasing wind speed.

The variation in lift coefficient with relative wind-cylinder angle displays some seemingly span-wise-dependent characteristics. Principally, at lower inclination angles the lift coefficient's deviation from zero appears at lower wind speeds, or is at least more noticeable, for rings 4 and 5 than for rings 2 and 3. The progression of wind speed levels given by Figure 5-24 through Figure 5-27 displays this behaviour. Again, the varying level of development, span-wise, of the axial flow on the leeward side of the cylinder could reasonably be responsible for this behaviour. The flow is potentially somewhat retarded at the upper rings due to the discontinuity imposed by the tunnel roof.

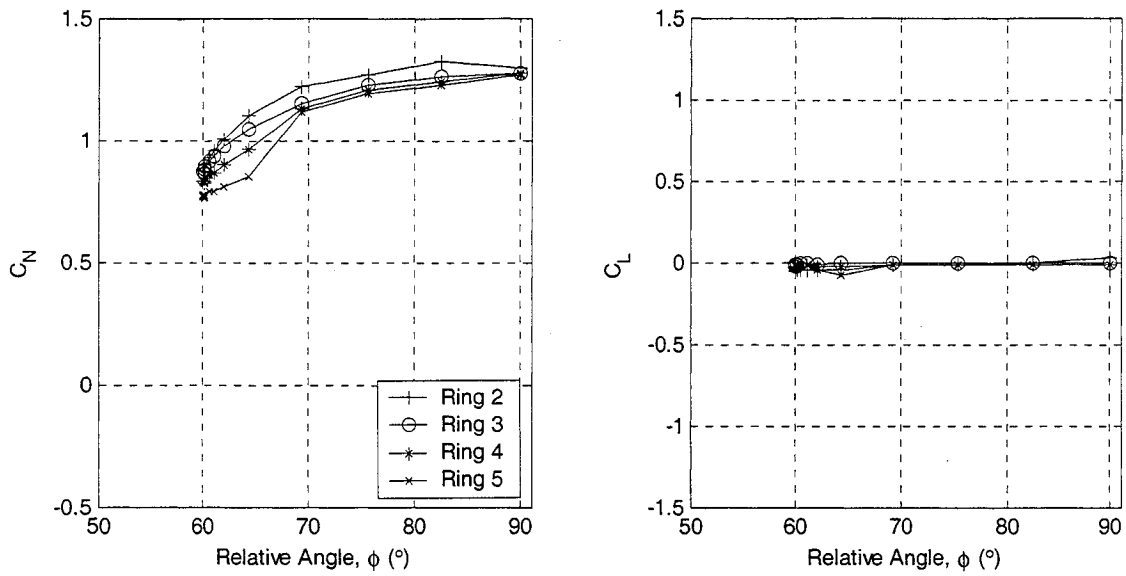

Figure 5-23: Variation of mean drag and lift with relative angle between wind and cylinder (R_e=8.65×10^4, θ=60°)

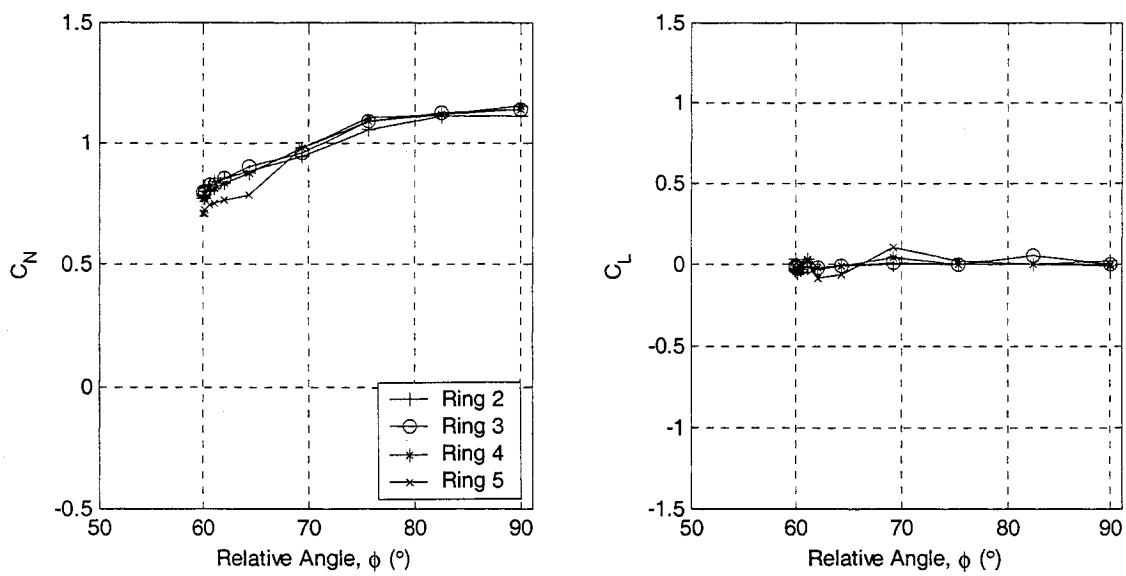

Figure 5-24: Variation of mean drag and lift with relative angle between wind and cylinder (R_e=2.04×10^5, θ=60°)

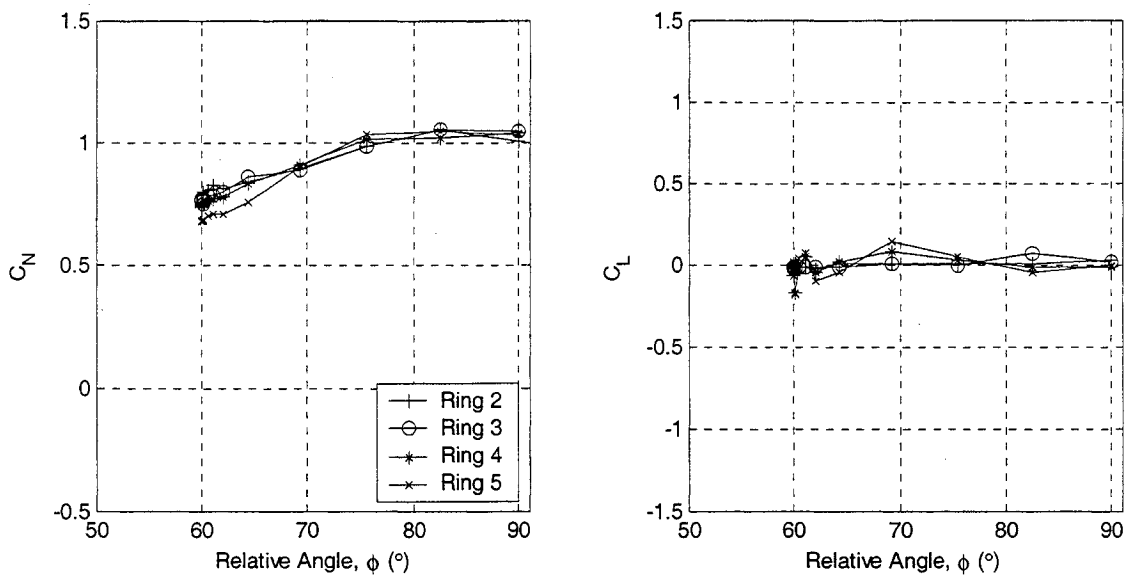

Figure 5-25: Variation of mean drag and lift with relative angle between wind and cylinder (R_e=2.33×10^5, θ=60°)

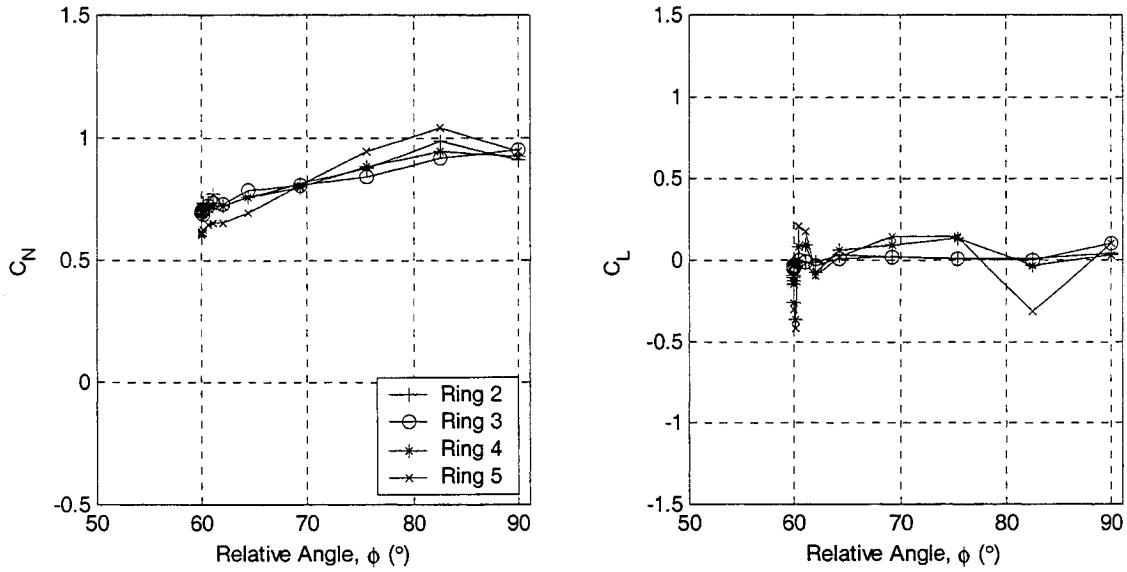

Figure 5-26: Variation of mean drag and lift with relative angle between wind and cylinder (R_e=2.63×10^5, θ=60°)

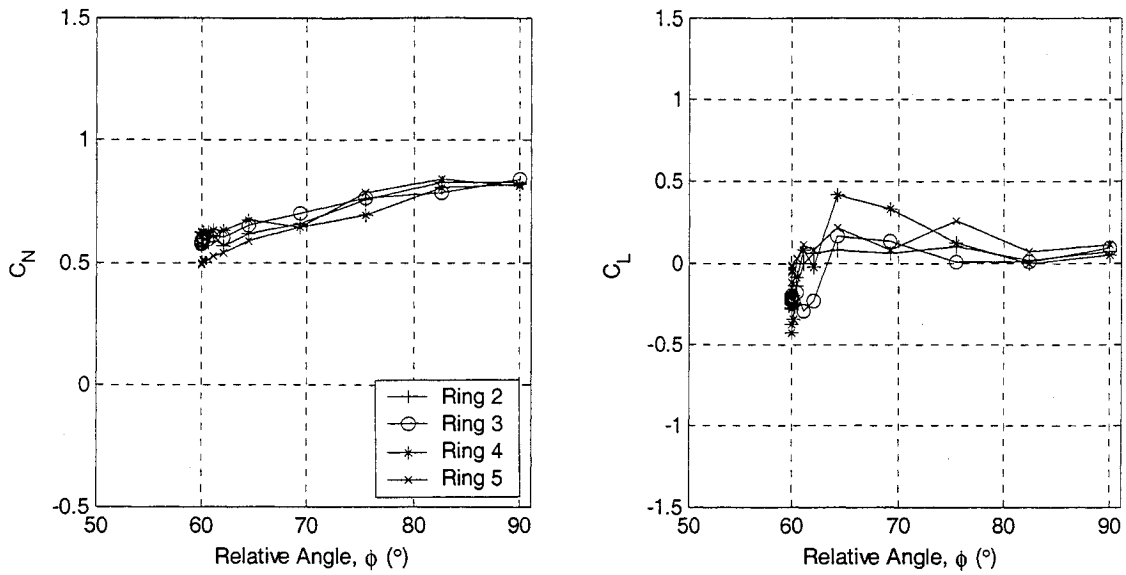

Figure 5-27: Variation of mean drag and lift with relative angle between wind and cylinder (R_e=2.93×10^5, θ=60°)

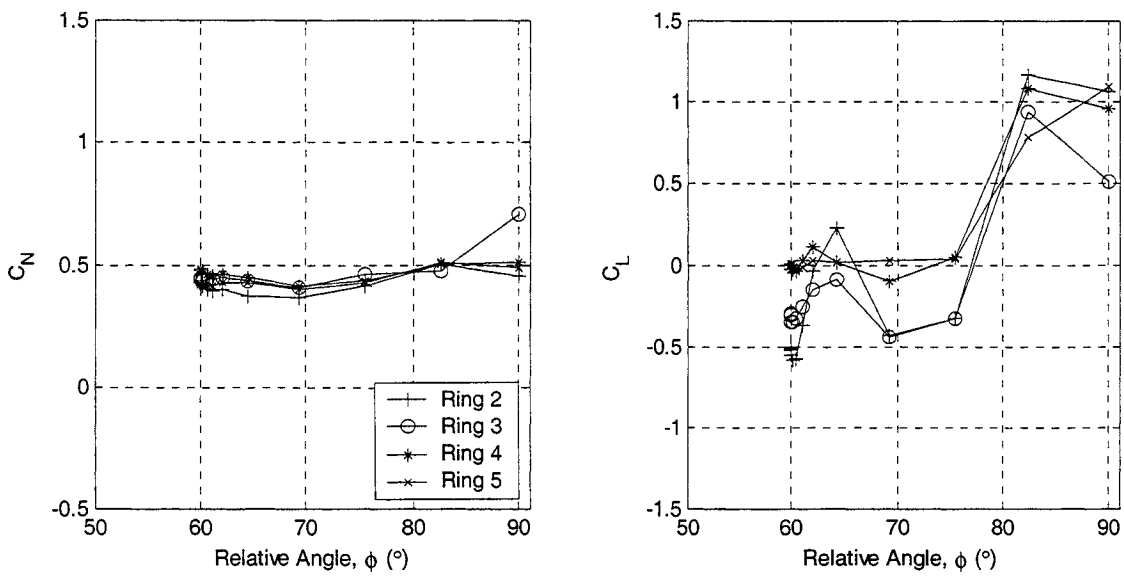

Figure 5-28: Variation of mean drag and lift with relative angle between wind and cylinder (R_e=3.21×10^5, θ=60°)

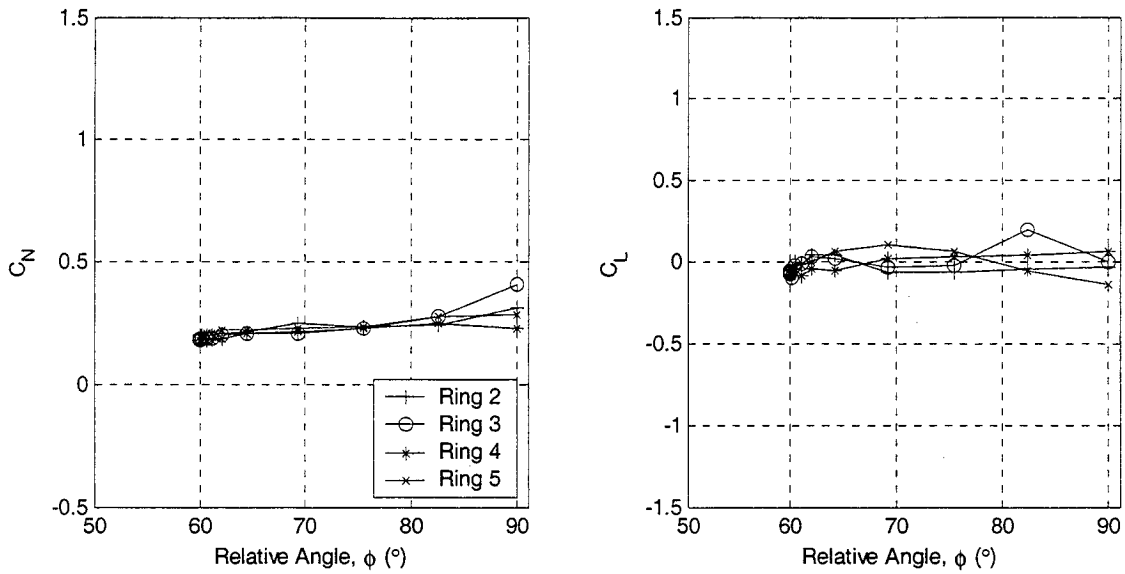

Figure 5-29: Variation of mean drag and lift with relative angle between wind and cylinder (R_e=3.81×10^5, θ=60°)

5.5 Galloping Instability

5.5.1 Evaluation of the Glauert-Den Hartog Criterion for Prediction of Instability

In the field of aerodynamics, the Glauert-Den Hartog criterion, given by Equation (3.4), is regarded as a necessary condition for galloping instability (Simiu and Scanlan, 1996). This concept has historically been applied to bluff bodies such as power transmission lines with ice accretion or other irregularly shaped cylinders. Circular cylinders placed normal to a flow cannot gallop because of continuous radial symmetry; $dC_L/d\alpha \approx 0$. Little attention has been given, however, to circular cylinders inclined to the flow. In a two-dimensional context, with the cable inclined the wind no longer encounters a circular section but rather an ellipse. Though this ellipse is not symmetrical in a radial sense, it is always symmetrical about the direction of flow, with a varying aspect ratio dependant upon the relative angle between the cable axis and wind direction. In a three-dimensional context, inclination of the cylinder will result in a decidedly three-dimensional flow as the cylinder's span includes an along-wind component and therefore simplification to two-dimensional flow is no longer acceptable.

The completed wind tunnel testing subjected a stationary, rigid cable model to various wind speeds, at varying angles of inclination and yaw. From the pressure data collected, the sum:

$$\frac{dC_L}{d\gamma} + C_D \tag{5.6}$$

may be evaluated to determine if the Glauert-Den Hartog criterion is applicable in predicting the supposed galloping instability witnessed for Setup 2C in Phase 1.

Figure 5-30 through Figure 5-39 present the variation of aerodynamic damping implied by Equation (5.6) with the effective angle of attack, γ, over a range of increasing wind speeds within the critical Reynolds number range. The slope of the lift coefficient at each angle value was approximated based on the simple average of the slopes of the lines connecting the lift coefficient value at the given angle to adjacent lift coefficient values on either side. The data presented in these figures is based on the low scan rate, thus showing rings 2 to 5, inclusive. The progression of plots show that as the wind speed increases the resulting sum generally decreases, driven by the lowering mean drag coefficient during the drag crisis. However the slope of the mean lift coefficient with respect to angle of attack also causes variations in the sum. These variations appear, for the most part, inconsistent between the rings and lack uniformity, with the result of Equation (5.6) from some rings occasionally dipping below zero and subsequently rebounding at the next wind speed. For the wind speed presented in

Figure 5-39 there is a notable harmonization in the results of the four rings, where all produce a decidedly negative sum of Equation (5.6), corresponding to an angle of attack, γ, in the vicinity of 35°. This angle of attack is the combination of the inclination angle, θ, of 54.7° and a yaw angle, β, in the vicinity of 30°. This combination produces an effective angle, ϕ, between the wind direction and cable axis of about 60°. (Refer to Figure 5-2 for angle references and to Appendix A for the derivation of the angle relationships.) The variations of mean drag and lift coefficients with angle of attack for this wind speed are presented in Figure 5-40.

Again, satisfying the Glauert-Den Hartog criterion is a necessary condition for galloping. This occurrence indicates that galloping can occur for the conditions of ϕ=60° and Reynolds number in the vicinity of 3.53×10^5. As given in Section 4.5, Phase 1 testing of the dynamic model found what was believed to be galloping to occur under such conditions. Thus, Figure 5-39 substantiates the hypothesis of galloping instability for Setup 2C in Phase 1.

The difference between Setup 2C and Setup 2A of Phase 1 was the rotation of the spring support axes; the wind-cable relative angle for both setups was 60°. The analysis of the pressure data from Phase 2 is independent of this spring support rotation. It is dependant upon Reynolds number and the wind-cable relative angle. Theoretically then, Setup 2A should also have exhibited galloping at the apparent critical wind speed. The absence of galloping for Setup 2A is not necessarily a significant result. In fact, a subsequent test run of Setup 2C failed to reproduce vibrations under the supposed critical conditions. This additional test run was carried out on a different day on which the weather was quite different. The airflow of the wind tunnel for Phase 1, being an open-circuit type tunnel, is somewhat dependant upon the weather conditions outside. Other researchers, including Saito *et al* (1994), have also commented on the sensitivity of this vibration phenomenon to test conditions in that vibrations will occur, or not, with only very slight differences in test conditions.

Further test speeds beyond that represented by Figure 5-39 were run focussing on the range of yaw angles between 20° and 40° to determine if the negative sum of Equation (5.6) had an upper bound. The additional tests included flows up to $R_c=3.97\times10^5$. The results are presented in Figure 5-41 through Figure 5-46 for increasing wind speeds. As the wind speed is increased, the concerted negative sum of Equation (5.6) from the four rings shifts back into positive values. Such behaviour indicates that this mechanism, unlike the classical mechanism of galloping, is a velocity-restricted phenomenon.

Tests completed with the high scan rate produced similar results. They are presented in Appendix C.

Satisfaction of the Glauert-Den Hartog criterion for conventional galloping of a bluff body is predominantly controlled by the negative slope of the lift coefficient which is due to the cross-sectional shape of the body, itself. Though also satisfying this well-known criterion, dry, inclined cable galloping is not similarly caused, but rather it is a result of the orientation of a circular cylinder—a section that would not otherwise be expected to gallop. The negative slope of the lift coefficient is produced by a span-wise interaction of the flow resulting from the along-wind component of the span. The regime in which the negative slope of the lift coefficient occurs also corresponds to approximately the lowest value of the drag coefficient (about 0.3). These two factors combine to produce a negative sum of Equation (5.6), thus satisfying the Glauert-Den Hartog criterion.

As noted in Section 3.2.1.2, regarding the other investigations into inclined cable vibrations and specifically the dry, inclined cable galloping phenomenon (Honda *et al*, 1995; Saito *et al*, 1994), in general the vibrations found in those tests arose at much lower wind speeds for models quite similar to that tested in Phase 1. In fact, due to the apparent similarity in models, the wind speeds in those tests would fall into the pre-critical Reynolds number range (Honda *et al* (1995) found an upper limit of the onset velocity to be $Re=2\times10^5$ for a wind-cable relative angle of 60°, regardless of the level of damping). Further, the other investigations found the vibrations to have no upper bound of velocity, contrary to what has been indicated by the results of this test. Therefore one must question as to whether these vibrations—both apparently galloping—are a result of the same mechanism. Matsumoto *et al* (1990) proposed that the axial flow in the near-wake of an inclined cylinder acts as a splitter plate, preventing the interaction of the shear layers in the wake as vortex shedding occurs, thus causing instability. For those studies, this mechanism is a possible explanation if the critical wind speed falls into the sub-critical Reynolds number range, however for the present study, since the wind speed falls into the critical Reynolds number range in which the fluctuating lift component (produced by vortex formation) practically disappears, this explanation is somewhat deficient.

The apparent critical wind speed in this case corresponds to a Reynolds number of approximately 3.5×10^5, which falls approximately into the range of TrBL1. The formation of the single laminar separation bubble seemingly contributes to the galloping mechanism. The necessary galloping conditions disappear as the speed further increases, indicating that the formation of the second laminar separation bubble potentially stabilizes the galloping tendencies. Questions still remain as to the reasons why this galloping phenomenon has not truly been witnessed in a prototype scenario. Through extensive testing of a cylinder normal to flow, turbulence has been found to affect the transition between the TrBL1 and TrBL2 regimes. Higher turbulence results in a more gradual transition between the two regimes. As well, these two regimes are very sensitive to flow conditions to

the extent that they can be eliminated if the level of turbulence is substantial enough (Zdravkovich, 1997a). Perhaps the explanation for the absence of this phenomenon from prototype stay cables is simply that natural wind is turbulent enough, or varies enough spatially, that these regimes do not occur, or do not occur simultaneously over enough length of a cable, such that dry inclined galloping will not occur in natural wind. As has been already stated, many researchers have found this mechanism very sensitive to test conditions. Also already stated, Phase 1 testing produced galloping for Setup 2C on one day, but not the next. The only apparent difference between the two days was the outside weather which was known to affect the flow characteristics in the open-circuit wind tunnel. Further research is clearly needed to examine the effects of turbulence, with closer simulation of natural wind required. Research is also needed to further define the actual mechanism, and to explain why this particular combination of relative angle and wind speed are conducive to galloping.

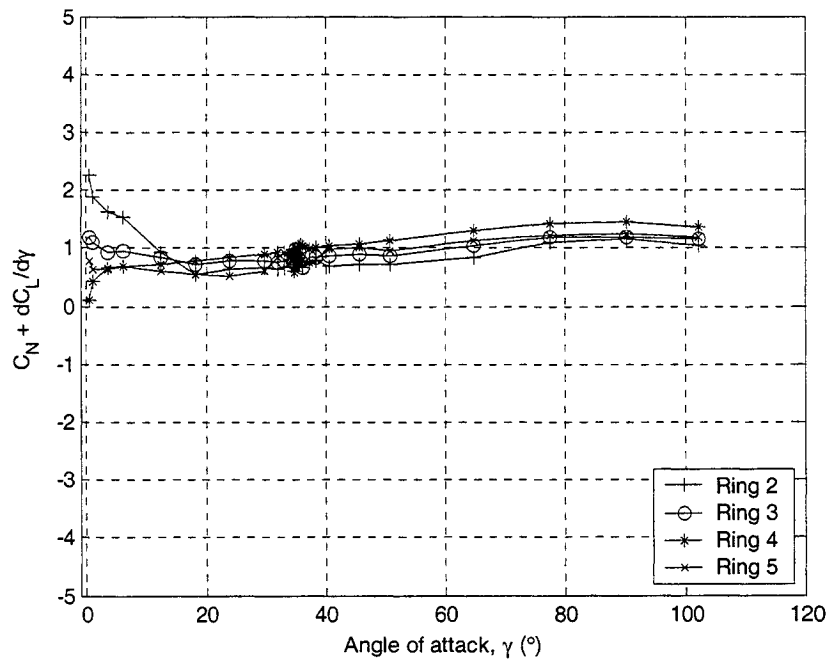

Figure 5-30: Variation of Equation (5.6) with effective angle of attack, γ, for R_e=8.67×10⁴; θ=54.7°, low scan rate

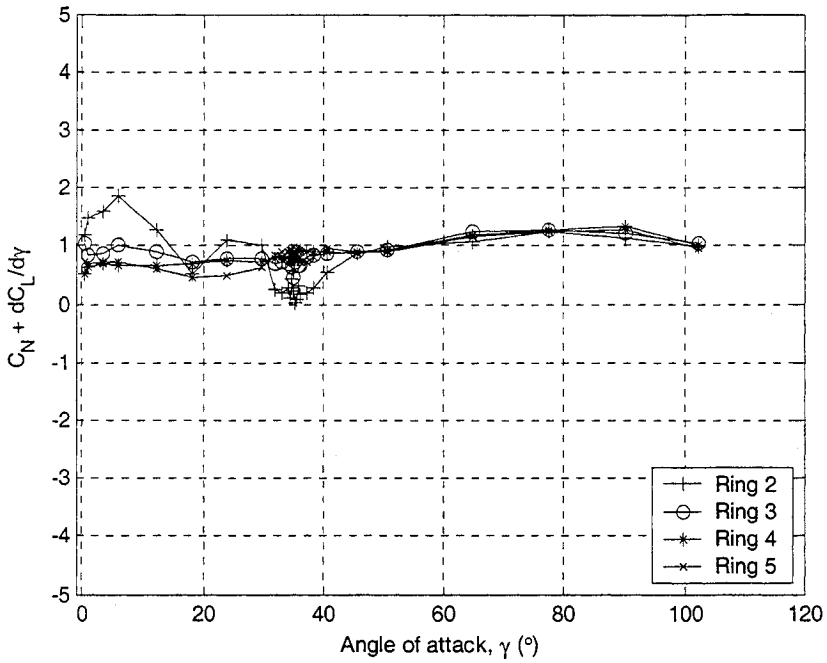

Figure 5-31: Variation of Equation (5.6) with effective angle of attack, γ, for R_e=1.16×10^5; θ=54.7°, low scan rate

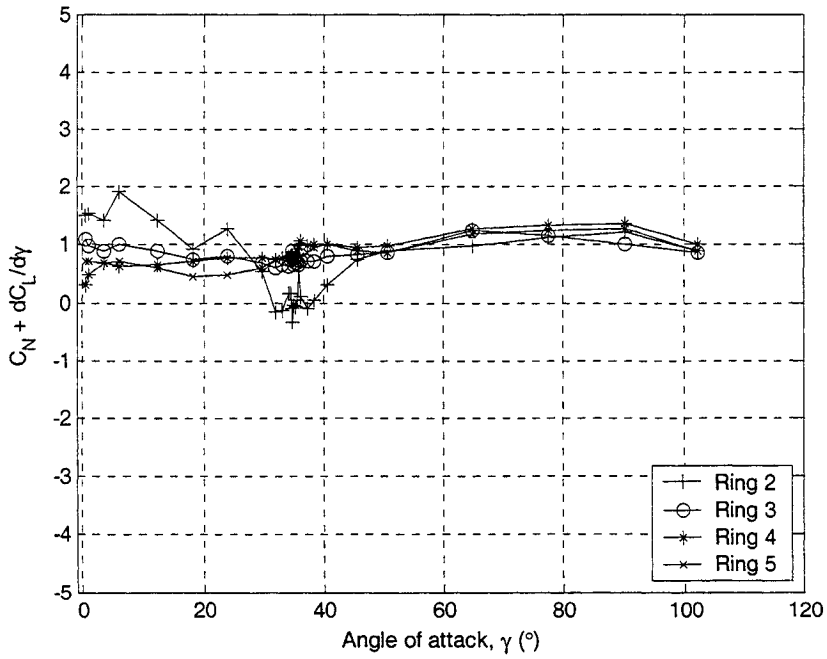

Figure 5-32: Variation of Equation (5.6) with effective angle of attack, γ, for R_e=1.43×10^5; θ=54.7°, low scan rate

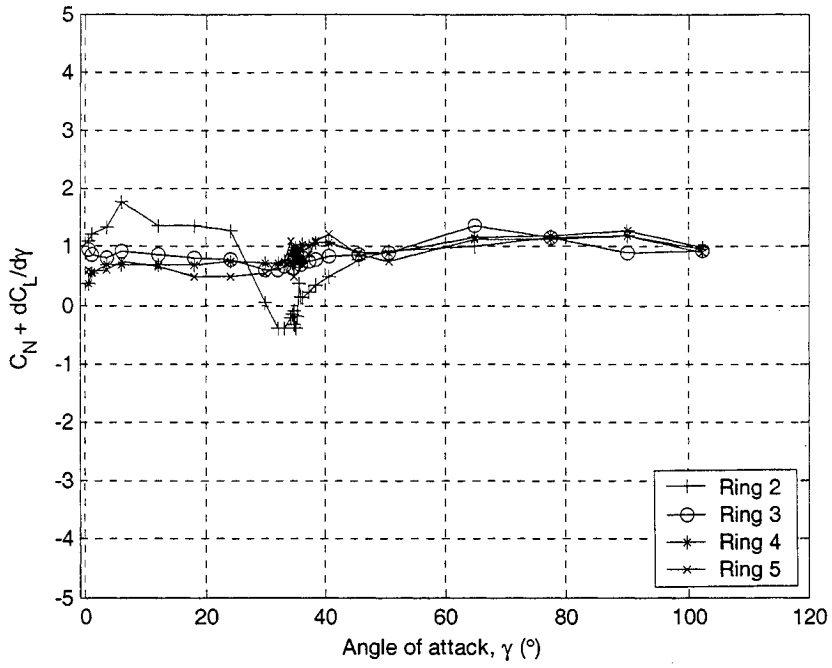

Figure 5-33: Variation of Equation (5.6) with effective angle of attack, γ, for R_e=1.74×10^5; θ=54.7°, low scan rate

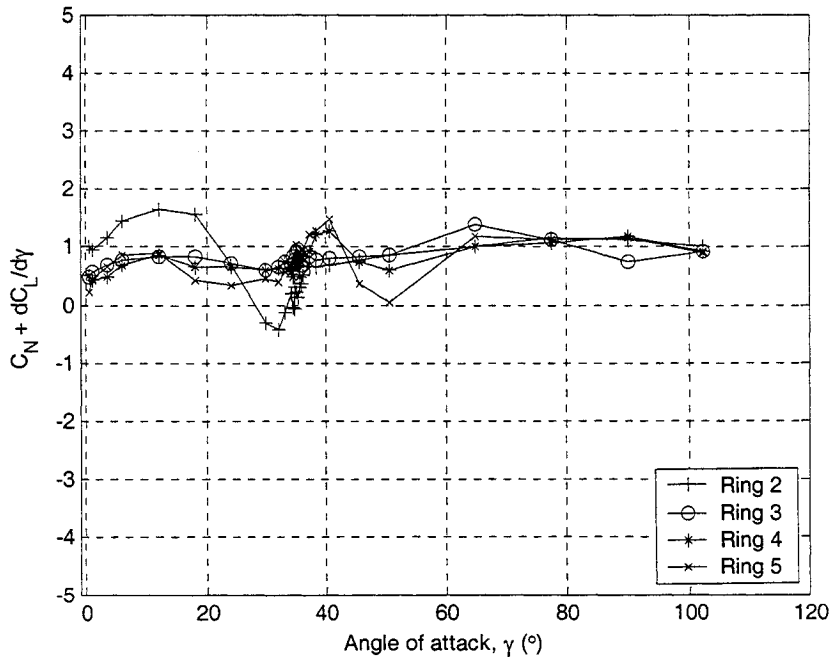

Figure 5-34: Variation of Equation (5.6) with effective angle of attack, γ, for R_e=2.02×10^5; θ=54.7°, low scan rate

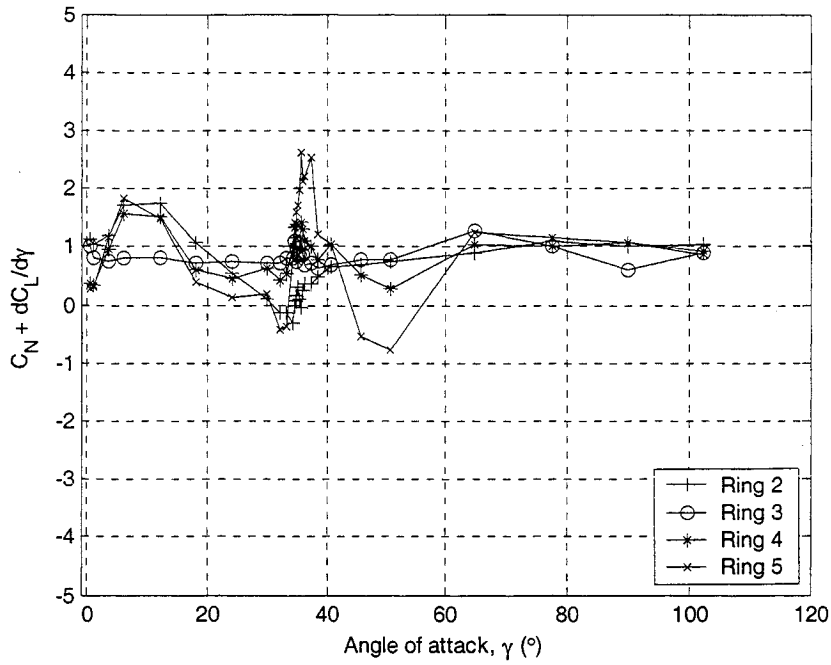

Figure 5-35: Variation of Equation (5.6) with effective angle of attack, γ, for R_e=2.34×10^5; θ=54.7°, low scan rate

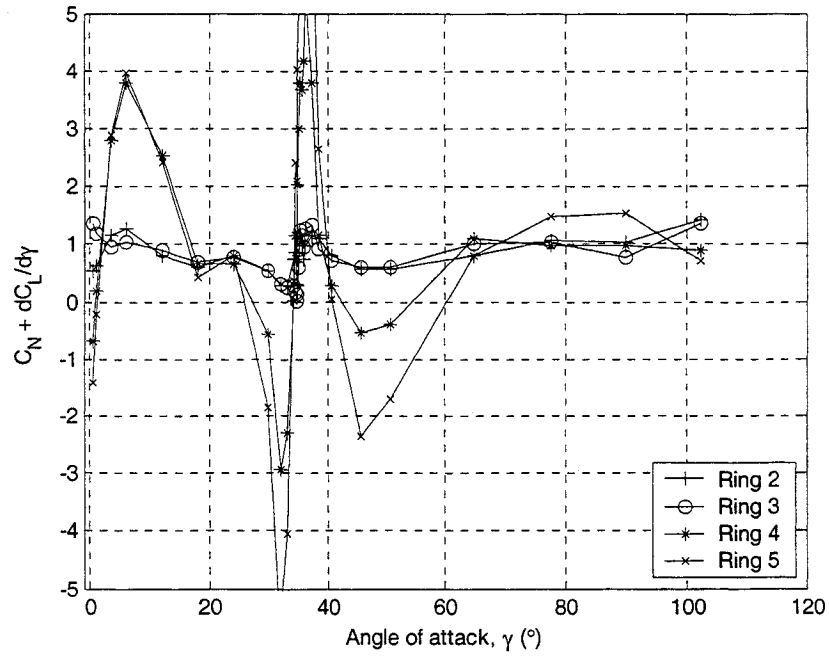

Figure 5-36: Variation of Equation (5.6) with effective angle of attack, γ, for R_e=2.64×10^5; θ=54.7°, low scan rate

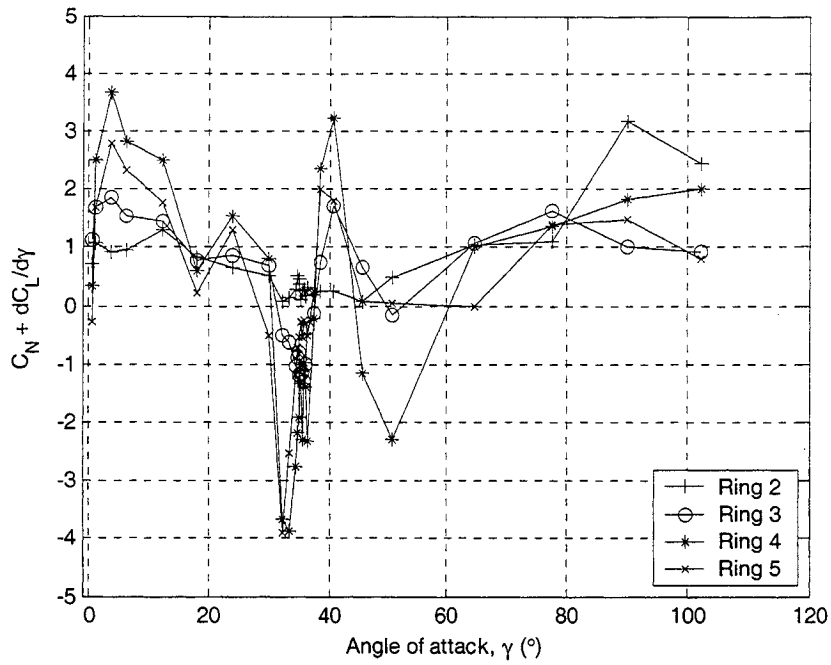

Figure 5-37: Variation of Equation (5.6) with effective angle of attack, γ, for R_e=2.94×10^5; θ=54.7°, low scan rate

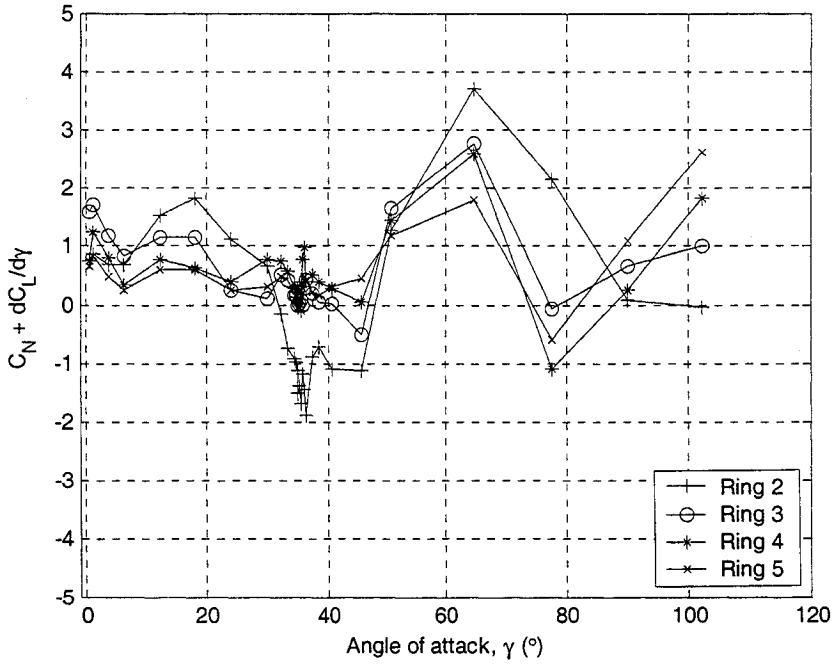

Figure 5-38: Variation of Equation (5.6) with effective angle of attack, γ, for R_e=3.24×10^5; θ=54.7°, low scan rate

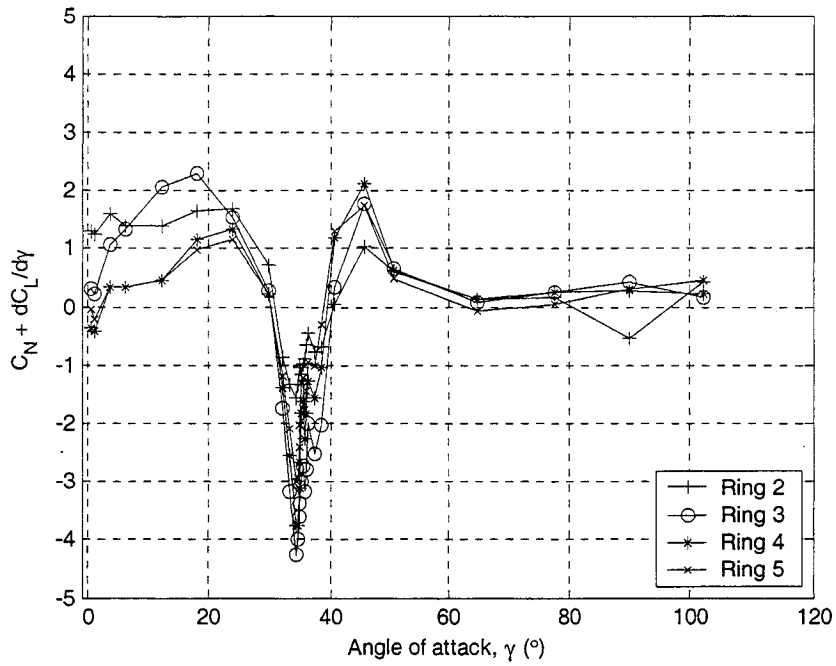

Figure 5-39: Variation of Equation (5.6) with effective angle of attack, γ, for R_e=3.53×10^5; θ=54.7°, low scan rate

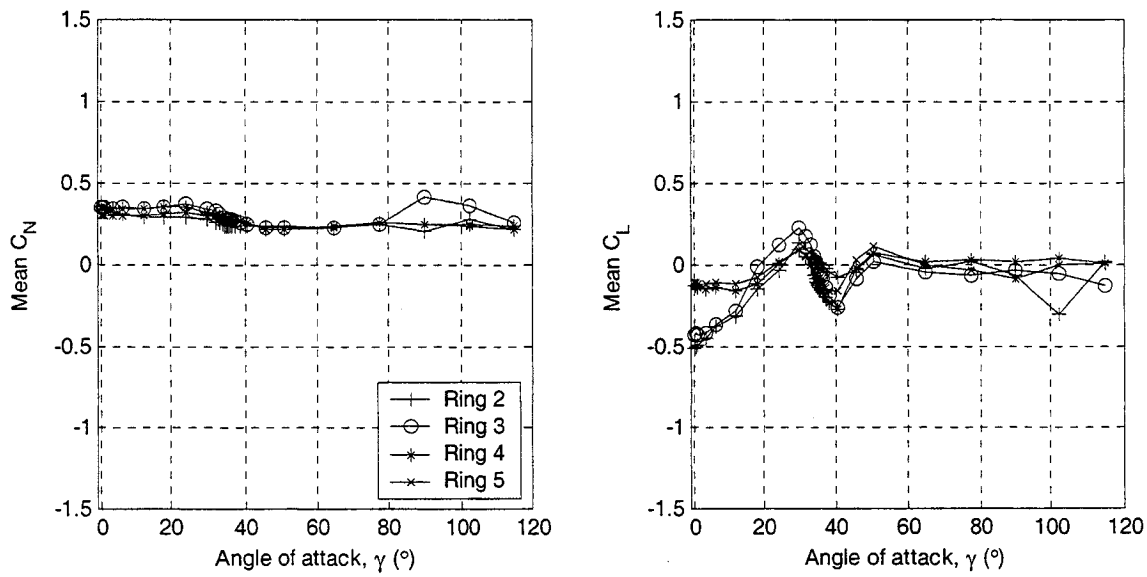

Figure 5-40: Variation of mean drag and lift with effective angle of attack, γ, for R_e=3.53×10^5; θ=54.7°, low scan rate

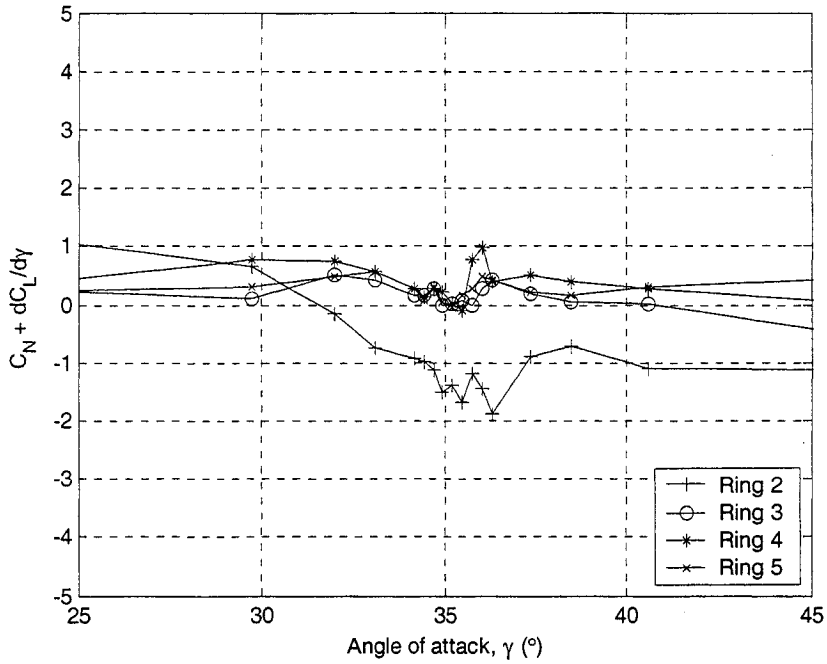

Figure 5-41: Variation of Equation (5.6) with effective angle of attack, γ, for R_e=3.24×10^5; θ=54.7°, low scan rate; excerpt from Figure 5-38

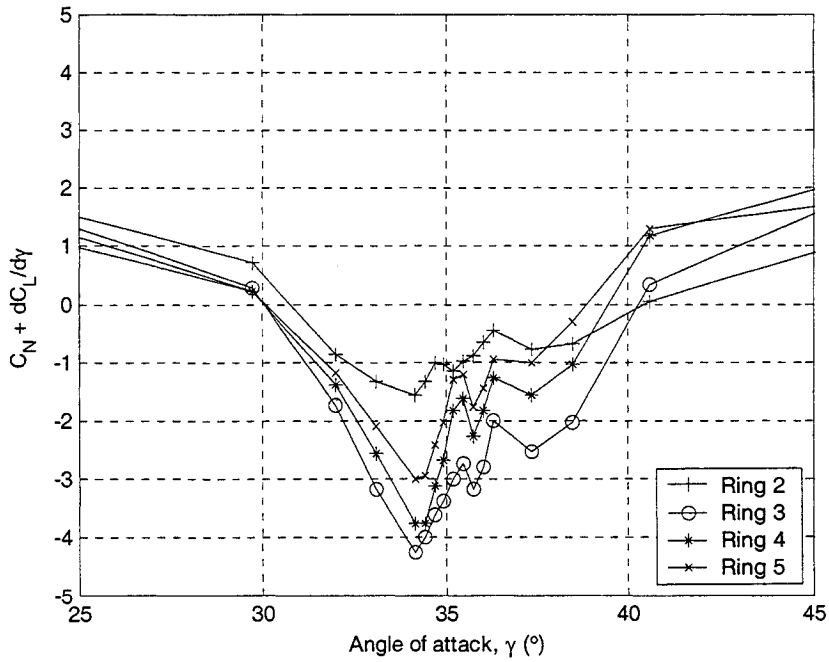

Figure 5-42: Variation of Equation (5.6) with effective angle of attack, γ, for R_e=3.53×10^5; θ=54.7°, low scan rate; excerpt from Figure 5-39

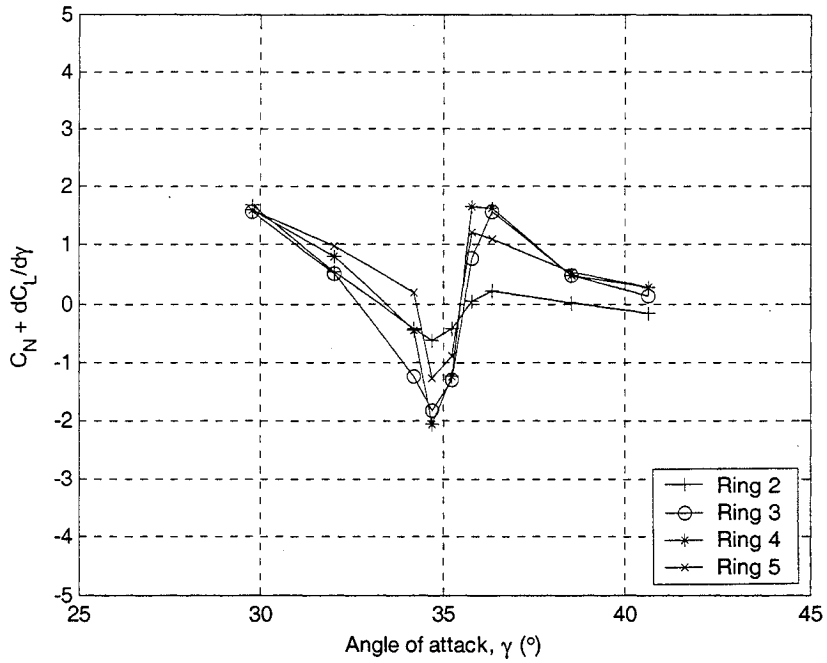

Figure 5-43: Variation of Equation (5.6) with effective angle of attack, γ, for R_e=3.56×10^5; θ=54.7°, low scan rate

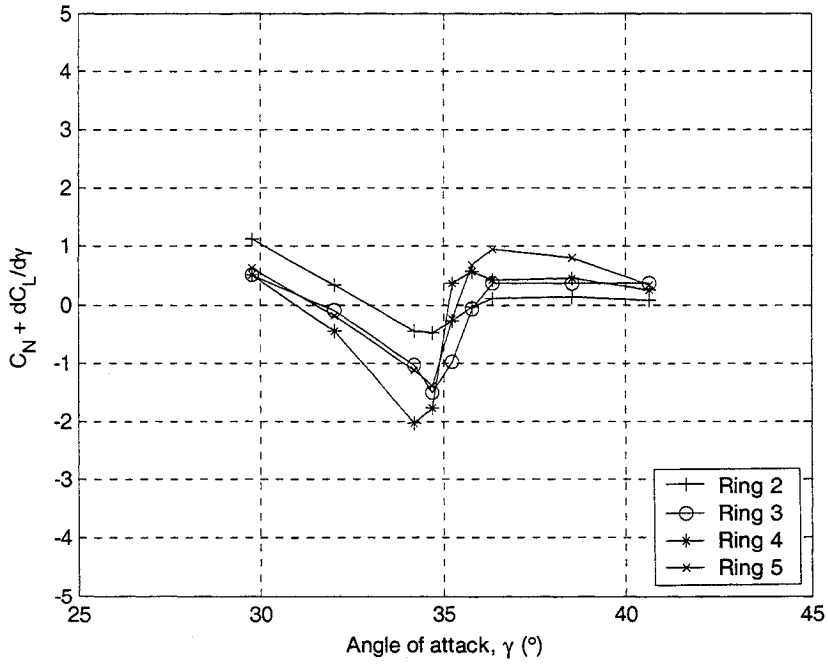

Figure 5-44: Variation of Equation (5.6) with effective angle of attack, γ, for R_e=3.62×10^5; θ=54.7°, low scan rate

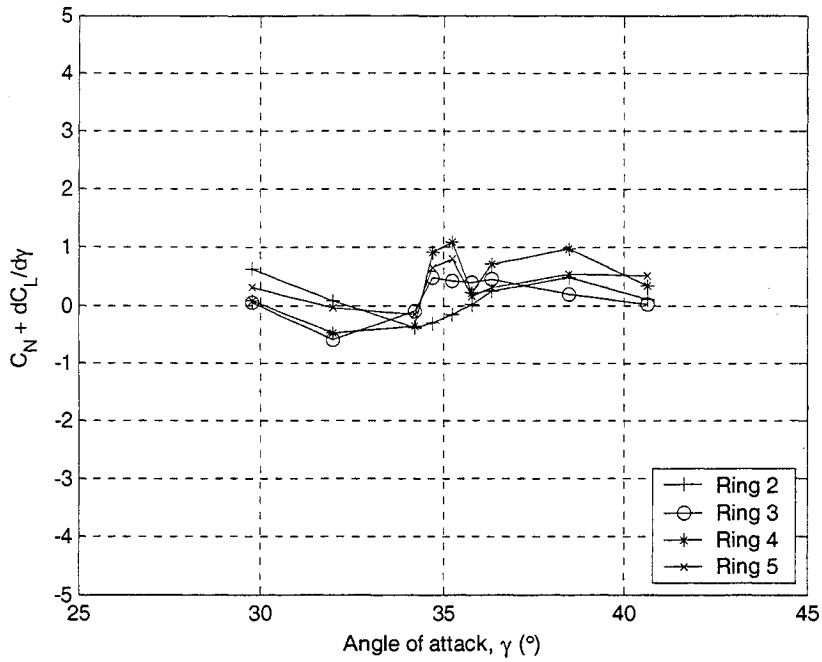

Figure 5-45: Variation of Equation (5.6) with effective angle of attack, γ, for R_e=3.74×10^5; θ=54.7°, low scan rate

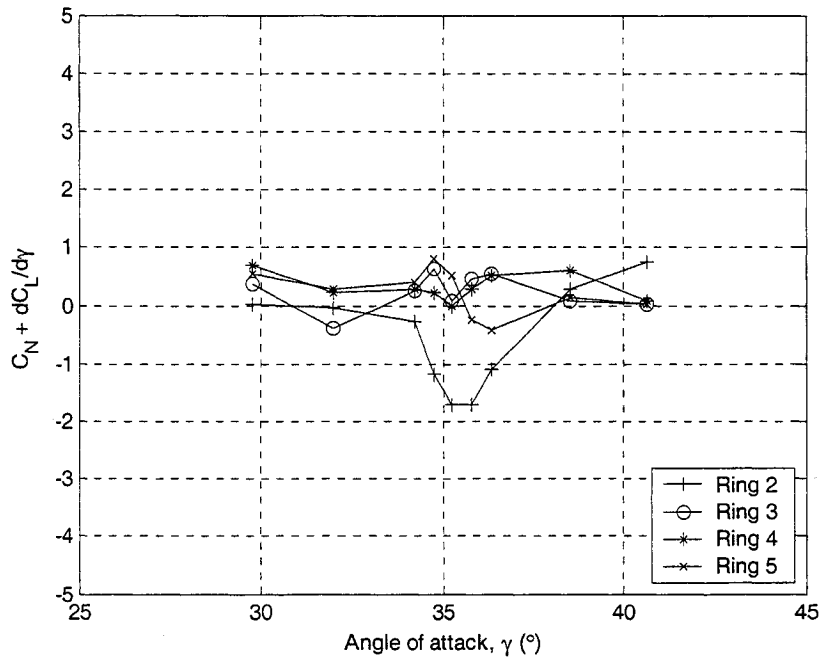

Figure 5-46: Variation of Equation (5.6) with effective angle of attack, γ, for R_e=3.97×10^5; θ=54.7°, low scan rate

5.5.2 Estimation of Required Mechanical Damping to Prevent Galloping Vibrations

Introduced in Section 3.2.1.1, the total damping of a dynamic system can be expressed by Equation (3.3):

$$2m\zeta\omega + \tfrac{1}{2}\rho UB\left(\frac{dC_L}{d\alpha} + C_D\right)_0 = c$$

where the system will be stable if $c>0$, and may be unstable if $c<0$. Based on the results presented in the previous section, one may estimate an approximate value of mechanical damping required to prevent galloping from occurring under the given critical conditions.

Consider the following parameters from the dynamic test of Phase 1:

- B=160 mm (cable diameter)
- f_0=1.415 Hz (natural frequency, Y-direction)
- m=60.8 kg/m (effective mass per length)

The critical wind speed at which galloping occurred for Phase 1 was U_{crit}=32 m/s.

Also consider, from Figure 5-42, an approximate average of the minimum sum of the drag coefficient plus the slope of the lift coefficient to be:

$$\frac{dC_L}{d\gamma} + C_D = -3$$

Based on these parameters, instability may occur if the damping ratio is less than 0.0087; that is, if damping is less than 0.87% of critical damping. Calculation of this value is presented in Appendix D. As noted in Section 2.2, typical values of mechanical damping for stay cables of existing bridges range from 0.01% to 0.2% of critical. Thus, by this result, existing bridge stay cables have not nearly enough mechanical damping potential to prevent this type of galloping.

In terms of Scruton number, given by Equation (2.3), these results indicate an approximate limit of $S_C>17$ to prevent galloping vibrations. This is significantly higher than the condition of $S_C>10$ suggested by Irwin (1997) for prevention of rain-wind vibrations.

5.5.3 Spectral Analysis of Lift

From Section 5.5.1, determination of conditions conducive to galloping has been shown to be satisfactorily based on the mean lift and drag coefficients obtained under static conditions, and thus dry, inclined cable galloping is seemingly controlled by quasi-static forces. One would therefore not expect significant information to result from a spectral analysis of the time-dependent fluctuations in the aerodynamic forces. The power spectra of the lift coefficient for each ring of pressure taps confirm this, presenting no obvious indication of a specific dynamic mechanism corresponding to a wind-cable angle of 60° at a Reynolds number of approximately 3.5×10^5, as presented in Figure K-1 (low scan rate) and Figure K-2 (high scan rate) in Appendix K. As well, there is no obvious or substantial difference between the power spectra of the apparent critical case compared to a non-critical case at the same wind speed. To compare, Figure K-3 presents the power spectra of each ring for a wind-cable relative angle of 54.7° (θ=54.7°, β=0°).

There is, however, a very notable effect on the correlation between the dynamic lift coefficients of the four rings when the apparent critical angle and wind speed conditions are experienced. Correlation among the lift coefficients for the rings was determined through a coherence function analysis. As the apparent critical wind-cable angle of 60° is approached, from either above or below, the coherence function noticeably increases. This is clearly shown by the progression of plots in each of Figure K-4 through Figure K-9. These figures respectively represent the correlation between the various combinations of rings 2 to 5. Further, as the apparent critical wind speed is approached, again from either above or below, the coherence in lift coefficients between rings noticeably increases. This trend is shown in the progression of plots beginning with Figure K-10, with each subsequent plot representing a higher wind speed, through Figure K-16. A FFT length of 1024 was used in the analysis. The plots are arranged beginning with the coherence function for rings farthest apart (2 and 5, distance of 7 diameters), progressing to the rings closest together (4 and 5, distance of one diameter). As expected, the greatest correlation is between the rings closest together, but all combinations follow the same notable trend.

This correlation is somewhat at odds with the results of Section 5.5.1. Those results indicate galloping to be governed by a quasi-steady mechanism however this trend of higher correlation of the lift coefficients between rings obviously peaks at the critical configuration. Thus, though the independent spectra do not indicate a dominant frequency-dependent action, whatever frequency-dependent action exists is somewhat uniform span-wise, and is concentrated toward the lower frequencies.

5.6 High-speed Vortex Excitation

5.6.1 Static Model Test Results

As detailed in Section 3.2.2, the mechanism causing high-speed vortex vibration is believed to be the intermittent amplification of regular Kármán vortices by so-called axial vortices generated by the axial flow on the leeward side of the cable. These axial vortices are of a significantly lower frequency than the Kármán vortices, and when conditions are right the shedding frequency of the axial vortex will be one-third (or one-quarter, or one-fifth, and so on) of the Kármán frequency. Thus there is potential to produce a low frequency vibration at a relatively high wind speed. Observations of prototype cable vibrations indicate that these vibrations always occur at a reduced velocity (Equation 3.6) of a multiple of 20. This characteristic has been confirmed by wind tunnel testing.

Phase 1 of the study produced limited-amplitude vibrations under various conditions summarized in Table 3-1. Presently relevant is Setup 2A; vibrations occurred for a wind-cable relative angle of 60° and over the velocity range of 18-19 m/s, corresponding to a reduced velocity of 80. Maintaining Reynolds number similarity for the static model test of Phase 2, this translates into a wind speed of 32.3–34.2 m/s.

One can conclude that a distinct difference is evident between the vibrations of Setups 2A and 2C of Phase 1. The vibrations produced at the higher wind speed in Setup 2C have been shown in Section 5.5.1 to be a result of a galloping-type mechanism based on satisfaction of the Glauert-Den Hartog criterion. The vibrations produced in Setup 2A are not similarly caused. As shown by Figure 5-30 (15 m/s) through Figure 5-35 (40 m/s), the sum presented in Equation (5.6) does not approach zero, consistently and uniformly, for all rings through the range of wind speeds surrounding the anticipated critical wind speed between 30 and 35 m/s.

The power spectral densities of the lift coefficients of rings 2 to 5 are presented over a range of speeds in Figure 5-47 (nominally 25 m/s) through Figure 5-51 (nominally 45 m/s), increasing in increments of 5 m/s, covering the region of expected vibration conditions. These wind speeds cover the range from the end of the TrSL3 regime, through the TrBL0 regime and just into the TrBL1 regime. All are for a wind-cable relative angle of 60°. The spectra for the lower wind speeds include the expected peak corresponding to the Kármán vortex shedding frequency. This peak diminishes as the speed is increased into the critical range where vortex shedding intensity lessens. None of the spectra, however, include a dominant peak at a relatively low frequency corresponding to a potential axial vortex shedding mechanism. Similar spectra result for the model inclined and yawed to achieve

the same wind-cable relative angle. Lift coefficient power spectra for the case of ϕ=60° (achieved with θ=54.7° and β=30°) are presented, for both the high and low scan rates, in Appendix E.

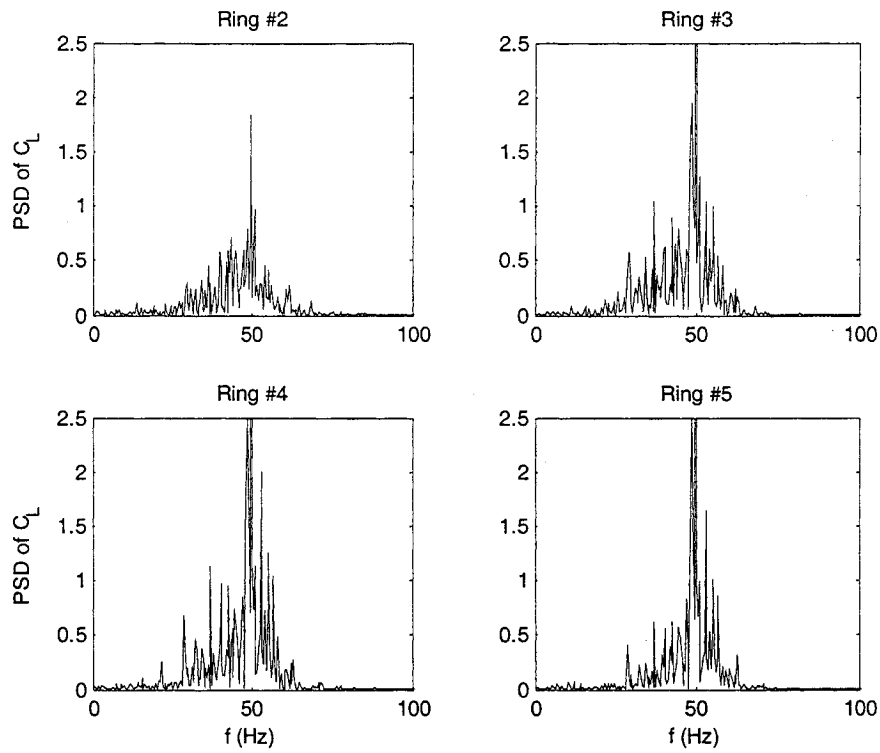

Figure 5-47: Power spectral density of C_L for U=24.6 m/s, R_e=1.45×10^5; θ=60°, β=0°, ϕ=60°, low scan rate

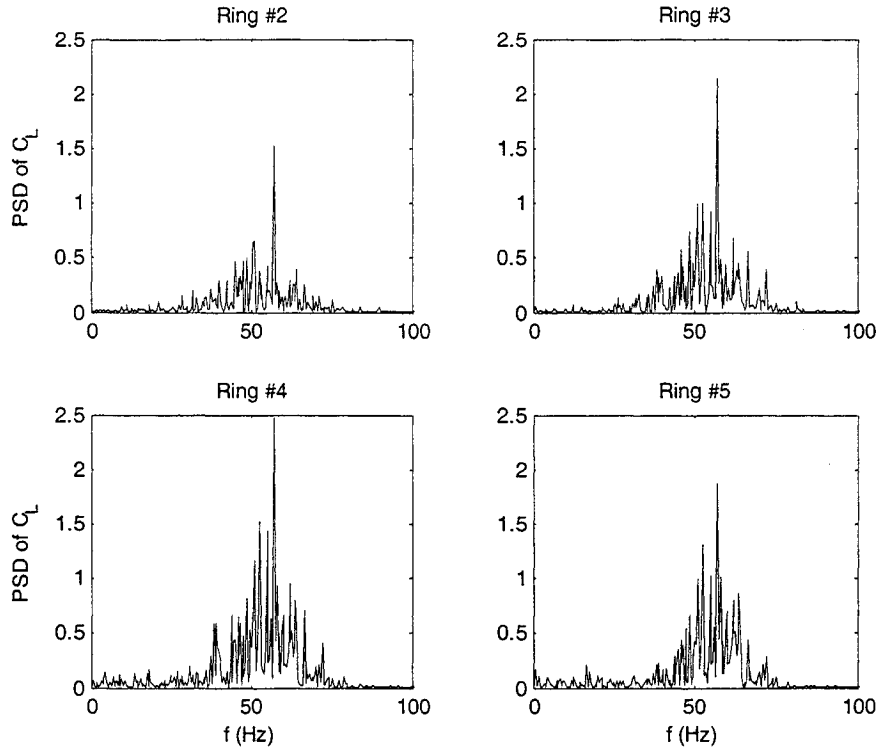

Figure 5-48: Power spectral density of C_L for U=29.4 m/s, R_e=1.76×10^5; θ=60°, β=0°, ϕ=60°, low scan rate

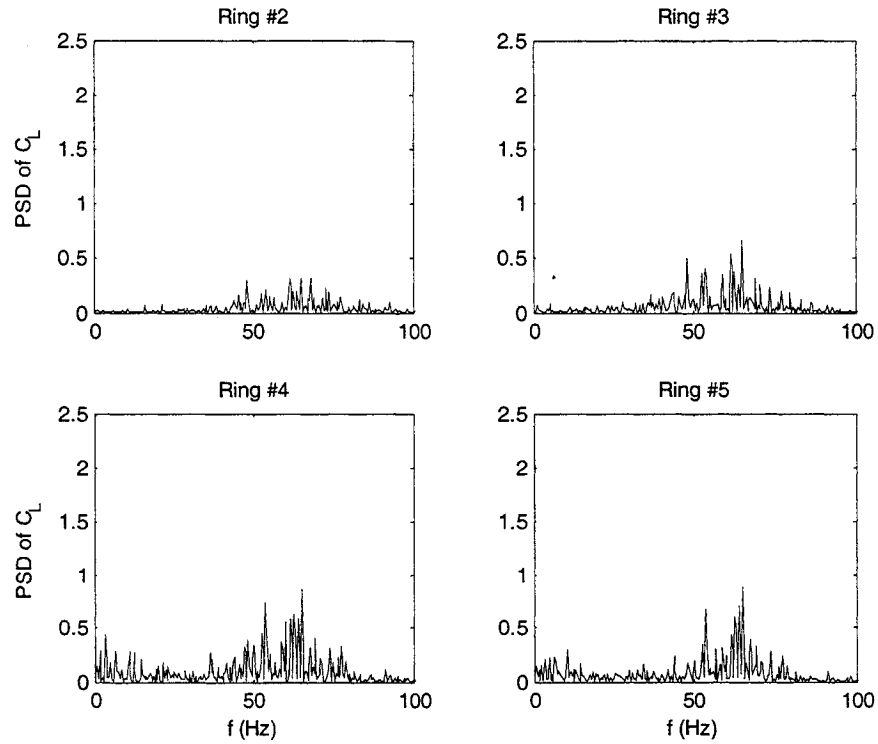

Figure 5-49: Power spectral density of C_L for U=34.6 m/s, R_e=2.04×10^5; θ=60°, β=0°, ϕ=60°, low scan rate

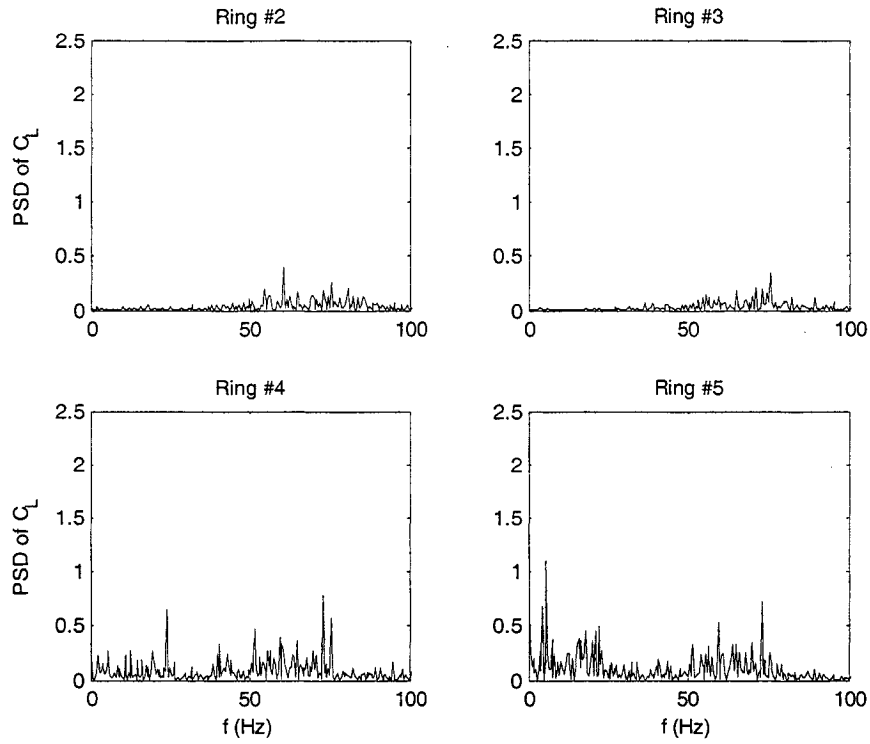

Figure 5-50: Power spectral density of C_L for U=39.7 m/s, R_e=2.33×10^5; θ=60°, β=0°, ϕ=60°, low scan rate

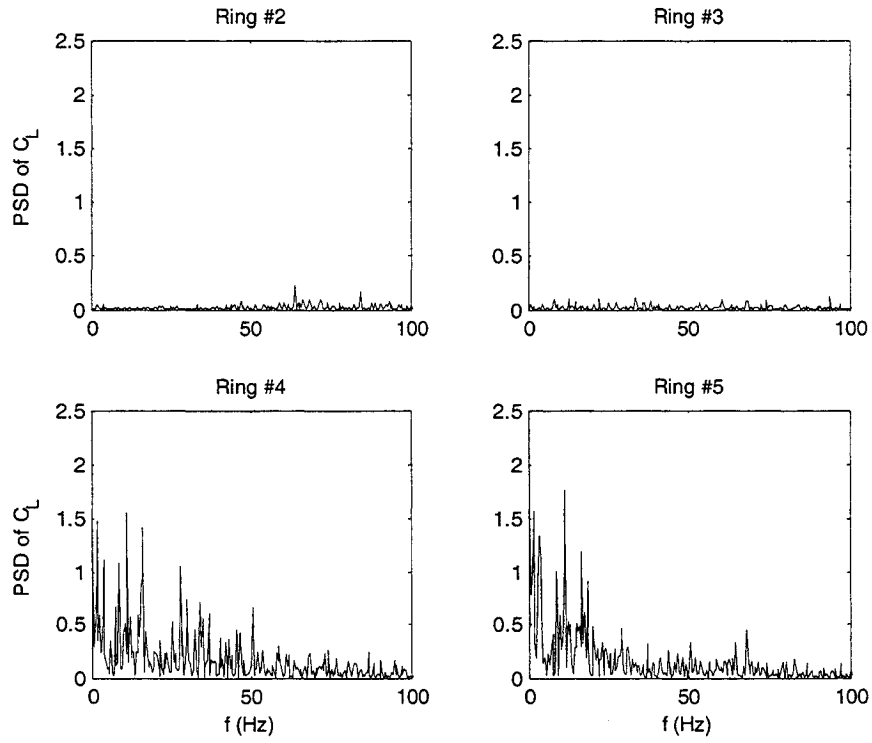

Figure 5-51: Power spectral density of C_L for U=44.6 m/s, R_e=2.63×10^5; θ=60°, β=0°, ϕ=60°, low scan rate

The pressure taps aligned along the leeward (model at 0° yaw) side of the model were intended for capturing the span-wise effects of the axial flow and axial vortex shedding—the suspected cause for high-speed vortex vibration—at the anticipated critical wind speed. The power spectral densities of the pressure coefficient for each tap along each leeward line are presented below for a wind speed of 29.4 m/s in Figure 5-52 (line 1, 180° from forward stagnation point) and Figure 5-53 (line 2, 160° from forward stagnation point), and for a wind speed of 34.6 m/s in Figure 5-54 (line 1) and Figure 5-55 (line 2). A FFT length of 512 was used.

The four or five taps located close to the roof of the wind tunnel (x/D close to 0) have obviously been adversely influenced by the proximity to the end plates and tunnel roof as indicated by the spectra, and so neglecting their contribution is prudent. For the remainder, the spectra indicate the Kármán vortex shedding frequency—particularly in Figure 5-53—but do not indicate any particularly dominant low frequency mechanism over the span. The apparent peaks occurring at low frequencies close to zero are regarded as random noise effects. For the case of the model positioned normal to the flow, similar low frequency peaks appear in the spectra for the lines of pressure taps, as presented in Figure 5-56 (line 1) and Figure 5-57 (line 2), though they do not appear in the spectra of the lift coefficient, as in Figure 5-18. Thus, no low frequency mechanism with the potential to combine with Kármán vortex shedding is apparent for this static model.

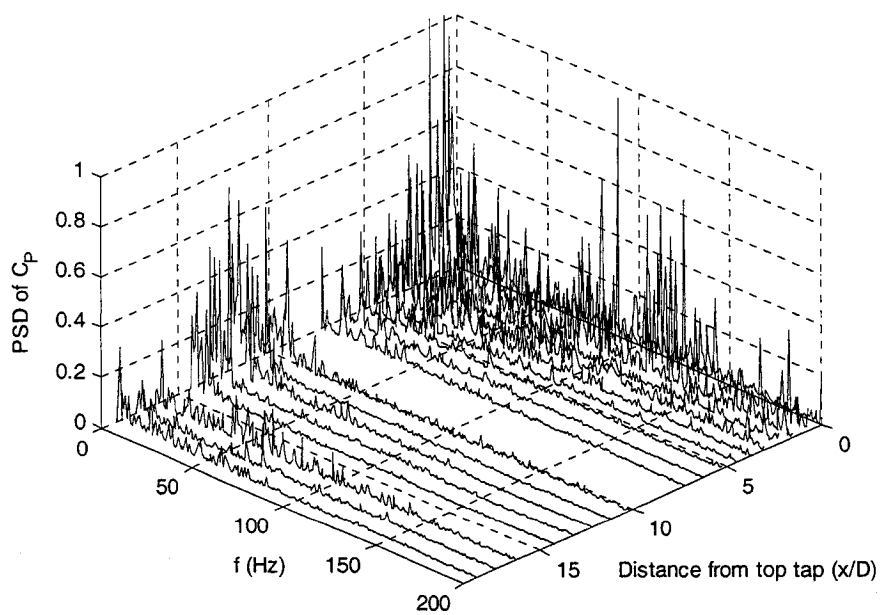

Figure 5-52: Power spectral density of pressure coefficient, C_p, along line 1 located 180° from forward stagnation point; U=29.4 m/s, R_e=1.76×10^5, θ=60°, β=0°, ϕ=60°

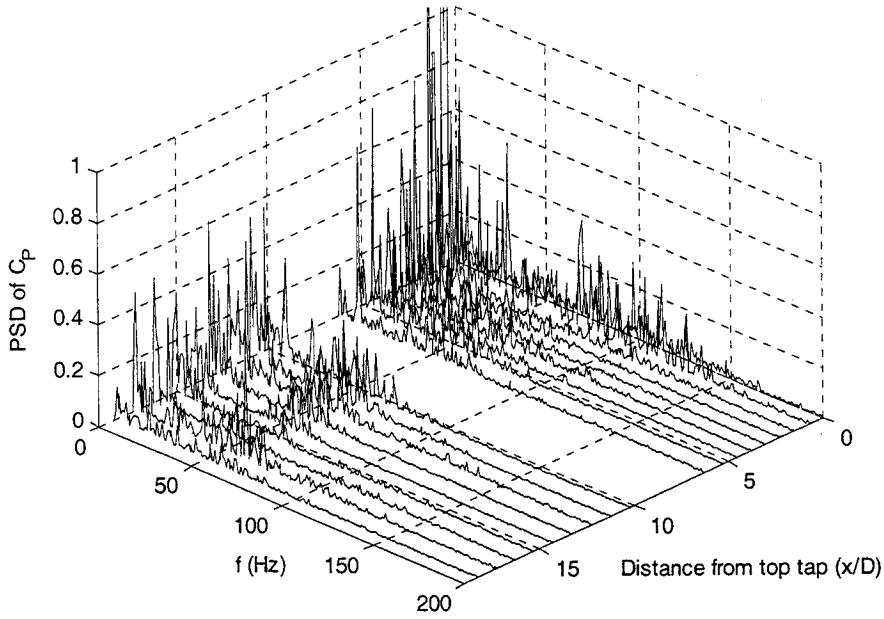

Figure 5-53: Power spectral density of pressure coefficient, C_p, along line 2 located 160° from forward stagnation point; U=29.4 m/s, R_e=1.76×10^5, θ=60°, β=0°, ϕ=60°

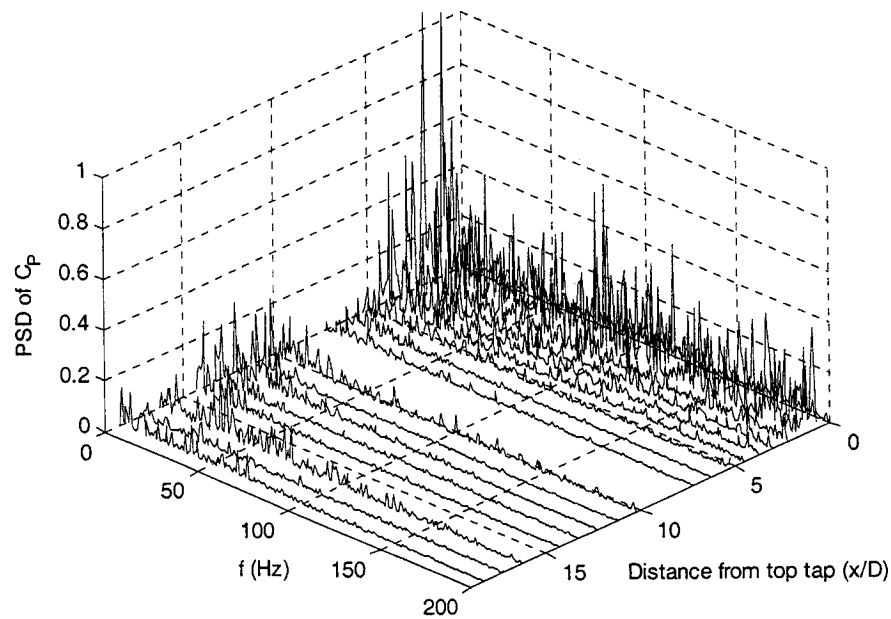

Figure 5-54: Power spectral density of pressure coefficient, C_p, along line 1; U=34.6 m/s, R_e=2.04×10^5, θ=60°, β=0°, ϕ=60°

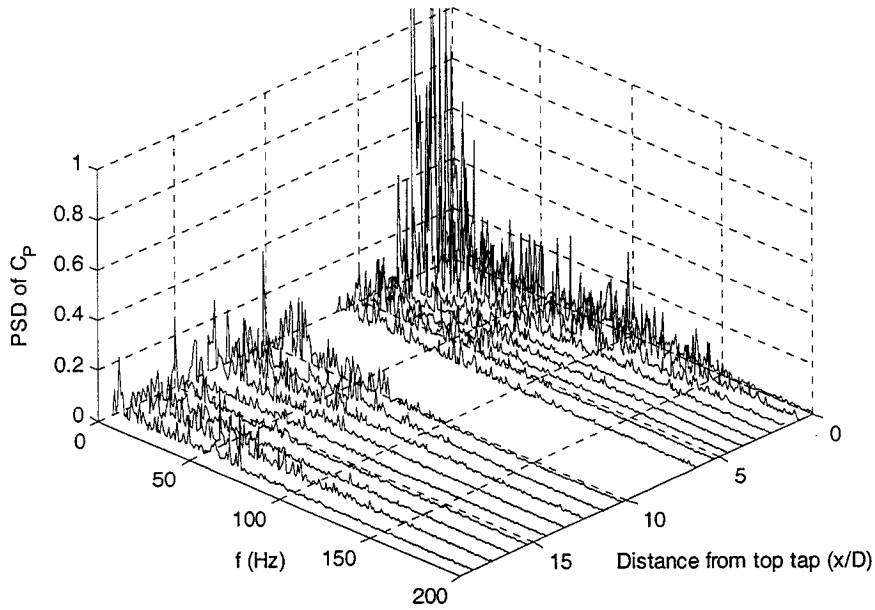

Figure 5-55: Power spectral density of pressure coefficient, C_p, along line 2; U=34.6 m/s, R_e=2.04×10^5, θ=60°, β=0°, ϕ=60°

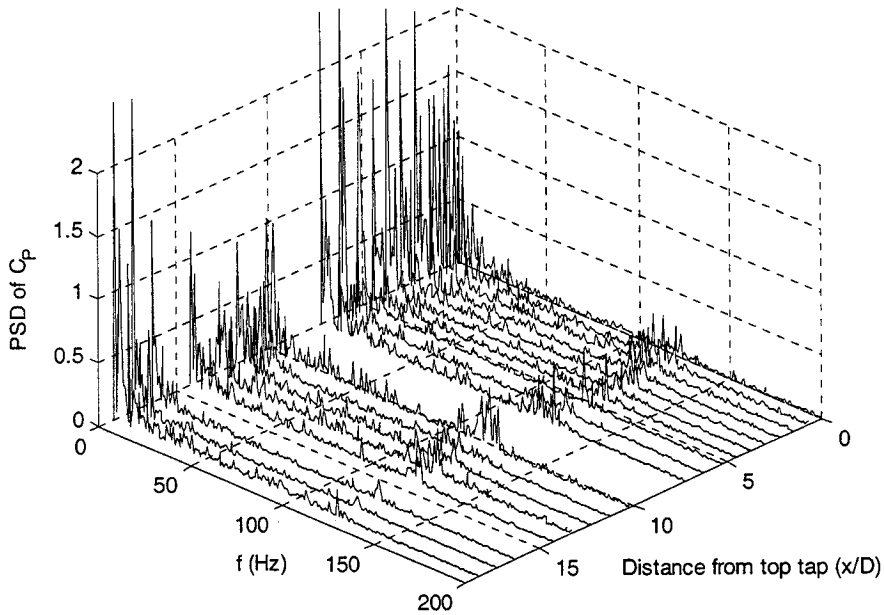

Figure 5-56: Power spectral density of pressure coefficient, C_p, along line 1; U=29.6 m/s, R_e=1.76×10^5, θ=90°, β=0°, ϕ=90°

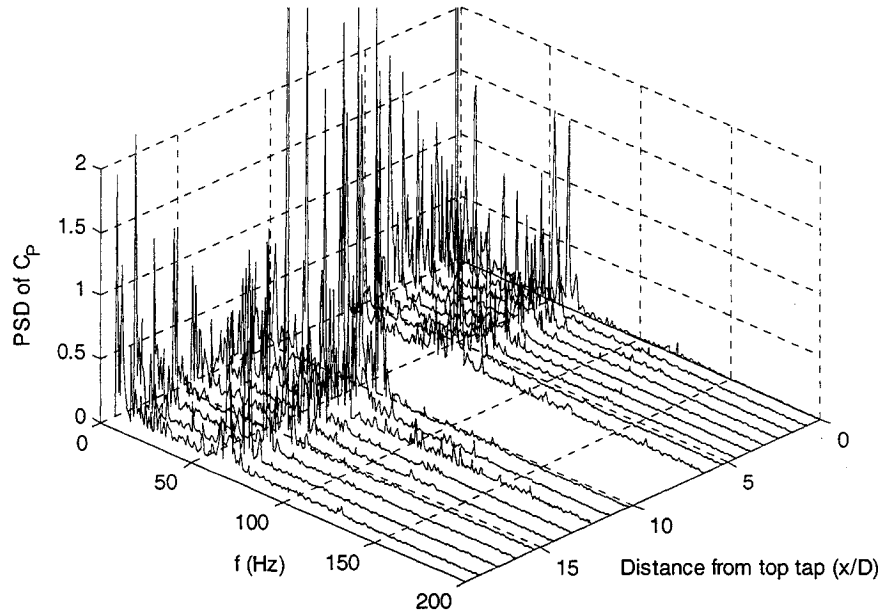

Figure 5-57: Power spectral density of pressure coefficient, C_p, along line 2; U=29.6 m/s, R_e=1.76×10^5, θ=90°, β=0°, ϕ=90°

One explanation for the lack of a dominant low frequency peak indicating a potential high-speed vortex shedding mechanism is that the critical speed at which the axial flow sheds vortices was missed by the testing regime. This is unlikely. The shedding of axial vortices would in all likelihood occur at wind speeds above and below the expected critical speed. At the critical speed the axial vortex shedding would intermittently synchronize with the Kármán vortex shedding producing the necessary vibration conditions. The lack of a dominant low frequency spectral peak indicates an absence of a low frequency mechanism—the axial flow is not apparently shedding vortices. In fact the lack of a dominant low frequency peak could be due to the lack of a generating mechanism, that being, potentially, movement of the cable, itself.

Oil film visualization confirms the above spectra results as no significant indication of an axial flow vortex-type mechanism was apparent. Refer to Appendix G.

Select testing was completed with the addition of artificial axial flow imposed along the leeward side of the model. No significant observations resulted; refer to Appendix H.

Accepting, for the moment, the theory that Kármán vortices are intermittently amplified by an axial vortex creating high-speed vortex vibrations, perhaps the motion of the cable, itself, causes the formation of an axial vortex. Wind tunnel tests in which high-speed vortex vibration has arisen have

been dynamic model tests[2], thus potentially the motion of the cable causes the shedding of axial vortices from the axial flow. Intuitively, once the cable is in motion the axial flow will follow the motion of the cable, moving back and forth slightly across the leeward side of the cable somewhat lagging behind and aligned along the effective wind direction. The motion and interaction with the airflow at the limits of the cable motion may trigger a vortex to form from the axial flow. This shedding frequency would be of the same frequency as the motion. The Kármán frequency depends upon the wind speed. At a certain wind speed, if the Kármán frequency was an appropriate multiple of the axial vortex frequency, the Kármán vortices would be intermittently enhanced. Further research is needed to determine the mechanism causing the shedding of axial vortices—if they exist—and to determine what characteristic of the flow, cylinder, or cylinder motion governs the shedding frequency.

5.6.2 Similitude Considerations

A consideration for future study of high-speed vortex excitation is the dimensional attributes of the model, airflow, and phenomenon. Consideration should be made with respect to differences between model parameters and prototype parameters. Phase 1, Setup 2A, was a full scale representation of a stay cable. The model diameter was 160 mm, the natural frequency was 1.4 Hz and the critical wind speed was 18 – 19 m/s. These parameters are directly applicable to a prototype situation. Other studies reported in the literature have been completed with models of various diameters (some as small as 20 mm (Matsumoto *et al*, 1997)) and natural frequencies. Complications due to similitude may result in findings which are not applicable to a prototype situation.

---

[2] In general, high-speed vortex vibrations have been produced in dynamic wind tunnel tests however Matsumoto *et al* (2001a) performed a wind tunnel test on a stationary model, reporting evidence of high-speed vortex formation. The conditions found for the apparent high-speed vortex formation differ significantly from those found in Phase 1 of the present study. The model was a cylinder of either 50 or 54 mm in diameter, and the apparent critical wind speed was found to be 3 m/s. In maintaining a constant Reynolds number, these parameters would translate into a wind speed of less than 1 m/s for a full scale model similar to that of Phase 1 for which vibrations occurred at a minimum wind speed of 18 m/s. Given the resulting frequency from the former study, the vibrations could be regarded as occurring at a high reduced velocity, but certainly not at a high wind speed. In addition, the limited results published by Matsumoto *et al* (2001a) include power spectra of the lift force for a non-yawed cylinder with and without end plates in place. Both plots indicate a spectral peak corresponding to the Kármán shedding frequency. The plot for the case without end plates also has an additional and significant peak at a relatively low frequency. Therefore this low frequency peak is seemingly the result of boundary conditions, and so, based on this plot, one must question the validity of the low frequency spectral peaks for the cases of a yawed cylinder without end plates. They also may simply be the result of boundary conditions.

Frequently in wind-tunnel tests, concessions must be made with respect to scale modelling and facility limitations. A long-span bridge may be reduced to a 1:250 scale model in a wind tunnel. To maintain Reynolds number similarity, the maximum test wind speed in the wind tunnel would have to be 250 times the maximum design wind speed. This is not possible. However in such a test Reynolds number effects are of secondary concern compared to other parameters such as the Froude number.

In tests such as the present study of stay cable aerodynamics, Reynolds number effects may be critical to the behaviour of a stay cable as, given typical diameters of stay cables, typical wind speeds span the critical Reynolds number range. Being an apparent frequency-based mechanism related to Kármán vortex shedding, high-speed vortex excitation also then requires consideration of the Strouhal number. To maintain Reynolds number and Strouhal number similarities, complications arise. To illustrate, consider a model of 50 mm diameter used to represent a 200 mm diameter prototype stay cable ($D_{prototype}=4D_{model}$). Maintaining Reynolds number similarity produces a wind speed ratio of:

$$\left(\frac{UD}{\nu}\right)_m = \left(\frac{UD}{\nu}\right)_p$$
$$\therefore U_m = 4U_p$$

Translating these ratios to Kármán vortex shedding frequencies which are based on the Strouhal number (Equation 2.2), the ratio of the Kármán shedding frequency of the model to that of the prototype would be:

$$\frac{f_{vm}}{f_{vp}} = \frac{\left(\frac{US_t}{D}\right)_m}{\left(\frac{US_t}{D}\right)_p} = \frac{U_m D_p}{U_p D_m} = 4\times 4 = 16$$

High-speed vortex excitation is thought to be caused by the interaction of Kármán vortices with vortices produced by axial flow in the near wake of the cable. If the frequency of the axial vortex shedding is dependent upon the natural frequency of the cable, there must be a similar increase of the model's natural frequency in order for vibrations to arise. No intermittent enhancement of the Kármán vortices by axial vortices may occur if only the Kármán shedding frequency is altered by the modelling parameters. If the shedding frequency of the axial vortex is dependent upon the diameter of the cylinder, the wind speed, or a combination of these parameters, then an appropriate dynamic model frequency must be chosen to provide conditions appropriate for vibrations to arise through an interaction of the two mechanisms—conditions that are then applicable to a prototype situation. Essentially, to model high-speed vortex vibrations accurately, a sectional full-scale model should be used, unless the parameters affecting the formation of the so-called axial vortex are determined (so that an adequate translation of prototype parameters to model parameters can be achieved).

Chapter 6: Conclusions and Recommendations

6.1 Conclusions

A wind tunnel study was performed to investigate the pressure distribution about a static circular cylinder model positioned at various angles to the flow and subjected to various wind speeds spanning the critical Reynolds number range (R_e=1×10^5 – 6×10^5). Time history pressure measurements were recorded about and along the model. The results of the analysis of these pressure measurements have provided significant insight into the characteristics of flow about an inclined cylinder, as well as into the mechanisms behind dry, inclined cable galloping and high speed vortex vibration, as these two mechanisms pertain to the cables of cable-stayed bridges.

The results of this study provide information regarding the effects of variation of the relative angle between the flow direction and the cylinder axis for flows in the region of the drag crisis (critical Reynolds number range). The drag coefficient (based on the flow speed and the drag force perpendicular to the cylinder) is generally lower for lower angles of inclination than it is for higher angles. An exception to this trend appears to occur in the range of Reynolds number indicating the so-called one-bubble regime (TrBL1) where the opposite trend is evident; that is, the drag is higher for lower angles of inclination.

The rate of reduction in drag through the drag crisis region is greater for larger relative angles up to 90° than for those angles closer to 54.7° (the lowest inclination angle tested). The drag coefficient values converge during the drag crisis regardless of the wind-cable relative angle (based only on those angles tested).

The appearance of a net lift on a circular cylinder—the TrBL1 regime—occurs at a lower flow rate for smaller relative wind-cylinder angles than for larger (closer to 90°) wind-cylinder angles. The upper bound is seemingly unaffected by varying relative angle. The magnitude of the net lift appears to be higher for higher relative angles.

For a cylinder inclined to airflow, the dominant frequency of vortex shedding is dependent upon the inclination angle, in addition to the wind speed and cylinder diameter. Inclining the cylinder to the airflow results in lower intensity vortex shedding—the magnitude of the dynamic lift force is smaller.

The Glauert-Den Hartog criterion (Equation (3.4)) is applicable to predict dry, inclined cable galloping based on results of the completed static model wind-tunnel test involving measurement of

mean lift and drag on the cable model. These results substantiate the galloping case from the Phase 1 dynamic model test, Setup 2C (model inclined to 60°, spring support rotated 54.7°, U=32 m/s).

Based on the results, an estimation was made of the mechanical damping level required to prevent galloping vibrations. This required damping estimate was found to be 0.87% of critical—more than four times higher than the typical upper limit of mechanical damping levels for existing bridge stay cables.

Conditions necessary for dry, inclined cable galloping have been found to include, but are not limited to, a relative angle between the wind and cable of approximately 60°, and a wind speed at the upper end of the critical R_e range (~3.5×10^5) in the range of the TrBL1 (one-bubble) regime.

The correlation of the dynamic lift coefficients of the rings 2 to 5 peaks under the same conditions at which the Glauert-Den Hartog criterion predicts galloping behaviour. The strong correlation occurs over a large range of frequencies, but is greater toward lower frequencies.

The apparent necessary conditions for dry, inclined cable galloping indicate that Setup 2A from Phase 1 (model inclined to 60°, no spring support rotation) should also have exhibited galloping at approximately 32 m/s. The absence of galloping could have been simply the result of support conditions or flow conditions, to which vibration mechanisms have been observed to be quite sensitive. Satisfaction of the Glauert-Den Hartog criterion does not necessarily result in galloping.

Unlike the classical definition of galloping, this form of galloping instability appears to be velocity restricted based on the static model test results.

The galloping vibrations found in Phase 1 and confirmed by Phase 2 may not be caused by the same mechanism as those found by other researchers. The tests completed at the NRC wind tunnels found galloping to occur at a significantly higher wind speed than previous studies—a wind speed that falls into the high end of the critical range (TrBL1 regime). The results from previous studies found no upper velocity limit and the onset velocity apparently fell into the pre-critical flow range.

The pressure data from this study indicates that the mechanism causing the limited amplitude vibration for Setup 2A of Phase 1 cannot be predicted by the Glauert-Den Hartog criterion and so confirms two distinct vibration phenomena—galloping and high-speed vortex vibration of a dry, inclined cable. The pressure data contains no clear or significant indication of the existence of a relatively low frequency mechanism—such as the possible shedding of vortices from the axial flow—corresponding to the conditions under which vibrations occurred for Setup 2A of Phase 1. This

absence of a low frequency mechanism perhaps indicates that actual motion of the model is required to trigger axial vortex formation.

Unless one uses a full-scale cable model, similitude in Reynolds number as well as Strouhal number must be considered for a dynamic test investigating a vortex shedding-based aerodynamic mechanism.

6.2 Recommendations for Future Study

Research concerning flow about an inclined or yawed circular cylinder has usually involved specific applications rather than the fundamental concept, and as a result comprehensive information is quite limited. Further study concerning the fundamental concepts of flow about an inclined cylinder is warranted. Particularly, a full examination of the aerodynamics of inclined cylinders throughout the entire critical Reynolds number range is advised.

Several research studies have touched on, to varying extents, dry, inclined cable galloping and high-speed vortex excitation, however few have expressly focussed on them. The great majority of these studies focussed on rain-wind vibration, and galloping or high-speed vortex vibration arose unexpectedly. In addition to further testing focussed on these two phenomena, a thorough compilation of all existing test data from the various researchers would aid tremendously in the definition of the required conditions for galloping or high-speed vortex vibration. Such data would include specific information concerning:

- wind-tunnel characteristics – size, level of turbulence, etc.
- model characteristics – size, static or dynamic (frequency), roughness, etc.
- specific conditions under which the phenomenon occurred – wind speed/Reynolds number, relevant angles between wind and cable, direction of movement (for dynamic tests), etc.

At present, published results do not necessarily present all of the above-mentioned data pertaining to the galloping or high-speed vortex vibration incidents, and thus defining conditions based on an aggregate of data is not possible at this time.

Particular attention should be given in the future to Reynolds number effects in the examination of wind-induced vibration of stay cables. In addition, when modelling vortex-induced mechanisms, care must be taken in choosing an appropriate vibration frequency when not using a full-scale model. Until the actual mechanism causing the so-called axial vortex is determined, full-scale sectional dynamic models are recommended to achieve results directly applicable to prototype situations.

A logical third phase to this study would be the combination of the first two; that is, a dynamic model test recording pressure variations about the cable model for comparison with the static test. Such a comparison could reveal how the pressure variations differ between the static and dynamic cases.

Perhaps most importantly, as natural wind contains varying degrees of turbulence, the effect of turbulence should be further examined, particularly with respect to the apparent critical conditions for galloping vibrations.

References

Bendat, J. S., A. G. Piersol. (1986), ***Random Data: Analysis and Measurement Procedures***, 2nd ed., John Wiley & Sons, New York.

Blevins, Robert (1977), ***Flow-induced Vibration***, Van Nostrand Reinhold Company, New York.

Bursnall, W. J., L.K. Loftin, Jr. (1951), ***Experimental Investigation of the Pressure Distribution about a Yawed Circular Cylinder in the Critical Reynolds Number Range***, Technical Note 2463, National Advisory Committee for Aeronautics, Washington.

Cheng, S. H., H. Tanaka (2001), ***Inclined Cable Aerodynamics***, Engineering Research Report for RWDI, No. 00-166, University of Ottawa.

Cheng, S., P. A. Irwin, J. B. Jakobson, J. Lankin, G. L. Larose, M. G. Savage, H. Tanaka, C. Zurell (2003), ***Divergent Motion of Cables Exposed to Skewed Wind***, Submitted to the 5th Intl. Symp. on Cable Dynamics, Santa Margherita Ligure.

Den Hartog, J. P. (1956), ***Mechanical Vibrations***, 4th ed., McGraw-Hill Book Company, New York.

ESDU (1980), ***Mean forces, pressures and flow field velocities for circular cylindrical structures: single cylinder with two-dimensional flow***. Engineering Sciences Data Item No. 80025, London, October 1980, with Amendments A to C, June 1986.

ESDU (1980), ***Blockage corrections for bluff bodies in confined flows***, Engineering Science Data Item No. 80024, London, November 1980.

Fargier, C., J. Stubler (2001), ***Improved Cable Damping with Elastomeric Injection Compound***, Proc. of the 4th Intl. Symp. on Cable Dynamics, Montreal, p271-275.

Fujino, Y., M. Abe, and T. Le Diouron (2001), ***Passive and Semi-active Control of Self-Excited Oscillations by Transfer of Internal Energy to Higher Modes of Vibration***, Proc. of the 4th Intl. Symp. on Cable Dynamics, Montreal, p265-270.

Gimsing, N. (1983), ***Cable Supported Bridges – Concept and Design***, John Wiley & Sons, Chichester.

Goldstein, S. (ed.) (1965), ***Modern Developments in Fluid Dynamics***, Volumes 1 and 2, Dover Publications Inc. New York.

Hikami, Y., N. Shiraishi (1988), ***Rain-wind Vibrations of Cables in Cable Stayed Bridges***, Journal of Wind Engineering and Industrial Aerodynamics (JWEIA), 29, p409-418.

Hjorth-Hansen, E., E. Strommen, F. Myrvoll, C. Hansvold, and R. Ronnebrant (2001), ***Performance of a Friction Damping Device for the Cables on Uddevalla Cable-Stayed Bridge***, Proc. of the 4th Intl. Symp. on Cable Dynamics, Montreal, p179-186.

Honda, A., T. Yamanaka, T. Fujiwara, and T. Saito (1995), ***Wind-tunnel Test on Rain-Induced Vibration of the Stay-Cable***, Proc. of the Intl. Symp. on Cable Dynamics, Liège, p255-262.

Irwin, P. (1997), ***Wind Vibrations of Cables on Cable-Stayed Bridges***, Proc. of the Structures Congress XV, Portland, p.383-387.

Irwin, P., N. Alca, and N. Telang (1999), ***Wind Induced Stay Cable Oscillations – A Case Study***, Proc. of the 3rd Intl. Symp. on Cable Dynamics, Trondheim, p171-176.

Kovacs, I. E. Strommen, and E. Hjorth-Hansen (1999), ***Damping Devices Against Cable Oscillations on Sunningesund Bridge***, Proc. of the 3rd Intl. Symp. on Cable Dynamics, Trondheim, p145-150.

Lalanne, C. (2002), ***Mechanical Vibration & Shock Volume III: Random Vibration***, Hermes Penton Ltd.

Larose, G. L., S. J. Zan (2001), ***The Aerodynamic Forces on the Stay Cables of Cable-Stayed Bridges in the Critical Reynolds Number Range***, Proc. of the 4th Intl. Symp. on Cable Dynamics, Montreal, p77-84.

Larose, G. L., M. G. Savage, and J. Bogunović Jakobsen (2003), ***Wind Tunnel Experiments on an Inclined and Yawed Circular Cylinder in the Critical Reynolds Number Range***. Proceedings of the 11th Intl. Conf. on Wind Engineering, Lubbock, Texas.

Mahar, P. S., P. K. Pande, and M. E. Akbari (1985), ***Aerodynamic Forces on Rigid Inclined Bars***, Proc. of the Aisa-Pacific Symposium on Wind Engineering, Roorkee, India, p155-165.

Matsumoto, M., C. W. Knisely, N. Shiraishi, M. Kitazawa, and T. Saito (1989a), ***Inclined-Cable Aerodynamics***, Proceedings of the ASCE Structural Congress, San Francisco, May 1989, p81-90.

Matsumoto, M., K. Yokoyama, T. Miyata, Y. Fujino, and H. Yamaguchi (1989b), ***Wind-induced Cable Vibration of Cable-stayed Bridges in Japan***, Proc. of the Canada-Japan Joint Workshop on Bridge Aerodynamics, Ottawa, p101-110.

Matsumoto, M., N. Shiraishi, M. Kitazawa, C. Knisely, H. Shirato, Y. Kim, and M. Tsujii (1990), ***Aerodynamic Behaviours of Inclined Circular Cylinders – Cable Aerodynamics***, Journal of Wind Engineering and Industrial Aerodynamics (JWEIA), 33, p63-72.

Matsumoto, M., N. Shiraishi, and H. Shirato (1992), ***Rain-wind Induced Vibration of Cables of Cable-stayed Bridges***, JWEIA 41-44, p2011-2022.

Matsumoto, M., Y. Hikami, and M. Kitazawa (1994), ***Cable Vibration and its Aerodynamic/ Mechanical Control***, Proc. of the Intl. Conf. on Cable-stayed and Suspension Bridges (AFPC), Deauville, Volume 2, p439-452.

Matsumoto, M., M. Yamagishi, J. Aoki, and N. Shiraishi (1995a), ***Various Mechanisms of Inclined Cable Aerodynamics***, Proc. of the 9th ICWE, New Delhi, Volume 2, p759-770.

Matsumoto, M., H. Ishizaki, M. Kitazawa, J. Aoki, and D. Fujii (1995b), ***Cable Aerodynamics and Its Stabilization***, Proc. of the Intl. Symp. on Cable Dynamics, Liège, 1995, p289-296.

Matsumoto, M., Y. Shigemura, Y. Daito, and T. Kanamura (1997), ***High Speed Vortex Shedding Vibration of Inclined Cables***, Proc. of the 2nd Intl. Symp. on Cable Dynamics, Tokyo, p27-35.

Matsumoto, M. (1998), ***Observed Behaviour of Prototype Cable Vibration and Its Generation Mechanism***, Bridge Aerodynamics, Larsen & Esdahl (eds.), Balkema, Rotterdam, 1998, p189-211.

Matsumoto, M., T. Yagi, and D. Tsushima (1999), ***Inclined Cable Aerodynamics – Velocity Restricted Response at High Reduced Velocity***, Proc. of the 3rd Intl. Symp. on Cable Dynamics, Trondheim, p91-96.

Matsumoto, M. (1999), ***Wind Induced Vibration Control of Inclined Cable***, Proc. of the 3rd Intl. Symp. on Cable Dynamics, Trondheim, p123-132.

Matsumoto, M., T. Yagi, D. Tsushima, and Y. Shigemura (2001a), ***Vortex-induced Vibration of Inclined Cables at High Wind Velocity***, Wind Engineering into the 21st Century, Larsen, Larose & Livesey (eds.) Balkema, Rotterdam, 1999, Volume 2, p979-986. Also published under the title: ***Vortex-Induced Cable Vibration of Cable-Stayed Bridges at High Reduced Wind Velocity***, JWEIA 89, p633-647.

Matsumoto, M., T. Yagi, M. Goto, and S. Sakai (2001b), ***Cable Aerodynamic Vibration at High Reduced Velocity***, Proc. of the 4th Intl. Symp. on Cable Dynamics, Montreal, p43-50.

Matsumoto, M., H. Shirato, T. Yagi, N. P. Jones, and T. Hayashi (2001c), ***Field Observation System of Cable Aerodynamics in Natural Wind***, Proc. of the 4th Intl. Symp. on Cable Dynamics, Montreal, p219-225.

Melbourne, W. H. (1982), ***Wind Tunnel Blockage Effects and Corrections***, Wind Tunnel Modeling for Civil Engineering Applications, T. A Reinhold (ed.), Cambridge University Press, Cambridge, p197-216.

Miyata, T., H. Yamada, and T. Hojo (1994), ***Aerodynamic Response of PE Stay Cables with Pattern-Indented Surface***, Proc. of the Intl. Conf. on Cable-stayed and Suspension Bridges (AFPC), Deauville, Volume 2, p515-522.

Novak, M., H. Tanaka (1974), ***Effect of Turbulence on Galloping Instability***, Journal of the Engineering Mechanics Division, ASCE, Wol. 100, No. EM1, Proc. Paper 10338, p27-47.

Ostenfeld, K., A. Larsen (1992), ***Bridge Engineering and Aerodynamics***, Aerodynamics of Large Bridges, Balkema, Rotterdam, p3-22.

Ruscheweyh, H. P. (1999a), ***Vortex-induced Vibrations – Physical Background, Risk and Reliability of Estimations***, Wind Engineering into the 21st Century, Larsen, Larose & Livesey (eds.) Balkema, Rotterdam, Volume 1, p545-549.

Ruscheweyh, H. P. (1999b), ***The Mechanism of Rain-wind-induced Vibration***, Wind Engineering into the 21st Century, Larsen, Larose & Livesey (eds.) Balkema, Rotterdam, Volume 2, p1041-1047.

Saito, T., M. Matsumoto, and M. Kitazawa (1994), ***Rain-wind Excitation of Cables on Cable-stayed Higashi-Kobe Bridge and Cable Vibration Control***, Proc. of the Intl. Conf. on Cable-stayed and Suspension Bridges (AFPC), Deauville, Volume 2, p507-514.

Sauter, D., Qian Liu, P. Hagedorn, and A. Rahman (2001), ***On the Damping of Vortex-Excited Vibrations of Stay-Cables***, Proc. Of the 4th Intl. Symp. on Cable Dynamics, Montreal, p277-284.

Simiu, E., R. H. Scanlan (1996), ***Wind Effects of Structures: Fundamentals and Applications to Design***, John Wiley & Sons, New York.

Stubler, J., P. Ladret, JB. Domage, and M. Peltier (1999), ***Bridge Stay Cable Vibration: Phenomena, Criteria and Damper Technology***, Proc. of the 3rd Intl. Symp. on Cable Dynamics, Trondheim, p163-170.

Verwiebe, C. (1998), ***Exciting Mechanisms of Rain-Wind-Induced Vibrations***, Structural Engineering International, 2/98, p112-117.

Virlogeux, M. (1995), ***Design of Cables for Cable-Stayed Bridges: The Example of the Normandie Bridge***, Proc. of the Intl. Symp. on Cable Dynamics, Liège, p13-31.

Virlogeux, M. (1998), ***Cable Vibrations in Cable-Stayed Bridges***, Bridge Aerodynamics, Larsen & Esdahl (eds.), Balkema, Rotterdam, p213-233.

West, G. S., C. J. Apelt (1981), ***Blockage and Aspect Ratio Effects on Flow Past a Circular Cylinder for $10^4<R<10^5$***, Research Report No. CE29, Department of Civil Engineering, University of Queensland, Australia, October 1981.

Wianecki, J. (1979), ***Cables Wind Excited Vibrations of Cable-stayed Bridge***, Proc. of the 5th Intl. Conf. On Wind Engineering, Fort Collins, Volume 2, p1381-1393.

Wootton, L. R., C. Scruton, ***Aerodynamic stability***, National Physical Laboratory, Teddington.

Yamaguchi, H., Y. Fujino (1998), ***Stayed Cable Dynamics and its Vibration Control***, Bridge Aerodynamics, Larsen & Esdahl (eds.), Balkema, Rotterdam, p235-253.

Yoshimura, T., M. G. Savage, and H. Tanaka (1995), ***Wind-induced Vibrations of Bridge Stay-cables***, Proc. of the Intl. Symp. on Cable Dynamics, Liège, p437-444.

Zdravkovich, M. M. (1997a), ***Flow Around Circular Cylinders, Volume 1: Fundamentals***, Oxford University Press, Oxford.

Zdravkovich, M. M. (1997b), ***Flow Around Circular Cylinders, Volume 2: Applications***, Oxford University Press, Oxford, 1997.

The following conference papers were generated all or in part from this wind tunnel study:

Aerodynamic Behaviour of Cables Against Skew Wind
by S. Cheng, P. A. Irwin, J. B. Jakobsen, J. Lankin, G. L. Larose, M. G. Savage, H. Tanaka, C. Zurell. Proceedings of the 11th Intl. Conf. on Wind Engineering, Lubbock, Texas, 2003, p301-308.

Divergent Motion of Cables Exposed to Skewed Wind
by S. Cheng, P. A. Irwin, J. B. Jakobsen, J. Lankin, G. L. Larose, M. G. Savage, H. Tanaka, C. Zurell. Submitted to the 5th Intl. Symp. on Cable Dynamics, Santa Margherita Ligure, Italy, 2003.

Instantaneous Wind Forces on Inclined Circular Cylinders in Critical Reynolds Number Range
by J. Bogunović Jakobsen, G. L. Larose, and M. G. Savage, Proceedings of the 11th Intl. Conf. on Wind Engineering, Lubbock, Texas, 2003, p.2165-2173.

Wind Tunnel Experiments on an Inclined and Yawed Circular Cylinder in the Critical Reynolds Number Range
by G. L. Larose, M. G. Savage and J. Bogunović Jakobsen, Proceedings of the 11th Intl. Conf. on Wind Engineering, Lubbock, Texas, 2003, p.1705-1712.

Wind Tunnel Experiments on an Inclined and Yawed Stay Cable Model in the Critical Reynolds Number Range
by G. L. Larose, M. G. Savage and J. Bogunović Jakobsen, Submitted to the 5th Intl. Symp. on Cable Dynamics, Santa Margherita Ligure, Italy, 2003.

Appendix A: Wind-Cable Angle Relationships

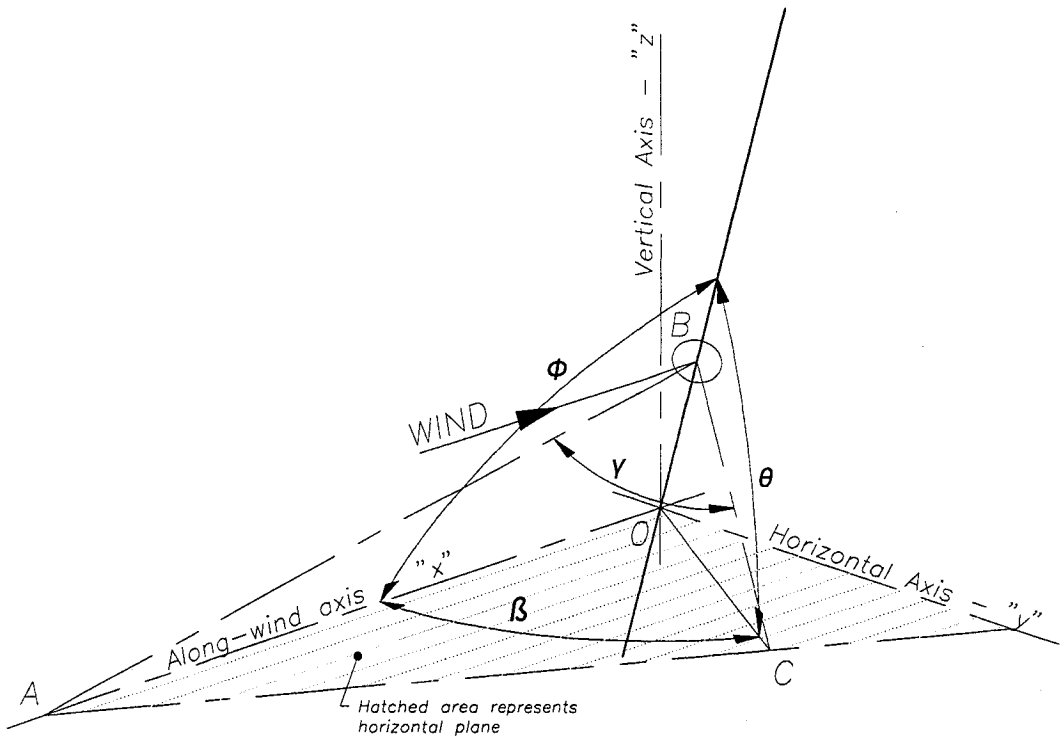

Figure A-1: Cable-Wind Angle Relationships

Pertaining to Figure A-1, above:

- $\angle AOC$ is a horizontal plane
- $\angle AOB$ is a plane containing the direction of the wind and the axis of the cable
- COB is a vertical plane containing the cable axis
- OC is the horizontal projection of the cable axis
- $AB \perp OB$
- $CB \perp OB$
- $OC \perp AC$
- Angle θ is the angle of vertical inclination between the cable axis, OB, and the horizontal plane, $\angle AOC$
- Angle β is the horizontal yaw angle between the wind direction, AO, and the horizontal projection of the cable axis, OC
- Angle Φ is the angle between the cable axis, OB, and the wind direction, AO
- Angle γ is the angle between plane $\angle AOB$ and plane COB

Since: $$\cos\theta = \frac{OB}{OC}$$

and, $$\cos\beta = \frac{OC}{AO}$$

then, $$\cos\theta\cos\beta = \frac{OB}{OC}\frac{OC}{AO}$$

$$\therefore \cos\theta\cos\beta = \frac{OB}{AO} = \cos\phi$$

Therefore:

$$\boxed{\cos\phi = \cos\theta\cos\beta}$$

Since: $$\sin\theta = \frac{BC}{OC}$$

and, $$\tan\beta = \frac{AC}{OC}$$

$$\frac{\tan\beta}{\sin\theta} = \frac{AC}{OC}\frac{OC}{BC}$$

$$\therefore \frac{\tan\beta}{\sin\theta} = \frac{AC}{BC} = \tan\gamma$$

Therefore:

$$\boxed{\tan\gamma = \frac{\tan\beta}{\sin\theta}}$$

exception: when $\beta=90°$, $\gamma=90°$

Appendix B: Wind Tunnel Test Log

Speeds 1: 20,30,40,50,55,60,65,70,75,80,90,99
Speeds 2: 20,30,40,50,52,55,57,60,65,70,75,80,90,99
Speeds 3: 30,40,45
Speeds 4: 15,20,30,40,45,50,55,60,65,70,80,90,99
Speeds 5: 15,20,30,40,42,45,47,50,55,60,65,70,80,90,99
Speeds 6: 20,30,45,55
Speeds 7: 20,30,45,55,62

Angles 1: 0.00,0.25,0.50,0.75,1.0,2.0,3.0,5.0,10.0,15.0,20.0,30.0,45.0,60.0,75.0,90.0,105.0,120.0
Angles 2: 0.00,0.50,1.0,3.0,5.0,10.0,15.0,20.0,25.0,27.0,28.0,29.0,29.25,29.5,29.75,30.0,30.25,30.5,30.75,31.0,32.0,33.0,35.0,40.0,45.0,60.0,75.0,90.0,105.0,120.0 (400 h
Angles 2(a): 0.00,0.50,1.0,3.0,5.0,10.0,20.0,25.0,27.0,29.0,29.5,30.0,30.5,31.0,33.0,35.0,40.0,60.0,90.0,120.0 (1200 hz)
Angles 3: 20.0,25.0,27.0,29.0,29.5,30.0,30.5,31.0,33.0,35.0,40.0
Angles 4: 29.0,29.5,30.0,30.5,31.0

Date	Case No.	HYSCAN Filename	Tare Filename	Sampling Rate (Hz)	Sampling Time (s)	Inclination (deg.)	Yaw (deg.)	Wind speed (m/s)	Comments
March 21, 2002	1	750_010	750_009	1200	60	90	0	20	scap
March 21, 2002	1	750_012	750_011	1200	60	90	0	Speeds 1	low frequency noise at 30m/s
March 21, 2002	1	750_014	750_013	1200	60	90	45	Speeds 1	
March 21, 2002	1	750_016	750_015	400	120	90	0	Speeds 1	Lower section (rings 3-5) rotated 23.5deg. c-w. upper section (rings 1,2) rotated 43.5deg. c-w.
March 22, 2002	1	750_018	750_017	400	120	90	0	Speeds 2	model realigned - retest of run 750_016 with added speeds of 52m/s and 57m/s
March 22, 2002	1	750_020	750_019	1200	60	90	-45	Speeds 3	
March 25, 2002	1	750_027	750_026	1200	60	90	-90	Speeds 3	
March 25, 2002	2	750_029	750_028	1200	60	60	0	Speeds 4	without end plates; leeward tap of first ring is 199mm, measured vertically from tunnel roof
March 26, 2002	2	750_031	750_030	1200	60	60	0	Speeds 5	with end plates 100mm from tunnel roof and floor
March 26, 2002	2	750_033	750_032	1200	60	60	Angles 1	15 m/s	with end plates
March 26, 2002	2	750_035	750_034	1200	60	60	Angles 1	20 m/s	with end plates
March 26, 2002	2	750_037	750_036	1200	60	60	Angles 1	30 m/s	with end plates
March 26, 2002	2	750_039	750_038	1200	60	60	Angles 1	40 m/s	with end plates
March 26, 2002	2	750_041	750_040	1200	60	60	Angles 1	45 m/s	with end plates
March 26, 2002	2	750_043	750_042	1200	60	60	Angles 1	50 m/s	with end plates
March 26, 2002	2	750_045	750_044	1200	60	60	Angles 1	55 m/s	with end plates
March 26, 2002	2	750_047	750_046	1200	60	60	Angles 1	65 m/s	with end plates
March 26, 2002	2(b)	750_050	750_048	400	120	60	Angles 1	15 m/s	with end plates (note: run 750_049 was aborted)
March 27, 2002	2(b)	750_052	750_051	400	120	60	Angles 1	20 m/s	with end plates
March 27, 2002	2(b)	750_054	750_053	400	120	60	Angles 1	25 m/s	with end plates; rattling sound heard when model was yawed 75, 90, 105deg. Stopped at 120deg. - a counterweight on the force balance was vibrating
March 27, 2002	2(b)	750_056	750_055	400	120	60	Angles 1	30 m/s	with end plates
March 27, 2002	2(b)	750_058	750_057	400	120	60	Angles 1	35 m/s	with end plates
March 27, 2002	2(b)	750_060	750_059	400	120	60	Angles 1	40 m/s	with end plates
March 27, 2002	2(b)	750_062	750_061	400	60	60	Angles 1	45 m/s	with end plates (changed to 60 sec sample time)
March 27, 2002	2(b)	750_064	750_063	400	60	60	Angles 1	50 m/s	with end plates
March 27, 2002	2(b)	750_067	750_066	400	60	60	Angles 1	55 m/s	with end plates
March 27, 2002	2(b)	750_069	750_068	400	60	60	Angles 1	65 m/s	with end plates
March 28, 2002	3	750_071	750_070	1200	60	54.7	Angle 2(a)	15 m/s	with end plates
March 28, 2002	3	750_073	750_072	1200	60	54.7	Angle 2(a)	20 m/s	with end plates
March 28, 2002	3	750_075	750_074	1200	60	54.7	Angle 2(a)	25 m/s	with end plates
April 2, 2002	3	750_077	750_076	1200	60	54.7	Angle 2(a)	30 m/s	with end plates
April 2, 2002	3	750_079	750_078	1200	60	54.7	Angle 2(a)	35 m/s	with end plates
April 2, 2002	3	750_081	750_080	1200	60	54.7	Angle 2(a)	40 m/s	with end plates
April 2, 2002	3	750_083	750_082	1200	60	54.7	Angle 2(a)	45 m/s	with end plates
April 2, 2002	3	750_085	750_084	1200	60	54.7	Angle 2(a)	50 m/s	with end plates
April 2, 2002	3	750_087	750_086	1200	60	54.7	Angle 2(a)	55 m/s	with end plates
April 2, 2002	3	750_089	750_088	1200	60	54.7	Angle 2(a)	65 m/s	with end plates
April 2, 2002	4	750_091	750_090	400	120	54.7	Angle 2	15 m/s	with end plates
April 2, 2002	4	750_093	750_092	400	120	54.7	Angle 2	20 m/s	with end plates
April 3, 2002	4	750_095	750_094	400	120	54.7	Angle 2	25 m/s	with end plates
April 3, 2002	4	750_097	750_096	400	120	54.7	Angle 2	30 m/s	with end plates
April 3, 2002	4	750_099	750_098	400	120	54.7	Angle 2	35 m/s	with end plates
April 3, 2002	4	750_101	750_100	400	120	54.7	Angle 2	40 m/s	with end plates
April 4, 2002	4	750_103	750_102	400	120	54.7	Angle 2	45 m/s	with end plates
April 4, 2002	4	750_105	750_104	400	120	54.7	Angle 2	50 m/s	with end plates
April 4, 2002	4	750_107	750_106	400	120	54.7	Angle 2	55 m/s	with end plates
April 4, 2002	4	750_109	750_108	400	120	54.7	Angle 2	60 m/s	with end plates
April 4, 2002	4	750_111	750_110	1200	60	54.7	Angle 3	52.5 m/s	with end plates
April 4, 2002	4	750_113	750_112	1200	60	54.7	Angle 3	57.5 m/s	with end plates
April 4, 2002	4	750_115	750_114	1200	60	54.7	Angle 3	60 m/s	with end plates
April 4, 2002	4	750_117	750_116	1200	60	54.7	Angle 3	62.5 m/s	with end plates

April 4, 2002	4	750_119	750_118	1200	60	54.7	0	speed 6	without end plates
April 4, 2002	4	750_120	750_118	1200	60	54.7	30	speed 6	without end plates, (note no tare taken for this run)
April 4, 2002	5	750_122	750_121	400	60	54.7	30	30 m/s	without end plates, vary axial flow: 16,14,12,10,8,6,4 psi, (air aligned with dimple, ie. Pos. 1)
April 5, 2002	5	750_124	750_123	400	60	54.7	0	Speeds 6	without end plates, axial flow: 14 psi, 10 psi, 6 psi at each wind speed (air aligned with dimple, ie. Pos. 1)
April 15,2002		750_126	750_125	400	120	54.7	0	Speeds 7	without end plates, top - 4psi and 4m/s, suction - 6m/s with two 1.5in dia.hose (both located along dimple line)
April 15,2002		750_128	750_127	400	120	54.7	30	Speeds 7	without end plates, top - 4psi and 4m/s, suction - 6m/s with two 1.5in dia.hose (both located along dimple line)
April 15,2002		750_130	750_129	400	60	54.7	Angle 3	61	with end plates
April 15,2002		750_132	750_131	400	60	54.7	Angle 3	62	with end plates
April 15,2002		750_134	750_133	400	60	54.7	Angle 3	68	with end plates
April 15,2002		750_136	750_135	400	60	54.7	Angle 3	64	with end plates

Appendix C: Sum of Drag Coefficient and the Slope of the Lift Coefficient – High Scan Rate

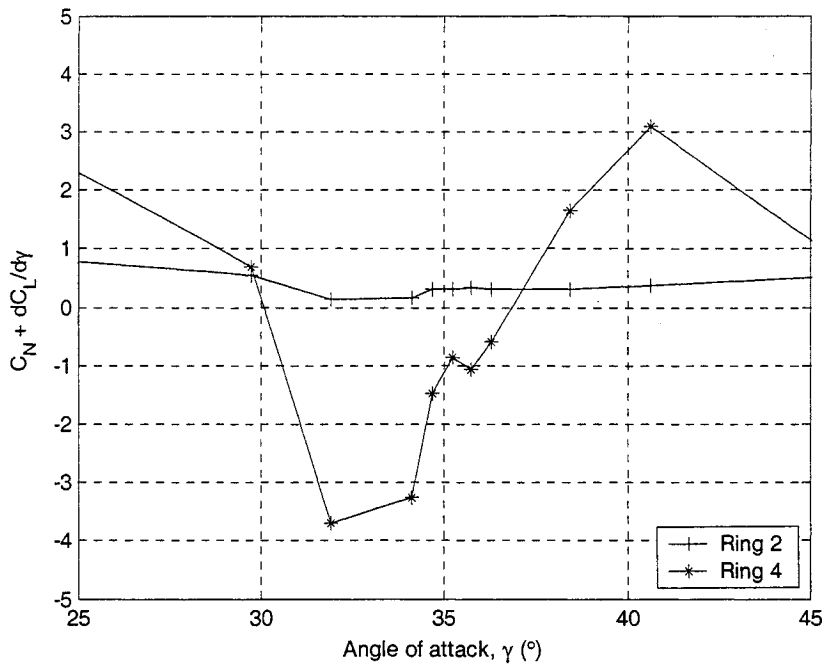

Figure C-1: Variation of Equation (5.6) with effective angle of attack, γ, for $R_c=2.93\times10^5$; θ=54.7°, high scan rate

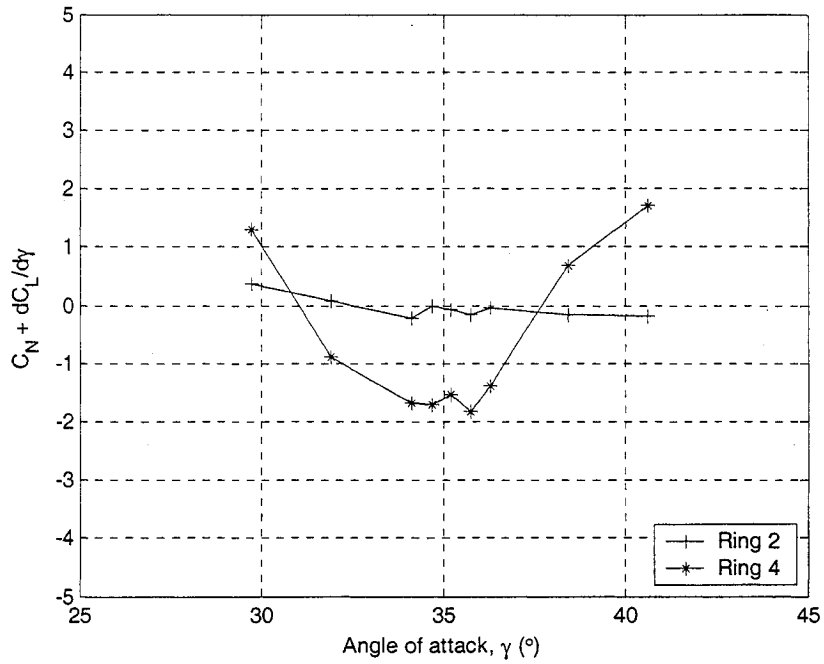

Figure C-2: Variation of Equation (5.6) with effective angle of attack, γ, for R_e=3.09×10^5; θ=54.7°, high scan rate

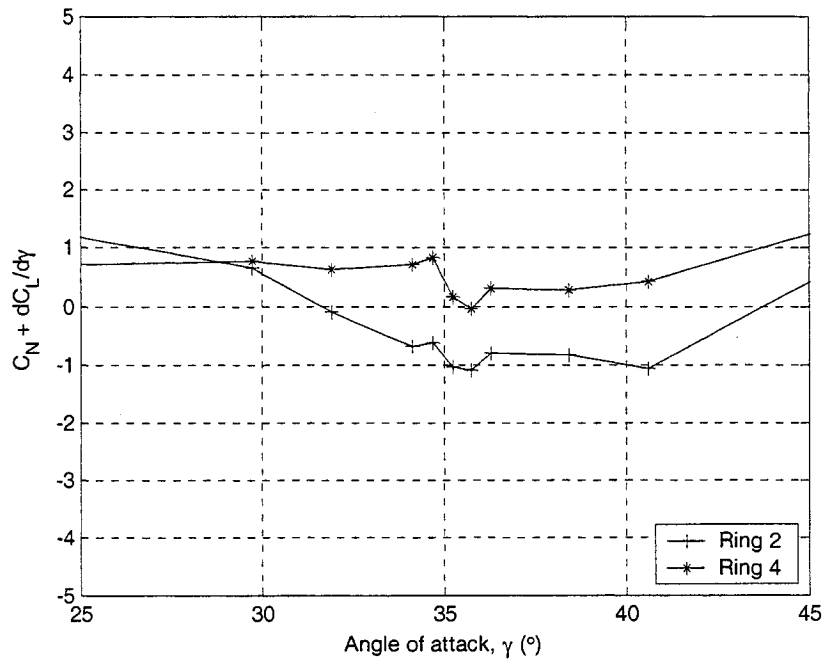

Figure C-3: Variation of Equation (5.6) with effective angle of attack, γ, for R_e=3.22×10^5; θ=54.7°, high scan rate

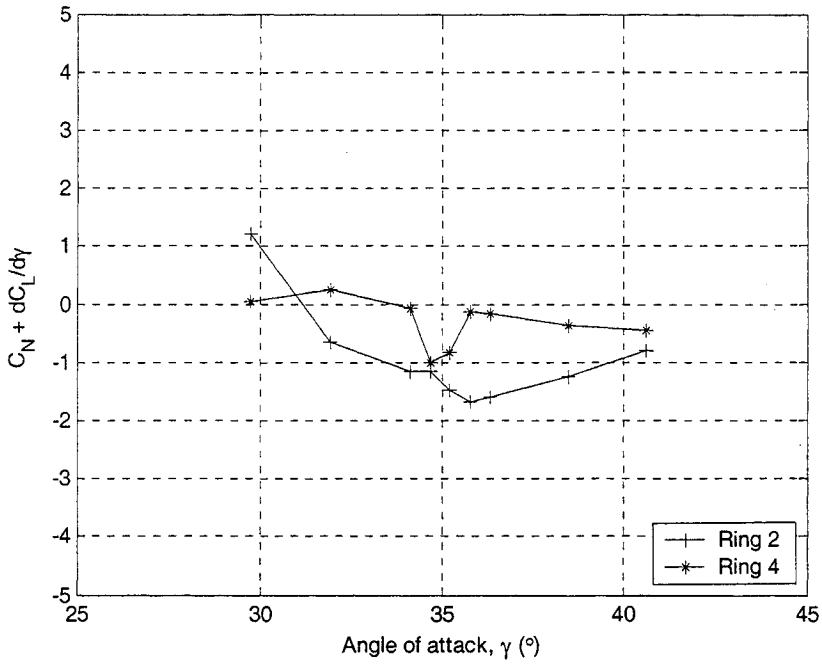

Figure C-4: Variation of Equation (5.6) with effective angle of attack, γ, for R_e=3.39×10^5; θ=54.7°, high scan rate

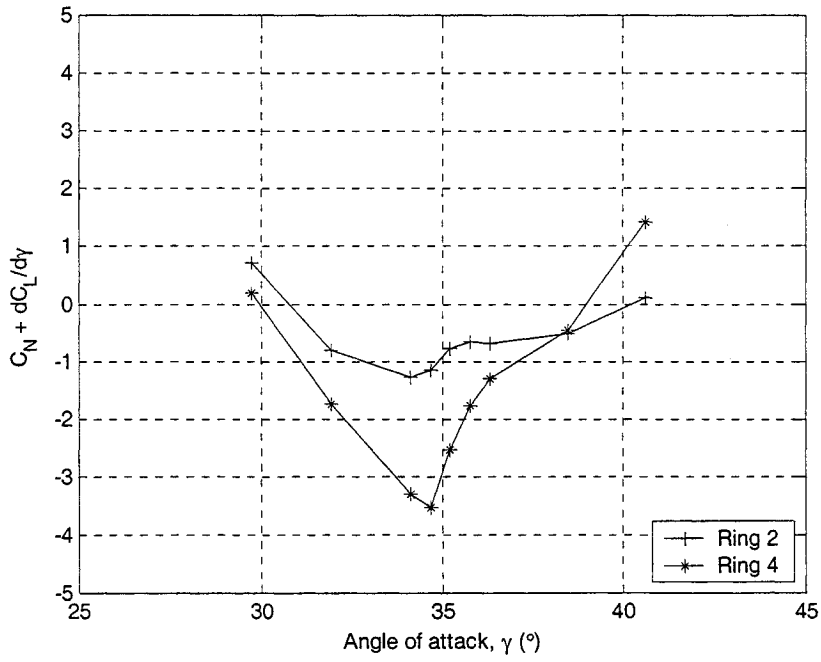

Figure C-5: Variation of Equation (5.6) with effective angle of attack, γ, for R_e=3.53×10^5; θ=54.7°, high scan rate

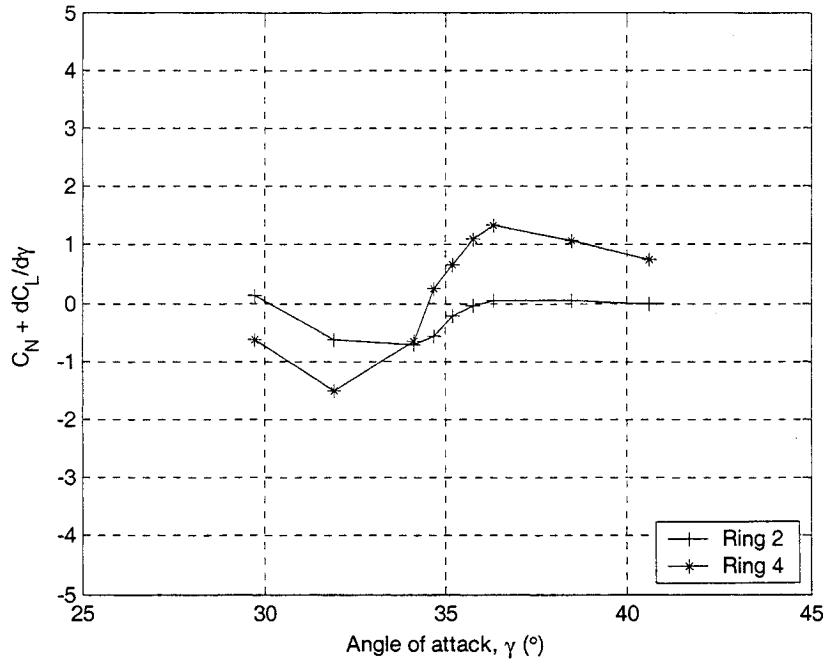

Figure C-6: Variation of Equation (5.6) with effective angle of attack, γ, for R_e=3.68×10^5; θ=54.7°, high scan rate

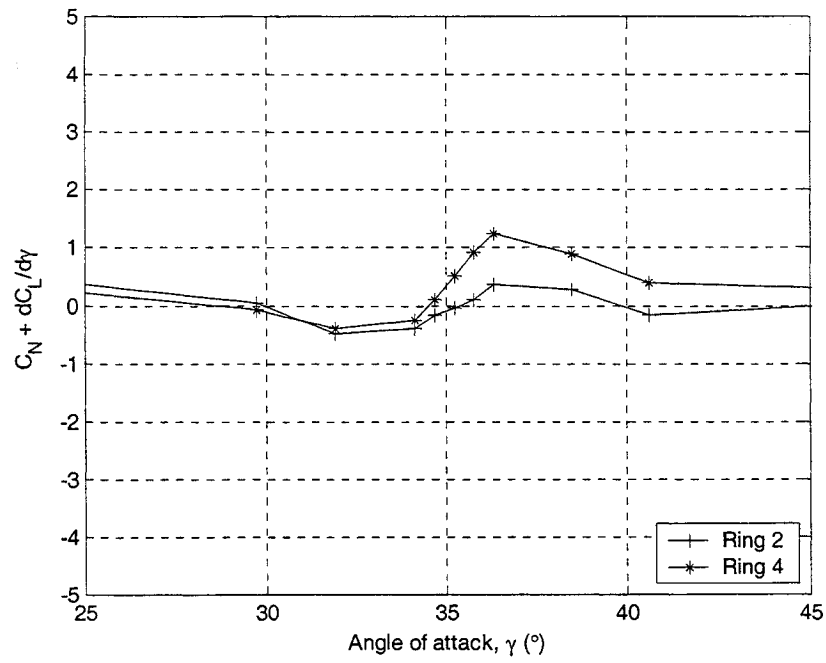

Figure C-7: Variation of Equation (5.6) with effective angle of attack, γ, for R_e=3.81×10^5; θ=54.7°, high scan rate

Appendix D: Estimation of Mechanical Damping Required to Prevent Galloping

Consider the equation of the total damping of a system:

$$2m\zeta\omega + \tfrac{1}{2}\rho UB\left(\frac{dC_L}{d\alpha} + C_D\right) = c \qquad \text{(D.1)}$$

where the system will be stable if c>0 and may be unstable when c<0.

Consider the parameters from Phase 1:

- B=160 mm (cable diameter)
- f=1.415 Hz (cable frequency)
- m=60.8 kg/m (cable mass per unit length)
- U_{crit}=32 m/s

Also assuming an average of -3 for the term $dC_L/d\alpha+C_D$, and substituting into Equation (D.1), the condition for stability is:

$$2(60.8)\zeta(2\pi(1.415)) + \tfrac{1}{2}(1.225)(32)(0.16)(-3) > 0$$

$$1081.1\zeta - 9.408 > 0$$

$$\boxed{\zeta > 0.0087}$$

Alternatively, given in terms of Scruton number:

$$S_C = \frac{m\delta}{2\pi\rho D^2} = \frac{m\zeta}{\rho D^2}$$

Therefore the condition for stability becomes:

$$\frac{m\zeta}{\rho B^2} + \tfrac{1}{4}\frac{U}{B\omega}\left(\frac{dC_L}{d\alpha} + C_D\right) > 0$$

$$S_C + \tfrac{1}{4}\frac{32}{0.16(2\pi(1.415))}(-3) > 0$$

$$\boxed{S_C > 16.87}$$

Appendix E: Power Spectra of C_L

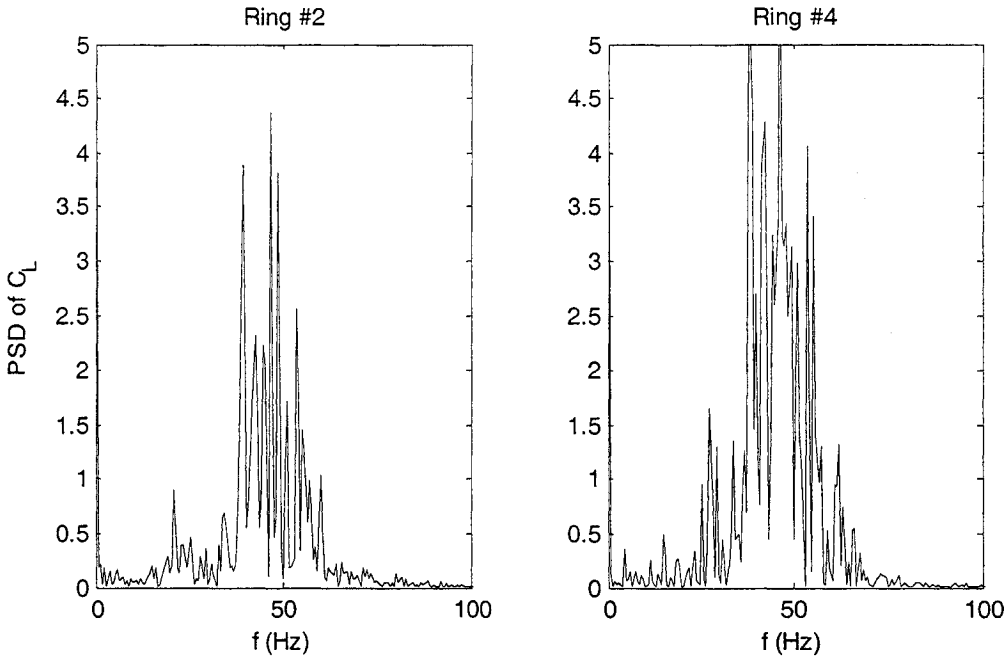

Figure E-1: Power spectral density of C_L for U=24.7 m/s, R_e=1.45×10^5; θ=54.7°, β=30°, ϕ=60°, high scan rate

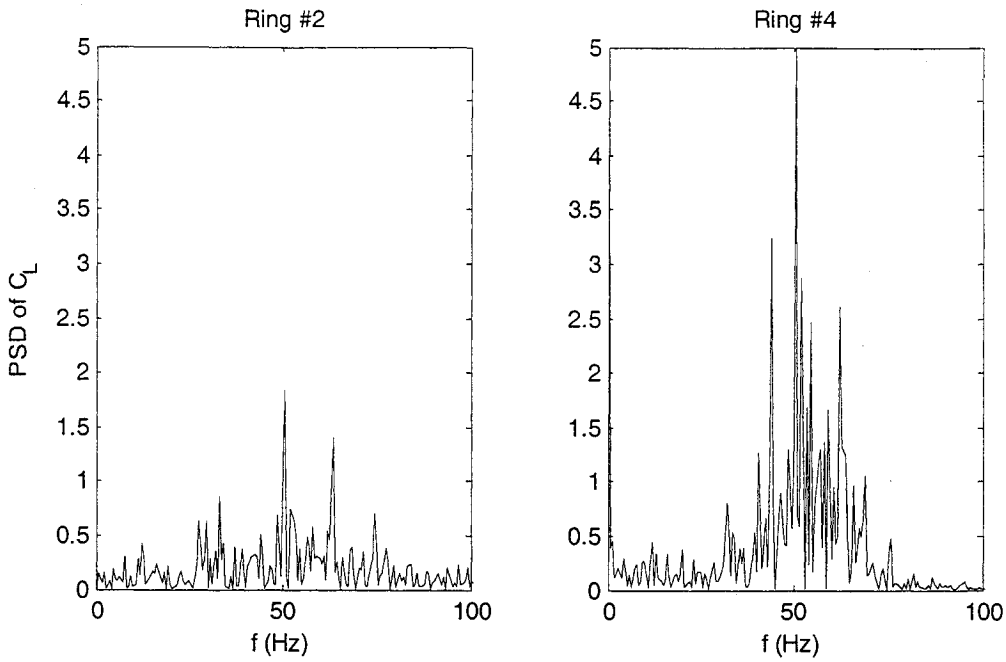

Figure E-2: Power spectral density of C_L for U=29.6 m/s, R_e=1.75×10^5; θ=54.7°, β=30°, ϕ=60°, high scan rate

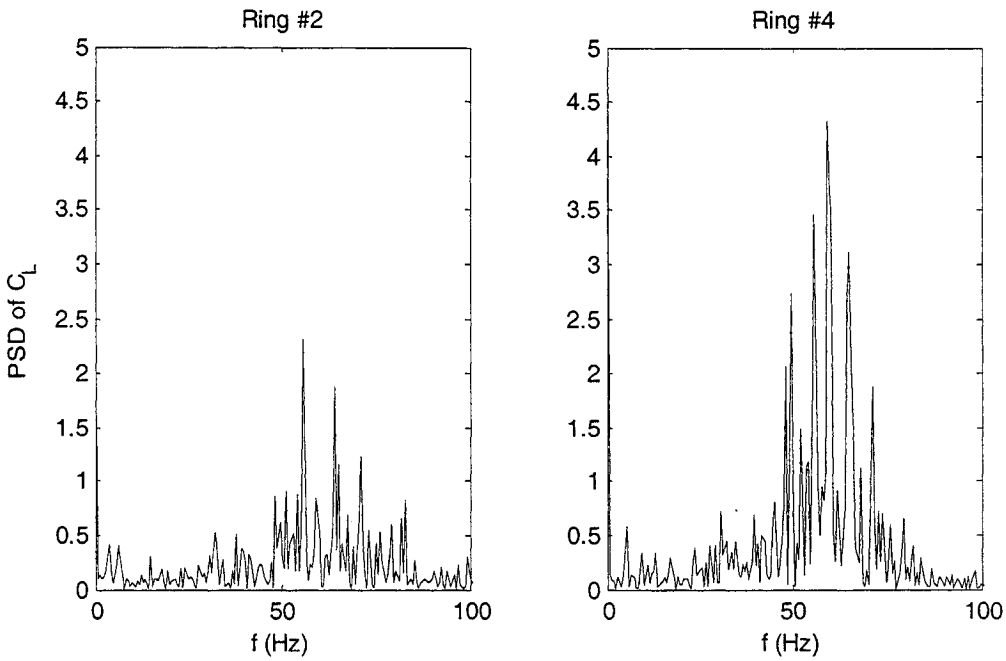

Figure E-3: Power spectral density of C_L for U=34.6 m/s, R_e=2.04×10^5; θ=54.7°, β=30°, ϕ=60°, high scan rate

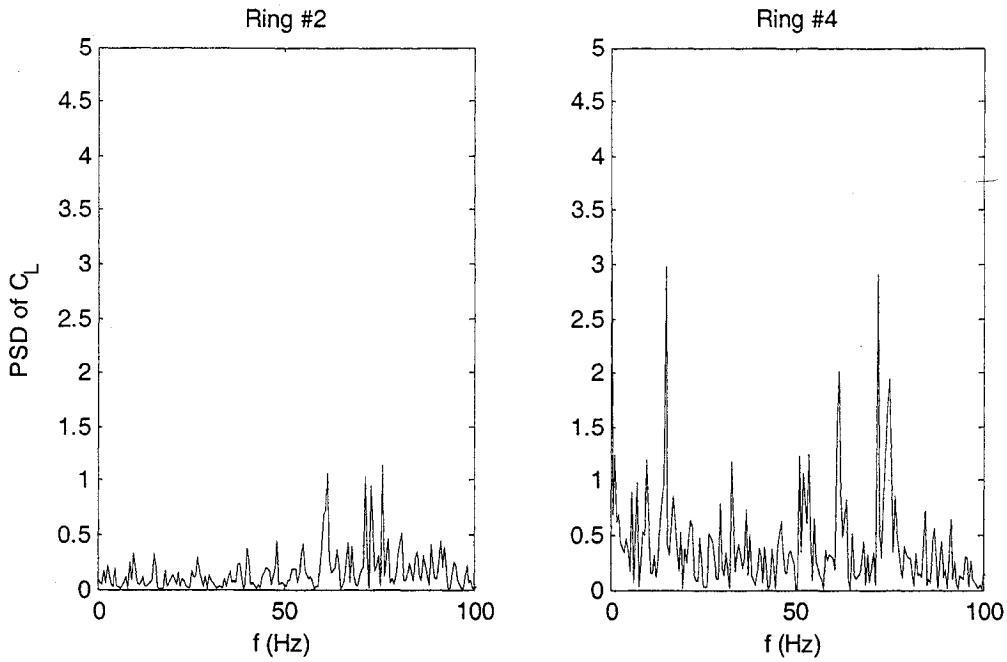

Figure E-4: Power spectral density of C_L for U=39.6 m/s, R_e=2.34×10^5; θ=54.7°, β=30°, ϕ=60°, high scan rate

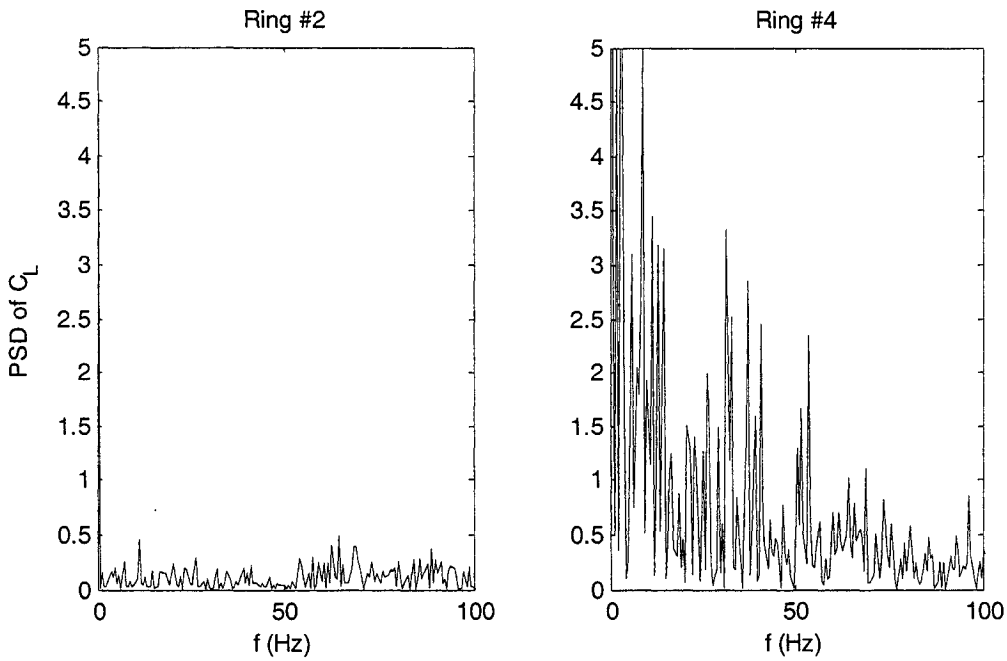

Figure E-5: Power spectral density of C_L for U=44.6 m/s, R_e=2.63×10^5; θ=54.7°, β=30°, ϕ=60°, high scan rate

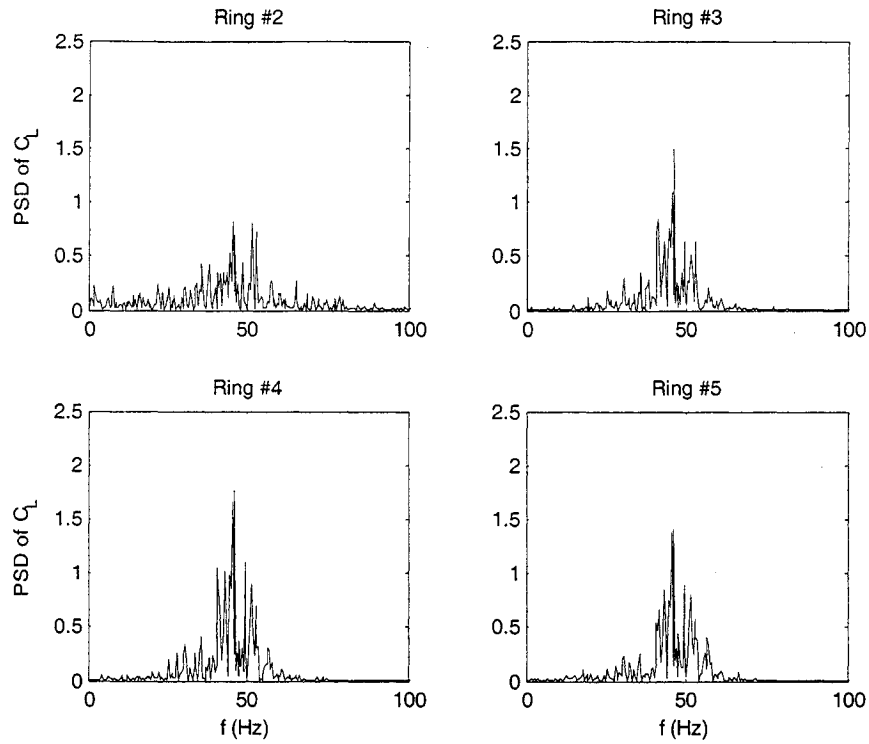

Figure E-6: Power spectral density of C_L for U=24.6 m/s, R_e=1.43×10^5; θ=54.7°, β=30°, ϕ=60°, low scan rate

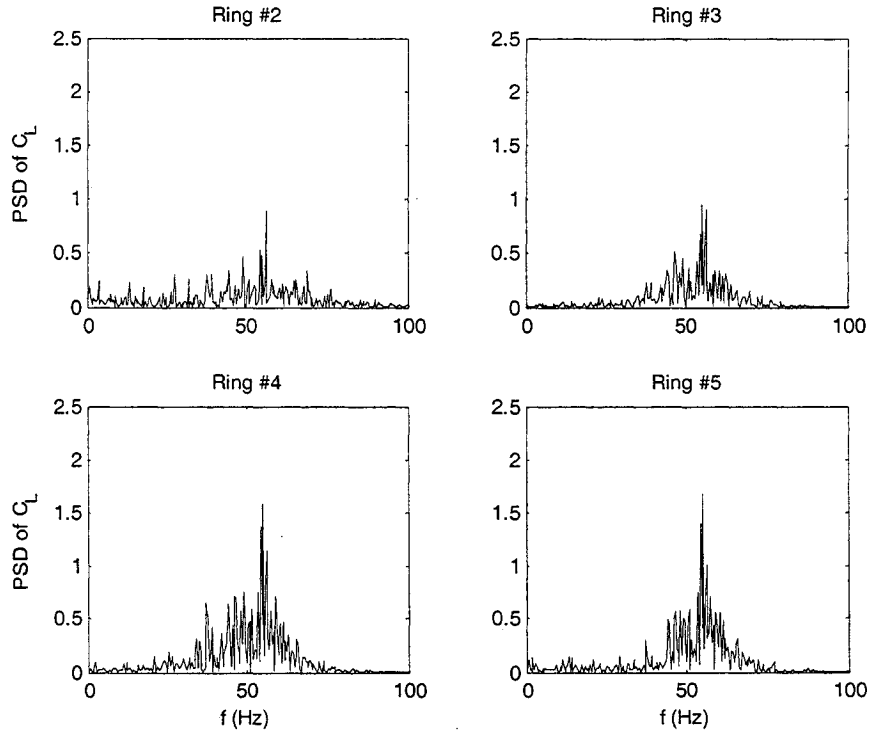

Figure E-7: Power spectral density of C_L for U=29.6 m/s, R_e=1.73×10^5; θ=54.7°, β=30°, ϕ=60°, low scan rate

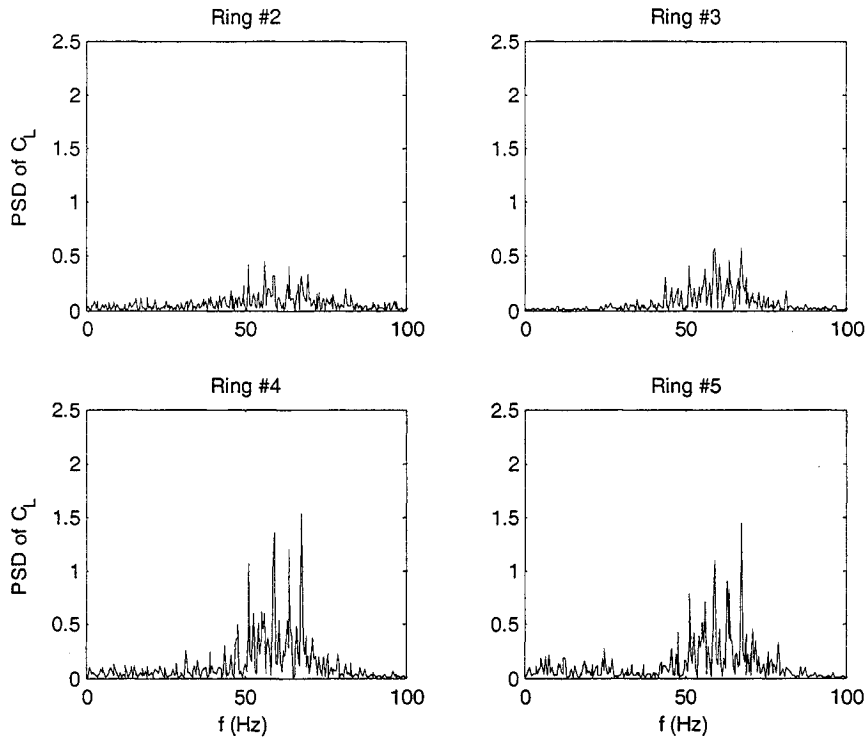

Figure E-8: Power spectral density of C_L for U=34.6 m/s, R_e=2.03×10^5; θ=54.7°, β=30°, ϕ=60°, low scan rate

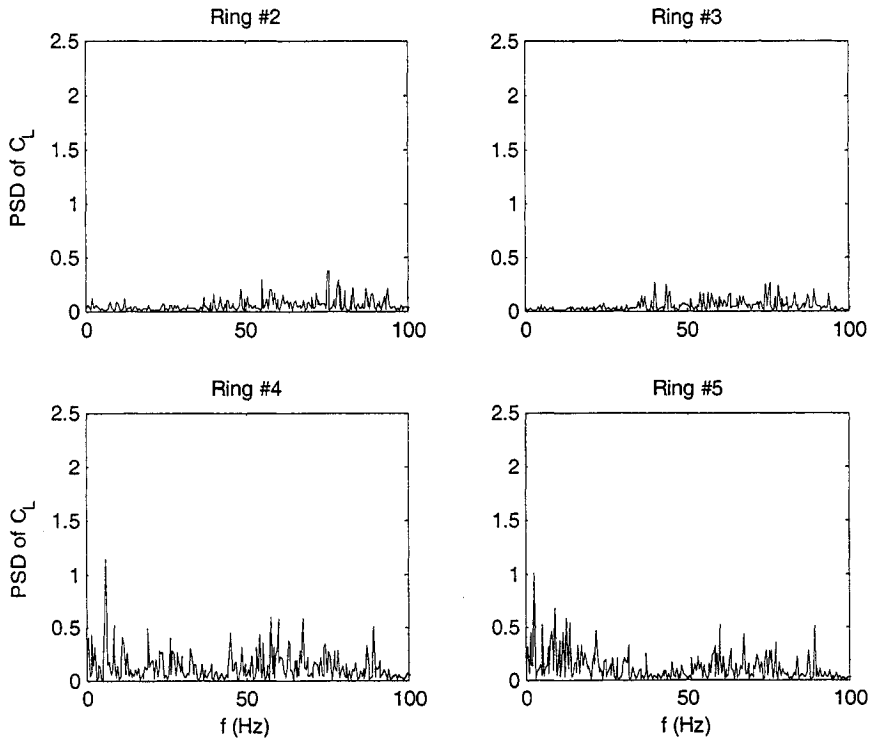

Figure E-9: Power spectral density of C_L for U=39.4 m/s, R_e=2.31×10^5; θ=54.7°, β=30°, ϕ=60°, low scan rate

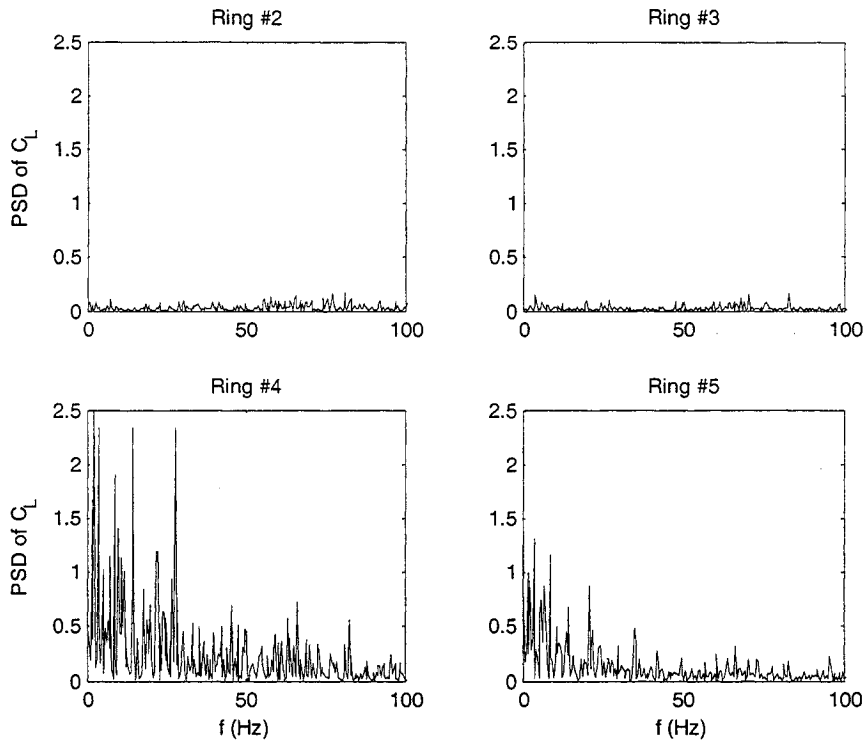

Figure E-10: Power spectral density of C_L for U=44.3 m/s, R_e=2.63×10^5; θ=54.7°, β=30°, ϕ=60°, low scan rate

Appendix F: Pressure Tap Numbering Layout

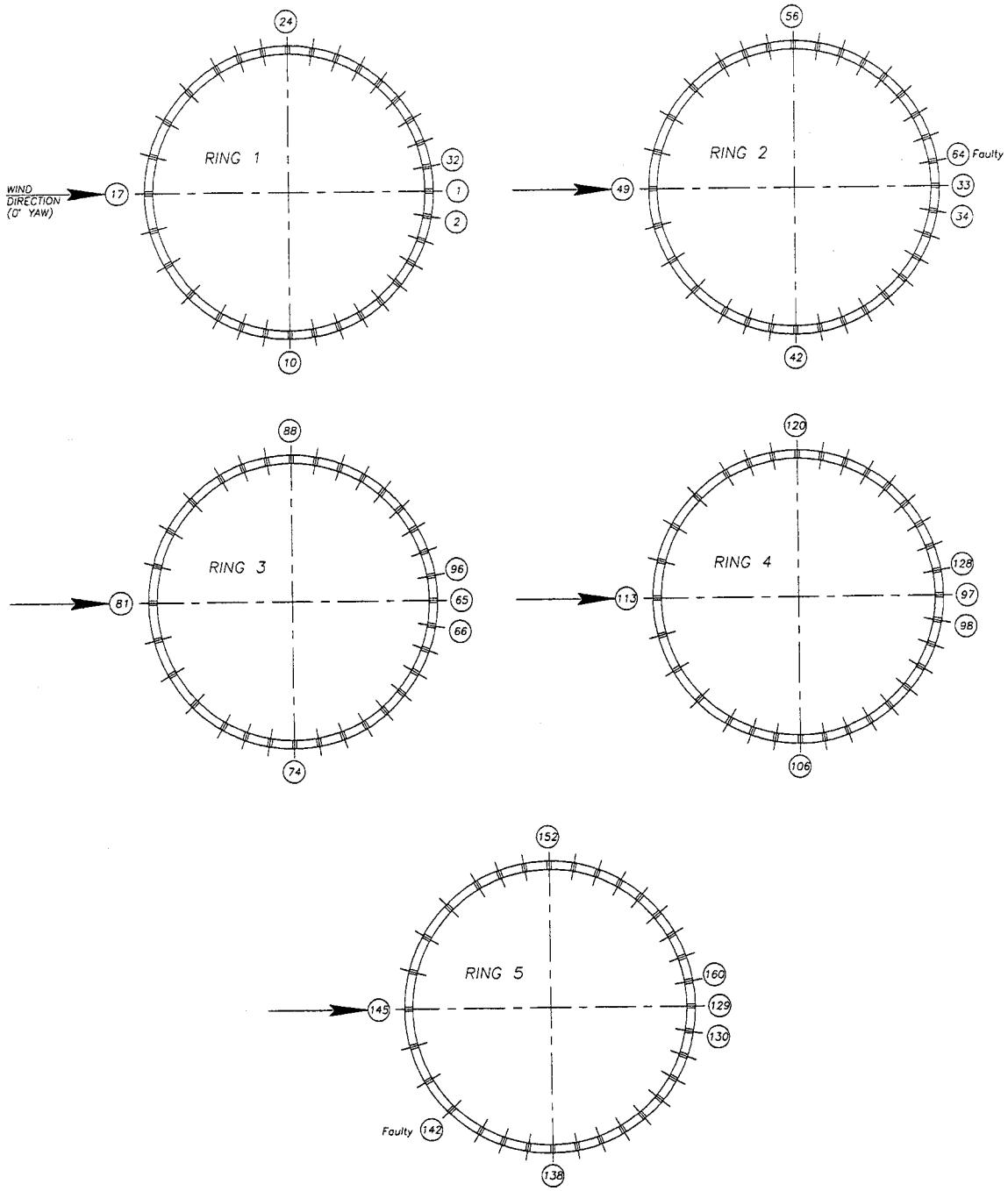

Figure F-1: Pressure Tap Layout – Rings

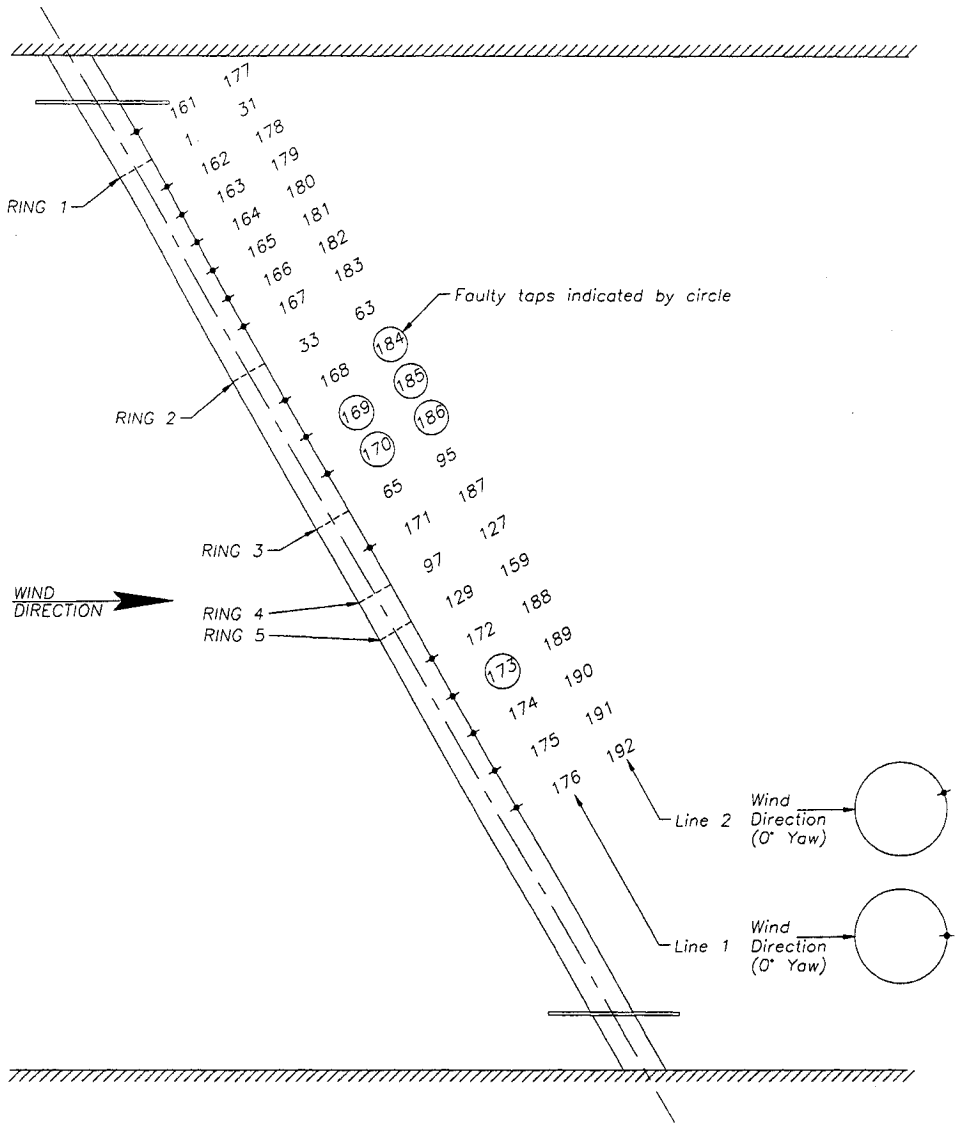

Figure F-2: Pressure Tap Layout – Leeward Lines

Appendix G: Oil Film Visualization

Oil film visualization was employed in an attempt to physically observe any indication of axial vortex formation. No clear or significant indication of a regular formation was observed, though the three-dimensionality of the flow around an inclined cylinder, and particularly the axial flow, is very clearly illustrated in Figures G-1 and G-2. For the case of a circular cylinder positioned normal to the flow direction, three-dimensionality would not be so obviously apparent.

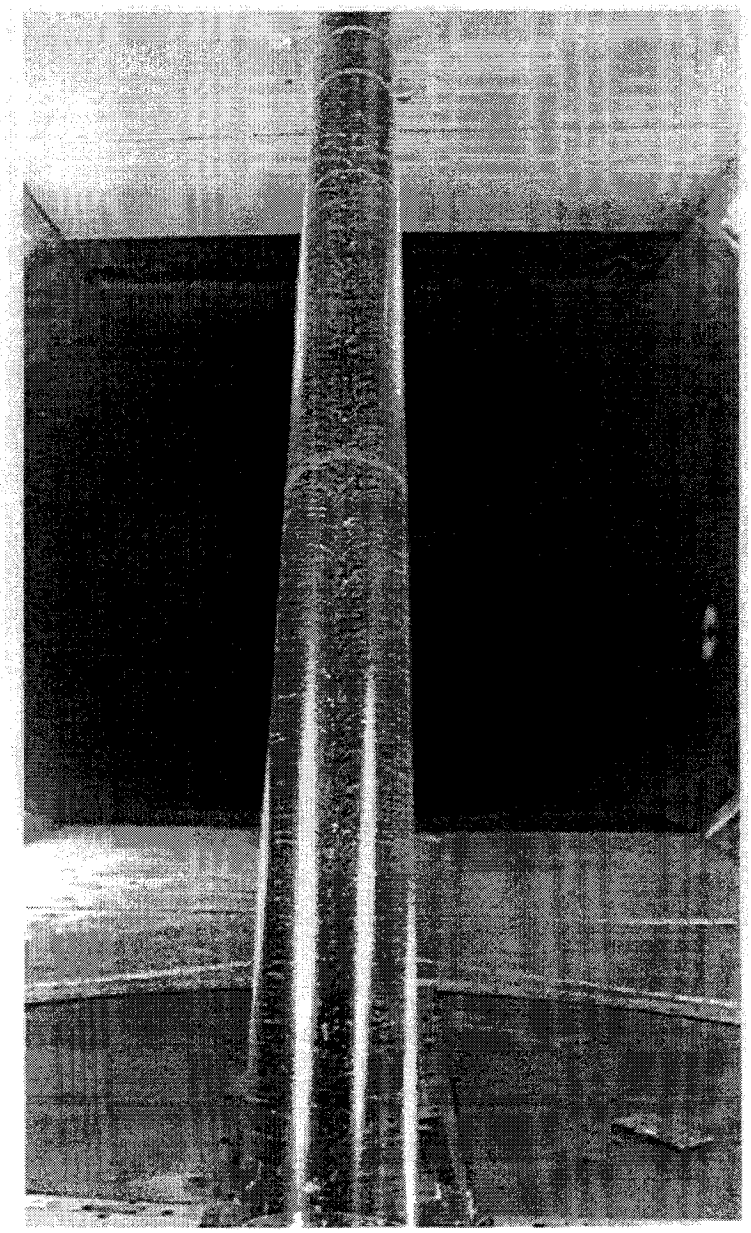

Figure G-1: Oil film visualization, leeward side of cable model, 30 m/s, θ=54.7°

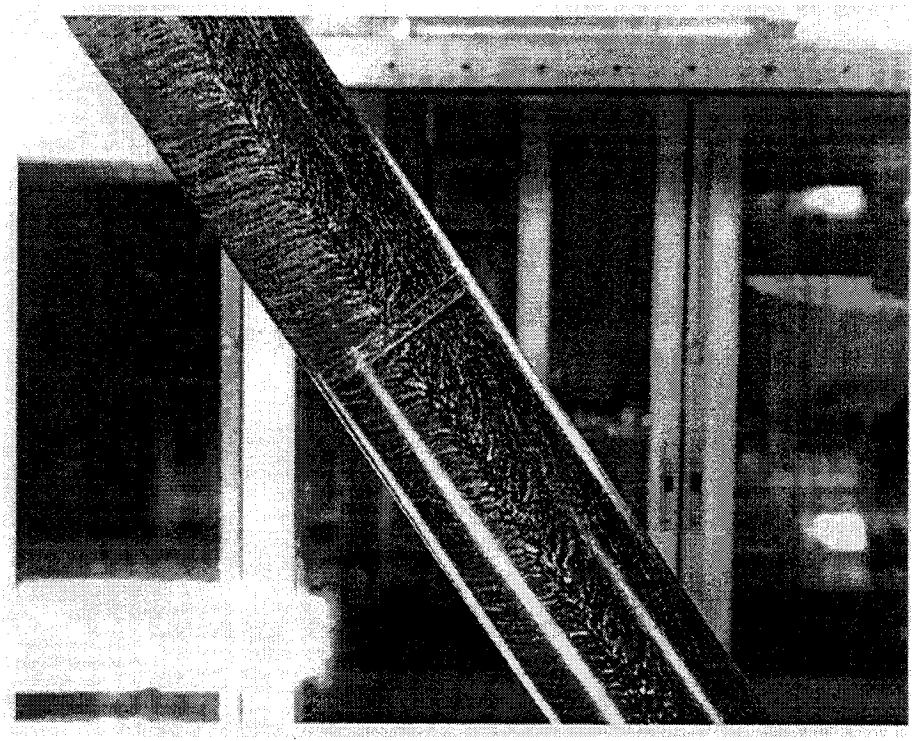

Figure G-2: Oil film visualization, 40 m/s, θ=54.7°, β=30°

Appendix H: Artificial Axial Flow Results

Select tests were completed with the addition of artificial axial flow induced along the leeward side of the model using compressed air and suction so as to attempt to create a semblance of continuity otherwise restricted by the wind tunnel roof and floor. Various levels of pressure were induced for comparison. The addition of this artificial axial flow had little or no effect on the aerodynamic forces acting on the cable model. For instance, Figure H-1 through Figure H-3 present the PSD of the lift force coefficient for rings 2 to 5 for a wind speed of about 30 m/s with the model inclined into the wind to 54.7°. The first figure depicts the benchmark result with no axial flow, the second includes the effects of an imposed axial flow pressure of 4psi (27.6 kPa, 4 m/s) at the top and suction equivalent to 6 m/s at the bottom of the model, while the third includes the effects of an imposed axial flow pressure of 14 psi (96.6 kPa) at the top of the model. The only noticeable difference between the three results is a low frequency peak for ring 2 when the lower level of axial flow is induced. This peak diminishes with the higher axial flow. The remainder of the rings are unaffected. Consequently, the addition of the axial flow in this case appears to result in a localized effect and would indicate that rings 3 to 5 are not significantly affected by boundary conditions.

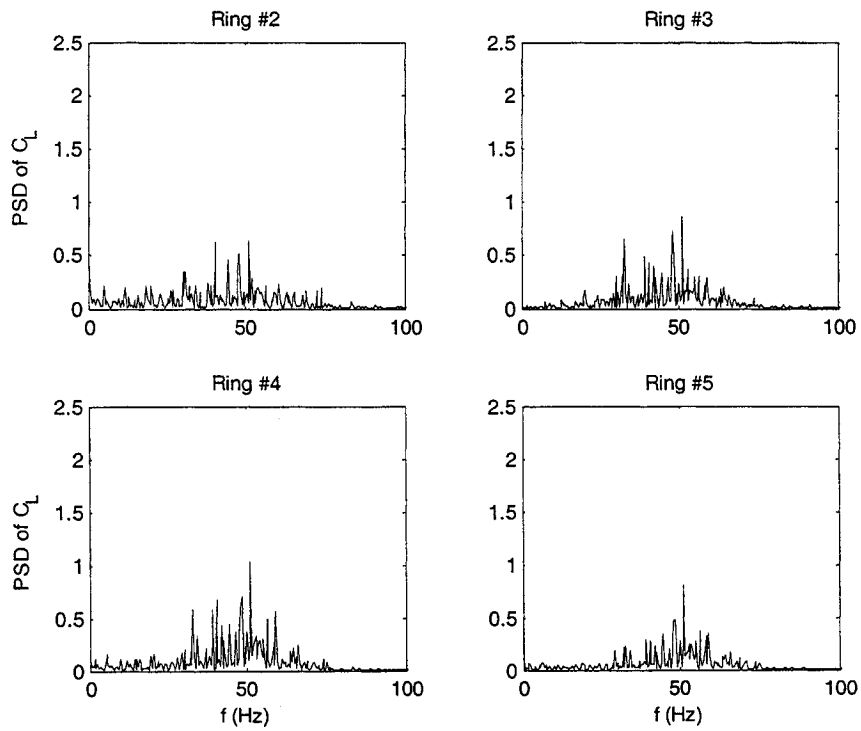

Figure H-1: Power spectral density of C_L for U=29.5 m/s, R_e=1.74×10^5; θ=54.7°, β=0°, ϕ=54.7°, low scan rate, no artificial axial flow

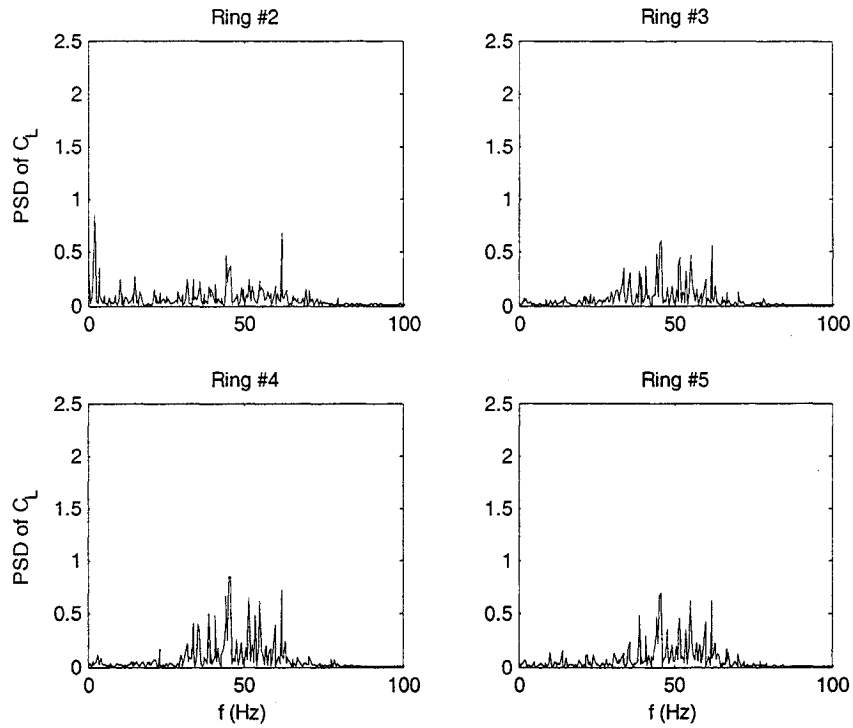

Figure H-2: Power spectral density of C_L for U=29.7 m/s, R_e=1.76×10^5; θ=54.7°, β=0°, ϕ=54.7°, low scan rate, artificial axial flow added: 4 psi (4 m/s) pressure, top, and 6 m/s suction, bottom

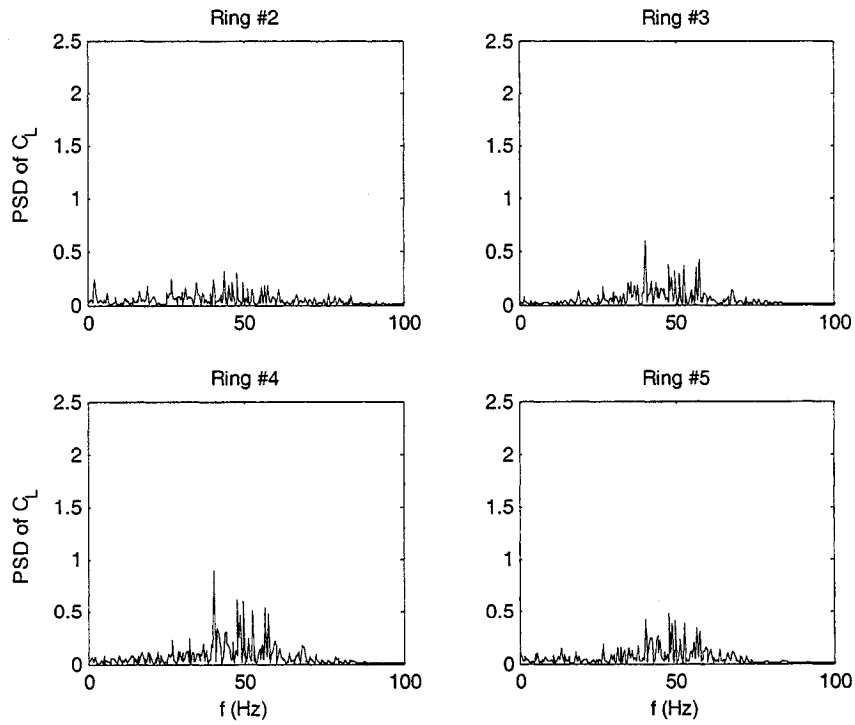

Figure H-3: Power spectral density of C_L for U=29.8 m/s, R_e=1.76×10^5; θ=54.7°, β=0°, ϕ=54.7°, low scan rate, artificial axial flow added: 14 psi pressure, top

Appendix J: Record of Aberrant Data

An irregularity is apparent in run 750_012 (θ=90°, β=0°, varying wind speeds, high scan rate) at the second wind speed level of about 30 m/s. The mean pressure readings vary significantly over the course of the 60 second sample time illustrated by the drag coefficient variation given in Figure J-1. A low frequency noise was noted during testing at this wind speed, however no cause was immediately evident and the effect did not reappear in subsequent test runs.

Test run 750_018 (θ=90°, β=0°, varying wind speeds, low scan rate) presents an irregularity at the wind speed of U=59.7 m/s, and only for ring 3. A sudden variation in the pressure readings results in a sudden shift in the mean value of the lift and drag coefficients at approximately 10 seconds into the 120 second test run, as shown in Figure J-2. The readings for the other rings displayed no such aberration. No reason for this shift was apparent during testing.

Test runs 750_058 (U=34.6 m/s, θ=60°, varying yaw), 750_071 (U=14.5 m/s, θ=54.7°, varying yaw), and 750_093 (U=19.7 m/s, θ=54.7°, varying yaw) present irregularities in the records for β=0.94°, β=3°, and β=105°, respectively, and only for ring 2. In all cases the pressure values deviate suddenly and significantly over a short period, as shown in Figure J-3 (750_058), Figure J-4 (750_071), and Figure J-5 (750_093). No apparent reason for this variation was evident during testing.

Lastly, test run 750_105 (U=49.7 m/s, θ=54.7°, varying yaw) presents an irregularity in the record for a yaw of β=105° for both ring 1 and ring 2. (Note that data for ring 1 has been largely ignored for all cases in which the model is inclined; this matter is discussed later in Section 5.3.4.) The pressure values deviate suddenly at several places throughout the 120 second runtime, having a similar effect on the aerodynamic coefficients as was seen in run 750_018. The resulting variation in drag coefficient with time is presented in Figure J-6. Again, no reason for this shift was apparent during testing.

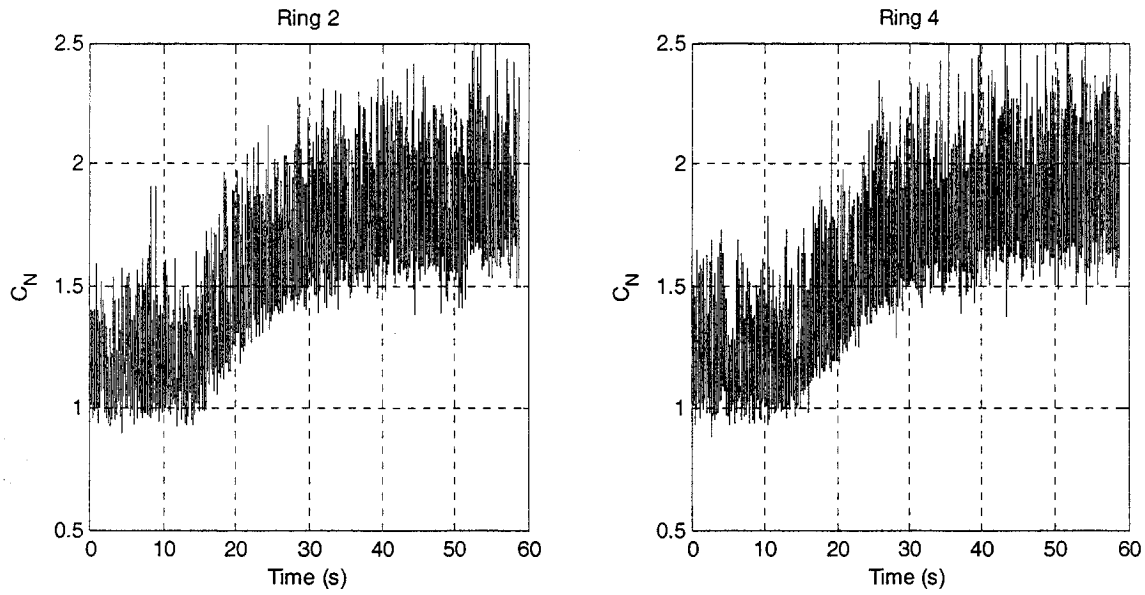

Figure J-1: Variation of drag coefficient with time for U=29.75 m/s of test run 750_012 (θ=90°, β=0°, high scan rate)

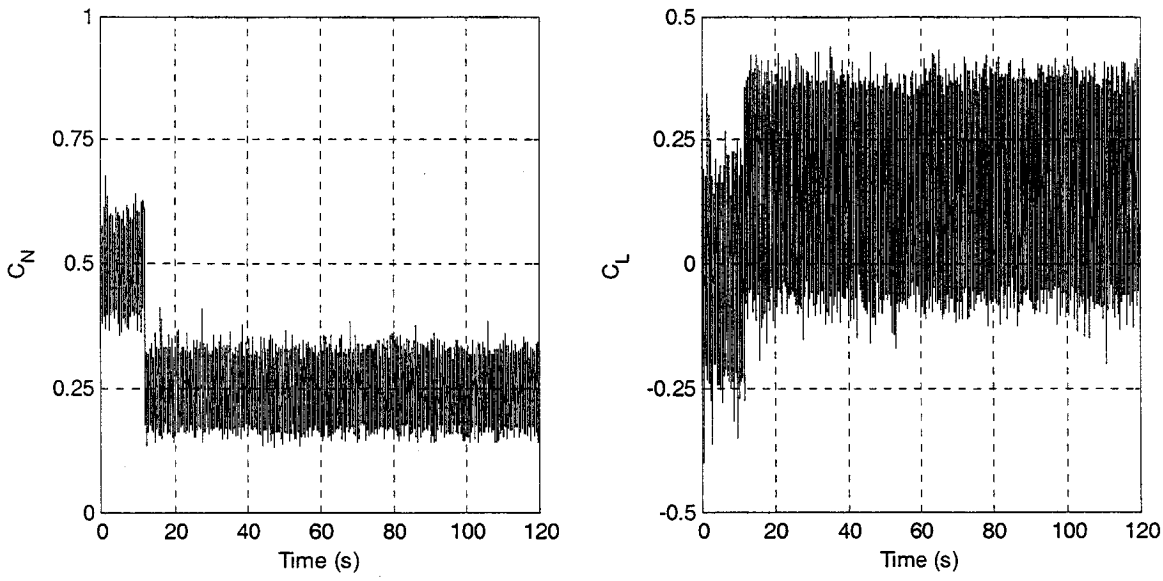

Figure J-2: Variation of drag and lift coefficients with time for ring 3 of test run 750_018 (U=59.7 m/s, θ=90°, β=0°, low scan rate)

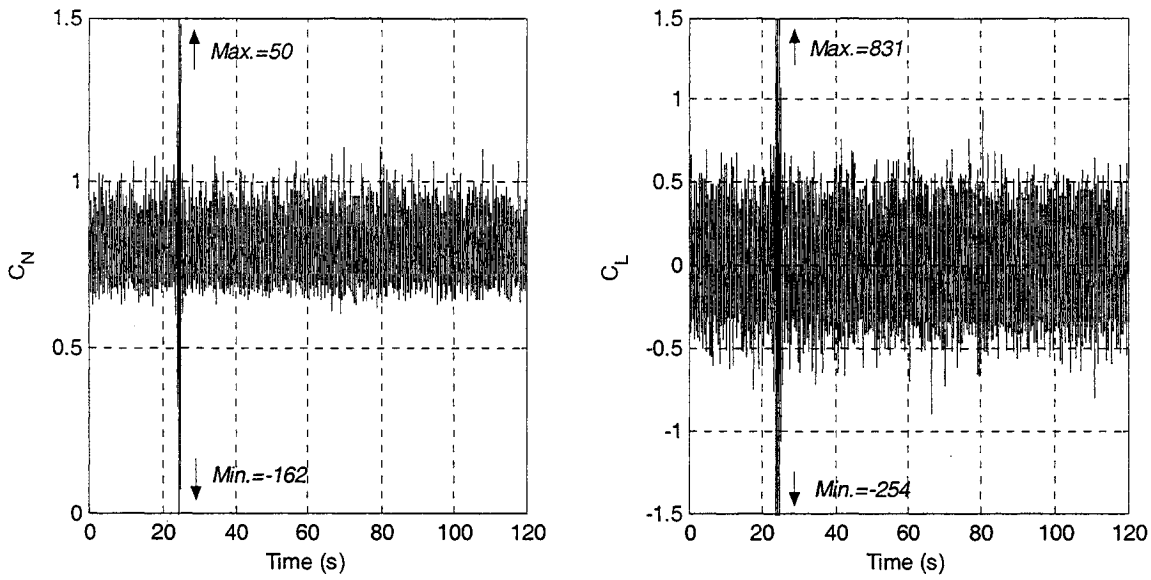

Figure J-3: Variation of drag and lift coefficients with time for ring 2 of test run 750_058 (U=34.6 m/s, θ=60°, β=0.94°)

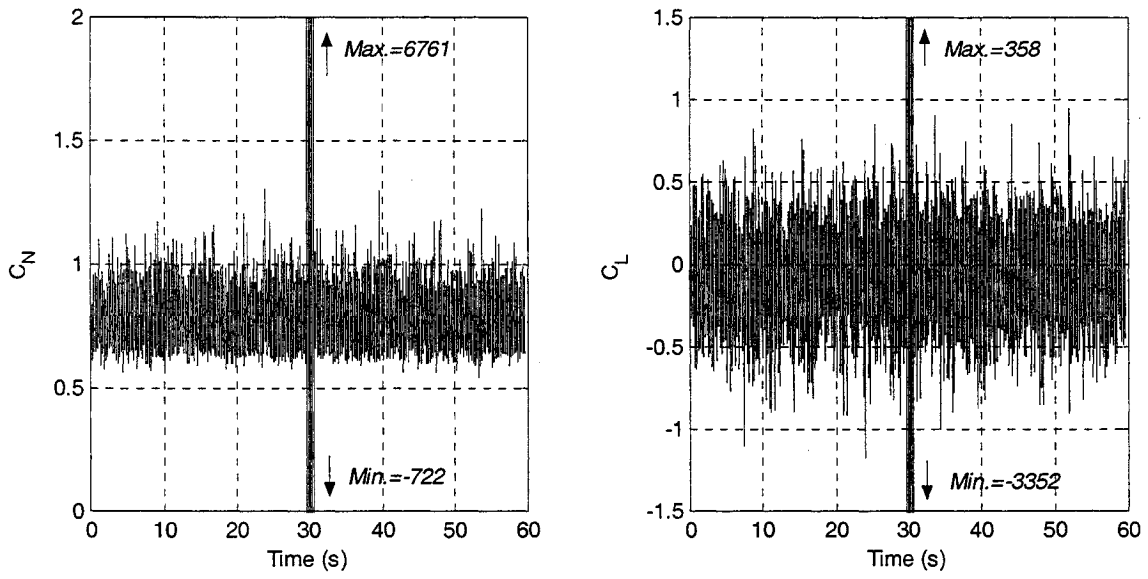

Figure J-4: Variation of drag and lift coefficients with time for ring 2 of test run 750_071 (U=14.5 m/s, θ=54.7°, β=3°)

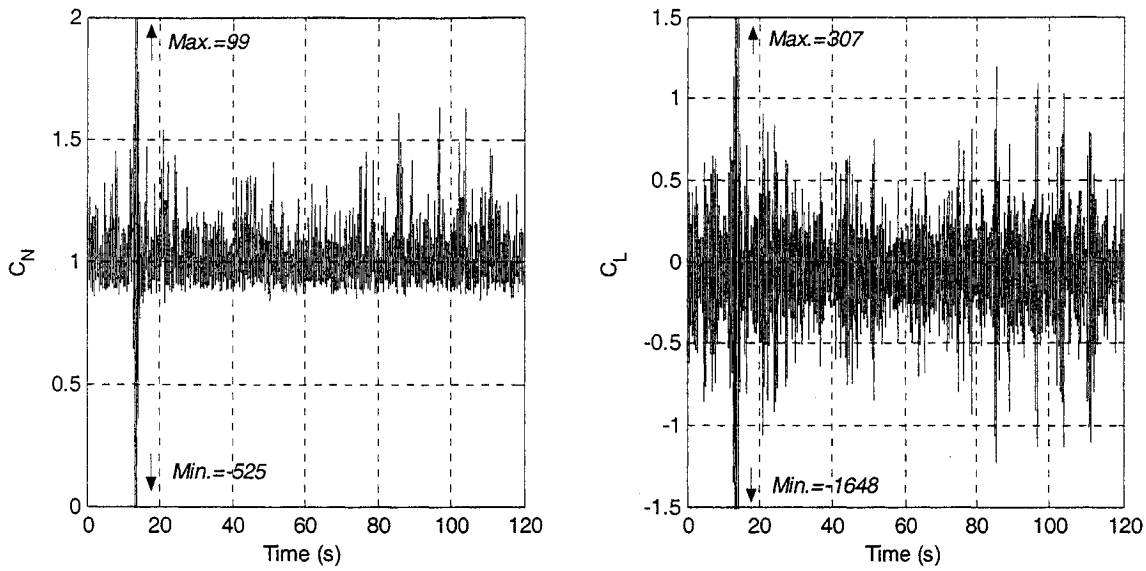

Figure J-5: Variation of drag and lift coefficients with time for ring 2 of test run 750_093 (U=19.7m/s, θ=54.7°, β=105°)

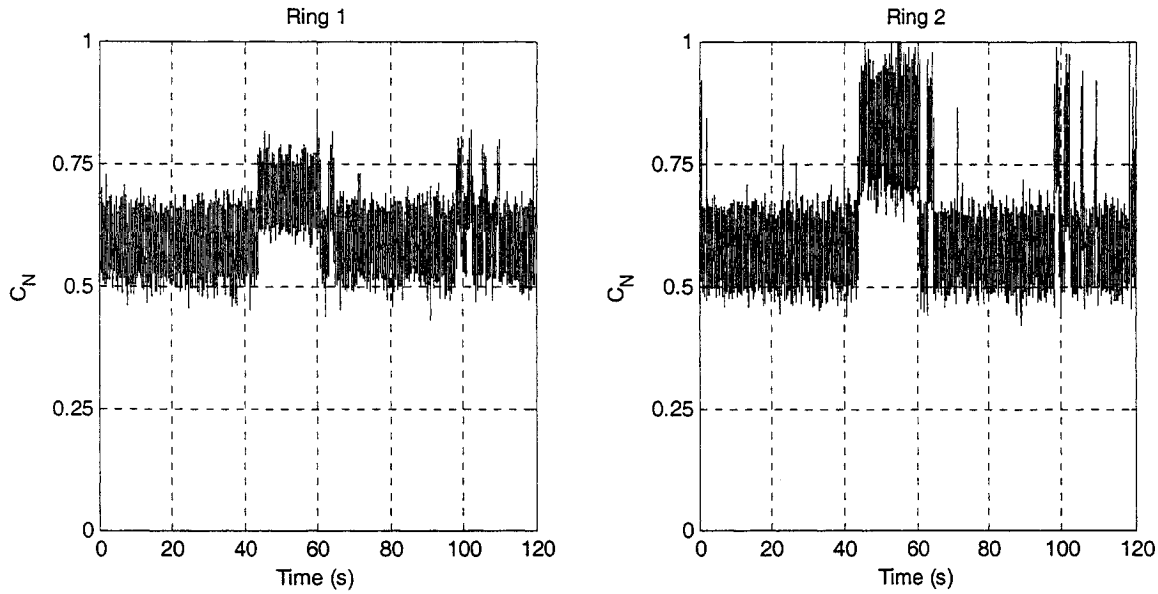

Figure J-6: Variation of drag coefficient with time for rings 1 and 2 of test run 750_105 (U=49.7 m/s, θ=54.7°, β=105°)

Appendix K: Spectral Analysis of Lift

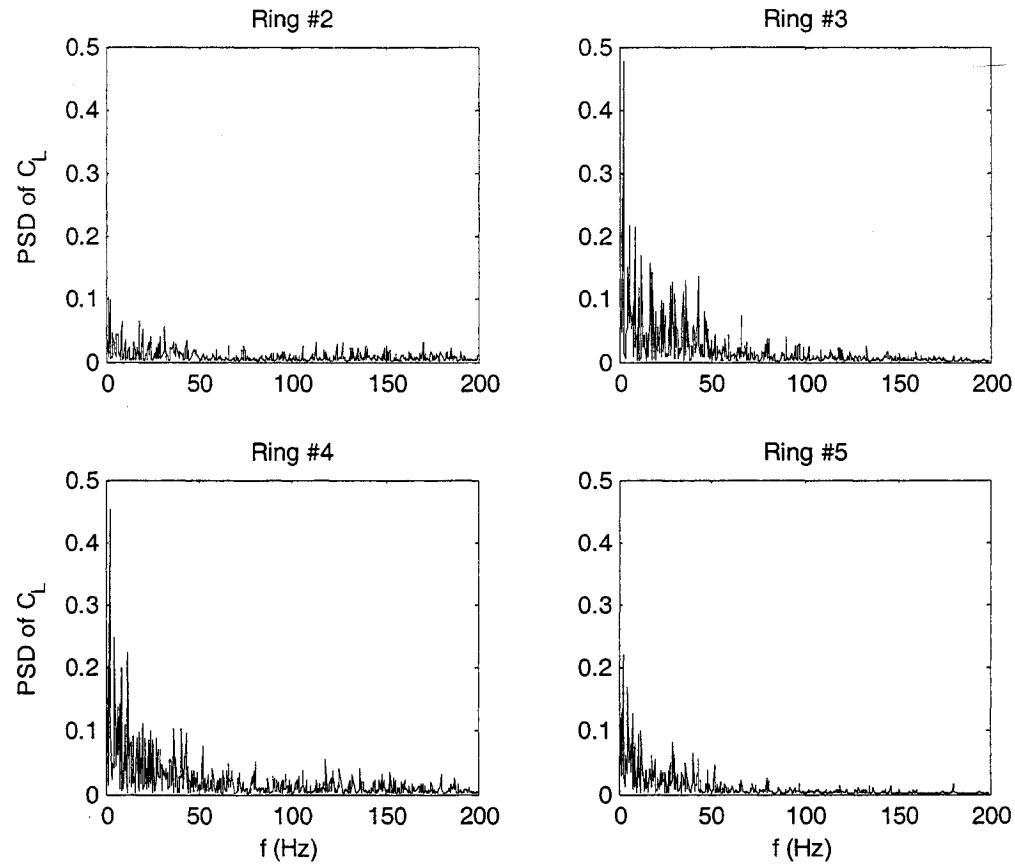

Figure K-1: Power spectral density of C_L for $R_e=3.53\times10^5$; $\theta=54.7°$, $\beta=30.0°$, $\phi=60°$, low scan rate

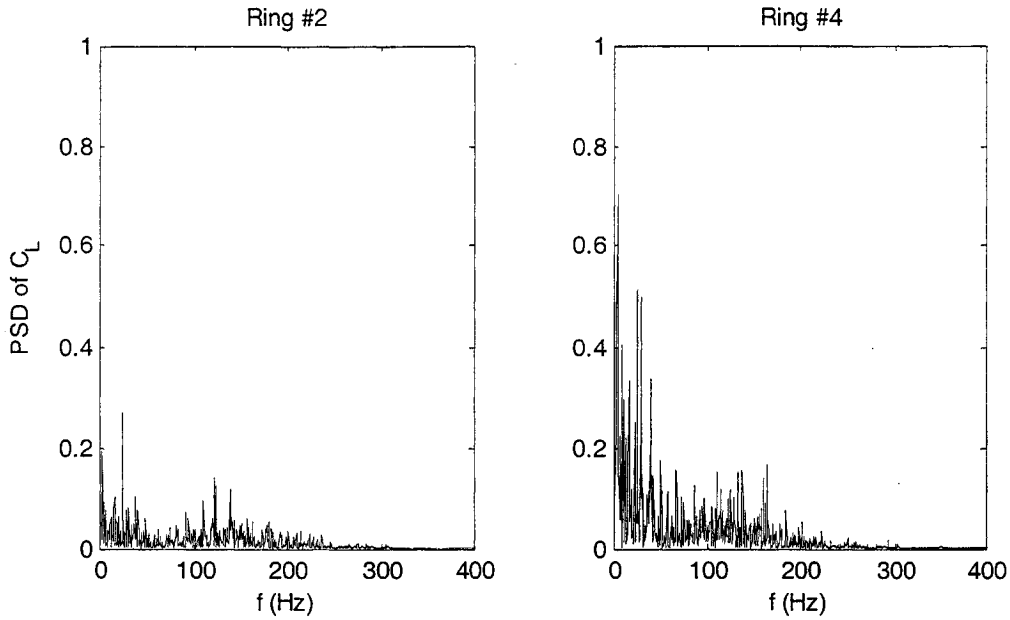

Figure K-2: Power spectral density of C_L for R_e=3.55×10^5; θ=54.7°, β=30.0°, ϕ=60°, high scan rate

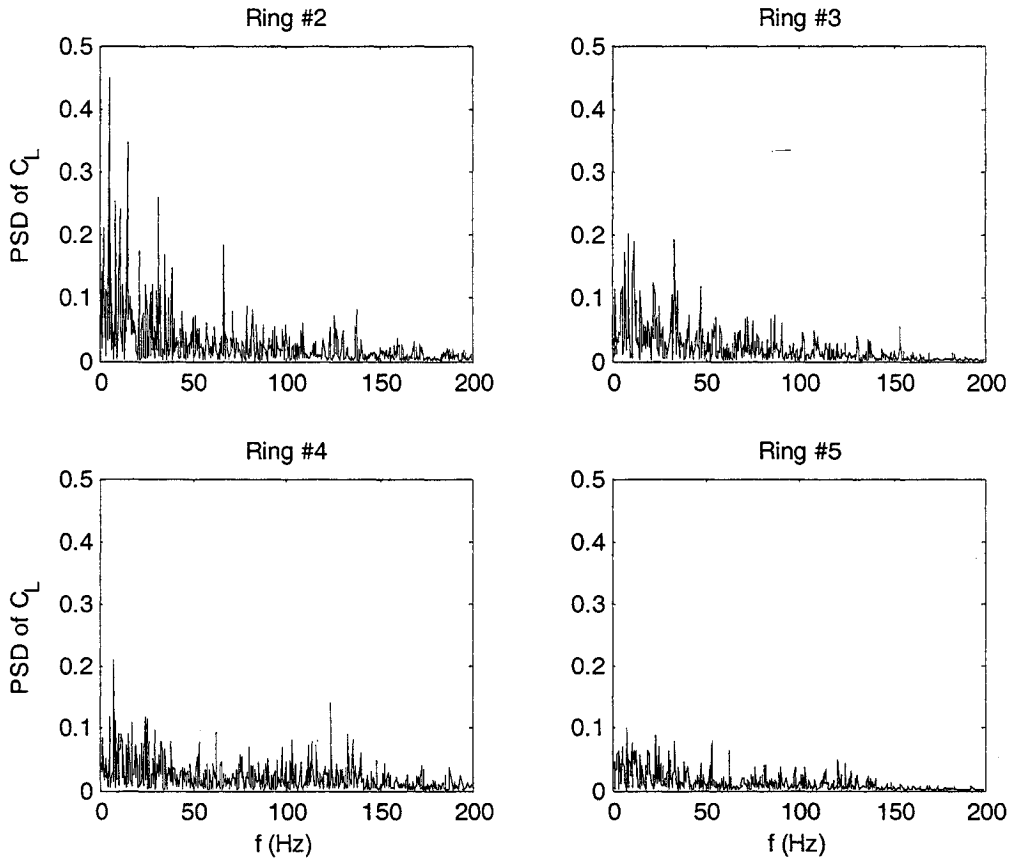

Figure K-3: Power spectral density of C_L for R_e=3.53×10^5; θ=54.7°, β=0.0°, ϕ=54.7°, low scan rate

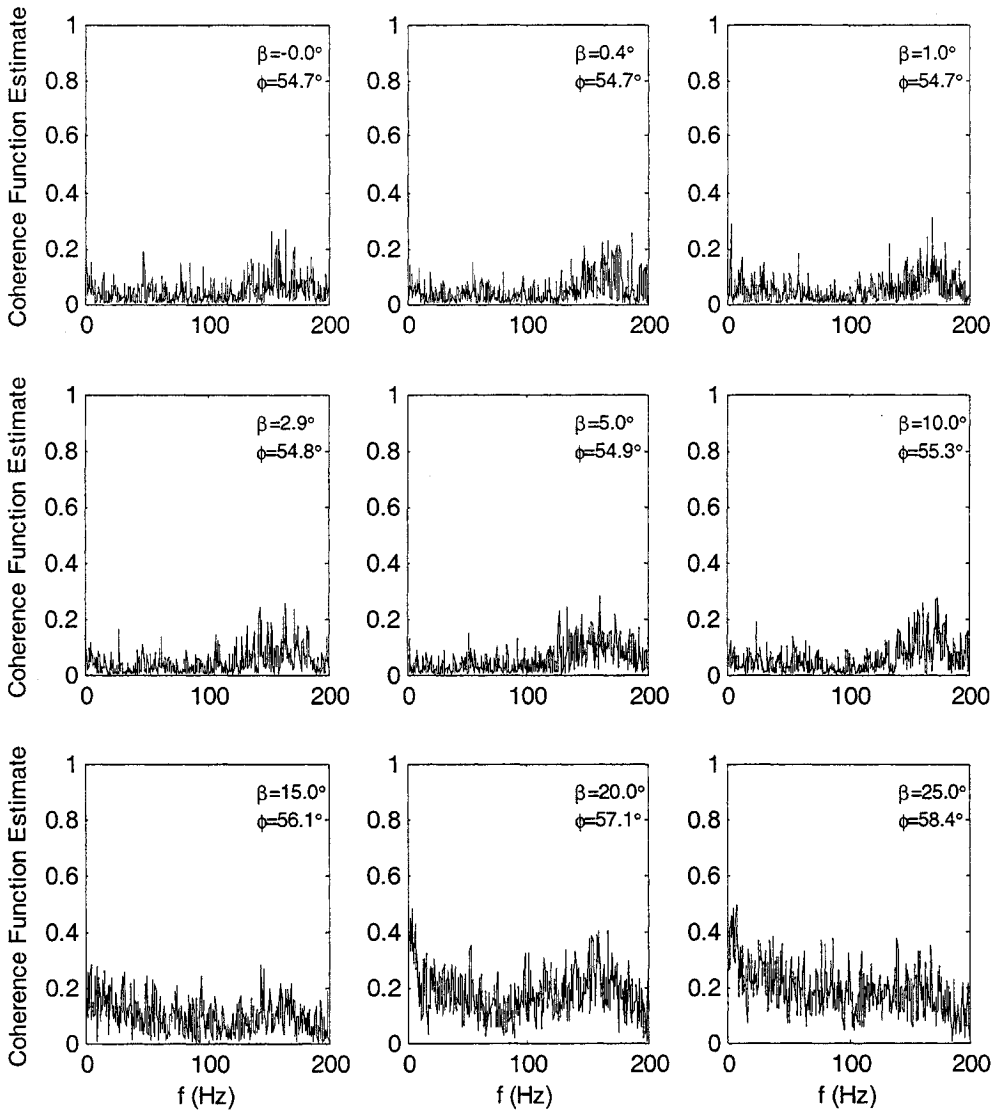

Figure K-4(a): Variation of coherence function of C_L for rings 2 and 5; $R_e=3.53\times10^5$, $\theta=54.7°$, low scan rate

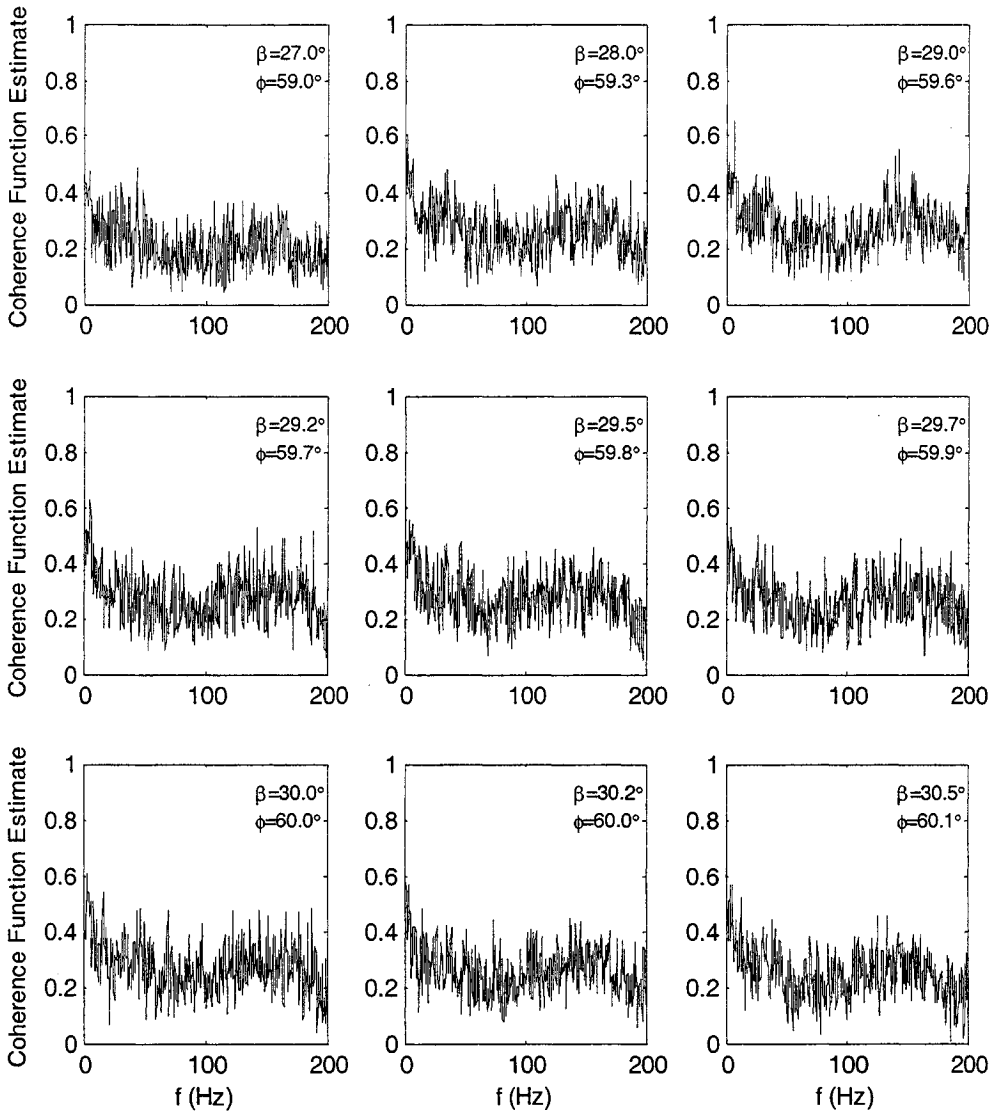

Figure K-4(b): Variation of coherence function of C_L for rings 2 and 5; $R_e=3.53\times10^5$, $\theta=54.7°$, low scan rate

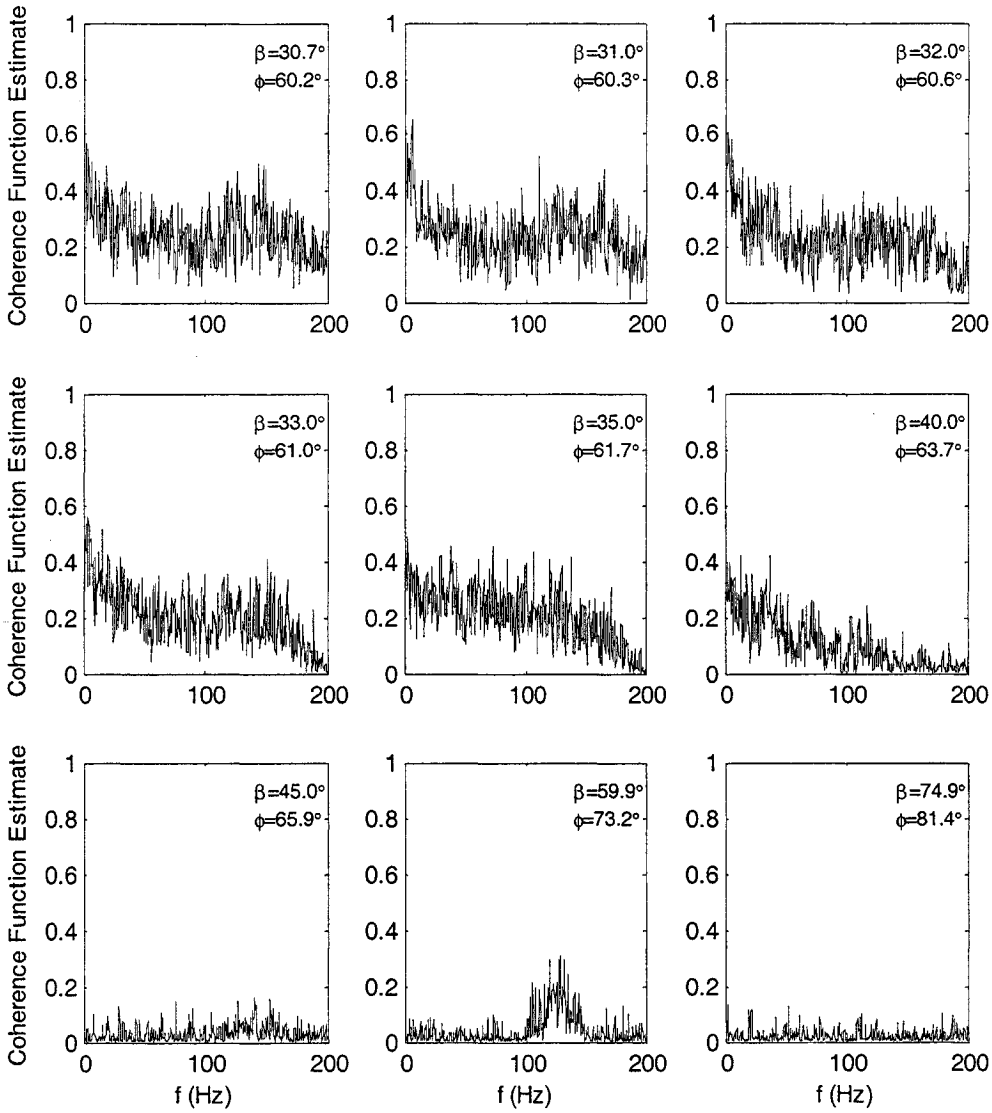

Figure K-4(c): Variation of coherence function of C_L for rings 2 and 5; $R_e=3.53\times10^5$, $\theta=54.7°$, low scan rate

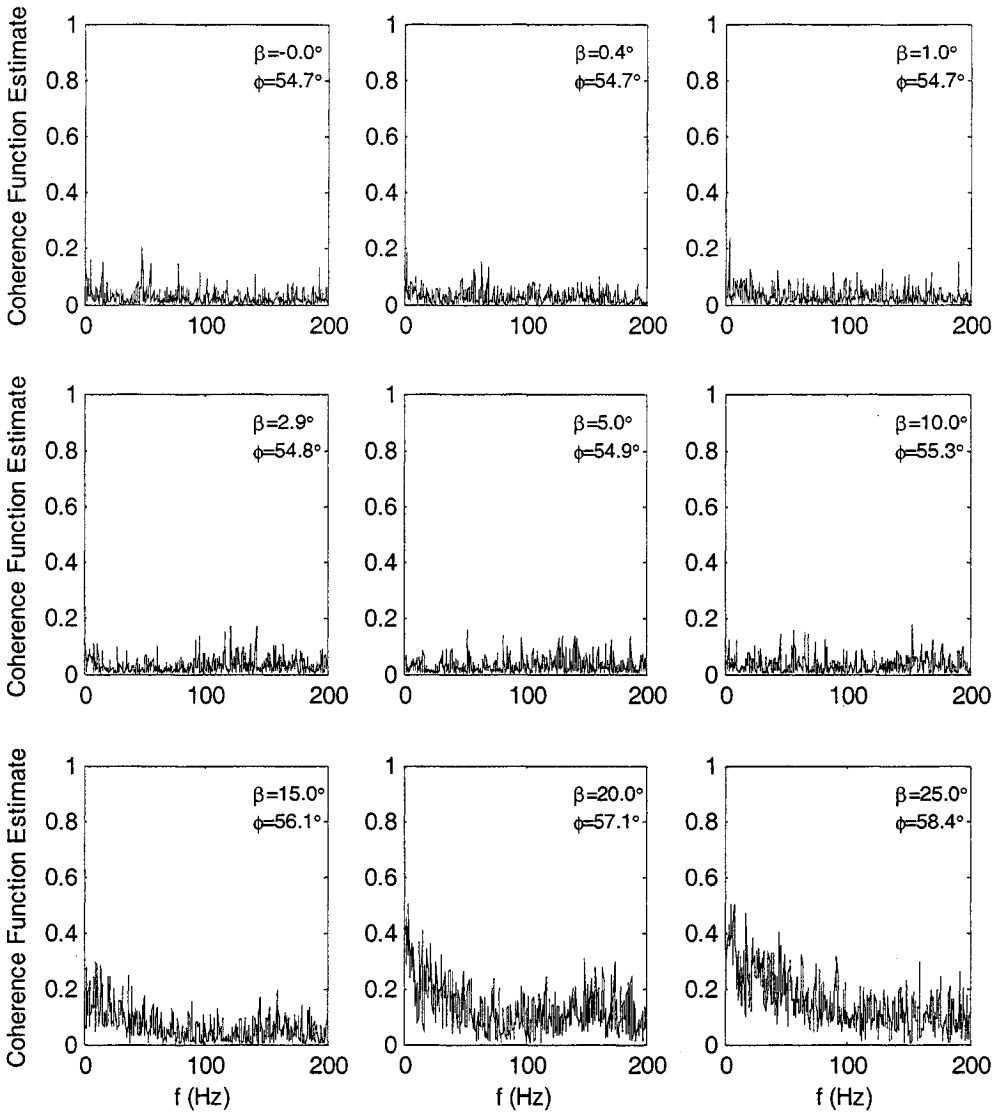

Figure K-5(a): Variation of coherence function of C_L for rings 2 and 4; $R_e=3.53\times10^5$, $\theta=54.7°$, low scan rate

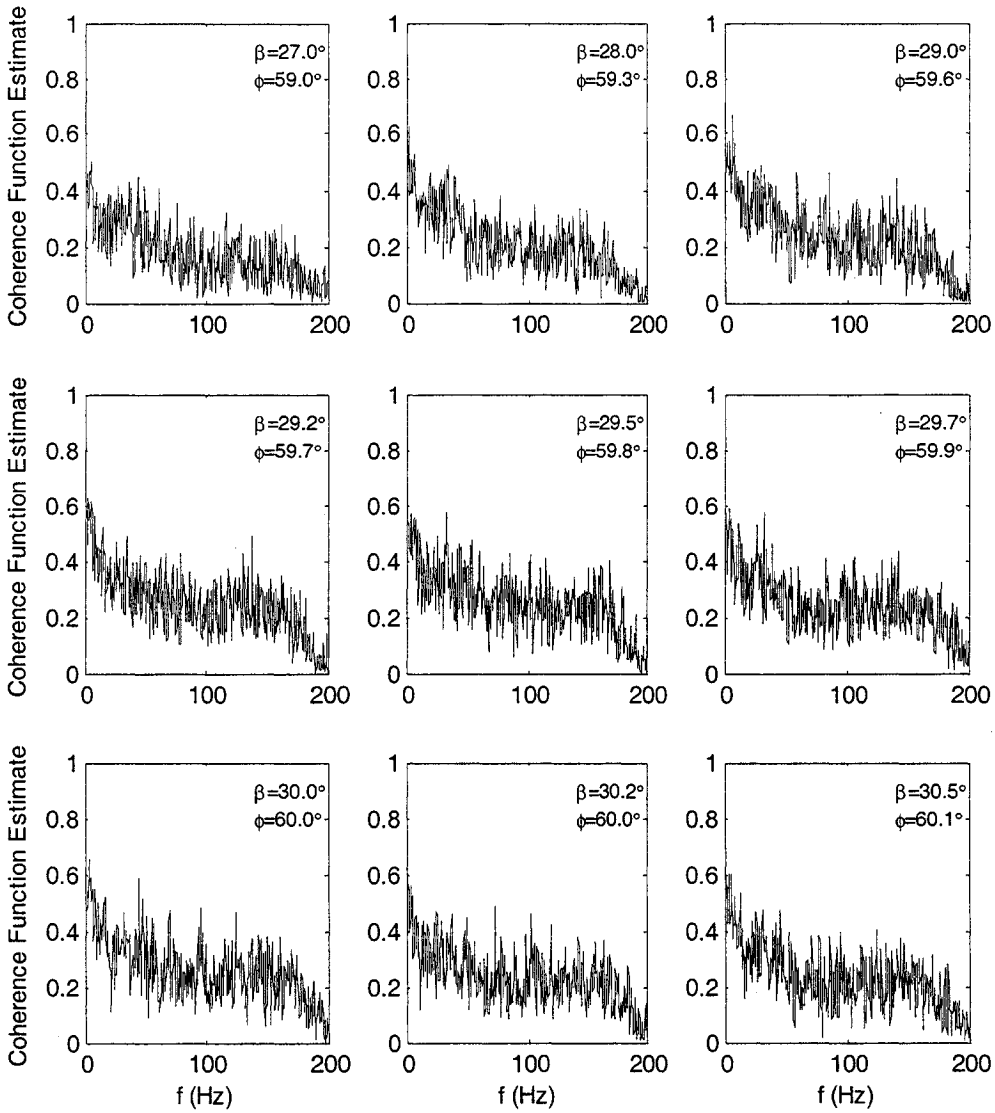

Figure K-5(b): Variation of coherence function of C_L for rings 2 and 4; $R_e=3.53\times10^5$, $\theta=54.7°$, low scan rate

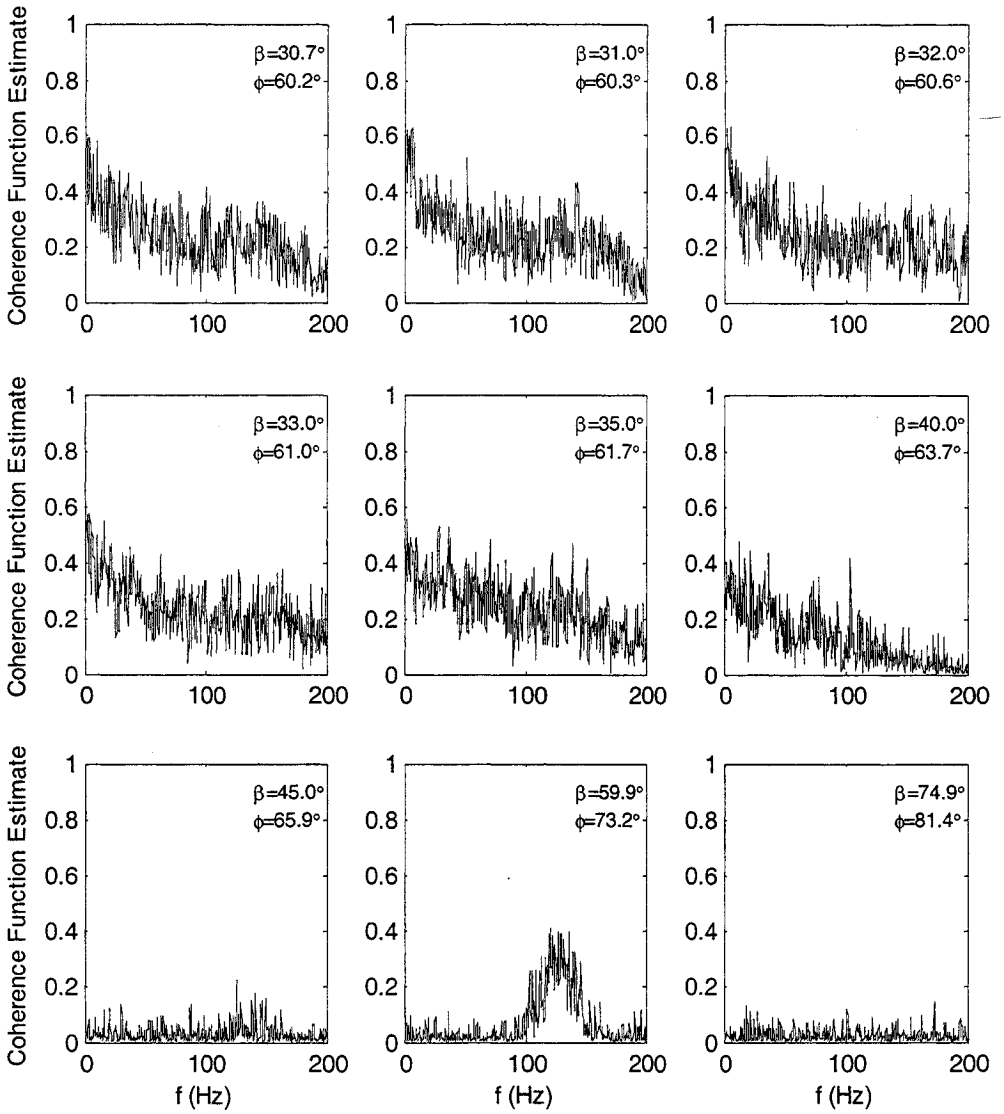

Figure K-5(c): Variation of coherence function of C_L for rings 2 and 4; $R_e=3.53\times10^5$, $\theta=54.7°$, low scan rate

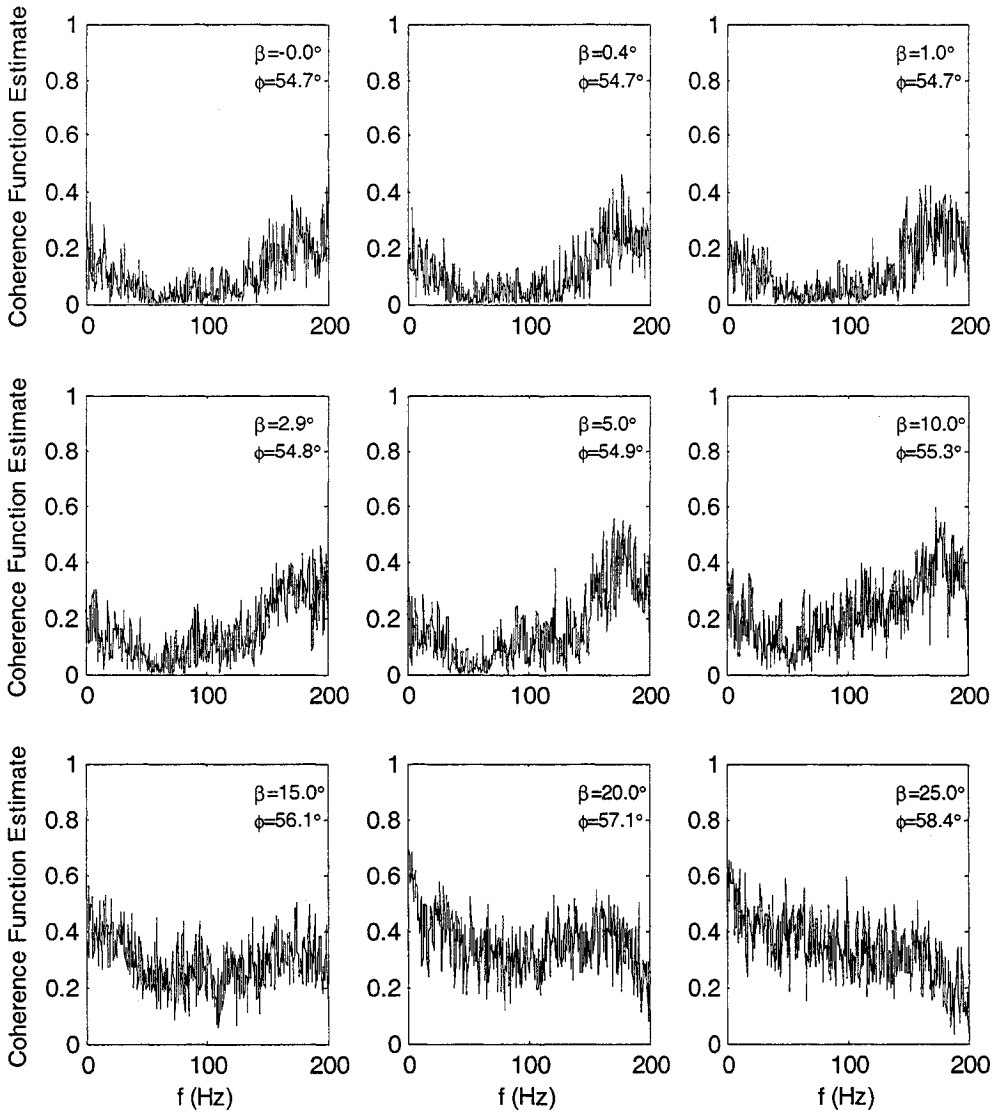

Figure K-6(a): Variation of coherence function of C_L for rings 2 and 3; $R_e=3.53\times10^5$, $\theta=54.7°$, low scan rate

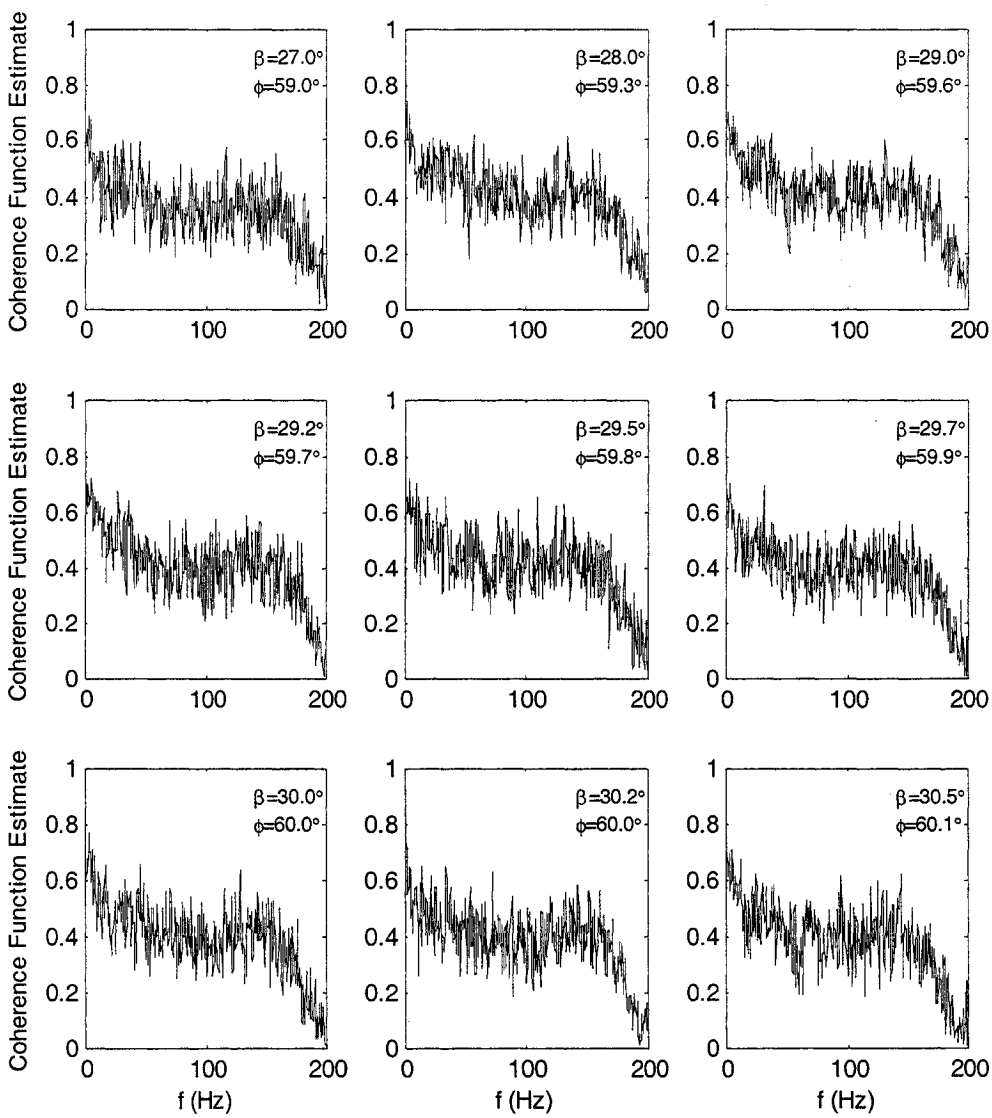

Figure K-6(b): Variation of coherence function of C_L for rings 2 and 3; $R_e=3.53\times10^5$, $\theta=54.7°$, low scan rate

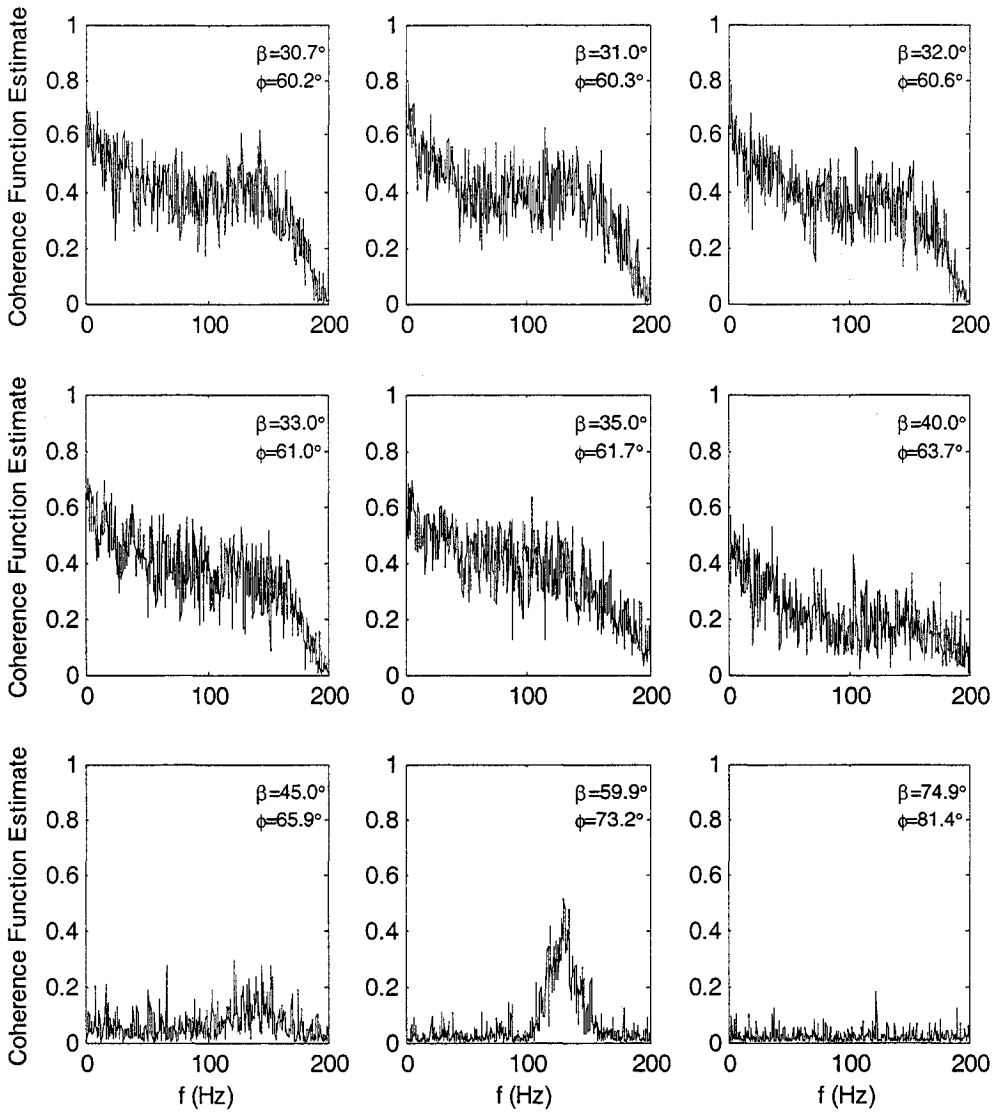

Figure K-6(c): Variation of coherence function of C_L for rings 2 and 3; $R_e=3.53\times10^5$, $\theta=54.7°$, low scan rate

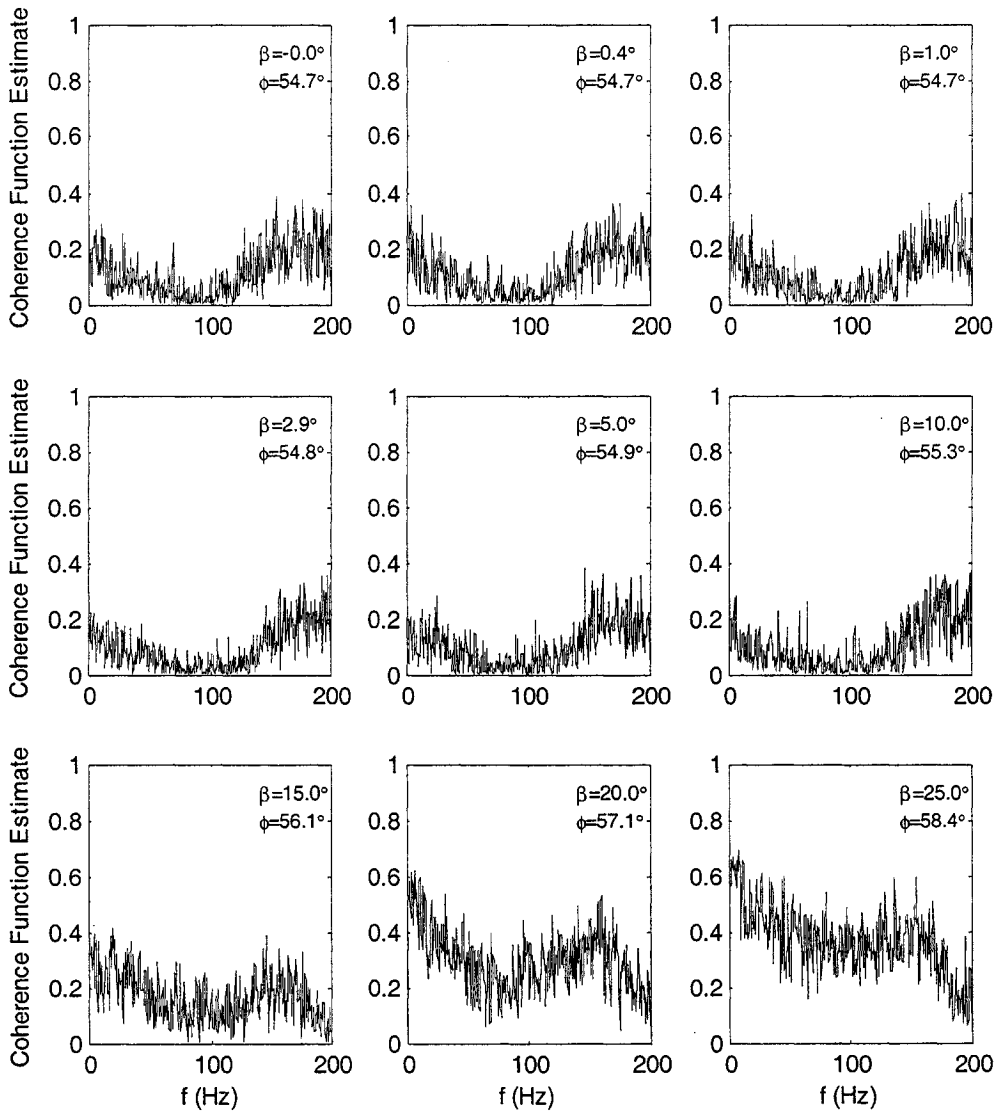

Figure K-7(a): Variation of coherence function of C_L for rings 3 and 5; $R_e=3.53\times10^5$, $\theta=54.7°$, low scan rate

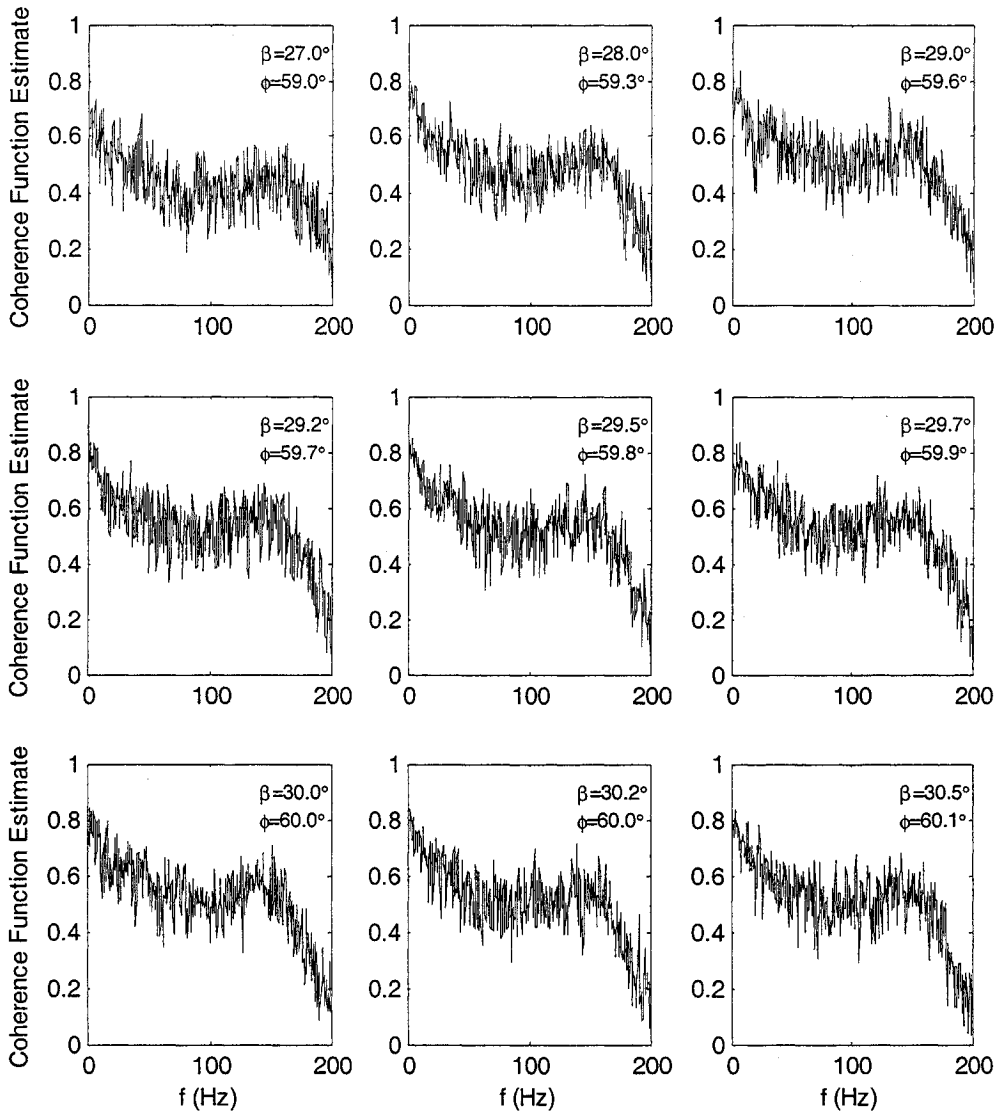

Figure K-7(b): Variation of coherence function of C_L for rings 3 and 5; $R_e=3.53\times10^5$, $\theta=54.7°$, low scan rate

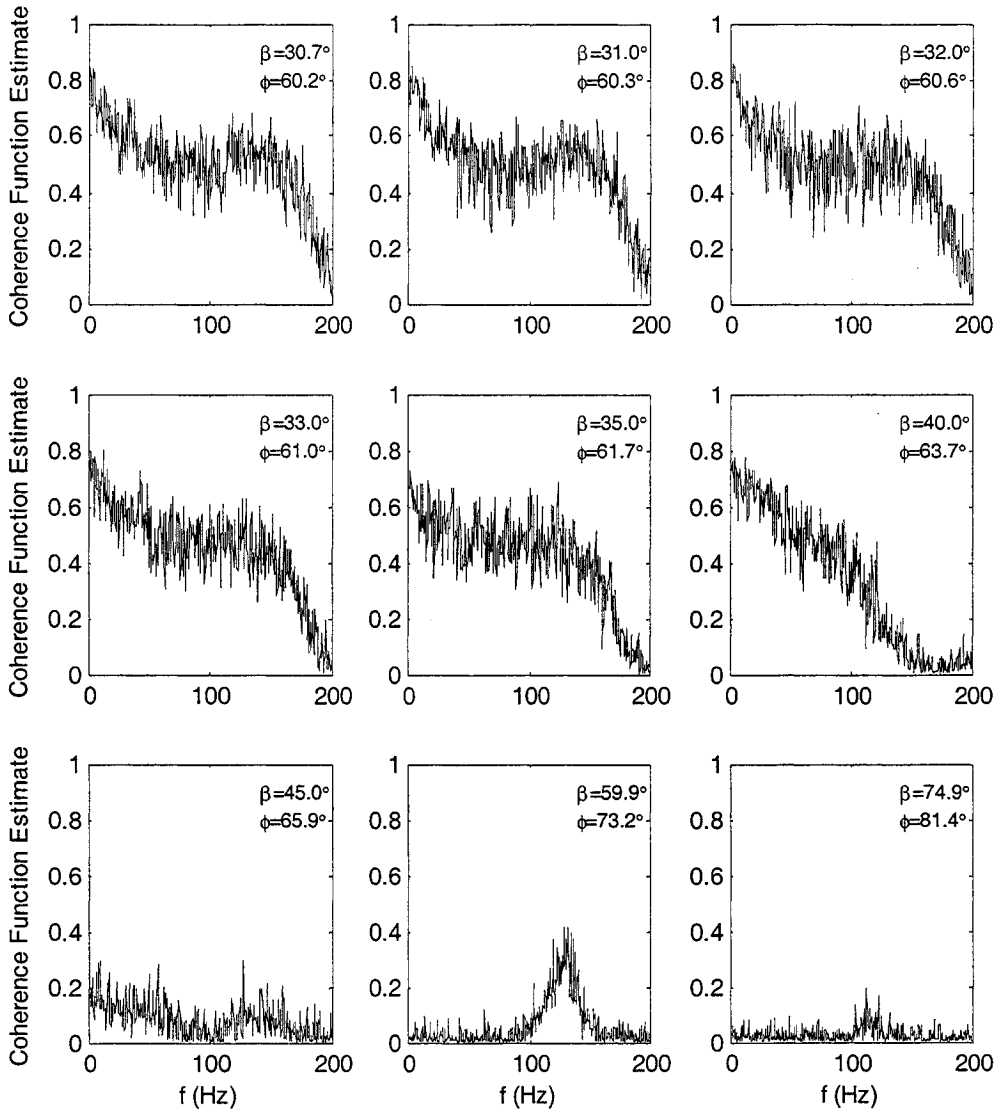

Figure K-7(c): Variation of coherence function of C_L for rings 3 and 5; $R_e=3.53\times10^5$, $\theta=54.7°$, low scan rate

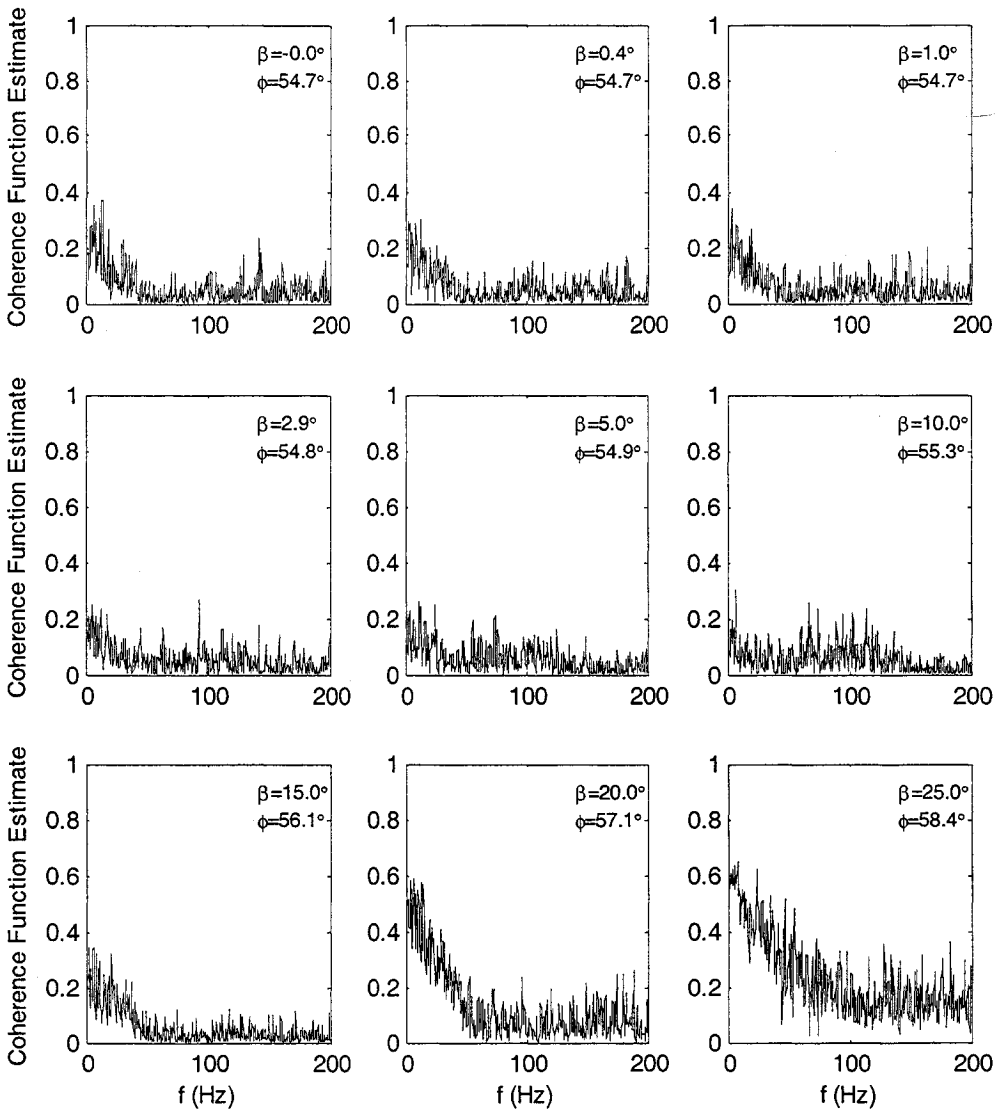

Figure K-8(a): Variation of coherence function of C_L for rings 3 and 4; $R_e=3.53\times10^5$, $\theta=54.7°$, low scan rate

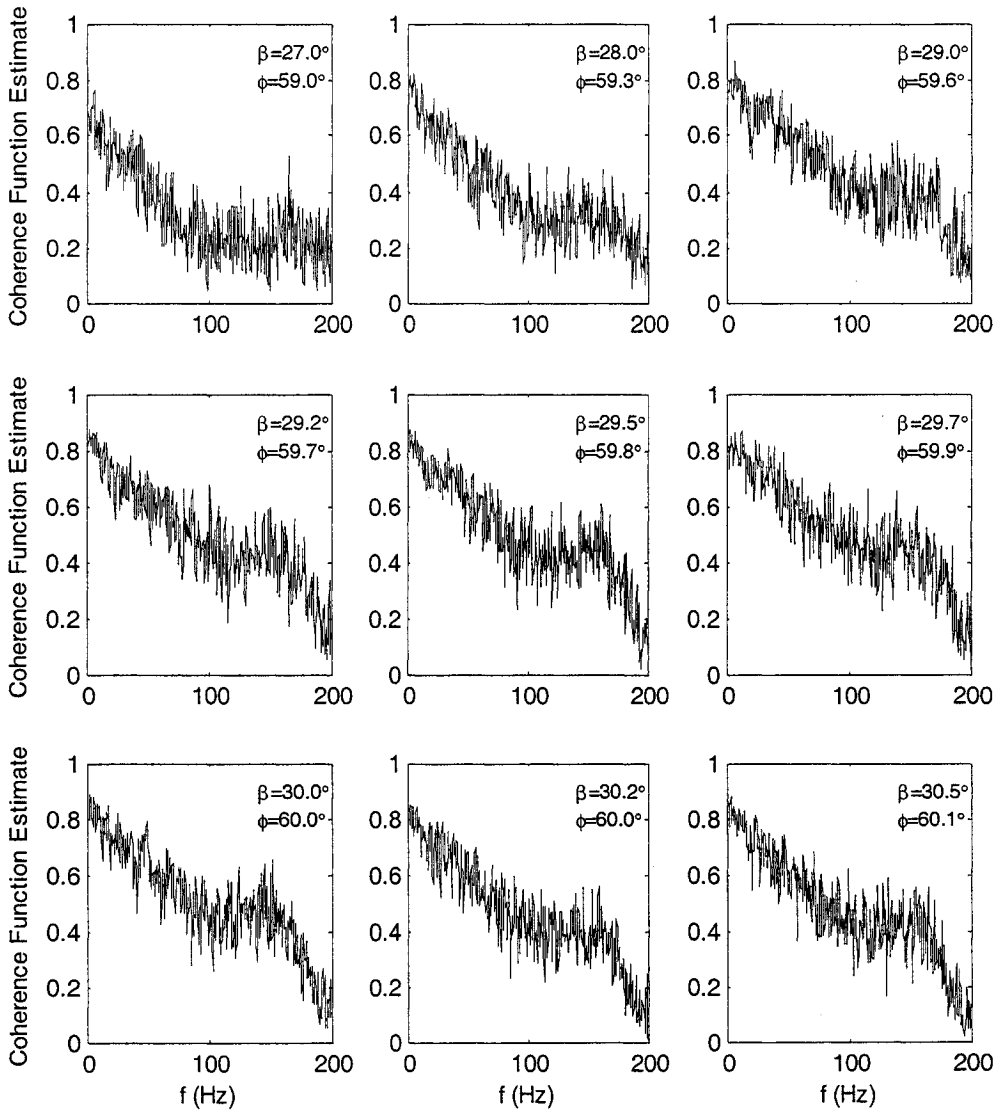

Figure K-8(b): Variation of coherence function of C_L for rings 3 and 4; $R_e=3.53\times10^5$, $\theta=54.7°$, low scan rate

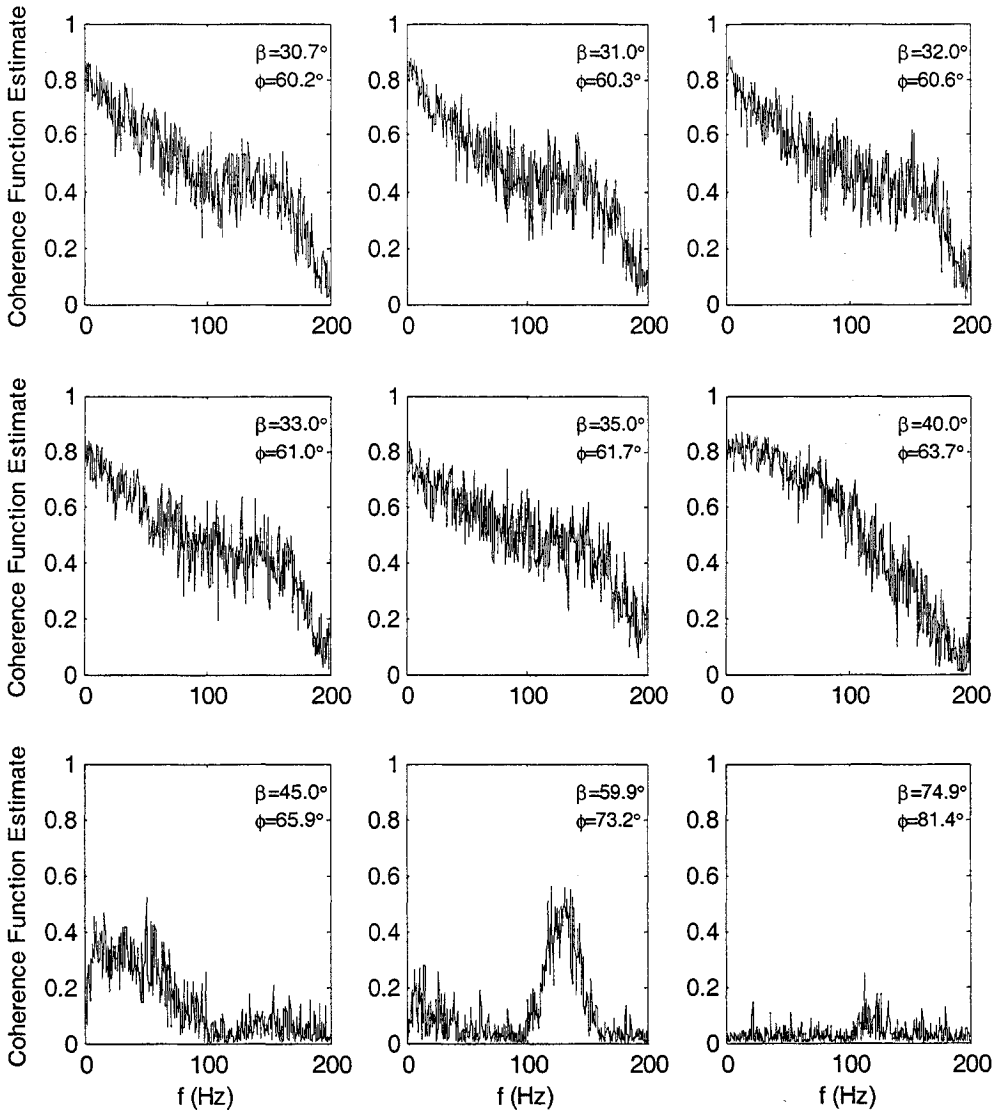

Figure K-8(c): Variation of coherence function of C_L for rings 3 and 4; $R_e=3.53\times10^5$, $\theta=54.7°$, low scan rate

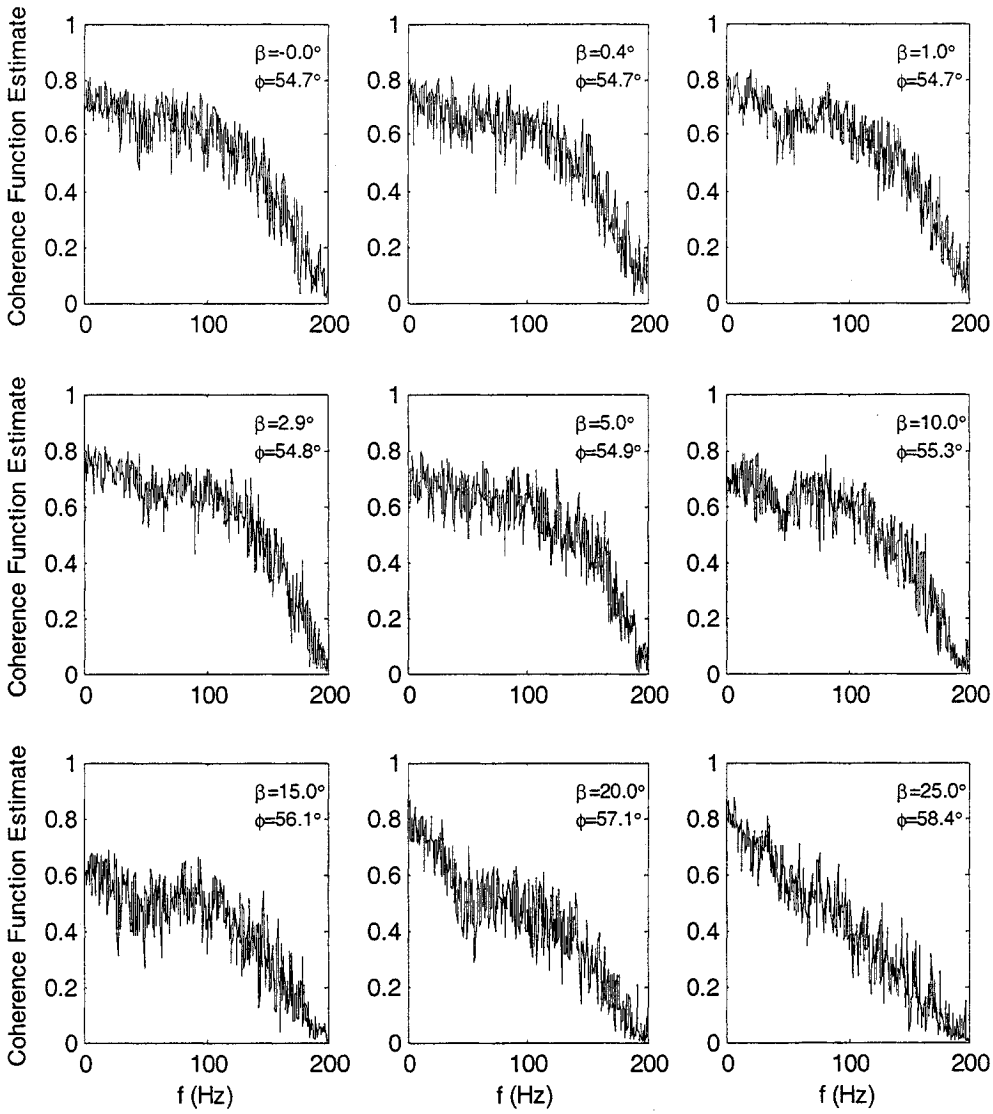

Figure K-9(a): Variation of coherence function of C_L for rings 4 and 5; $R_e=3.53\times10^5$, $\theta=54.7°$, low scan rate

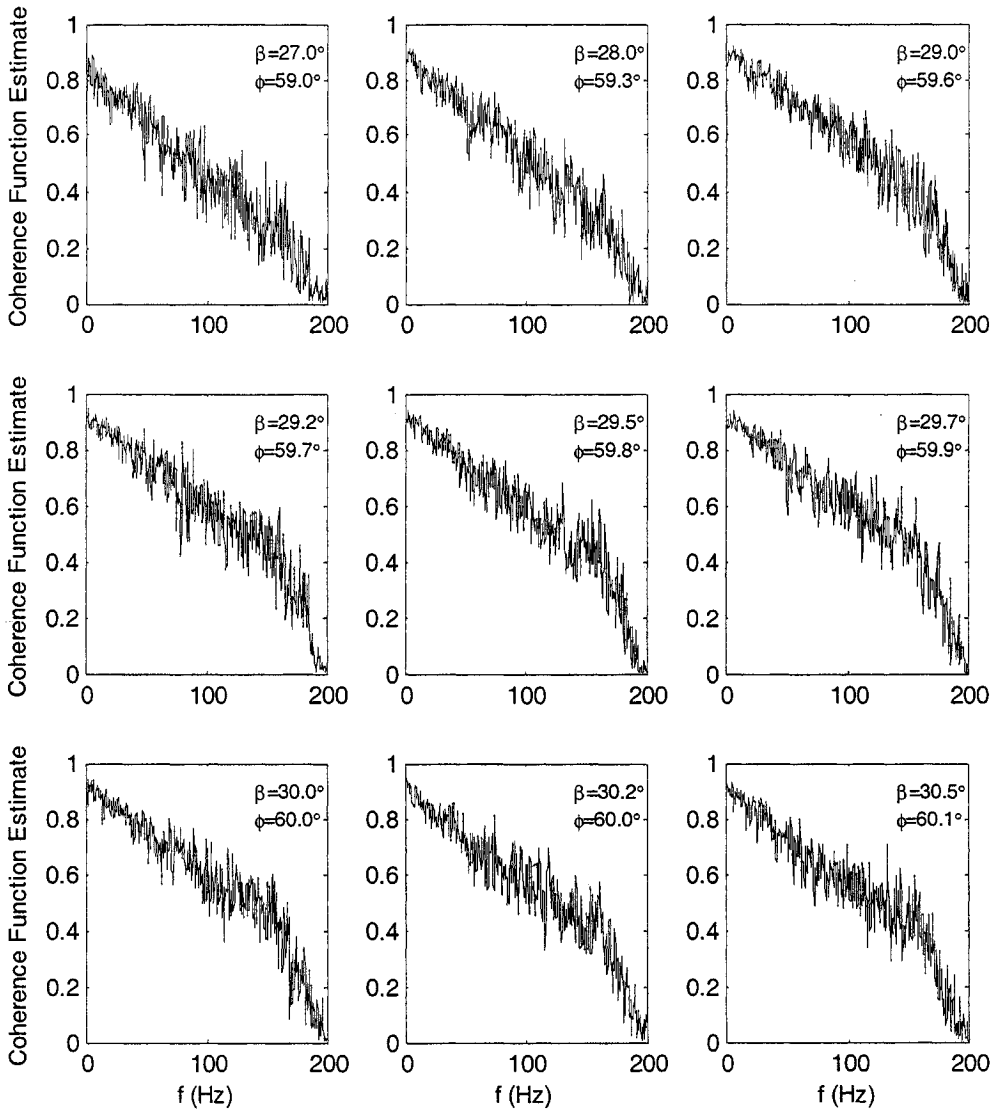

Figure K-9(b): Variation of coherence function of C_L for rings 4 and 5; $R_e=3.53\times10^5$, $\theta=54.7°$, low scan rate

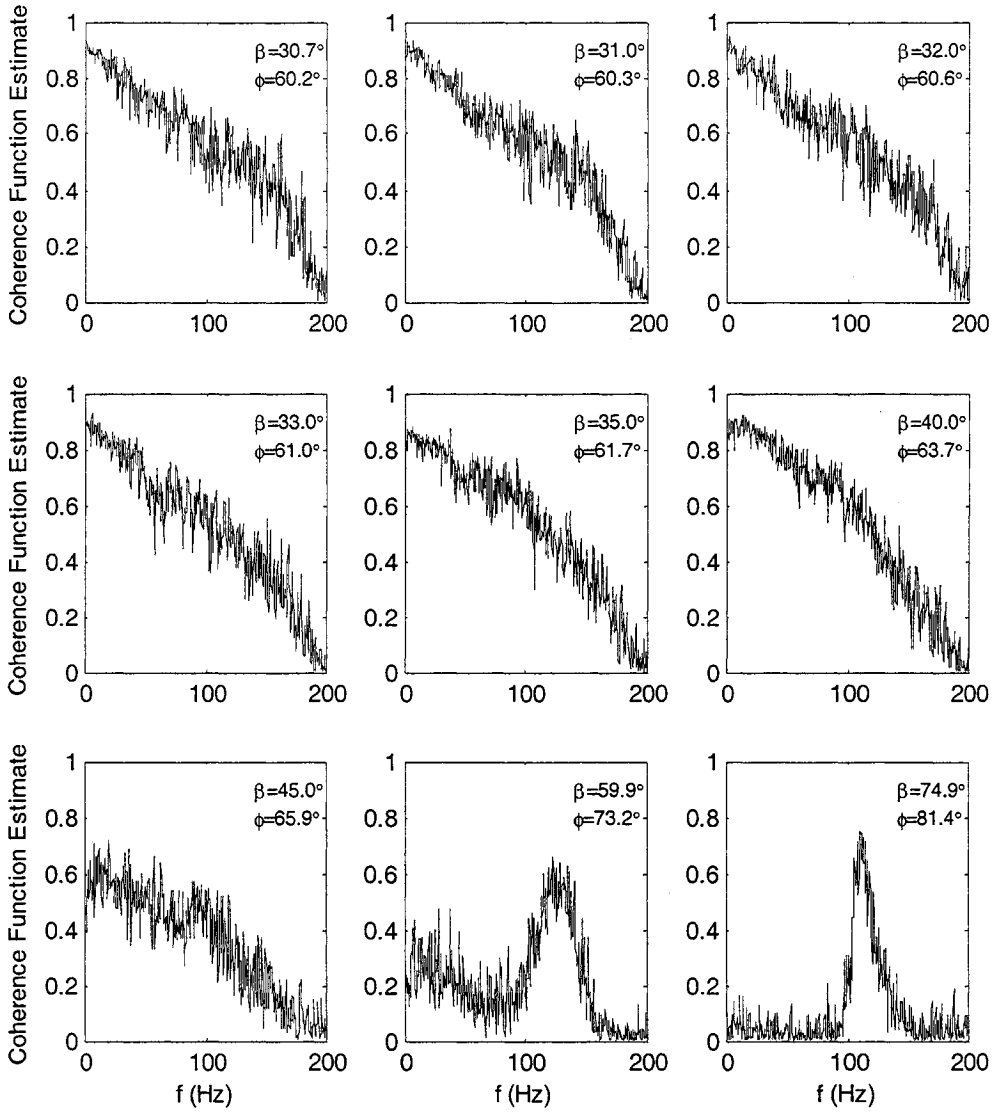

Figure K-9(c): Variation of coherence function of C_L for rings 4 and 5; $R_e=3.53\times10^5$, $\theta=54.7°$, low scan rate

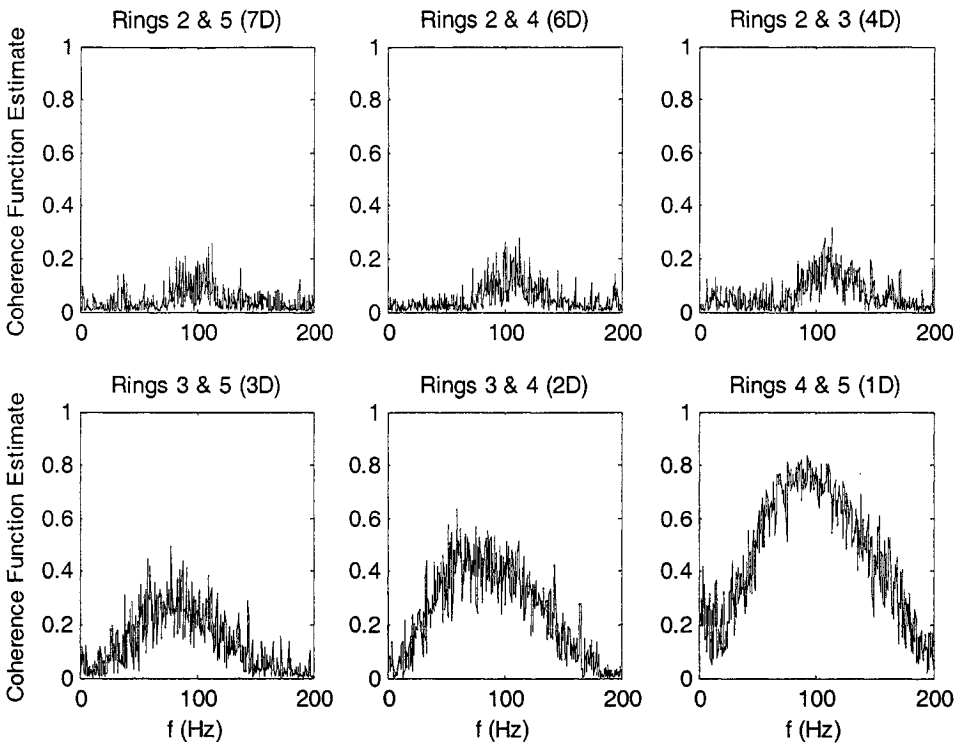

Figure K-10: Variation of coherence function of C_L for $R_e=2.95\times10^5$; $\theta=54.7°, \beta=30.0°, \phi=60°$, low scan rate

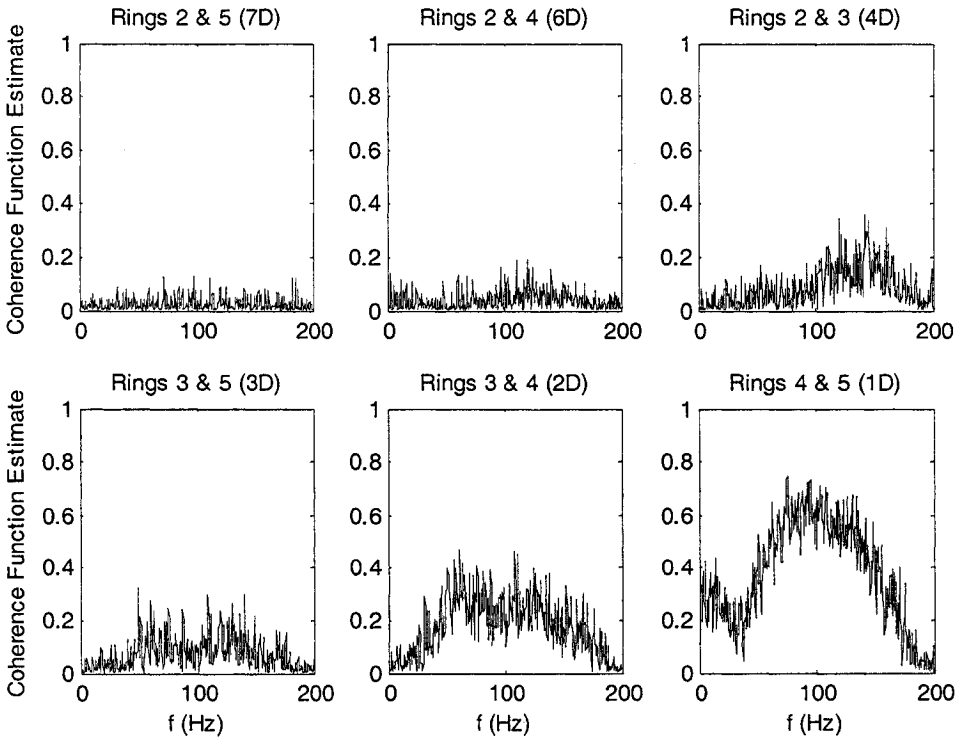

Figure K-11: Variation of coherence function of C_L for $R_e=3.25\times10^5$; $\theta=54.7°, \beta=30.0°, \phi=60°$, low scan rate

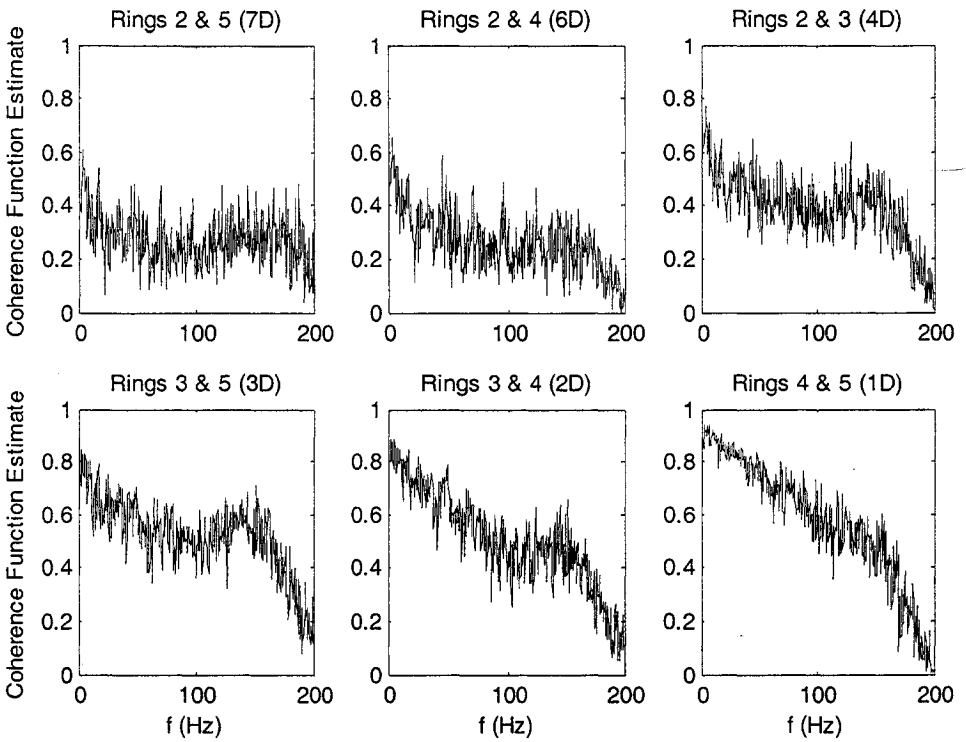

Figure K-12: Variation of coherence function of C_L for $R_e=3.53\times10^5$; $\theta=54.7°$, $\beta=30.0°$, $\phi=60°$, low scan rate

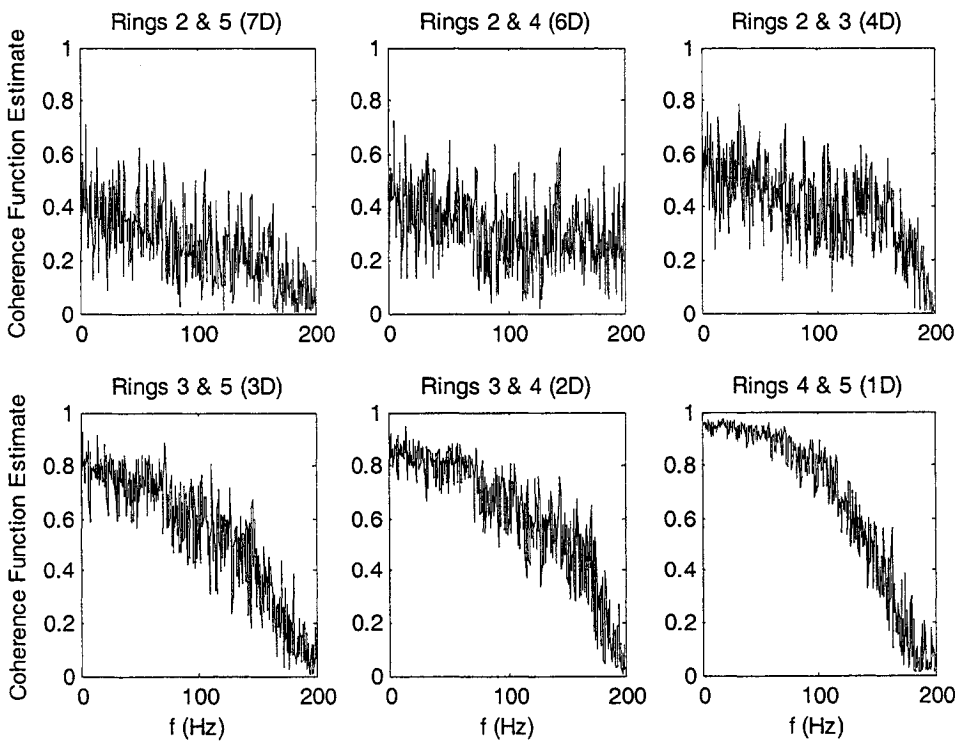

Figure K-13: Variation of coherence function of C_L for $R_e=3.55\times10^5$; $\theta=54.7°$, $\beta=30.0°$, $\phi=60°$, low scan rate

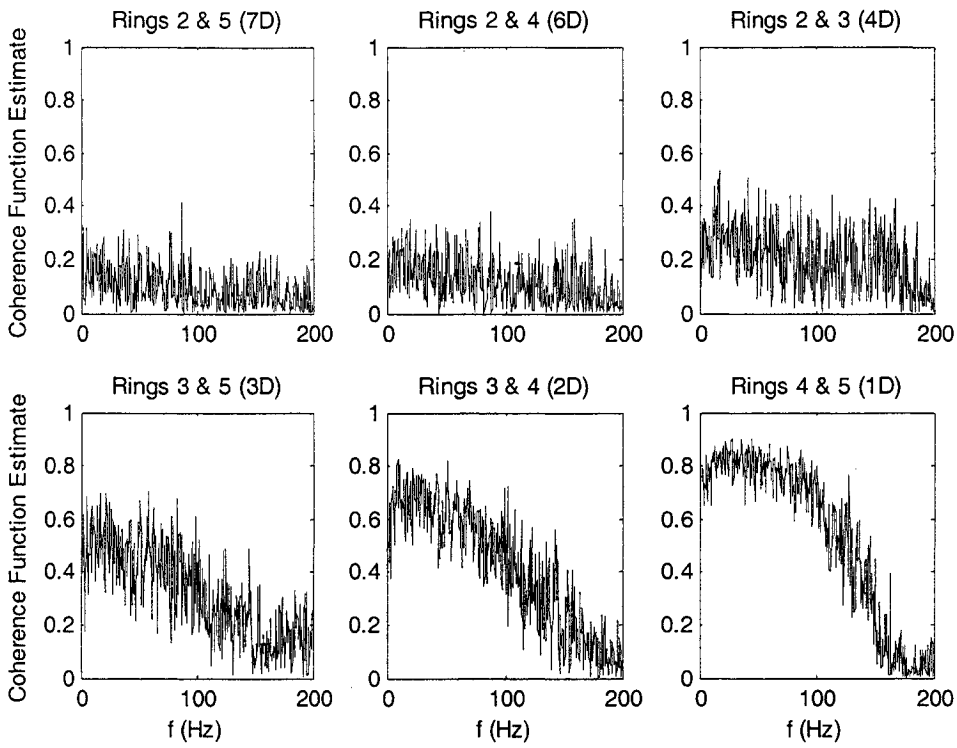

Figure K-14: Variation of coherence function of C_L for $R_e=3.62\times10^5$; $\theta=54.7°$, $\beta=30.0°$, $\phi=60°$, low scan rate

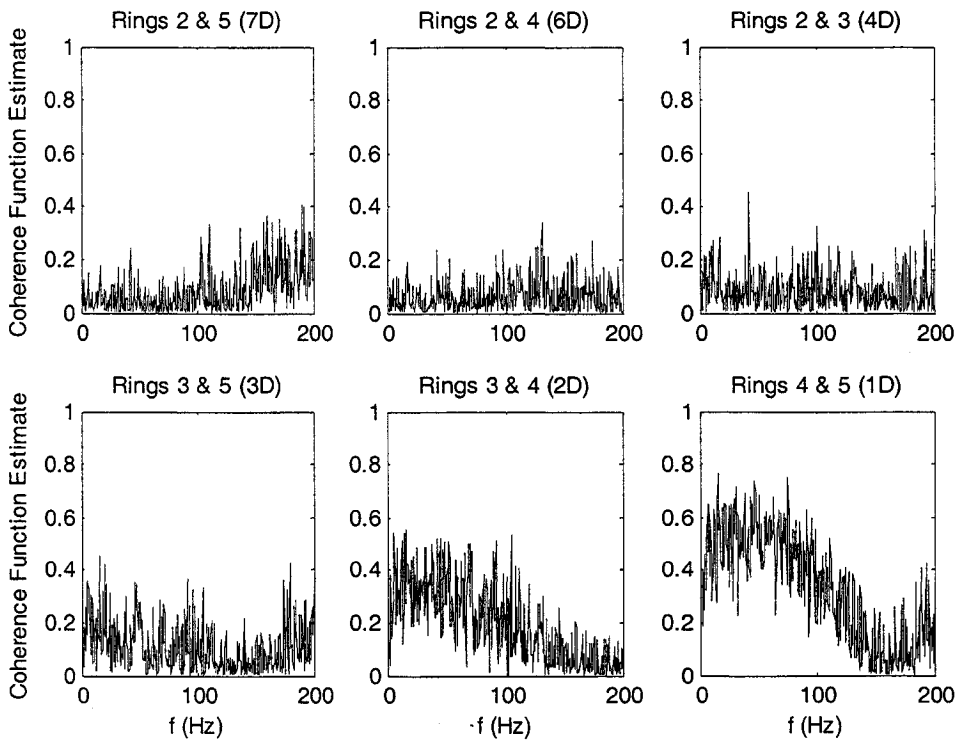

Figure K-15: Variation of coherence function of C_L for $R_e=3.74\times10^5$; $\theta=54.7°$, $\beta=30.0°$, $\phi=60°$, low scan rate

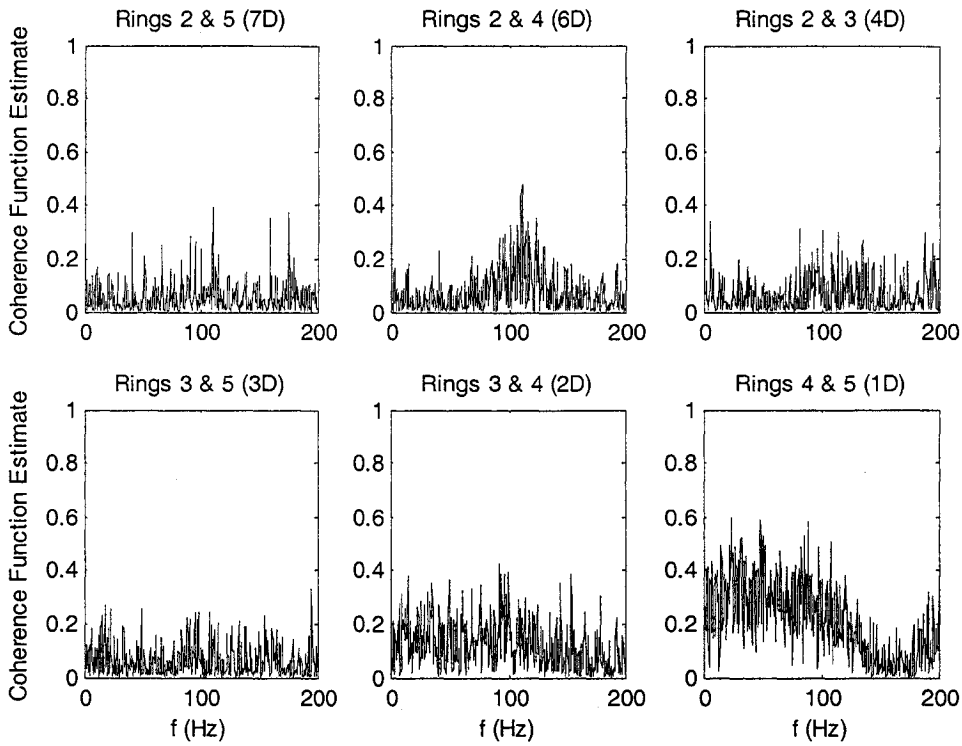

Figure K-16: Variation of coherence function of C_L for $R_e=4.0\times10^5$; $\theta=54.7°$, $\beta=30.0°$, $\phi=60°$, low scan rate

Appendix L: Wind Tunnel Model Natural Frequency Records

In the following figures:

Tare represents the record of the ambient conditions.

Strong Axis and *Weak Axis* refer to the (initially) along-wind and across-wind directions, respectively, in which the model was caused to vibrate.

Lower Mode and *Higher Mode* refer to the manner in which the model was struck so as to attempt to excite the fundamental vibration mode and higher vibration modes, respectively.

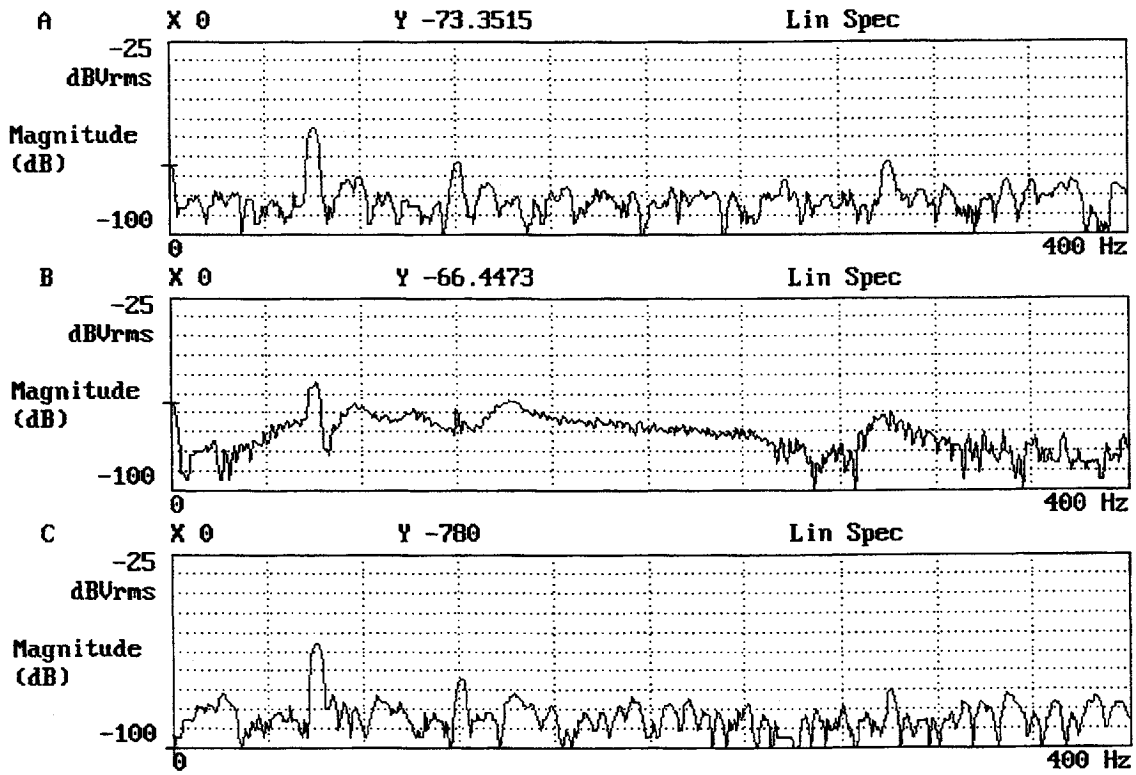

Figure L-1: Model vertical: A) Tare; B) Strong Axis Lower Mode; C) Strong Axis Higher Mode

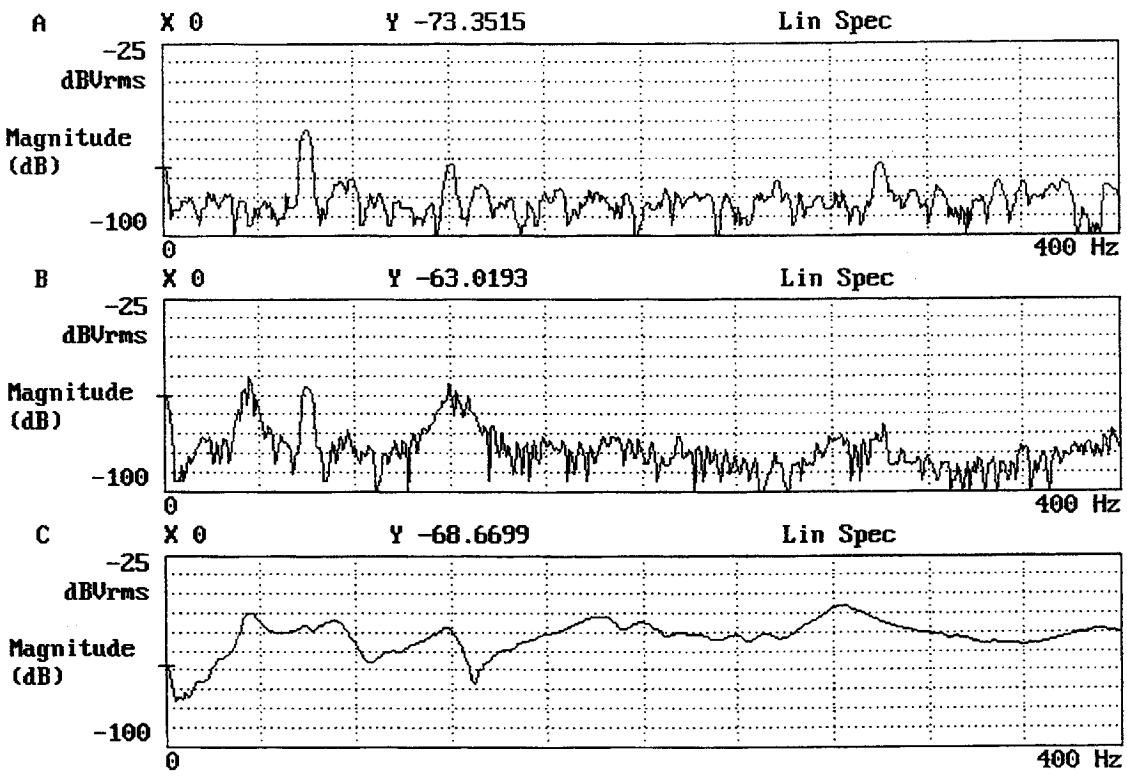

Figure L-2: Model vertical: A) Tare; B) Weak Axis Lower Mode; C) Weak Axis Higher Mode

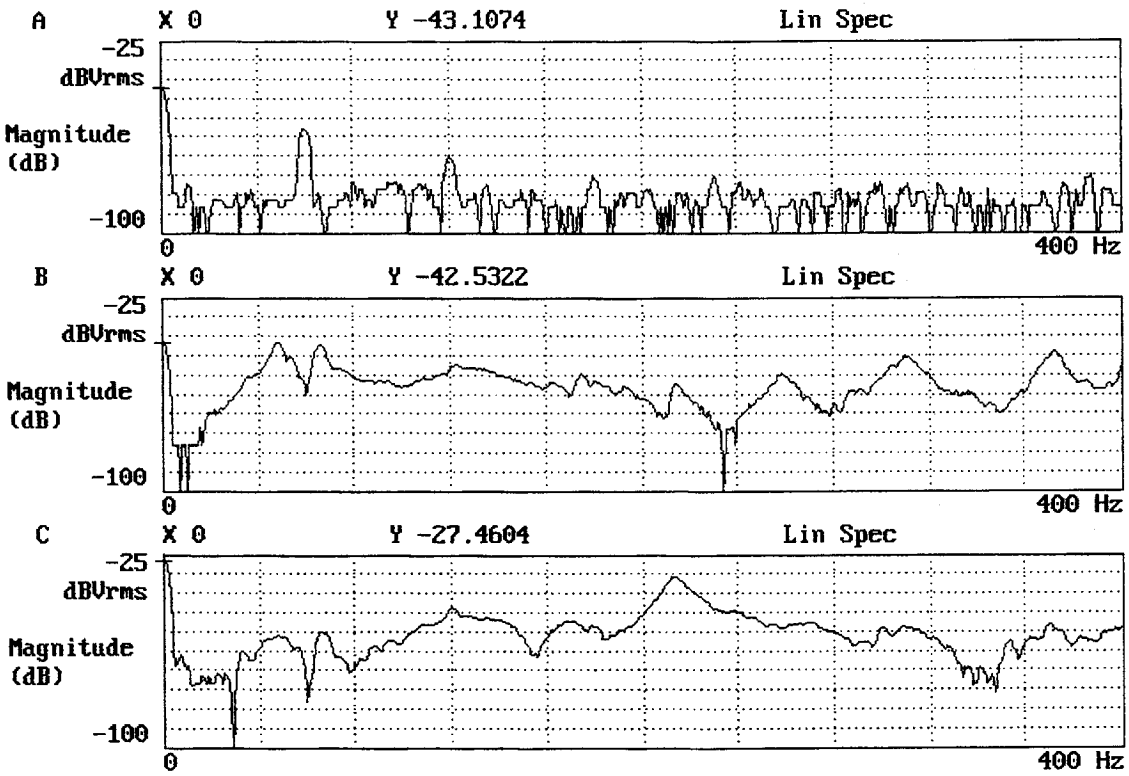

Figure L-3: Model inclined to θ=60°: A) Tare; B) Strong Axis Lower Mode; C) Strong Axis Higher Mode

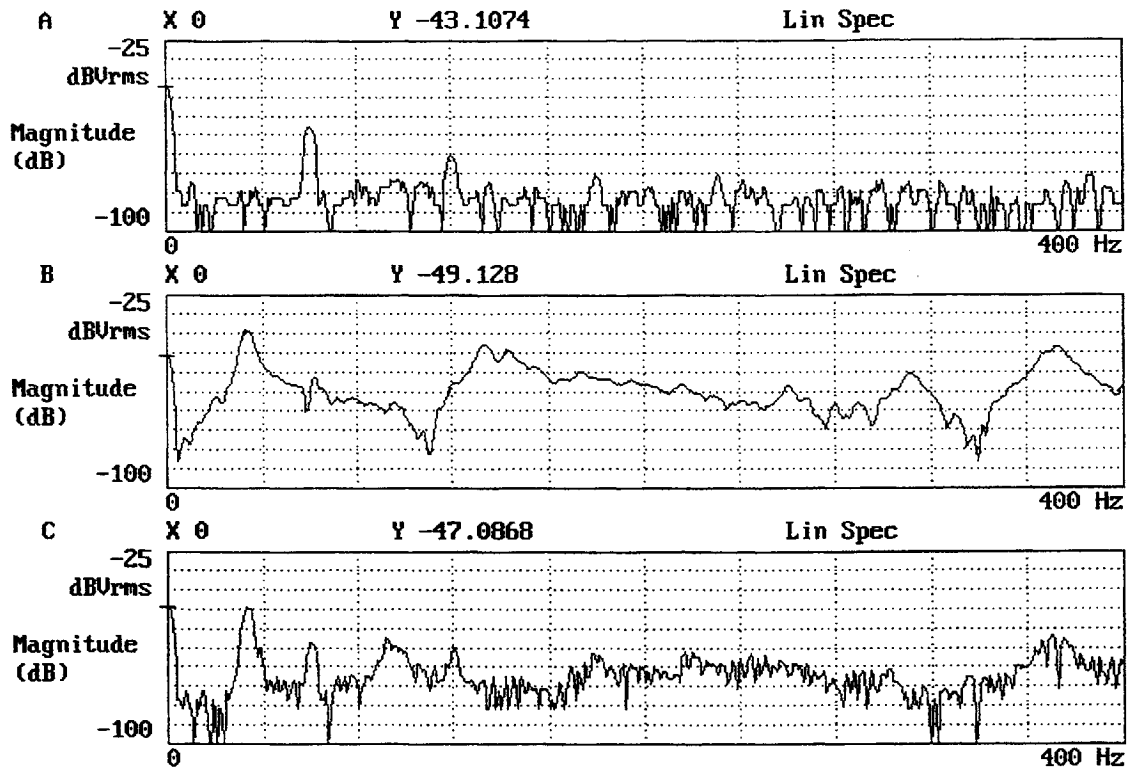

Figure L-4: Model inclined to θ=60°: A) Tare; B) Weak Axis Lower Mode; C) Weak Axis Higher Mode

Appendix M: MATLAB Programs

```
function pressure
%
%created by Cory Zurell
%November 2002
%
%This program performs the following functions:
%1. Calculates the resultant forces, lift and drag, for each ring of  pressure taps of the cable model.
%2. calculates the lift and drag coefficients for use in the evaluation of  the Den Hartog criterion for aerodynamic instability.
%
%Required Input:
%  A   -frame list - 192x3, each row holds module#/port#/tap#
%  l   -tap position list - 192x1, each row represents a tap# - row 1=3
%  indicates that tap 1 information is located in row 3 of "pressureData"
%  Re  -1x1, holds the Reynolds Number for the run
%  U   -1x1, holds the windspeed for the run - "19.597" [m/s]
%  fname      1x11, characters, holds file name
%  frameFILE   1x12, characters, holds frame list file name
%  hBeta      1x1, yaw angle for the run - "14.98" [degrees]
%  pressureData 192x48098, holds time history pressure data for each tap
%             each row represents one tap, the order of taps is given
%             in array "l" - values are in [psi]
%  q   1x1, mean dynamic pressure of the free stream
%     static pressure of the air flow - "1.4807" [kPa]
%  spRate  1x1, sampling rate - "400.64" [Hz]
%  spTime  1x1, sampling duration - "120.13" [s]
%  valpha  1x1, vertical inclination angle - "54.7" [degrees]
%  z_off   1x1, tunnel pressure, static offset - "0.081594" [kPa]
%
%  The above info is contained in *.mat files labelled as follows:
%  2 digits - vertical inclination angle (90, 60, 55(54.7))
%  5 digits - horizontal yaw angle (00025=0.25deg, 00100=1.00deg)
%  3 digits - wind velocity (100=10.0m/s, 525=52.5m/s)
%  1 digit  - sampling rate (h - 1200 Hz (64 taps), m- 400 Hz (192 taps))
%  2 digits - running sequence (01 - run 1)
%  2 letters- type of file (rd - raw data, cd - corrected data, rs - raw
%           data summary, cs - corrected data summary)
% Example: 90_00000_896_m_01_cd.mat
%
%
%*****
load directory.mat;
k=size(directory);
for j=1:1:k(1);
   load directory.mat;
   cd([directory(j,:)]);
   file=strcat('files',directory(j,18:20),'.mat');
%*****
%
%*****
   load(file); %contains a list of the file names in each directory
   m=size(files);
for i=1:1:m(1);
   z=files(i,:);
   load(z);
   pressureData=double(pressureData(l,:)); %convert to double precision and
   %data in order of taps given by matrix l
   if (frameFile(6)=='1');
      pressureData=pressureData(1:160,:); %truncates the array of the data
% taps corresponding to the longitudinal lines are not needed at this time
   end
%
   pressureData=pressureData*6894.4; %converts "pressureData" to Pa from psi
   hBeta=hBeta*pi/180; %converts units from degrees to radians for calculations
   vAlpha=vAlpha*pi/180;
   phi=acos(cos(vAlpha)*cos(hBeta)); %relative angle between wind and cable
   if hBeta>pi/2; %This corrects phi for yaw angles greater than 90
```

```
      phi=pi-phi;
   end;
   gamma=atan(tan(hBeta)/sin(vAlpha)); %relative angle between wind direction and benchmark tap
   if hBeta>pi/2;
      if gamma<0; %This line corrects gamma for yaw angles greater than 90 degrees
         gamma=pi+gamma;
      end;
   end;
   q=q*1000; %convert to Pa
   z_off=z_off*1000;
%
% Correction for damaged taps and set calculation variables
   if (frameFile(6)=='1');%low scan case, frameFile is of the form wt750192.frm
      pressureData(64,:)=mean(pressureData([33 63],:));
      pressureData(142,:)=mean(pressureData([141 143],:));
      x=1;
      y=5;
      n=1;
   end;
   if (frameFile(6)=='_');%high scan case, frameFile is of the form wt750_64.frm
      pressureData(32,:)=mean(pressureData([1 31],:));
      x=2;
      y=4;
      n=2;
   end;
% The mean values of pressure are required for each tap to calculate the
% lift and drag forces
   meanpress=(-1)*mean(pressureData,2); % Column vector "meanpress" contains
   %the mean values of each tap
%
   load coords.mat; %coordinates of tap locations
% Calculation of the drag and lift forces and coefficients for each ring.
   for ring=x:n:y;
      base=32*((ring/n)-1);
      drag(ring)=sum(meanpress(base+1:base+32).*coords(:,3).*(cos(coords(:,2)).*cos(gamma)...
         +sin(coords(:,2)).*sin(gamma)));
      lift(ring)=(-1)*sum(meanpress(base+1:base+32).*coords(:,3).*(sin(coords(:,2)).*cos(gamma)...
         -cos(coords(:,2)).*sin(gamma)));
      Cd(ring)=drag(ring)/(q*0.0889);
      Cl(ring)=lift(ring)/(q*0.0889);
   end;
%
   output(i,:)=[U,Re,phi,gamma,vAlpha,hBeta,Cd,Cl];
end;
if (frameFile(6)=='_'); %condenses output data
   output(:,7)=output(:,8);
   output(:,8)=output(:,10);
   output(:,9)=output(:,12);
   output(:,10)=output(:,14);
   output=output(:,1:10);
end;
filename=strcat(z(1:2),'_summary_',file(6:8),'.mat');
save(filename,'output');
clear;
end;
```

```
function reynolds
%This function plots the lift and drag coefficients, Cn and Cl, against the
%windspeed and Reynolds number.
%
%Required input is files of the form **_summary_***.mat produced using "pressure"
%
file=input('Enter the summary "**_summary_***.mat" filename corresponding \n to the data in this directory:','s')
load(file);
figure;
style=['-dk';'-+k';'-ok';'-*k';'-xk'];
titleline=strcat('\bfC_N versus windspeed');
xlabeltag='Wind speed, U(m/s)';
m=size(output);
%
subplot(1,2,1); %plots Cd versus U
if m(2)==10;
   plot(output(:,1),output(:,7),style(2,:),output(:,1),output(:,8),style(4,:));
   legend('Ring 2','Ring 4',4);
end;
if m(2)==16;
%    plot(output(:,1),output(:,7),style(1,:),output(:,1),output(:,8),style(2,:),...
%       output(:,1),output(:,9),style(3,:),output(:,1),output(:,10),style(4,:),...
%       output(:,1),output(:,11),style(5,:));
%    legend('Ring 1','Ring 2','Ring 3','Ring 4','Ring 5',4);
   plot(output(:,1),output(:,8),style(2,:),...
      output(:,1),output(:,9),style(3,:),output(:,1),output(:,10),style(4,:),...
      output(:,1),output(:,11),style(5,:));
   legend('Ring 2','Ring 3','Ring 4','Ring 5',4);
end;
axis([10 100 -1.5 1.5]);
ax=[10 100 -1.5 1.5]; %limits to set secondary axis - same as 'axis' above
xlabel(xlabeltag);
ylabel('Mean C_N');
title(titleline);
grid on;
%This section adds the secondary x-axis with Reynolds Number
 pos=get(gca,'position');
 shift=[0 .11 0 -.11];
 pos= pos + shift;
 set(gca,'position',pos);
 axes('position', [pos(1:3)-(shift(1:3)) 0.01]);
 low=ax(1)*output(1,2)/output(1,1)/1000;
 high=ax(2)*output(m(1),2)/output(m(1),1)/1000;
 set(gca,'XLim',[low high]);
 xlabel('Reynolds Number (x1000)');
%
subplot(1,2,2); %plots Cl versus U
%
if m(2)==10;
   plot(output(:,1),output(:,9),style(2,:),output(:,1),output(:,10),style(4,:));
end;
if m(2)==16;
%    plot(output(:,1),output(:,12),style(1,:),output(:,1),output(:,13),style(2,:),...
%       output(:,1),output(:,14),style(3,:),output(:,1),output(:,15),style(4,:),...
%       output(:,1),output(:,16),style(5,:));
   plot(output(:,1),output(:,13),style(2,:),...
      output(:,1),output(:,14),style(3,:),output(:,1),output(:,15),style(4,:),...
      output(:,1),output(:,16),style(5,:));
end
axis([10 100 -1.5 1.5]);
ax=[10 100 -1.5 1.5]; %This value has to be the same as 'axis' above
xlabel(xlabeltag);
ylabel('Mean C_L');
title('\bfC_L versus windspeed');
grid on;
%
%This section adds the secondary x-axis with Reynolds Number
 pos=get(gca,'position');
 shift=[0 .11 0 -.11];
 pos= pos + shift;
```

```
  set(gca,'position',pos);
  axes('position', [pos(1:3)-(shift(1:3)) 0.01]);
  low=ax(1)*output(1,2)/output(1,1)/1000;
  high=ax(2)*output(m(1),2)/output(m(1),1)/1000;
  set(gca,'XLim',[low high]);
  xlabel('Reynolds Number (x1000)');
%
% This section adds run information to the bottom of the figure
    h = axes('Position',[0 0 1 1],'Visible','off');
    set(gcf,'CurrentAxes',h);
    str={strcat('\bf\theta=',file(1:2),'\circ incline, \beta=',num2str(output(1,6)*180/pi,'%2.0f'),'\circ yaw')};
    text(0.4,0.025,str,'Fontsize',10);
    set(gcf,'Color',[1,1,1]);
```

```
function denhartogplot
%This function plots the drag coefficient, Cd, the lift coefficient, Cl, the
%slope of the lift coefficient, dCl/d(gamma), and the sum of the drag coeff.
%plus the slope of the lift coeff. against the wind angle of attack
%The slope of the lift coefficient ,dCl/d(gamma), is calculated based
%on the average of the slopes taken on either side of the angle of
%interest. e.g. the slope at an angle of 30 will be based on the average of
%the slopes taken from 29.75 to 30 and from 30 to 30.25.
%
file=input('Enter the summary "**_summary_***.mat" filename corresponding \n to the data in this directory:','s')
load(file);
figure;
style=[': k';'-+k';'-ok';'-*k';'-xk'];
titleline=strcat('\bfC_N versus \gamma');
xlabeltag='Angle of attack, \gamma (\circ)';
m=size(output);
 axis1=[-1 120 -1 1.5];
 axis2=[-1 120 -5 5];
if m(2)==10;
%Plot of drag coefficient versus angle of attack
   subplot(2,2,1);
      plot(output(:,4)*180/pi,output(:,7),style(2,:),output(:,4)*180/pi,output(:,8),style(4,:));
      legend('Ring 2','Ring 4',4);
      axis(axis1);
      xlabel(xlabeltag);
      ylabel('C_N');
      title(titleline);
      grid on;
%Plot of lift coefficient versus angle of attack
   subplot(2,2,2);
      plot(output(:,4)*180/pi,output(:,9),style(2,:),output(:,4)*180/pi,output(:,10),style(4,:));
      axis(axis1);
      xlabel(xlabeltag);
      ylabel('C_L');
      title('\bfC_L versus \gamma');
      grid on;
% Calculate the slope of the lift coefficient at each angle of attack
   for i=2:1:m(1)-1;
      slopeCL(i,1)=output(i,4)*180/pi;
      slopeCL(i,2)=(((output(i,9)-output(i-1,9))/(output(i,4)-output(i-1,4)))+...
         ((output(i+1,9)-output(i,9))/(output(i+1,4)-output(i,4))))/2;
      slopeCL(i,3)=(((output(i,10)-output(i-1,10))/(output(i,4)-output(i-1,4)))+...
         ((output(i+1,10)-output(i,10))/(output(i+1,4)-output(i,4))))/2;
      slopeCL(i,4)=output(i,7)+slopeCL(i,2);%Cd+dCL/dg
      slopeCL(i,5)=output(i,8)+slopeCL(i,3);
   end;
   slopeCL(1:m(1)-2,:)=slopeCL(2:m(1)-1,:);
%Plot of the slope of the lift coefficient versus angle of attack
   subplot(2,2,3);
      plot(slopeCL(:,1),slopeCL(:,2),style(2,:),slopeCL(:,1),slopeCL(:,3),style(4,:));
      axis(axis2);
      xlabel(xlabeltag);
      ylabel('dC_L/d\gamma');
      title('\bfSlope of C_L versus \gamma');
      grid on;
%Plot of Den Hartog criterion
   subplot(2,2,4);
      plot(slopeCL(:,1),slopeCL(:,4),style(2,:),slopeCL(:,1),slopeCL(:,5),style(4,:));
end;
if m(2)==16;
   subplot(2,2,1);
      plot(output(:,4)*180/pi,output(:,8),style(2,:),output(:,4)*180/pi,output(:,9),style(3,:),...
         output(:,4)*180/pi,output(:,10),style(4,:),output(:,4)*180/pi,output(:,11),style(5,:));
      legend('Ring 2','Ring 3','Ring 4','Ring 5',4);
      axis(axis1);
      xlabel(xlabeltag);
      ylabel('C_N');
      title(titleline);
      grid on;
   subplot(2,2,2);
```

```
    plot(output(:,4)*180/pi,output(:,13),style(2,:),output(:,4)*180/pi,output(:,14),style(3,:),...
      output(:,4)*180/pi,output(:,15),style(4,:),output(:,4)*180/pi,output(:,16),style(5,:));
    axis(axis1);
    xlabel(xlabeltag);
    ylabel('C_L');
    title('\bfC_L versus \gamma');
    grid on;
  for i=2:1:m(1)-1;
    slopeCL(i,1)=output(i,4)*180/pi;
    slopeCL(i,2)=(((output(i,12)-output(i-1,12))/(output(i,4)-output(i-1,4)))+...
      ((output(i+1,12)-output(i,12))/(output(i+1,4)-output(i,4))))/2;
    slopeCL(i,3)=(((output(i,13)-output(i-1,13))/(output(i,4)-output(i-1,4)))+...
      ((output(i+1,13)-output(i,13))/(output(i+1,4)-output(i,4))))/2;
    slopeCL(i,4)=(((output(i,14)-output(i-1,14))/(output(i,4)-output(i-1,4)))+...
      ((output(i+1,14)-output(i,14))/(output(i+1,4)-output(i,4))))/2;
    slopeCL(i,5)=(((output(i,15)-output(i-1,15))/(output(i,4)-output(i-1,4)))+...
      ((output(i+1,15)-output(i,15))/(output(i+1,4)-output(i,4))))/2;
    slopeCL(i,6)=(((output(i,16)-output(i-1,16))/(output(i,4)-output(i-1,4)))+...
      ((output(i+1,16)-output(i,16))/(output(i+1,4)-output(i,4))))/2;
    slopeCL(i,7)=output(i,7)+slopeCL(i,2);%Cd+dCl/dg
    slopeCL(i,8)=output(i,8)+slopeCL(i,3);
    slopeCL(i,9)=output(i,9)+slopeCL(i,4);
    slopeCL(i,10)=output(i,10)+slopeCL(i,5);
    slopeCL(i,11)=output(i,11)+slopeCL(i,6);
  end;
  slopeCL(1:m(1)-2,:)=slopeCL(2:m(1)-1,:);
  subplot(2,2,3);
    plot(slopeCL(:,1),slopeCL(:,3),style(2,:),slopeCL(:,1),slopeCL(:,4),style(3,:),...
      slopeCL(:,1),slopeCL(:,5),style(4,:),slopeCL(:,1),slopeCL(:,6),style(5,:));
    axis(axis2);
    xlabel(xlabeltag);
    ylabel('dC_L/d\gamma');
    title('\bfSlope of C_L versus \gamma');
    grid on;
  subplot(2,2,4);
    plot(slopeCL(:,1),slopeCL(:,8),style(2,:),slopeCL(:,1),slopeCL(:,9),style(3,:),...
      slopeCL(:,1),slopeCL(:,10),style(4,:),slopeCL(:,1),slopeCL(:,11),style(5,:));
end;
axis(axis2);
xlabel(xlabeltag);
ylabel('C_N + dC_L/d\gamma');
title('\bfC_N+dC_L/d\gamma versus \gamma');
grid on;
  h = axes('Position',[0 0 1 1],'Visible','off');
  set(gcf,'CurrentAxes',h);
  str={strcat('\bfU=',num2str(output(1,1),'%4.1f'),...
      ' m/s, Re=',num2str(output(1,2),'%4.2e'),', \theta=',file(1:2),'\circ inclination')};
  text(0.25,0.025,str,'Fontsize',10);
  set(gcf,'Color',[1,1,1]);
figure;
if m(2)==10;
  plot(slopeCL(:,1),slopeCL(:,4),style(2,:),slopeCL(:,1),slopeCL(:,5),style(4,:));
  legend('Ring 2','Ring 4',4);
end;
if m(2)==16;
  plot(slopeCL(:,1),slopeCL(:,8),style(2,:),slopeCL(:,1),slopeCL(:,9),style(3,:),...
      slopeCL(:,1),slopeCL(:,10),style(4,:),slopeCL(:,1),slopeCL(:,11),style(5,:));
  legend('Ring 2','Ring 3','Ring 4','Ring 5',4);
end;
axis(axis2);
xlabel(xlabeltag);
ylabel('C_N + dC_L/d\gamma');
title('\bfC_N+dC_L/d\gamma versus \gamma');
grid on;
  h = axes('Position',[0 0 1 1],'Visible','off');
  set(gcf,'CurrentAxes',h);
  str={strcat('\bfU=',num2str(output(1,1),'%4.1f'),...
      ' m/s, Re=',num2str(output(1,2),'%4.2e'),', \theta=',file(1:2),'\circ inclination')};
  text(0.05,0.025,str,'Fontsize',10);
  set(gcf,'Color',[1,1,1]);
```

```
function pressuredistribution
%created by Cory Zurell
%April 2003
%
%The M-file performs the following functions:
%1. Calculates the mean, ,rms, max, and min pressure value for each tap  on the cable model.
%2. Saves these values along with wind speed info etc. into a file for further operations.
%
%Required Input: same as pressure
load directory.mat;
k=size(directory);
for j=1:1:k(1);
   load directory.mat;
   cd([directory(j,:)]);
   file=strcat('files',directory(j,18:20),'.mat');
%*****
   load(file); %contains a list of the file names in each directory
   m=size(files);
%
for i=1:1:m(1);
   z=files(i,:);
   load(z); %each file in the directory is loaded and processed in turn
   pressureData=double(pressureData(l,:));
   if (frameFile(6)=='1');
      pressureData=pressureData(1:160,:); %truncates the array of the data
% corresponding to the longitudinal lines of taps - not needed at this time
   end
   pressureData=pressureData*6894.76; %converts "pressureData" to Pa from psi
   hBeta=hBeta*pi/180; %converts units from degrees to radians for calculations
   vAlpha=vAlpha*pi/180;
   phi=acos(cos(vAlpha)*cos(hBeta));
   if hBeta>pi/2; %This corrects phi for yaw angles greater than 90 - phi is the
      phi=pi-phi; %complementary angle to that calculated above when hBeta>90
   end;
   gamma=atan(tan(hBeta)/sin(vAlpha));
   if hBeta>pi/2;
      if gamma<0; %This line corrects gamma for yaw angles greater than
         gamma=pi+gamma; %90 degrees.  The comparison angle of -10 degrees
      end; %            is arbitrary.
   end;
% The values in "q" and "z_off" are in [kPa] - convert these to [Pa]
   q=q*1000;
   z_off=z_off*1000;
%Correction for damaged taps
   if (frameFile(6)=='1');%low scan case, frameFile is of the form wt750192.frm
      pressureData(64,:)=mean(pressureData([33 63],:));
      pressureData(142,:)=mean(pressureData([141 143],:));
   end;
   if (frameFile(6)=='_');%high scan case, frameFile is of the form wt750_64.frm
      pressureData(32,:)=mean(pressureData([1 31],:));
   end;
% The mean values of pressure are required for each tap to calculate the
% lift and drag forces
   stats(:,2,i)=(-1)*mean(pressureData,2); %mean pressure at each tap
   stats(:,3,i)=sqrt(mean(pressureData.*pressureData,2)); %rms
   stats(:,4,i)=(-1)*max(pressureData,[],2); %max
   stats(:,5,i)=(-1)*min(pressureData,[],2); %min
   stats(1,1,i)=[U];
   stats(2,1,i)=[Re];
   stats(3,1,i)=[phi];
   stats(4,1,i)=[gamma];
   stats(5,1,i)=[vAlpha];
   stats(6,1,i)=[hBeta];
   stats(7,1,i)=[q];
   stats(8,1,i)=[z_off];
end;
filename=strcat(z(1:2),'_press_',file(6:8),'.mat');
save(filename,'stats');
clear;
end;
```

```
function ESDU80025
%This function determines the pressure coefficient at each pressure tap, determines the drag coefficient for the
% model, and plots the pressure distribution around the ring based on theoretical values produced from ESDU 80025
%
file=input('Enter the summary "**_press_***.mat" filename corresponding \n to the data in this directory:','s')
load(file);
load coords.mat;
m=size(stats);
%
angle(:,1)=pi-coords(:,2);
% Theoretical parameters for evaluation of theoretical pressure distribution
D=0.0889;       %(m) diameter of model
epsilon=5.78e-7; %(m) height of surface roughness
E=epsilon/D*1000;%surface roughness to diameter ratio x10^3
Iu=0.0013;      %turbulence intensity - info from NRC
rLu=0.001;      %(m) scale of turbulence - our tests were conducted in smooth flow
%  therefore this is very small - it has been set at 1 mm arbitrarily to
%  achieve ~1.4 for lambdaTcrit below as noted in ESDU 80025
prod=Iu*((D/rLu)^0.2);
lambdaR=7-6*exp(-0.11*E);
v=0.000015;     %viscosity of air
lambdaTcrit=13-12*exp(-11.5*prod); %noted to be about 1.4 for a low turbulence windtunnel
Recrit=4.5e5/(lambdaTcrit*lambdaR);
ReeA=10^(5.55+0.19*exp(-0.32*(E^0.35)));
ReeB=10^(5.65+0.22*exp(-0.7*(E^0.5)));
b=4.5/(1+5*(log10(E)-0.15)^2)+4;
CM=1.04-0.47*exp(-(0.9*E+0.55*E^0.5))+0.11*(1-exp(-8e-4*E^2));
CB=1.1-0.83*exp(-(0.01*E+0.34*E^0.5));
n=0.06*exp(-0.04*E^2);
%
%The following section determines the theoretical drag force on a circular
%section.
%
for i=1:1:m(3);
   ESDU(1:8,1,i)=stats(1:8,1,i); %copies info on windspeed, relatvie angles etc. from test data
   Re=stats(1,1,i)*D./(cos(pi/2-stats(3,1,i))*v); %Re=V D/v cos(pi/2-phi) - the angle
   %is taken between the wind direction and the normal to the cable axis
   ESDU(9,1,i)=Re;
   ratio=Re/Recrit;
   R1=log10(2*ratio);
   if ratio<=0.5;
      lambdiff=1.28*exp(-20*((-1*R1)^2.8)); %(lambdaT-1)/(lambdaTcrit-1)
   end;
   if ratio>0.5;
      lambdiff=1.28*exp(-1.3*(R1^1.4)-0.1*(R1^4));
   end;
   lambdaT=lambdiff*(lambdaTcrit-1)+1;
   Ree=Re*lambdaT*lambdaR;
   R=log10(Ree/ReeB);
   f1=1-exp(-(R + 2*b*R^2 - b*R^3)); % f1
   if Ree<=ReeA;
      CD01=0.27+0.93*exp(-1.65e-7*(Ree*1e-5)^10); %CD0/(1+2e/D)
   end;
   if Ree>ReeA;
      CD01=f1*(CM-CB)+CB-n*(1-exp(-0.5*R^4));
   end;
   CD0=CD01*(1+2*epsilon/D); %CD0
   if Ree>3e7;
      CD01=f1*(CM-CB)+CB-n*(1-exp(-0.5*(log10(3e7/ReeB)^4)));
      CD0=CD01*(1+2*epsilon/D);
   end;
   ESDU(10,1,i)=CD0;
   % The following sections determines the theoretical pressure distribution
   % around a circular section based on the theoretical drag calculated above.
   Cpb=0.0796*(1.3-(CD0)^0.8)^10 - 0.918*CD0 - 0.098;
   c=(1.3+Cpb)^3;
   k=(Ree-ReeA)/(ReeB-ReeA);
   if Ree<=ReeA;
      k=0;
   end;
```

```
   if Ree>=ReeB;
      k=1;
   end;
   thetab=145.4 + 42.4*Cpb - 7.8*Cpb^2 + k/(0.076+0.939*(c^2+c));
   thetam=90-23*exp(-0.363*(0.01*thetab)^5);
   dtheta=thetab-thetam;
   dCp=4*(1.013-exp(-6e-6*dtheta^3)) - 1/(4.7+0.028*(abs(dtheta-28))^3);
   Cpm=Cpb-dCp;
   thetab=thetab*pi/180; %converts to radians for calculations
   thetam=thetam*pi/180;
   dtheta=dtheta*pi/180;
   for j=1:1:32;
      if abs(angle(j,1))<=thetam;
         ESDU(j,2,i)=1-(1-Cpm)*(sin((angle(j,1)/thetam)*pi/2))^2;
      end;
      if abs(angle(j,1))>thetam;
         ESDU(j,2,i)=Cpb-(Cpb-Cpm)*(cos(((abs(angle(j,1))-thetam)/dtheta)*pi/2))^2;
      end;
      if abs(angle(j,1))>=thetab;
         ESDU(j,2,i)=Cpb;
      end;
   end;
end;
%
%
%
style=['- ^k';'- +k';'- ok';'- *k';'- xk';'-- r'];
   if (m(1)==160);%low scan case, 5 rings
      x=1;
      y=5;
      n=1;
   end;
   if (m(1)==64);%high scan case, 2 rings
      x=2;
      y=4;
      n=2;
   end;
for i=1:1:m(3);
   Cp(:,1,i)=(stats(:,2,i)+stats(8,1,i))/(stats(7,1,i)); %Cp=(p-p0)/1/2rhoV^2
   %z_off has been added in the above command since cazpressdist switches
   %the signs of pressure and suction
   for ring=x:n:y;
      base=32*((ring/n)-1);
      drag(ring,i)=sum(stats(base+1:base+32,2,i).*coords(:,3).*(cos(coords(:,2)).*cos(stats(4,1,i))...
         +sin(coords(:,2)).*sin(stats(4,1,i))));
      lift(ring,i)=(-1)*sum(stats(base+1:base+32,2,i).*coords(:,3).*(sin(coords(:,2)).*cos(stats(4,1,i))...
         -cos(coords(:,2)).*sin(stats(4,1,i)))); %the -1 at the beginning makes lift in the negative
   %y direction which in this case is the lift
      Cn(ring,1,i)=drag(ring,i)/(stats(7,1,i)*0.0889); % /((sin(stats(3,1,i)))^2);
      Cl(ring,1,i)=lift(ring,i)/(stats(7,1,i)*0.0889); % /((sin(stats(3,1,i)))^2);
      Cp(1:32,ring,i)=Cp(base+1:base+32,1,i);
      infor(1:8,1,i)=stats(1:8,1,i); %array containing wind speed, Re, angles, etc.
   end;
end;
if n==2; %consolidates data if only 2 rings
   Cp(:,1,:)=Cp(:,2,:);
   Cp(:,2,:)=Cp(:,4,:);
   Cp=Cp(1:32,1:2,:);
   Cn(1,:,:)=Cn(2,:,:);
   Cn(2,:,:)=Cn(4,:,:);
   Cn=Cn(1:2,:,:);
   Cl(1,:,:)=Cl(2,:,:);
   Cl(2,:,:)=Cl(4,:,:);
   Cl=Cl(1:2,:,:);
end;
Cp=Cp(1:32,:,:); %gets rid of extra zeros in column 1
Cpp=-1*Cp; %makes pressure positive and suction negative
Cpp(33,:,:)=-1*Cp(1,:,:);
coordsp=coords;
coordsp(33,2)=2*pi;
```

```
%
% plot pressure distribution around the ring
filename=strcat(file(1:2),'_CpCnCl_',file(10:12),'.mat');
save(filename,'infor','Cn','Cl','Cp','ESDU');
%
ESDU(33,2,:)=ESDU(1,2,:);
%
theta=coordsp(:,2);
circ(1:33,1)=5;
[x y]=pol2cart(theta,circ); %produces coordinates for a circle of radius 5
%   plotted on the pressure distribution figures, this circle is the pipe section
%
%The following section plots the pressure distribution for ESDU and either
%only one ring specified by 'ring' or an average of the rings
%figure;
%
for i=1:1:m(3);
   figure;
   rho1=5-ESDU(:,2,i);
   %******These lines result in the plot of only one ring******
   %
     ring=2; %this is the ring number to be plotted
     rho=5-Cpp(:,ring,i);
     str2={strcat('C_N=',num2str(Cn(ring,1,i),'%4.1f'))};
     str3={strcat('C_L=',num2str(Cl(ring,1,i),'%4.1f'))};
   %
   %******
   %
   %
   %******These lines result in the plot of the mean pressure of all rings
   %together******
%        for j=1:1:5;
%           rho(:,j)=5-Cpp(:,j,i);
%        end;
%        rho=mean(rho,2);
%        str2={strcat('C_N=',num2str(mean(Cn(:,1,i)),'%4.2f'))};
%        str3={strcat('C_L=',num2str(mean(Cl(:,1,i)),'%4.2f'))};
   %******
   %
   [X Y]=pol2cart(theta,rho1);
   [X1 Y1]=pol2cart(theta,rho);
%    subplot(3,4,i);
   plot(x,y,'-  k',X1,Y1,'- k',X,Y,'-- r');
   axis([-5.5 5.5 -8 8.5]);
   axis equal;
   axis off;
%    str={strcat('\bfU=',num2str(infor(1,1,i),'%4.1f'),' m/s, Re=',num2str(infor(2,1,i),'%4.2e'),...
%           ', \theta=',file(1:2),'\circ inclination',' \gamma=',num2str(infor(4,1,i)*180/pi,'%4.2f'),'\circ')};
%    title(str);
   strU={strcat('U=',num2str(infor(1,1,i),'%4.1f'),' m/s')};
   strR={strcat('Re=',num2str(infor(2,1,i),'%3.0f'))};
   str1={'Flow'};
   text(0,0.5,str1);
   text(-2,-2,str2);
   text(-2,-3.25,str3);
   text(-2,3,strU);
   text(-2,2,strR);
   hold on;
   XX(1,:)=x';
   YY(1,:)=y';
   XX(2,:)=X1';
   YY(2,:)=Y1';
   line(XX,YY,'Color','k','LineStyle',':');
   hold on;
   compass(2,0,'k');
%
   h = axes('Position',[0 0 1 1],'Visible','off');
   set(gcf,'CurrentAxes',h);
   set(gcf,'Color',[1 1 1]);
end;
```

```
function plotphi
%This function plots the drag coefficient, Cd, the lift coefficient, Cl, the against the relative angle between the wind
%direction and the cable axis to investigate the relationship between the lift and drag coefficient behaviour and
% the relative angle. It also plots Cd and Cl against U for a range of varying angles
%
file=input('Enter the summary "files_**_***.mat" filename corresponding \n to the data in this directory:','s')
load(file);
m=size(files);
for i=1:1:m(1);
   z=files(i,:);
   load(z);
   n=size(output);
% n(1) is the number of attack angles, n(2) determines whether there is
% data for 2 or 5 rings
   for j=1:1:n(1);
      totaloutput(j,:,i)=output(j,:);
   end;
end;
filename=strcat(file(7:8),'_totaloutput_',file(10:12),'.mat');
save(filename,'totaloutput');
% totaloutput(i,:,:) is the angle of attack, totaloutput(:,j,:), is the
% info for each angle of attack (U, Re, phi, Cd, Cl, etc.) and
% totaloutput(:,:,k) is the wind speed
m=size(totaloutput);
for i=1:1:m(1);
   for k=1:1:m(3);
      if m(2)==10;
         totaloutput(i,7,k)=mean(totaloutput(i,7:8,k));% takes average of lift and drag coeff of rings 2 and 4
         totaloutput(i,8,k)=mean(totaloutput(i,9:10,k));
      end;
      if m(2)==16;
         totaloutput(i,7,k)=mean(totaloutput(i,8:11,k));%takes average of lift and drag coeff of rings 2 to 5
         totaloutput(i,8,k)=mean(totaloutput(i,13:16,k));
      end;
   end;
end;
%
figure;
style=['-^k';'-+k';'-ok';'-*k';'-xk';'-dk';'-sk';'-vk';'-<k';'->k'];
titleline=strcat('\bfC_N versus relative angle, \phi');
xlabeltag='Relative angle, \phi (\circ)';
%
      led1=strcat('Re=',num2str(totaloutput(1,2,2),'%6.0f'));
      led2=num2str(totaloutput(1,2,m(3)-4),'%6.0f');
      led3=num2str(totaloutput(1,2,m(3)-3),'%6.0f');
      led4=num2str(totaloutput(1,2,m(3)-2),'%6.0f');
      led5=num2str(totaloutput(1,2,m(3)-1),'%6.0f');
      led6=num2str(totaloutput(1,2,m(3)),'%6.0f');
%
axis1=[50 91 -1.5 1.5];
axis2=[-1 120 -5 5];
if m(2)==10; %Plot of drag coefficient versus relative angle, phi
   totaloutput=totaloutput(1:m(1)-1,:,:);
   if file(7:8)=='60';
      totaloutput=totaloutput(1:m(1)-2,:,:);
   end;
end;
if m(2)==16;
   totaloutput=totaloutput(1:m(1)-2,:,:); %eliminates the values at yaw angles past 90
end;
   subplot(1,2,1);
      plot(totaloutput(:,3,2)*180/pi,totaloutput(:,7,2),style(1,:),totaloutput(:,3,m(3)-4)*180/pi,...
         totaloutput(:,7,m(3)-4),style(2,:),totaloutput(:,3,m(3)-3)*180/pi,totaloutput(:,7,m(3)-3),style(3,:),...
         totaloutput(:,3,m(3)-2)*180/pi,totaloutput(:,7,m(3)-2),style(4,:),totaloutput(:,3,m(3)-1)*180/pi,...
         totaloutput(:,7,m(3)-1),style(5,:),totaloutput(:,3,m(3))*180/pi,totaloutput(:,7,m(3)),style(6,:));
      legend(led1,led2,led3,led4,led5,led6,4);
      axis(axis1);
      xlabel(xlabeltag);
      ylabel('Mean C_N');
      title(titleline);
```

```
    grid on;
  subplot(1,2,2);
    plot(totaloutput(:,3,2)*180/pi,totaloutput(:,8,2),style(1,:),totaloutput(:,3,m(3)-4)*180/pi,...
        totaloutput(:,8,m(3)-4),style(2,:),totaloutput(:,3,m(3)-3)*180/pi,totaloutput(:,8,m(3)-3),style(3,:),...
        totaloutput(:,3,m(3)-2)*180/pi,totaloutput(:,8,m(3)-2),style(4,:),totaloutput(:,3,m(3)-1)*180/pi,...
        totaloutput(:,8,m(3)-1),style(5,:),totaloutput(:,3,m(3))*180/pi,totaloutput(:,8,m(3)),style(6,:));
axis(axis1);
xlabel(xlabeltag);
ylabel('Mean C_L');
title('\bfC_L versus relative angle, \phi');
grid on;
%
  h = axes('Position',[0 0 1 1],'Visible','off');
  set(gcf,'CurrentAxes',h);
  str={strcat('\theta=',file(7:8),'\circ inclination')};
  text(0.45,0.025,str,'Fontsize',10);
  set(gcf,'Color',[1,1,1]); %sets background colour to white
%
%plot drag versus U/Re for various angles
m=size(totaloutput);
for i=1:1:m(1);
  total(:,:,i)=squeeze(totaloutput(i,:,:));
end;
m=size(total);
%
figure;
  subplot(1,2,1);
  plot(total(1,:,1),total(7,:,1),style(1,:),total(1,:,6),total(7,:,6),style(2,:),total(1,:,8),total(7,:,8),style(3,:),...
      total(1,:,m(3)-4),total(7,:,m(3)-4),style(5,:),total(1,:,m(3)-2),total(7,:,m(3)-2),style(6,:),...
      total(1,:,m(3)-1),total(7,:,m(3)-1),style(7,:),total(1,:,m(3)),total(7,:,m(3)),style(8,:));
  ang1=strcat('\phi=',num2str(total(3,1,1)*180/pi,'%4.1f'),'\circ');
  ang2=num2str(total(3,1,6)*180/pi,'%4.1f');
  ang3=num2str(total(3,1,8)*180/pi,'%4.1f');
  ang5=num2str(total(3,1,m(3)-4,1)*180/pi,'%4.1f');
  ang6=num2str(total(3,1,m(3)-2)*180/pi,'%4.1f');
  ang7=num2str(total(3,1,m(3)-1)*180/pi,'%4.1f');
  ang8=num2str(total(3,1,m(3))*180/pi,'%4.1f');
  legend(ang1,ang2,ang3,ang5,ang6,ang7,ang8,4);
axis([10 100 -1.5 1.5]);
ax=[10 100 -1.5 1.5]; %This value has to be the same as 'axis' above
xlabel('Wind speed U(m/s)');
ylabel('Mean C_N');
title('\bfMean C_N versus windspeed for varying angles');
grid on;
%This part adds the secondary x-axis with Reynolds Number
 pos=get(gca,'position');
 shift=[0 .11 0 -.11];
 pos= pos + shift;
 set(gca,'position',pos);
 axes('position', [pos(1:3)-(shift(1:3)) 0.01]);
 low=ax(1)*total(2,1,1)/total(1,1,1)/1000;
 high=ax(2)*total(2,m(2),1)/total(1,m(2),1)/1000;
 set(gca,'XLim',[low high]);
 xlabel('Reynolds Number (x1000)');
 %
 subplot(1,2,2);
  plot(total(1,:,1),total(8,:,1),style(1,:),total(1,:,6),total(8,:,6),style(2,:),total(1,:,8),total(8,:,8),style(3,:),...
      total(1,:,m(3)-4),total(8,:,m(3)-4),style(5,:),total(1,:,m(3)-2),total(8,:,m(3)-2),style(6,:),...
      total(1,:,m(3)-1),total(8,:,m(3)-1),style(7,:),total(1,:,m(3)),total(8,:,m(3)),style(8,:));
axis([10 100 -1.5 1.5]);
ax=[10 100 -1.5 1.5]; %This value has to be the same as 'axis' above
xlabel('Wind speed U(m/s)');
ylabel('Mean C_L');
title('\bfMean C_L versus windspeed for varying angles');
grid on;
%This part adds the secondary x-axis with Reynolds Number
 pos=get(gca,'position');
 shift=[0 .11 0 -.11];
 pos= pos + shift;
 set(gca,'position',pos);
```

```
axes('position', [pos(1:3)-(shift(1:3)) 0.01]);
low=ax(1)*total(2,1,1)/total(1,1,1)/1000;
high=ax(2)*total(2,m(2),1)/total(1,m(2),1)/1000;
set(gca,'XLim',[low high]);
xlabel('Reynolds Number (x1000)');
%
  h = axes('Position',[0 0 1 1],'Visible','off');
  set(gcf,'CurrentAxes',h);
  str={strcat('\theta=',file(7:8),'\circ inclination')};
  text(0.45,0.025,str,'Fontsize',10);
  set(gcf,'Color',[1,1,1]); %sets background colour to white
%
```

```
function PSDprep
%created by Cory Zurell
%March 2003
%
%The M-file performs the following functions:
%1. Organizes the pressure data and corrects for faulty taps.
%2. Condenses the data into files on which to perform an analysis of the power spectral density.
%
%Required Input: same as pressure
%
load directory.mat;
k=size(directory);
for j=1:1:k(1);
   load directory.mat;
   cd([directory(j,:)]);
   file=strcat('files',directory(j,18:20),'.mat');
   %
%file=input('Enter the full "files***.mat" filename corresponding \n to the data in this directory:','s')
   load(file); %contains a list of the file names in each directory
   m=size(files);
   for i=1:1:m(1);
      z=files(i,:);
      load(z); %each file in the directory is loaded and processed in turn
% The following action accomplishes two functions: "pressureData" is a
% single array which must be converted into a double array, and the
% rows in "pressureData" must be arranged into ascending tap order from 1
% to 192 (or 1 to 64 in the case of the highscan runs)
      pressureData=double(pressureData(I,:));
%
      if (frameFile(6)=='1');
         pressureData=pressureData(1:160,:); %truncates the array of the data
% corresponding to the longitudinal lines of taps - not needed at this time
      end;
%
      pressureData=pressureData*6894.4*(-1); %converts "pressureData" to Pa from psi
   %and makes suction positive such that drag in the along wind direction
   %will be positive
      hBeta=hBeta*pi/180; %converts units from degrees to radians for calculations
      vAlpha=vAlpha*pi/180;
      phi=acos(cos(vAlpha)*cos(hBeta));
      if hBeta>pi/2; %This corrects phi for yaw angles greater than 90 - phi is the
         phi=pi-phi; %complementary angle to that calculated above when hBeta>90
      end;
      gamma=atan(tan(hBeta)/sin(vAlpha));
      if hBeta>pi/2;
         if gamma<0; %This line corrects gamma for yaw angles greater than
            gamma=pi+gamma; %90 degrees.  The comparison angle of -10 degrees
         end; %            is arbitrary.
      end;
% The values in "q" and "z_off" are in [kPa] - convert these to [Pa]
      q=q*1000;
      z_off=z_off*1000;
%
%corrects faulty taps and sets program parameters
     if (frameFile(6)=='1');%low scan case, frameFile is of the form wt750192.frm
         pressureData(64,:)=mean(pressureData([33 63],:));
         pressureData(142,:)=mean(pressureData([141 143],:));
         x=1;
         y=5;
         n=1;
      end;
      if (frameFile(6)=='_');%high scan case, frameFile is of the form wt750_64.frm
         pressureData(32,:)=mean(pressureData([1 31],:));
         x=2;
         y=4;
         n=2;
      end;
   %correction and organization of the data is complete
   %Now, the data will be reduced to a lift and drag force over the time
   %series
```

```
   %
      load coords.mat; %required for data calculations-contains angle location of taps
   %
% Calculation of the drag and lift forces and coefficients for each ring.
% Drag is in the along-wind direction given by axis X'. As the cable model
% yaws, axis X deviates from X' by the angle "gamma" calculated above.
      mult1=coords(:,3).*(cos(coords(:,2)).*cos(gamma)+sin(coords(:,2)).*sin(gamma));
      mult1=mult1';
      mult2=coords(:,3).*(sin(coords(:,2)).*cos(gamma)-cos(coords(:,2)).*sin(gamma));
      mult2=mult2';
      for ring=x:n:y;
         base=32*((ring/n)-1);
         w=size(pressureData);
         for v=1:1:w(2)
            drag(ring,v)=sum(mult1*pressureData(base+1:base+32,v));
            lift(ring,v)=(-1)*sum(mult2*pressureData(base+1:base+32,v));
         end;
         output(ring+1,:,i)=drag(ring,:)/(q*0.0889);%Cd
         output(ring+6,:,i)=lift(ring,:)/(q*0.0889);%Cl
      end;
%
      output(1,1:6,i)=[U,Re,phi,gamma,vAlpha,hBeta];
   end;
   clear pressureData;
   if (frameFile(6)=='_'); %condense data
      output(2,:,:)=output(3,:,:);
      output(3,:,:)=output(5,:,:);
      output(4,:,:)=output(8,:,:);
      output(5,:,:)=output(10,:,:);
      output=output(1:5,:,:);
   end;
   output=single(output); %converts to single precision to limit file size
   filename=strcat(z(1:2),'_PSDprep_',file(6:8),'.mat');
   save(filename,'output');
%
   clear;
end;
```

```
function PSDplot
%created by Cory Zurell
%March 2003
%The M-file performs the following functions:
%1. Plots the power spectral density of the lift coefficient for the given time series.
%Required Input: files of the form "55_PSDprep_091.mat" derived from the raw data by using the m-file 'cazPSDprep'
%
file=input('Enter the full "**_PSDprep_***.mat" filename corresponding \n to the data in this directory:','s')
load(file); %contains the time history lift and drag data
output=double(output); %converts to double precision
m=size(output); %output contains an i x j x k matrix - the first row in each 'page', k, contains the information
%about the test run (U, Re, phi, gamma, vAlpha, hBeta) the next rows contain Drag and lift coefficients over
%the complete time history of the run. The different 'pages', k, contain data for each run - usually differentiated
% by a different yaw angle.
fr=1024; %FFT length
for i=1:1:m(3); %m(3) gives the number of 'pages' of the matrix – from each 'page' a separate PSD plot will be derived
   figure;
   if m(1)==5; %high-scan case
      x=1;
      y=3;
      rings=2;
      count=[2 4];
      freq=1201.92; %scan rate in Hz
   end;
   if m(1)==11;
      x=2; %starting at 2 will ignore ring 1
      y=7; %starting at 7 will ignore ring 1
      rings=4; %ring 1 has been ignored
      count=[2 3 4 5];
      freq=400.64; %scan rate in Hz
   end;
   for j=1:1:rings;
      Y=fft(output(y+j,:,i),fr); %only determining the PSD of the lift coeff
      Pyy=Y.*conj(Y)/fr;
      Pyy(1)=0;
      f=freq/fr*(0:(fr/2-1));
%     f=freq/fr*(0:(fr/2-1))*0.089/(output(1,1,i)*sin(output(1,3,i))); %This line in lieu of that above plots PSD in
% terms of Strouhal number(dimensionless f) and uses velocity component perpendicular to cable axis
      subplot(rings/2,2,j);
      plot(f,Pyy(1:fr/2),'k');
      axis([0 100 0 2.5]);
      xlabel('f (Hz)');
%     axis([0 0.5 0 50]); %This axis defintion when plotting dimensionless frequency
%     xlabel('f D/Usin\phi');
      ylabel('PSD of C_L')
      title(strcat('Ring #',num2str(count(j))));
      %grid on;
      set(gcf,'Color',[1,1,1]); %sets background colour to white
   end;
   h = axes('Position',[0 0 1 1],'Visible','off');
   set(gcf,'CurrentAxes',h);
   str={strcat('PSD of C_L for \bfU=',num2str(output(1,1,i),'%4.1f'),' m/s, Re=',num2str(output(1,2,i),...
        '%4.2e'),', \theta=',num2str(output(1,5,i)*180/pi),'\circ inclination',...
        ', \beta=',num2str(output(1,6,i)*180/pi),'\circ yaw, \phi=',num2str(output(1,3,i)*180/pi),'\circ')};
   text(0.05,0.025,str,'Fontsize',10);
   set(gcf,'Color',[1,1,1]); %sets background colour to white
   %
end;
f=freq/fr*(0:(fr/2-1));
for i=1:1:m(3);
   Y1(i,:)=fft(output(y+1,:,i),fr);
   Y2(i,:)=fft(output(y+2,:,i),fr);
   Py1=Y1.*conj(Y1)/fr;
   Py2=Y2.*conj(Y2)/fr;
end;
```

```
function coherence
%created by Cory Zurell
%June 2003
%The M-file performs the following functions:
%1. Plots the coherence of the lift coefficient of two rings for the given time series. Each plot corresponds to a different
%relative angle
%Required Input: files of the form "55_PSDprep_091.mat" derived from the raw data by using the m-file 'cazPSDprep'
%
file=input('Enter the full "**_PSDprep_***.mat" filename corresponding \n to the data in this directory:','s')
load(file); %contains the time history lift and drag data
%
output=double(output); %converts to double precision
m=size(output); %output contains an i x j x k matrix - the first row in each 'page', k, contains the information about the
%test run (U, Re, phi, gamma, vAlpha, hBeta) the next rows contain Drag and lift coefficients over the complete time
%history of the run. The different 'pages', k, contain data for each run - usually differentiated by a different yaw angle.
for i=1:1:m(3); %m(3) gives the number of 'pages' of the matrix, from each 'page' a separate coherence plot will be derived
   figure;
   if m(1)==5; %high-scan case
      x=1;
      y=3;
      rings=2;
      count=[2 4];
      freq=1201.92; %scan rate in Hz
      [Cxy,f] = cohere(output(4,:,i),output(5,:,i),4096,freq);
      plot(f,Cxy,'k')
      axis([0 600 0 1])
      title('Coherence of Lift Coefficient of Rings 2 and 4');
      xlabel('f (Hz)');
      ylabel('Coherence Function Estimate');
   end;
   if m(1)==11; %low scan rate
      x=2;
      y=3;
      freq=400.64; %scan rate in Hz
      fre=1024;%512;
      [Cxy25,f]=cohere(output(8,:,i),output(11,:,i),fre,freq);
      subplot(x,y,1);
         plot(f,Cxy25,'k');
         axis([0 200 0 1]);
         xlabel('f (Hz)');
         ylabel('Coherence Function Estimate');
         title('Rings 2 & 5 (7D)');
      [Cxy24,f]=cohere(output(8,:,i),output(10,:,i),fre,freq);
      subplot(x,y,2);
         plot(f,Cxy24,'k');
         axis([0 200 0 1]);
         xlabel('f (Hz)');
         %ylabel('Coherence Function Estimate');
         title('Rings 2 & 4 (6D)');
      [Cxy23,f]=cohere(output(8,:,i),output(9,:,i),fre,freq);
      subplot(x,y,3);
         plot(f,Cxy23,'k');
         axis([0 200 0 1]);
         xlabel('f (Hz)');
         %ylabel('Coherence Function Estimate');
         title('Rings 2 & 3 (4D)');
      [Cxy35,f]=cohere(output(9,:,i),output(11,:,i),fre,freq);
      subplot(x,y,4);
         plot(f,Cxy35,'k');
         axis([0 200 0 1]);
         xlabel('f (Hz)');
         ylabel('Coherence Function Estimate');
         title('Rings 3 & 5 (3D)');
      [Cxy34,f]=cohere(output(9,:,i),output(10,:,i),fre,freq);
      subplot(x,y,5);
         plot(f,Cxy34,'k');
         axis([0 200 0 1]);
         xlabel('f (Hz)');
         %ylabel('Coherence Function Estimate');
         title('Rings 3 & 4 (2D)');
```

```
    [Cxy45,f]=cohere(output(10,:,i),output(11,:,i),fre,freq);
    subplot(x,y,6);
        plot(f,Cxy45,'k');
        axis([0 200 0 1]);
        xlabel('f (Hz)');
        %ylabel('Coherence Function Estimate');
        title('Rings 4 & 5 (1D)');
end;
set(gcf,'Color',[1,1,1]); %sets background colour to white
h = axes('Position',[0 0 1 1],'Visible','off');
set(gcf,'CurrentAxes',h);
str={strcat('Coherence of C_L for \bfU=',num2str(output(1,1,i),'%4.1f'),' m/s, Re=',num2str(output(1,2,i),...
        '%4.2e'),', \theta=',num2str(output(1,5,i)*180/pi),'\circ inclination',...
        ', \beta=',num2str(output(1,6,i)*180/pi),'\circ yaw, \phi=',num2str(output(1,3,i)*180/pi),'\circ')};
text(0.05,0.025,str,'Fontsize',10);
set(gcf,'Color',[1,1,1]); %sets background colour to white
end;
```

```
function coherence2
%created by Cory Zurell
%June 2003
%
%The M-file performs the following functions:
%1. Plots the coherence of the lift coefficient of two rings for the given time series. Each figure corresponds to a different
%combination of rings
%
%Required Input: files of the form "55_PSDprep_091.mat" derived from the
%raw data by using the m-file 'cazPSDprep'
%
file=input('Enter the full "**_PSDprep_***.mat" filename corresponding \n to the data in this directory:','s')
load(file); %contains the time history lift and drag data
%
output=double(output); %converts to double precision
%
m=size(output);
  figure;
  if m(1)==5; %high-scan case
    x=1;
    y=3;
    rings=2;
    count=[2 4];
    freq=1201.92; %scan rate in Hz
    [Cxy,f] = cohere(output(4,:,i),output(5,:,i),4096,freq);
    plot(f,Cxy,'k')
    axis([0 600 0 1])
    title('Coherence of Lift Coefficient of Rings 2 and 4');
    xlabel('f (Hz)');
    ylabel('Coherence Function Estimate');
  end;
%The following will plot the coherence plots for each comparison on one sheet
  if m(1)==11;
    freq=400.64;%scan rate in hertz
    fre=1024;%512;
    x=3;
    y=3;
    %
    %**************Rings 2 and 5*************
%     for i=1:1:9;
%       count=i;
    for i=10:1:18;
      count=i-9;
%    for i=19:1:27;
%      count=i-18;
      [Cxy25,f]=cohere(output(8,:,i),output(11,:,i),fre,freq);
      subplot(x,y,count);
        plot(f,Cxy25,'k');
%         axis([0 200 0 1]);
        axis([0 50 0 1]);
        xlabel('f (Hz)');
        ylabel('Coherence Function Estimate');
        angle1={strcat('\beta=',num2str(output(1,6,i)*180/pi,'%4.1f'),'\circ')};
        angle2={strcat('\phi=',num2str(output(1,3,i)*180/pi,'%4.1f'),'\circ')};
        text(140,0.9,angle1,'Fontsize',8);
        text(140,0.8,angle2,'Fontsize',8);
      set(gcf,'Color',[1,1,1]); %sets background colour to white
      h = axes('Position',[0 0 1 1],'Visible','off');
      set(gcf,'CurrentAxes',h);
      str={strcat('\bfCoherence of C_L for Rings 2 and 5 (7D) for U=',num2str(output(1,1,i),'%4.1f'),...
          ' m/s, Re=',num2str(output(1,2,i),'%4.2e'),', \theta=',num2str(output(1,5,i)*180/pi),'\circ inclination')};
      text(0.05,0.025,str,'Fontsize',10);
      set(gcf,'Color',[1,1,1]); %sets background colour to white
    end;
    %
    %**************Rings 2 and 4**************
    figure;
%     for i=1:1:9;
%       count=i;
    for i=10:1:18;
```

```
        count=i-9;
%       for i=19:1:27;
%          count=i-18;
        [Cxy24,f]=cohere(output(8,:,i),output(10,:,i),fre,freq);
        subplot(x,y,count);
           plot(f,Cxy24,'k');
%             axis([0 200 0 1]);
           axis([0 50 0 1]);
           xlabel('f (Hz)');
           ylabel('Coherence Function Estimate');
           angle1={strcat('\beta=',num2str(output(1,6,i)*180/pi,'%4.1f'),'\circ')};
           angle2={strcat('\phi=',num2str(output(1,3,i)*180/pi,'%4.1f'),'\circ')};
           text(140,0.9,angle1,'Fontsize',8);
           text(140,0.8,angle2,'Fontsize',8);
        set(gcf,'Color',[1,1,1]); %sets background colour to white
        h = axes('Position',[0 0 1 1],'Visible','off');
        set(gcf,'CurrentAxes',h);
        str={strcat('\bfCoherence of C_L for Rings 2 and 4 (6D) for U=',num2str(output(1,1,i),'%4.1f'),...
              ' m/s, Re=',num2str(output(1,2,i),'%4.2e'),', \theta=',num2str(output(1,5,i)*180/pi),'\circ inclination')};
        text(0.05,0.025,str,'Fontsize',10);
        set(gcf,'Color',[1,1,1]); %sets background colour to white
    end;
    %
    %
    %*****************Rings 2 and 3*****************
    figure;
%       for i=1:1:9;
%          count=i;
    for i=10:1:18;
        count=i-9;
%       for i=19:1:27;
%          count=i-18;
        [Cxy23,f]=cohere(output(8,:,i),output(9,:,i),fre,freq);
        subplot(x,y,count);
           plot(f,Cxy23,'k');
%             axis([0 200 0 1]);
           axis([0 50 0 1]);
           xlabel('f (Hz)');
           ylabel('Coherence Function Estimate');
           angle1={strcat('\beta=',num2str(output(1,6,i)*180/pi,'%4.1f'),'\circ')};
           angle2={strcat('\phi=',num2str(output(1,3,i)*180/pi,'%4.1f'),'\circ')};
           text(140,0.9,angle1,'Fontsize',8);
           text(140,0.8,angle2,'Fontsize',8);
        set(gcf,'Color',[1,1,1]); %sets background colour to white
        h = axes('Position',[0 0 1 1],'Visible','off');
        set(gcf,'CurrentAxes',h);
        str={strcat('\bfCoherence of C_L for Rings 2 and 3 (4D) for U=',num2str(output(1,1,i),'%4.1f'),...
              ' m/s, Re=',num2str(output(1,2,i),'%4.2e'),', \theta=',num2str(output(1,5,i)*180/pi),'\circ inclination')};
        text(0.05,0.025,str,'Fontsize',10);
        set(gcf,'Color',[1,1,1]); %sets background colour to white
    end;
    %
    %
    %*****************Rings 3 and 5*****************
    figure;
%       for i=1:1:9;
%          count=i;
    for i=10:1:18;
        count=i-9;
%       for i=19:1:27;
%          count=i-18;
        [Cxy35,f]=cohere(output(9,:,i),output(11,:,i),fre,freq);
        subplot(x,y,count);
           plot(f,Cxy35,'k');
%             axis([0 200 0 1]);
           axis([0 50 0 1]);
           xlabel('f (Hz)');
           ylabel('Coherence Function Estimate');
           angle1={strcat('\beta=',num2str(output(1,6,i)*180/pi,'%4.1f'),'\circ')};
           angle2={strcat('\phi=',num2str(output(1,3,i)*180/pi,'%4.1f'),'\circ')};
```

```
            text(140,0.9,angle1,'Fontsize',8);
            text(140,0.8,angle2,'Fontsize',8);
          set(gcf,'Color',[1,1,1]); %sets background colour to white
          h = axes('Position',[0 0 1 1],'Visible','off');
          set(gcf,'CurrentAxes',h);
          str={strcat('\bfCoherence of C_L for Rings 3 and 5 (3D) for U=',num2str(output(1,1,i),'%4.1f'),...
                ' m/s, Re=',num2str(output(1,2,i),'%4.2e'),', \theta=',num2str(output(1,5,i)*180/pi),'\circ inclination')};
          text(0.05,0.025,str,'Fontsize',10);
          set(gcf,'Color',[1,1,1]); %sets background colour to white
        end;
        %
        %
        %*****************Rings 3 and 4*****************
        figure;
%         for i=1:1:9;
%           count=i;
       for i=10:1:18;
         count=i-9;
%        for i=19:1:27;
%          count=i-18;
          [Cxy34,f]=cohere(output(9,:,i),output(10,:,i),fre,freq);
          subplot(x,y,count);
            plot(f,Cxy34,'k');
%             axis([0 200 0 1]);
            axis([0 50 0 1]);
            xlabel('f (Hz)');
            ylabel('Coherence Function Estimate');
            angle1={strcat('\beta=',num2str(output(1,6,i)*180/pi,'%4.1f'),'\circ')};
            angle2={strcat('\phi=',num2str(output(1,3,i)*180/pi,'%4.1f'),'\circ')};
            text(140,0.9,angle1,'Fontsize',8);
            text(140,0.8,angle2,'Fontsize',8);
          set(gcf,'Color',[1,1,1]); %sets background colour to white
          h = axes('Position',[0 0 1 1],'Visible','off');
          set(gcf,'CurrentAxes',h);
          str={strcat('\bfCoherence of C_L for Rings 3 and 4 (2D) for U=',num2str(output(1,1,i),'%4.1f'),...
                ' m/s, Re=',num2str(output(1,2,i),'%4.2e'),', \theta=',num2str(output(1,5,i)*180/pi),'\circ inclination')};
          text(0.05,0.025,str,'Fontsize',10);
          set(gcf,'Color',[1,1,1]); %sets background colour to white
        end;
        %
        %
        %*****************Rings 4 and 5*****************
        figure;
%         for i=1:1:9;
%           count=i;
       for i=10:1:18;
         count=i-9;
%        for i=19:1:27;
%          count=i-18;
          [Cxy45,f]=cohere(output(10,:,i),output(11,:,i),fre,freq);
          subplot(x,y,count);
            plot(f,Cxy45,'k');
%             axis([0 200 0 1]);
            axis([0 50 0 1]);
            xlabel('f (Hz)');
            ylabel('Coherence Function Estimate');
            angle1={strcat('\beta=',num2str(output(1,6,i)*180/pi,'%4.1f'),'\circ')};
            angle2={strcat('\phi=',num2str(output(1,3,i)*180/pi,'%4.1f'),'\circ')};
            text(140,0.9,angle1,'Fontsize',8);
            text(140,0.8,angle2,'Fontsize',8);
          set(gcf,'Color',[1,1,1]); %sets background colour to white
          h = axes('Position',[0 0 1 1],'Visible','off');
          set(gcf,'CurrentAxes',h);
          str={strcat('\bfCoherence of C_L for Rings 4 and 5 (1D) for U=',num2str(output(1,1,i),'%4.1f'),...
                ' m/s, Re=',num2str(output(1,2,i),'%4.2e'),', \theta=',num2str(output(1,5,i)*180/pi),'\circ inclination')};
          text(0.05,0.025,str,'Fontsize',10);
          set(gcf,'Color',[1,1,1]); %sets background colour to white
        end;
      end;
```

```
function pressurelines
%
%created by Cory Zurell
%July 2002
%The M-file performs the following functions:
%1. Arranges the data for the longitudinal rows of pressure taps
%Required Input: same as 'pressure'
%
load directory.mat;
k=size(directory);
for j=1:1:k(1);
   load directory2.mat;
   load leelines.mat; %this contains the order of the taps on the two leeward lines
   cd([directory(j,:)]);
   file=strcat('files',directory(j,18:20),'.mat');
   load(file); %contains a list of the file names in each directory
   m=size(files);
   m=m(1);
   for i=1:1:m;
      z=files(i,:);
      load(z); %each file in the directory is loaded and processed in turn
   if (frameFile(6)=='1');%low scan case, frameFile is of the form wt750192.frm
   % if the file is for a high scan case, there won't be any readings for the lines
      pressureData=double(pressureData(l,:));
      pressureData=pressureData(leeline,:); %arranges the data into the order of the
%pressure taps in the lines from top to bottom and truncates the data to only that of the leeward taps
%
      pressureData=pressureData*6894.4; %converts "pressureData" to Pa from psi
%
      hBeta=hBeta*pi/180; %converts units from degrees to radians for calculations
      vAlpha=vAlpha*pi/180;
      phi=acos(cos(vAlpha)*cos(hBeta));
      if hBeta>pi/2; %This corrects phi for yaw angles greater than 90 - phi is the
         phi=pi-phi; %complementary angle to that calculated above when hBeta>90
      end;
      gamma=atan(tan(hBeta)/sin(vAlpha));
      if hBeta>pi/2;
         if gamma<0; %This line corrects gamma for yaw angles greater than
            gamma=pi+gamma; %90 degrees.
         end; %
      end;
% The values in "q" and "z_off" are in [kPa] - convert these to [Pa]
      q=q*1000;
      z_off=z_off*1000;
%
      Cp(:,:,i)=(pressureData-z_off)/q;
      clear pressureData;
      stats(:,2,i)=mean(Cp(:,:,i),2);
      stats(:,3,i)=sqrt(mean(Cp(:,:,i).*Cp(:,:,i),2));
      stats(:,4,i)=max(Cp(:,:,i),[],2);
      stats(:,5,i)=min(Cp(:,:,i),[],2);
      stats(1,1,i)=[U];
      stats(2,1,i)=[Re];
      stats(3,1,i)=[phi];
      stats(4,1,i)=[gamma];
      stats(5,1,i)=[vAlpha];
      stats(6,1,i)=[hBeta];
      stats(7,1,i)=[q];
      stats(8,1,i)=[z_off];
   end;
   end;
   if (frameFile(6)=='1');%low scan case, frameFile is of the form wt750192.frm
   Cp=single(Cp); %converts to single precision to limit file size
   filename=strcat(z(1:2),'_lines_',file(6:8),'.mat');
   save(filename,'stats','Cp');
   end;
%
   clear;
end;
```

```
function PSDlines
%created by Cory Zurell
%July 10, 2003
%
%The M-file performs the following functions:
%1. Plots the power spectral density of Cp for taps of the leeward lines.
%
%Required Input: files of the form "90_lines_018.mat" derived from the raw data by using the m-file 'cazpressurelines'
%
file=input('Enter the full "**_lines_***.mat" filename corresponding \n to the data in this directory:','s')
load(file); %contains the time history lift and drag data
%
Cp=double(Cp); %converts to double precision
%
m=size(stats); %stats contains an i x j x k matrix - the first column (j) of each 'page', k, contains the information about the
%test run (U, Re, phi, gamma, vAlpha, hBeta, q, z_off) the next four columns contain the mean, rms, max and min
% values of the pressure coefficient Cp. The different 'pages', k, contain data for each run - usually differentiated
%by a different yaw angle.
for i=1:1:4;%m(3); %m(3) gives the number of 'pages' of the matrix - from
   %each 'page' a separate PSD plot will be derived
   figure;
%   count=[1 2 3 4 5 6 7 8 9 10 13 14 15 16 17 19 20 21];
   count=[22 23 24 25 26 27 28 29 30 34 35 36 37 38 39 40 41 42];
   for j=1:1:18;
      freq=400.64; %scan rate in Hz
      fr=512;
      Y=fft(Cp(count(j),:,i),fr);
      Pyy=Y.*conj(Y)/fr;
      Py(j,:)=Pyy(1:fr/2);
      Py(j,1)=0;
      f=freq/fr*(0:(fr/2-1));
   end;
   f=freq/fr*(0:(fr/2-1));
   %a=squeeze(output(1,3,:));
   line1=[0 0.75 1.5 2.25 3 3.75 4.5 5.25 6.25 7.25 10.25 11.25 12.25 13.25 14.25 16.25 17.25 18.25];
   line2=[0 0.75 1.5 2.25 3 3.75 4.5 5.25 6.25 10.25 11.25 12.25 13.25 14.25 15.25 16.25 17.25 18.25];
   [X,Y] = meshgrid(line2,f);
   %Py=Py1(:,1:fr/2);
   plot3(X,Y,Py','k');
   axis([0 19 0 200 0 1]);
   xlabel('Distance from top tap (x/D)');
   ylabel('f (Hz)');
   zlabel('PSD of C_P');
   grid on;
%   h = axes('Position',[0 0 1 1],'Visible','off');
%   set(gcf,'CurrentAxes',h);
  str={strcat('PSD of C_P for \bfU=',num2str(stats(1,1,i),'%4.1f'),' m/s, Re=',num2str(stats(2,1,i),...
        '%4.2e'),', \theta=',num2str(stats(5,1,i)*180/pi),'\circ inclination',...
        ', \beta=',num2str(stats(6,1,i)*180/pi),'\circ yaw, \phi=',num2str(stats(3,1,i)*180/pi),'\circ')};
  text(0.05,0.025,str,'Fontsize',10);
  set(gcf,'Color',[1,1,1]); %sets background colour to white
   %
end;
```